DROPLETS ON LOW FRICTION SURFACES

J H GUAN

PhD

2017

DROPLETS ON LOW FRICTION SURFACES

JIAN HUI GUAN

A thesis submitted in partial fulfilment of the requirements of the University of Northumbria at Newcastle for the degree of Doctor of Philosophy

Department of Mathematics, Physics & Electrical Engineering

June 2017

Declaration

I declare that the work contained in this thesis has not been submitted for any other award and that it is all my own work. I also confirm that this work fully acknowledges opinions, ideas and contributions from the work of others. The work was done in collaboration with the Durham University and is funded by Reece Innovation.

Any ethical clearance for the research presented in this thesis has been approved. Approval has been sought and granted by the Faculty Ethics Committee on 27/01/2016.

I declare that the word count of this thesis is currently 46658 words

Name: Jian Hui Guan

Signature:

Date: 02/06/2017

Abstract

Droplet mobility on surfaces is often hampered by the pinning of the droplet's contact line. External forces would be needed if motion is to continue. The development of Slippery Liquid-Infused Porous Surfaces (SLIPS) or Lubricant-Impregnated Surfaces (LIS) has since enabled the studies of droplets in low friction situations with virtually no contact angle hysteresis. This thesis presents three separate studies of droplet mobility in the absence of contact line pinning, made possible by the use of SLIPS/LIS. Firstly, the first study of evaporation of sessile droplet under true constant contact angle mode was demonstrated. The lack of contact line pinning meant that droplet's contact line receded smoothly with no stick-slip stepwise retreat as it evaporated. The absence of a contact angle due to the presence of the wetting ridge around the droplet led to the concept of an extrapolated apparent contact angle. The subsequent study saw the experimental realisation of both inward and outward motion of droplet having an apparent contact angle above 90° confined in a wedge geometry formed by a pair of SLIPS/LIS. Out of equilibrium, droplet was free to travel within the wedge until settling at a prescribed location, regardless to its initial position. This enabled the accurate control over the transport and localisation of the droplet by a reconfiguration of the system. The lack of pinning also suggests that the dynamics of the droplet is dictated purely by viscous dissipation. The final study showed that SLIPS/LIS can be created on macro-patterned surfaces. The macro-patterning introduced menisci features in the impregnating liquid layer which interact with the wetting ridge around a droplet. These interactions were used to induce motion to the droplet. It was also found that accurate positioning of the droplet on an otherwise completely slippery surface can be achieved using well-defined surface topography.

Ackonwledgements

First of all, I would like thank my Director of Studies, Prof. Glen McHale, and supervisors, Dr. Gary Wells and Dr. Ben Xu as well as external advisors Prof. David Wood from Durham, Dr. James Martin and Dr. Simone Stuart-Cole from Reece Innovation for their support and guidance through out this project. Their knowledge, expertise and experience have been invaluable. I would also like to thank Dr. Rodrigo Ledesma-Aguilar for his contribution to the project and his role as an advisor for a great portion of the project. I also owe many thanks to my fellow Ph.D student, Mr. Élfego Ruiz-Gutiérrez for his significant contribution to the theoretical aspect of the project and valuable discussions in the lab, and Mr. Ding Wang, for this help in the collection of confocal microscopic images.

I would like to show my gratitude to the technical staff, Dr. Pietro Maiello, Rebecca Payne here at Northumbria and Dr. Michael Cooke at Durham, for their knowledge and valuable experience.

I would like to thank all the members of staff and academics who I have had the pleasure to work beside at both Northumbria University and Durham University, especially Dr. Nicasio Geraldi, Dr. Richard Fu, Dr. Jingting Luo, and Dr. Linzi Dodd.

I would like to express my deepest gratitude to my parents for having always believed in me and my friends, for their support throughout this period in my life. Without them, this would not have been possible.

I am very grateful to Northumbria University for the provision of this Ph.D studentship.

This thesis is dedicated to my grandmother.

"*The imagination of nature is far, far greater than the imagination of man.*"

-Richard Feynman

Contents

Abbreviations

SLIPS - Slippery liquid-infused porous surface(s)

LIS - Lubricant-impregnated surface(s)

PTFE - Polytetrafluoroethylene

LISTA - Liquid-infused surfaces with trapped air

IPA - Isopropyl acohol

HMDS - Hexamethyldisilazane

RPM - Revolutions per minute

UV - Ultra-violet

PEB - Post-exposure bake

EC - Ethyl lactate

CTE - Coefficient of thermal expansion

PPM - Parts per million

OTS - Octadecyltrichlorosilane

SEM - Scanning electron microscopy

CCD - Charge-coupled device

LLD - Landau-Levich-Derjaguin

Nomenclature

γ - interfacial tension

γ_{SV} - solid-vapour interfacial tension

γ_{SL} - solid-liquid interfacial tension

γ_{LV} - liquid-vapour interfacial tension

κ^{-1} - capillary legnth

ρ - density

g - gravitational acceleration

P - pressure

R - radius of curvature

V - volume

A - area

S - spreading coefficient

θ - contact angle

θ_{e} - Young's contact angle

θ_{a} - advancing contact angle

θ_{r} - receding contact angle

θ_{CB} - Cassie-Baxter contact angle

θ_{W} - Wenzel contact angle

θ_{C} - critical contact angle

F - total surface free energy

f_{s} - surface fraction

r_{w} - Wenzel roughness

μ - viscosity

τ - timescale

E - interfacial energy per unit area

β - opening angle

D - diffusion coefficient

W - droplet width

X - droplet position

L - meniscus characteristic length

φ - azimuthal angle

h - droplet aspect ratio

$\pm$ - standard deviation

List of Figures

List of Tables

Chapter 1

Introduction

Wetting is a ubiquitous phenomena in nature as well as in a huge range of biological and technological processes [1–4]. Surfaces exposed to natural environments are almost invariably covered by liquids [2]. The most commonly seen examples include the rain drops beading up on leaves of plants or sliding down the glass windows of cars, dew in the morning due to condensation and formation of water droplets in foggy weather. Since the conception of the field of wetting by Thomas Young and Pierre-Simon Laplace in the early 1800s [4, 5], wetting phenomena has provided a playground for the studies of physics, chemistry and engineering. The interaction between liquids and solids has formed the basis for many areas of scientific research and technological advancement in search for ways to manipulate and control these interactions.

Perhaps the biggest source of inspirations for the development in the field of wetting has been nature, which has "learnt" to control liquids in various ways [6]. Leaves of many plants, especially the leaves of the lotus flower, have evolved to clean itself of dust with rain water [7–9], some species of beetles are able survive in hot desert by collecting vital drinking water from early morning fog and small insects have exploited surface tension of water to gain the ability to walk on water [10, 11]. This control is gained not only through surface chemistry, which is of key importance in determining the wetting behaviour of liquids, much effort have been put into creating surfaces decorated with micro/nano-scale features [6]. The additional roughness to the surface act to amplify the wetting or non-wetting properties of the surface. On a surface that is already liquid repellent, droplets bead up and roll off, without ever making contact with the entire

surface. However, on a surface that likes to be wetted by a liquid, the surface features can cause droplets to pin on the surface and even imbibe completely into the surface. Another way to look at the effect of surface roughness is that a change in the surface chemistry can lead to the surface switching from super-repellent to super-wetting [12]. The combination of liquid repelling surface chemistry and surface texturing thus allows surfaces with even greater liquid-shedding abilities to be developed [7, 13].

The essential characteristic of a liquid-repellent surface is the ease of removal of droplets from the surface by small forces. Although textured surfaces can be used to achieve this, they suffer from various problems which can affect their robustness. Their reliance on the surface features also mean that they are prone to external pressure, which can force droplets to become pinned on the surface. Their ability to shed liquid also rely on the size of the droplets being sufficiently large, at smaller scale droplets may remain on the surface even when tilted at a large angle. The tendency for droplets to pin on the sharp edges of the surface features introduces constraints on the studies where smooth contact line dynamics are desired.

These problems have since motivated the development of new types of surfaces. It has been shown that textured or porous surfaces can be imbibed with lubricating liquid which in turn can be used to repel other immiscible liquids [4, 14, 15]. When designed appropriately, these surfaces are able to retain a layer of the lubricating liquid, separating the droplets and the underlying solid surface by introducing a lubricant-liquid interface. The lack of contact allows droplets to roll off at angles below 1° without any stepwise movement in its contact lines [16, 17]. The development of these surfaces has enabled the studies which have long suffered from the pinning of contact lines. However, such a liquid-liquid interface touches upon fundamental questions relating to wetting and interpretation of contact angles.

This report will present three studies made possible by the low hysteresis characteristics of SLIPS/LIS. Firstly, it will demonstrate the evaporation of sessile droplet in constant contact angle mode. The subsequent study will go on to demonstrate the control over the transport and localisation of highly mobile droplets through the reconfiguration of geometrical confinement and presents an improved method for surface

functionalisation. The final study will describe the autonomous transport and accurate positioning of droplets on macro-patterned (milimetre scale) textured surfaces rendered as SLIPS/LIS by exploited the long range interaction between the droplet and the lubricant layers, a mechanism similar to the "Cheerios effect".

Chapter 2 is the background chapter, it will give a summary of the general theory behind wetting and describes the current progress in the research on SLIPS/LIS. Chapter 3 will describe the methods used throughout the entire project, both in the fabrication and the characterisations of the SLIPS/LIS. The three aforementioned studies will then be presented in Chapter 4, 5 and 6, respectively. Each of these chapters will include specifically tailored sub-chapters on the background and methods. Chapter 7 will present an overall summary of the project and possible future works.

Chapter 2

Background

This chapter gives an overview of the general theory behind solid-liquid interactions and different wetting regimes. It is then followed by a summary of various methods in which the wettability of surfaces can be altered. It will then describe the current state of the research on lubricant-impregnated surfaces and the general theory behind it, laying the ground work for the rest of this thesis.

Wetting

2.1 Surface Tension

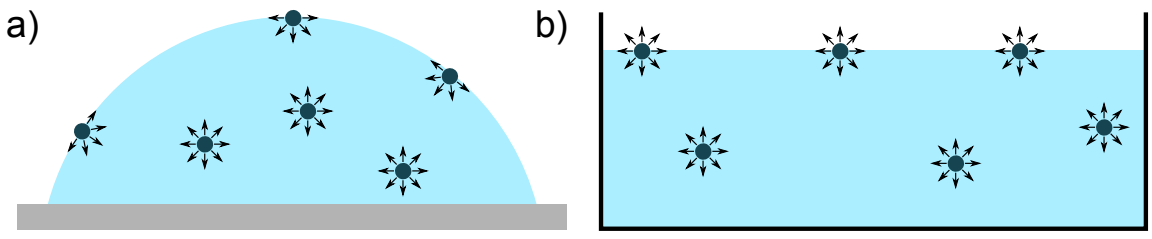

Figure 2.1: Illustrations showing the unbalanced forces of molecules at the surface of the liquid compared to those in the bulk: a. a water droplet, b. a bath of water.

In order to understand the behaviour of a liquid, one should start by considering the interactions between molecules in said liquid. In a liquid, which is a condensed state, molecules are attracted to each other. The attractive forces between the molecules

can be understood as residual electrostatic forces which is referred to as the Van der Waals forces (Figure 2.1) [1]. In the bulk of a liquid, molecules are pulled equally in all directions by the cohesive forces between them. In the surface of the liquid, however, molecules lose half of their cohesive interactions. At the liquid-air interface, the greater attractions of the liquid molecules to each other than to those in the air result in a net force which manifests itself as what is known as surface tension, γ. It is an inward force at the surface of a liquid which causes it to behave like an elastic membrane and it acts to reduce the surface area to volume ratio of a liquid as a way to minimise its total surface free energy. Examples of the effects of surface tension in nature include: the beading of rain water on waxy leaves because the spherical shape has the smallest surface area to volume ratio. Small objects suspended on the surface of water whose downward force is balanced by the opposing surface tension which also allows small insects like water striders to "walk" on water [1].

The term "*surface tension*" is almost exclusively used to describe a liquid-vapour interface, whereas the more general term "*interfacial tension*" is used when describing the surface energy of liquid-vapour interfaces as well as the surface energy between two immiscible liquids, liquid 1 and liquid 2, γ_{12}. This term is also used for solid-liquid and solid-vapour interfaces. All of the above are measured in in units of energy per unit length, mJm^{-1} and can equivalently be expressed as the force per unit length, mNm^{-1}, it is defined as the energy that must be applied to increase the surface area by one unit and the energy difference per unit area between the molecules in the bulk and the surface of the liquid [1].

2.2 Capillary Length

On an ideal surface, the contact angle (see Section 2.5) a droplet makes with the surface is said to be a local quantity and is independent to the drop size, provided that its size is sufficiently large the effects of intermolecular forces and lines tensions to be neglected. In nature, droplets of varying sizes are commonly observed to adopt different shapes when they come into contact with a surface. Small droplets appear spherical whereas larger droplets have the appearance of small puddles. This variation in the droplets'

shapes depend on a particular length known as the capillary length, denoted as κ^{-1},

$$\kappa^{-1} = \left(\frac{\gamma}{\rho g}\right)^{\frac{1}{2}} \tag{2.1}$$

where γ is the liquid-vapour interfacial tension, ρ is the density of the liquid and g refers the acceleration due to gravity. The notation of κ^{-1} comes from the fact that the curvature of a circle is defined to be the reciprocal of the radius, $\kappa = 1/R$. At sizes $\leqslant \kappa^{-1}$, surface tension acts as the dominant force acting on the droplet which tends to impose a minimal surface, it therefore takes the shape of a spherical cap, which is the solution to the Young-Laplace equation in the absence of the effect of gravity (Figure 2.2a1,2). On the other hand, for sizes $> \kappa^{-1}$, surface tension is overcome by gravity and the droplet can no longer maintain a spherical shape and flattens (Figure 2.2a3) [1].

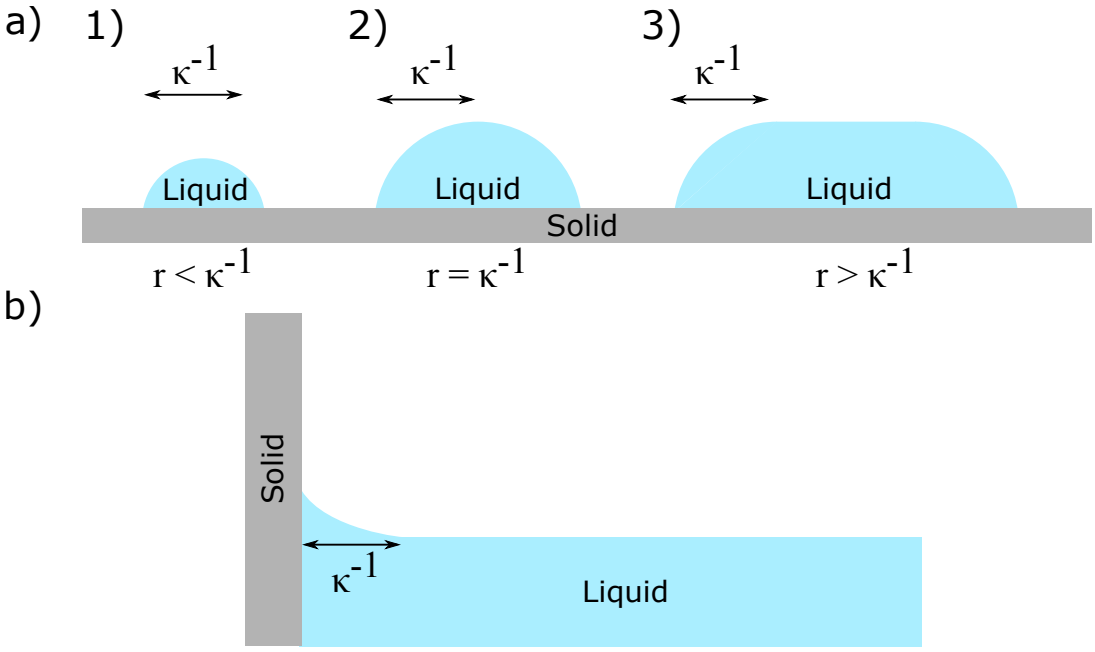

Figure 2.2: a. An illustration of droplets of increasing radius, r: 1. $r < \kappa^{-1}$, 2. $r = \kappa^{-1}$, 3. $r > \kappa^{-1}$. b. a liquid surface perturbed by the presence of a vertical wall.

Aside from liquid droplets, in order to visualise the capillary length, perhaps it is convenient to consider the one-dimensional situation in which a liquid surface is perturbed by the presence of a vertical wall. This perturbation should vanish at a distance of κ^{-1} away from the wall [1].

2.3 Laplace Pressure

When a curved surface is formed between the boundary between a liquid region and a vapour region, there exists a differential pressure between these two regions, first elucidated by French mathematician Pierre-Simon Laplace in 1805, and therefore is known as the "*Laplace Pressure*" [18]. This pressure difference is a result of the interfacial tension at the interface between the liquid and vapour phase [19]. Such pressure difference is responsible for various naturally occurring phenomenons. For instance, in an emulsion, small drops will vanish in favour of larger drops. The same applies to the collapse of small bubbles in a liquid to form bigger bubbles. It also explains phenomenon of capillary adhesion between two objects such as plates, fibres, or in granular media, due to the existence of capillary bridges. It can be determined from the Young-Laplace equation which describes the difference in capillary pressure across the interface between two fluids, it is given as [18],

$$\Delta P = P_{\text{inside}} - P_{\text{outside}} = \gamma\left(\frac{1}{R_1} + \frac{1}{R_2}\right) \tag{2.2}$$

where R_1 and R_2 are the principle radii of curvature and γ is the interfacial tension between the liquid and vapour interfaces and ΔP is the difference between the inside of the liquid, P_{inside}, and the outside, P_{outside}. Equation 2.2 is commonly used to determine differential pressure for spherical droplets or bubbles below the capillary length and therefore by matching the two radii, it can be re-written as,

$$\Delta P = \gamma\left(\frac{1}{R_1} + \frac{1}{R_2}\right) = \gamma\frac{2}{R} \tag{2.3}$$

Equation 2.3 can also be demonstrated by calculating the work done during an infinitesimally small displacement, dR, of a complete spherical drop in a second non-miscible fluid. For example, water (w) suspended in air (a) Figure 2.3). As a way to minimise its total surface energy, the droplet adopts a spherical shape with radius R. The work done thus becomes,

$$\delta W = -P_w dV_w - P_a dV_a + \gamma_{wa} dA \tag{2.4}$$

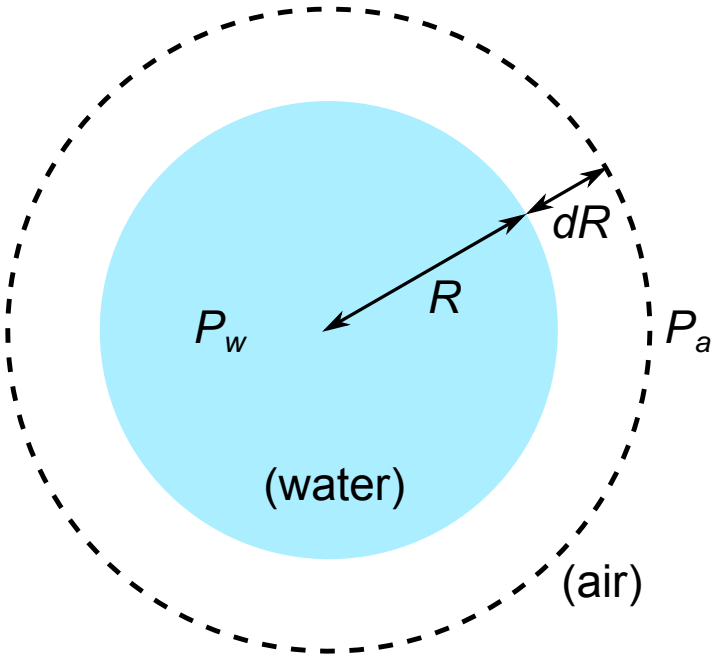

Figure 2.3: Overpressure inside a drop of water "w" in air "a".

where $dV_w = -dV_a = 4\pi R^2 dR$, and $dA = 8\pi R dR$ are the increase in volume and surface area of the droplet, respectively, P_w and P_a are the pressures in the water and air, and γ_{wa} is the interfacial tension between the water and air. The condition for mechanical equilibrium according to classical mechanics leads to $\delta W = 0$, Equation 2.4 can thus be re-written as,

$$\Delta P = P_w - P_a = \frac{2\gamma_{wa}}{R} \tag{2.5}$$

which is equivalent to Equation 2.3. It suggests that pressure difference increases with decreasing R. Smaller drops therefore have greater inner pressure [1].

2.4 Spreading Coefficient

On a smooth and flat surface the interfacial energy per unit area is γ_{SV} when it is dry (SV), when the same surface is coated in a thin layer of liquid the solid-vapour interface is replaced by a solid-liquid interface (SL) and an additional liquid-vapour interface (LV). The combined interfacial energy per unit area is therefore $\gamma_{\mathrm{SL}} + \gamma_{\mathrm{LV}}$. For this liquid to form a film on this surface, it must be energetically favourable such that the combined interfacial free energy is lower than that of a dry surface [3, 20, 21]. The

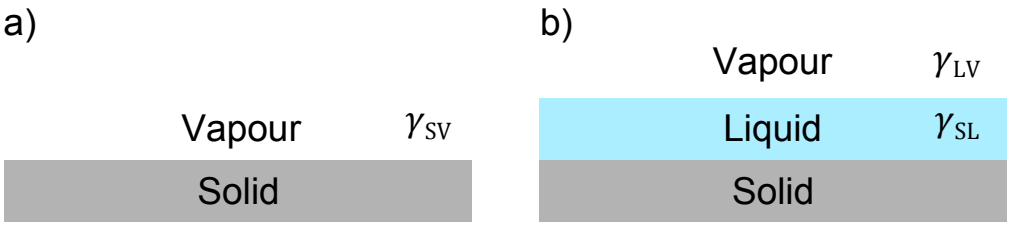

Figure 2.4: a. Dry surface, b. fully wetted surface.

condition for liquid film formation on a smooth and flat surface is therefore,

$$\gamma_{SL} + \gamma_{LV} < \gamma_{SV} \tag{2.6}$$

which can be understood using a parameter, S, which has been defined as the spreading coefficient,

$$S = \gamma_{SV} - (\gamma_{SL} + \gamma_{LV}) \tag{2.7}$$

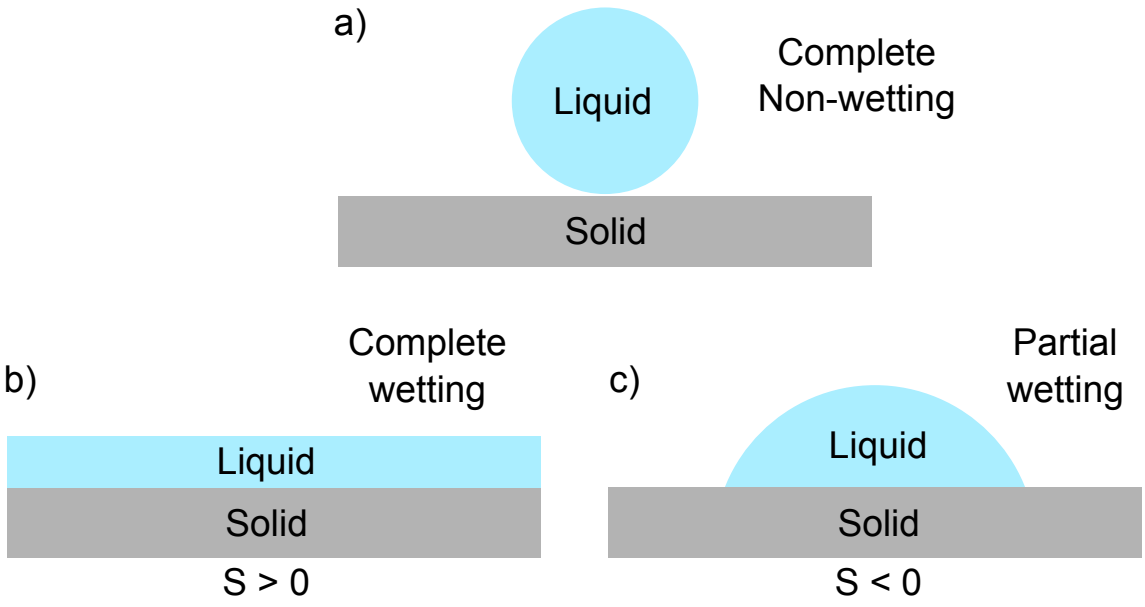

Figure 2.5: a. Complete non-wetting, b. complete wetting, c. partial wetting

$S \geqslant 0$ would lead to a system where the solid-vapour interfacial energy γ_{SV} is greater

than or equal to the combined solid-liquid γ_{SL} and γ_{LV} energies. Therefore, a liquid will spread over the surface to form a liquid film, as a way to reduce the solid-vapour area and thus reducing the overall total surface free energy (Figure 2.5a). Note that absolute energies are used in this energy comparison and it therefore does not concern itself with how one state transforms into the other or overcoming any energy barriers.

In the case of $S < 0$ or $\gamma_{SL} + \gamma_{LV} > \gamma_{SV}$, the complete spreading and the formation of a liquid film no longer results in the lowest overall surface free energy. Therefore, the liquid does not spread over the surface but instead only partially wets the surface (Figure 2.5c). In this regime, droplets below the capillary length will take on the shape of a spherical cap whereas larger droplets are flattened by the effect of gravity (Figure 2.2). Since a liquid film is not formed, the droplet forms a finite angle with the solid surface, $0 < \theta < 180$, where θ is known as the contact angle and 0° and 180° correspond to the values of θ in the complete wetting regime (Figure 2.5b) and the complete non-wetting regime(Figure 2.5a), respectively.

Equation 2.7 refers to the spreading power of liquid (L) on a solid (S) in the presence of vapour (V). It can be re-written in a more generalised form, $S_{12(3)}$, which describes the spreading coefficient for material 1 on material 2 in the presence of fluid 3, which can be vapour or a liquid,

$$S_{12(3)} = \gamma_{23} - (\gamma_{21} + \gamma_{13}) \tag{2.8}$$

As in the previous case, when $S \geqslant 0$, spontaneous spreading of material 1 on material 2 occurs in the presence of fluid 3 as this lowers the overall interfacial energies. The indices in the subscripts in Equation 2.8 are arranged in this way because the energy for $2 \rightarrow 3$ directly is larger than $2 \rightarrow 1$ followed by $1 \rightarrow 3$, but note that $\gamma_{ij} = \gamma_{ji}$. Therefore, this equation can be re-written for different material 1 and 2 and different fluid 3. For example,

$$\text{Oil on a solid in the presence of air} : S_{os(a)} = \gamma_{sa} - \gamma_{os} - \gamma_{oa}$$

$$\text{Oil on water in the presence of air} : S_{ow(a)} = \gamma_{wa} - \gamma_{wo} - \gamma_{oa}$$

2.5 Young's Contact Angle

When a droplet of a liquid rests on a solid surface, the balance between the three interfacial tensions γ_{SV}, γ_{SL} and γ_{LV} determines whether the droplet will eventually be pulled out into a film or whether it will remain as a droplet and if so, its footprint on the solid surface.

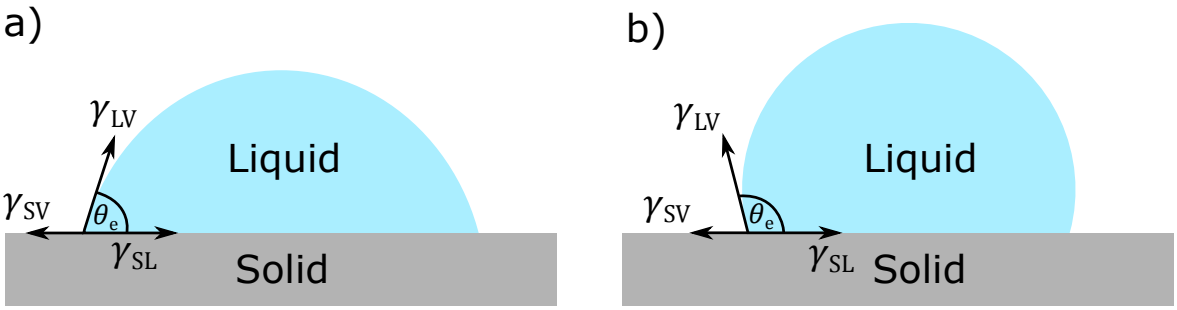

Figure 2.6: Illustration showing the balance of the three interfacial tensions at the three phase contact line of a liquid droplet on a solid, resulting in a contact angle, θ_e: a. $\theta_e < 90°$, b. $\theta_e > 90°$.

When a film is not formed, a droplet remains on a surface in a partial wetting state, there exists a contact angle, denoted as θ_e, at the edge of the droplet Figure 2.6. It is measured between the liquid-vapour and solid-liquid interfaces at the three-phase contact line. Figure 2.6a shows the balance of the three interfacial forces with the droplet forming a contact angle of $\theta_e < 90°$ with the surface. By resolving the three forces, the horizontal force balance per unit length becomes,

$$\gamma_{SV} = \gamma_{SL} + \gamma_{LV} \cos\theta_e \tag{2.9}$$

The same applied to a droplet with $\theta_e > 90°$,

$$\gamma_{SL} = \gamma_{SV} + \gamma_{LV} \cos(\pi - \theta_e) \tag{2.10}$$

Both equations can be re-arranged to make $\cos\theta_e$ the subject to give the Young's equation [5],

$$\cos\theta_e = \frac{\gamma_{SV} - \gamma_{SL}}{\gamma_{LV}} \tag{2.11}$$

Combining the spreading coefficient definition with Young's equation yeilds the Young-Dupré equation [20],

$$S = \gamma_{LV}(\cos\theta_e - 1) \tag{2.12}$$

$\cos\theta_e = 1$ leads to a $\theta_e = 0°$ which means that the liquid spreads and wets the entirety of the surface of the solid, whereas $\cos\theta_e = 0$ gives a contact angle of $\theta_e = 90°$ and will lead to a partially wetted surface (Figure 2.7).

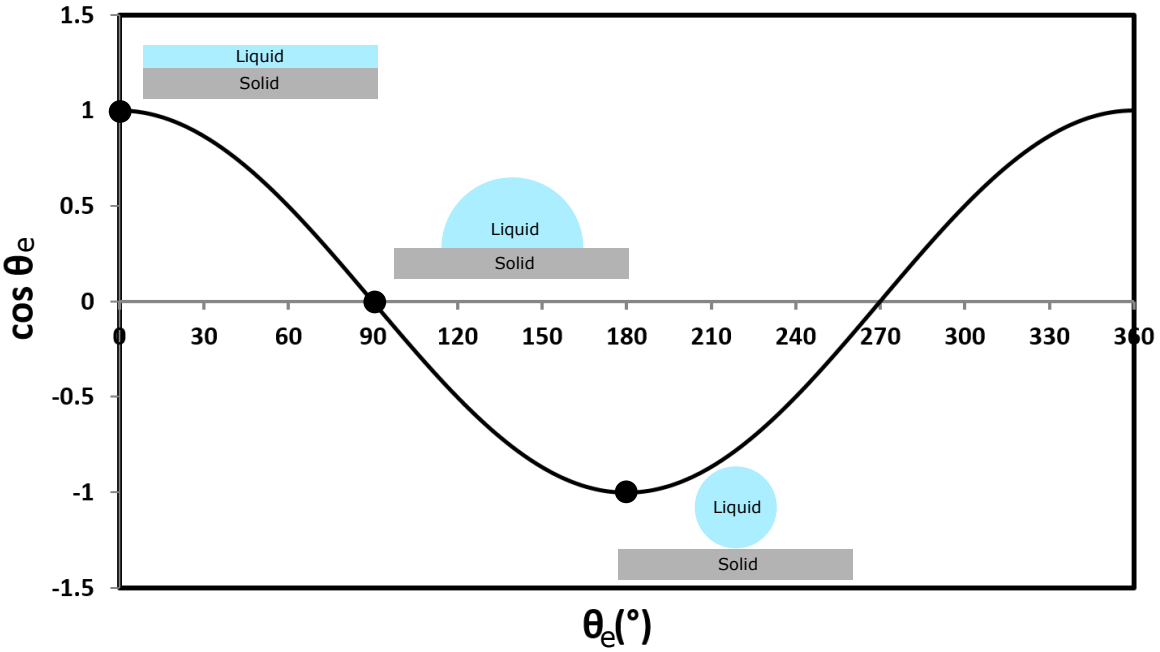

Figure 2.7: $\cos\theta_e$ as a function of contact angle.

The contact angle is independent of droplet size or volume. This means that Equation 2.11 is valid for all droplets on surfaces including large droplets which are flattened in shape in gravity. This equation was established for ideal solids which are smooth and chemically homogenous. The contact angle is governed solely by the chemical nature of the three phases. Figure 2.8 shows a surface which has different regimes with different wettabilities (different contact angles), the regime labelled as "1" has a contact angle of θ_1 and two regimes labelled as "2" have a different contact angle of θ_2, such that $\theta_1 \neq \theta_2$. Only the contact angle on the 2 regimes are the relevant

values to use when considering the droplet's contact angle on the solid surface because the three-phase contact lines are only situated on 2 [3].

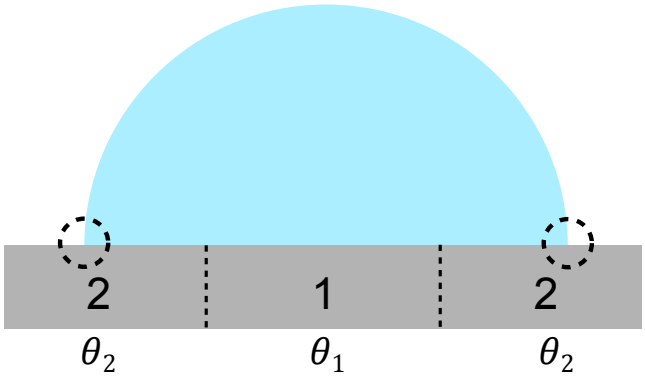

Figure 2.8: A surface with different contact angle regimes.

2.6 Contact Angle Hysteresis

When a droplet is placed on a solid surface, a contact angle θ_e is formed between its edges and the solid surface. For a smooth and flat surface, it is possible for a liquids placed on said surface to achieve contact angle as low as 0°. In the opposite case it is unlikely to achieve contact angle above 120° for smooth and flat surfaces, which are seen for fluoropolymers such as polytetrafluorothylene (PTFE) [22]. The concept of perfectly smooth surfaces is generally unrealistic and surfaces are often found to be marred by defects [23]. They can be chemical such as stains, blotches or physical surface irregularities such as scratches and grooves. These physical defects may have occurred during the fabrication process. Surfaces can be also be composed of compressed grains which naturally produce roughness of the scale of the grains. On these non-ideal surfaces, the static contact angle turns out not to be unique and can take on a range of values [1, 23].

If a droplet deposited on a non-flat surface is slowly inflated by the same liquid, it will begin to expand. As the volume increases, its contact angle θ also increases and can exceed θ_e whilst the line of contact remains stationary. Eventually, the value of θ reaches a threshold value θ_A. Beyond this value, the contact line exhibits a sudden

outward motion as the droplet occupies a larger surface area. This limiting value, θ_{A}, is referred to as the *advancing contact angle* (Figure 2.9a).

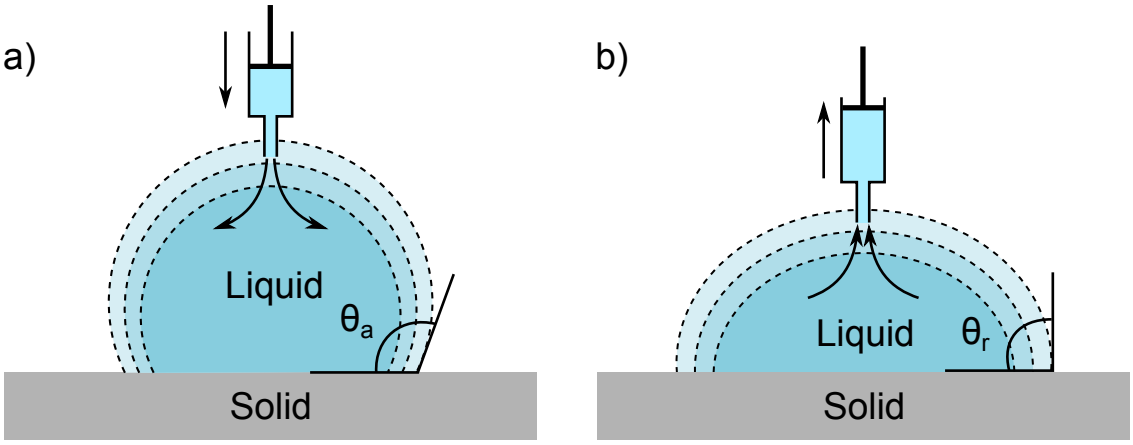

Figure 2.9: Illustration of the advancing contact angle (a) when the droplet is inflated and the receding contact angle (b) when the droplet is deflated.

Likewise, the reverse process would lead to a decrease in the droplet's volume and static contact angle. θ decreases down to another limiting value θ_{R}, at which point the droplet's contact line suddenly recedes to occupy a smaller surface area. This angle is therefore known as the *receding contact angle* (Figure 2.9b).

The advancing θ_{a} and receding θ_{r} contact angles represent the upper and lower limit, respectively, of the range of values the θ_{e} can take. The difference between the two limiting values is known as the *contact angle hysteresis* and θ_{e} is always within these values,

$$\theta_{\mathrm{a}} > \theta_{\mathrm{e}} > \theta_{\mathrm{r}} \tag{2.13}$$

The concept of a droplet having an unique contact angle when it is brought into contact with a surface is therefore an idealised view. It does not take into account the presence of contact angle hysteresis nor the fashion in which the droplet is deposited.

When a droplet is placed on an inclined plane, the contact angle of its leading edge increases and and trailing angle decreases. As a result of contact angle hysteresis, it is therefore possible for droplets to remain stationary on inclined planes; as long as the droplet's leading edge does not exceed the advancing contact angle and the trailing edge's angle drop below the receding contact angle. The difference between the leading

and trailing contact angle creates a difference in the Laplace pressure inside the droplet, generating opposing force on the droplet to gravitational forces, assuming the droplet is sufficiently small [24].

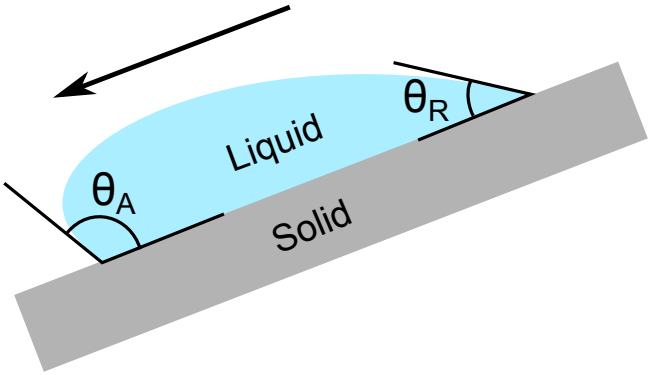

Figure 2.10: Droplet on a tilted surface.

Therefore, another way to determine the contact angle hysteresis is by tilting the substrate until the droplet begins to move. The angle at which the droplet starts to move is referred to as the *sliding angle*. However, there is no fundamental proof that this method would give the same result as in the expanding/contracting volume method. Moreover, for a sliding droplet the angles are influenced by its size.

2.7 Hydrophobicity and Hydrophilicity

The term "*hydro*" originated from the Greek word "*hudōr*" meaning water, "*philicity*" and "*phobicity*" have the definition of "affinity" and "lack of affinity", respectively. Hydrophobicity and hydrophilicity are perhaps the most recognisable definitions in the field of wetting and they are used to describe the behaviour of a liquid on a surface.

A surface is considered hydrophilic when its static water contact angle is below 90°, i.e. $\theta_e < 90°$. A completely hydrophilic surface has a spreading coefficient greater than 0, meaning that a droplet will completely spread over the surface and form a liquid film. This complete spreading leads to a contact angle of zero, which in turn leads to a $\cos\theta_e = 1$. Conversely, a completely hydrophobic surface leads to the complete disassociation of a droplet from the surface, leading to a contact angle of $\theta_e = 180°$ and $\cos\theta_e = -1$. Therefore, the sign of $\cos\theta_e$ in Equation 2.11 can be used to define the wettability of a surface (Figure 2.7).

$0 < \cos\theta_e < 1$ and $0^\circ < \cos\theta_e < 90^\circ$ leads to a solid-liquid interfacial tension lower than that of the solid-vapour interface, i.e. $\gamma_{SL} < \gamma_{SV}$, the surface is considered hydrophilic. (Figure 2.11a).

$0 > \cos\theta_e > -1$ and $90^\circ < \cos\theta_e < 180^\circ$ leads to a solid-liquid interfacial tension greater than that of the solid-vapour interface, i.e. $\gamma_{SL} > \gamma_{SV}$, the surface is considered hydrophobic. (Figure 2.11b).

When $\theta_e = 90^\circ$, the change in interfacial energies when the droplet comes into contact with the surface is equal, i.e. $\gamma_{SV} = \gamma_{SL}$. At this point there is no advantage for a droplet to either further wet or detwet the surface, leading to the formation of a hemispherical droplet.

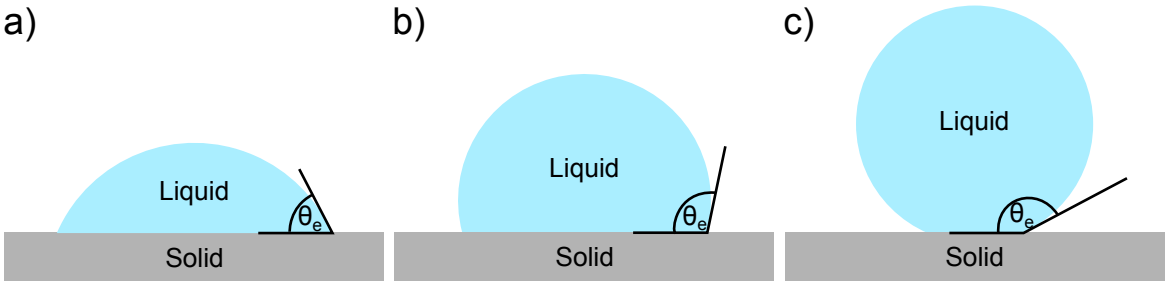

Figure 2.11: Different partial wetting states: a. hydrophilic, b. hydrophobic, c. superhydrophobic.

There is, however, very little rationalisation as why the surfaces can be considered hydrophobic or hydrophilic by a mere difference of 2°, i.e. 89° to 91°. Perhaps it can be argued that if a droplet attaches to a surface it must have some degree of hydrophilic tendencies, even for a hydrophobic surface [25]. Gao and McCarthy argued that under certain circumstances Teflon can be considered hydrophilic [26]. McHale demonstrated that, within a surface free energy model, all solids, including Teflon, could be considered hydrophilic but some may have hydrophobic tendencies induced by surface roughness [27].

A surface is considered superhydrophobic when $\theta_e > 150^\circ$. This value is beyond what can be achieved chemically. A combination of hydrophobic surface chemistry and surface texturing have often been used to create superhydrophobic surfaces. The additional roughness from the surface texturing can be considered as a physical amplification to the

surface chemistry [28]. Furthermore, some also consider a low sliding angle or contact angle hysteresis, i.e. $\Delta\theta < 10^{\circ}$ to be an essential characteristic of superhydrophobic surfaces [29].

The production of many superhydrophobic surfaces have been inspired by nature. The best known example is perhaps the leaves of the Sacred Lotus (Nelumbo nucifera), regarded by many as the symbol of purity which may be in reference to their self-cleaning properties [7–9, 30]. Although these properties have been known for a long time and referenced as early as the Hindu scripture *Bhagavad Gita*, its mechanism was not properly studied until the early 1970s after the introduction of the scanning electron microscopy (SEM) [31, 32]. Using a combination of a small hair-like features and a waxy surface chemistry, droplets of water would bead up and roll off the surface of the leaves, picking up and carrying away any dust or dirt particles as they roll off. This is therefore referred to as the "*Lotus effect*" [7]. Aside from the lotus leaves, many other plants have also been found to exhibit superhydrophobicity and self-cleaning properties, they include *Opuntia* (prickly pear), *Tropaeolum* (nasturtium) and *Lady's Mantle* (Alchemilla mollis). Many species of aquatic insects have also been observed to take advantage of superhydrophobicity, examples include the highly hydrophobic wings of large-winged insects such as butterflies, moths, dragonflies and lace wings, and the ability of the diving beetle (*Dytiscus marginalis*) to breath under water from a layer of air trapped between the tiny hairs on its body [3, 30, 33–35].

2.8 Surface Free Energy Argument

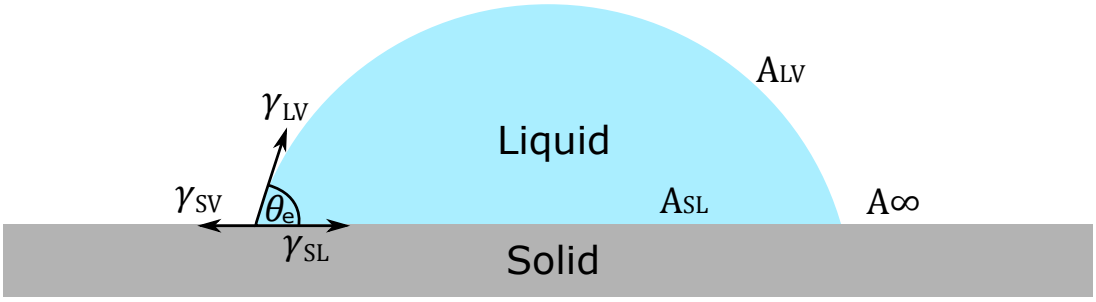

Figure 2.12: Droplet on an infinitely long surface.

When studying the behaviour of a liquid on a surface, it is useful to consider the surface free energy of the system. Imagine a 2-dimensional droplet on an infinitely (∞) long solid surface (Figure 2.12), then the total surface free energy for a droplet on this surface would be,

$$F = (A_\infty - A_{SL})\gamma_{SV} + A_{SL}\gamma_{SL} + A_{LV}\gamma_{LV} \tag{2.14}$$

where A_∞ is the surface area of the surface, A_{SL} is the surface area of the solid-liquid interface and A_{LV} is the area of the liquid-vapour interface.

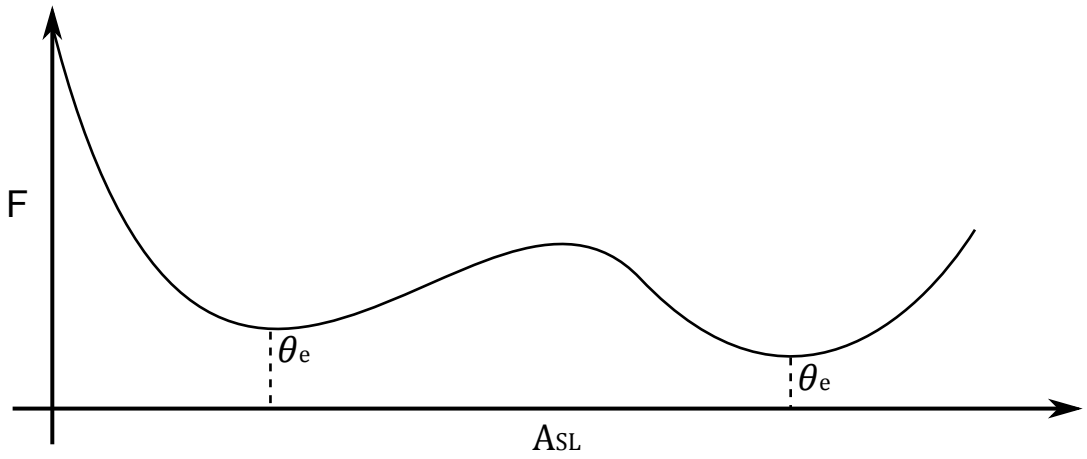

Figure 2.13: Surface free energy, F, as a function of solid-liquid surface area.

As mentioned in Section 2.6, on a complex surface the droplet may take on various values for θ_e. Therefore, a possible surface free energy curve as a function of the

solid-liquid surface area may contain a number of minimum points (Figure 2.13). One may observe multiple local equilibriums at the bottom of surface free energy wells when $\Delta F = 0$ and which one is observed would depend on how a droplet had been deposited.

Beyond considering the surface free energy of the entire system as a whole, another approach to survey a liquid's wetting behaviour would be to resolve the change in surface free energy for a small perturbation of the contact line (Figure 2.14).

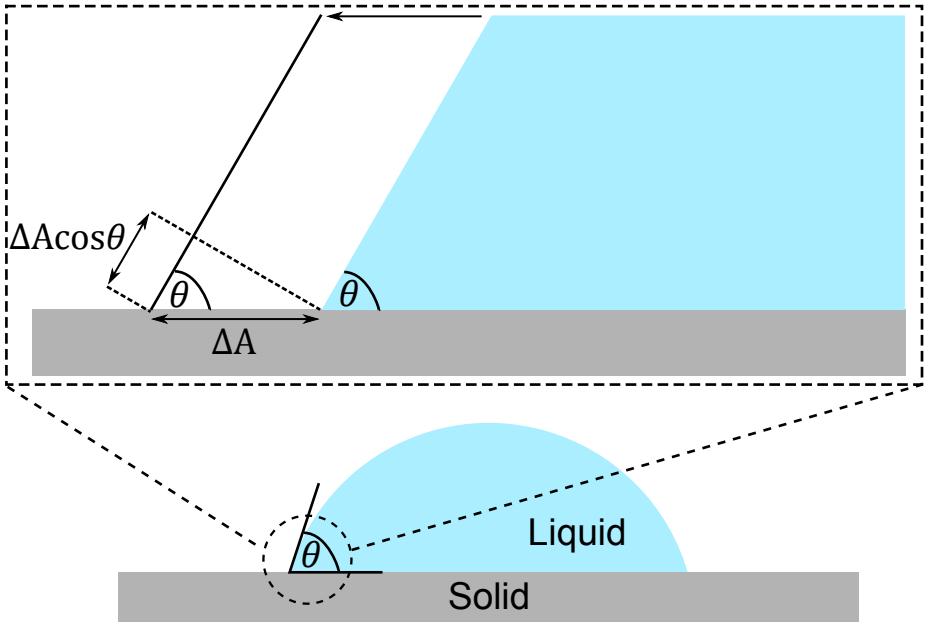

Figure 2.14: Change in area in the surface free energy approach.

A small advance of the contact line leads to a loss of the solid-vapour interface by an amount of ΔA, which is replaced by a gain in solid-liquid interface by the same amount, causing a change in the surface free energy of $(\gamma_{\mathrm{SL}} - \gamma_{\mathrm{SV}})\Delta A$. There is also a gain in the liquid-vapour interface which leads to change in the surface free energy by an amount of $\gamma_{\mathrm{LV}} \cos\theta_{\mathrm{e}} \Delta A$. In this approach, the movement in the contact line is assumed to be infinitesimal and therefore any change in the droplet's contact angle is considered a second order effect. Thus, the overall change in surface free energy is,

$$\Delta F = (\gamma_{\mathrm{SL}} - \gamma_{\mathrm{SV}})\Delta A + \gamma_{\mathrm{LV}} \cos\theta \Delta A \tag{2.15}$$

As shown in Figure 2.13, local equilibriums correspond to minima of surface free energy and a change in surface free energy for a small displacement of the contact line is considered zero, where $\Delta F = 0$. Therefore, equating Equation 2.15 to zero can lead

to the recovery of the Young's equation, i.e.

$$(\gamma_{\mathrm{SL}} - \gamma_{\mathrm{SV}})\Delta A + \gamma_{\mathrm{LV}} \cos\theta \Delta A = 0$$

$$\rightarrow (\gamma_{\mathrm{SV}} - \gamma_{\mathrm{SL}})\Delta A = \gamma_{\mathrm{LV}} \cos\theta \Delta A$$

$$\therefore \cos\theta_{\mathrm{e}} = \frac{\gamma_{\mathrm{SV}} - \gamma_{\mathrm{SL}}}{\gamma_{\mathrm{LV}}}$$

This approach relies on the contact line's freedom to survey changes in the energy landscapes through infinitesimal displacements from its current position and therefore neglects the effect of contact angle hysteresis. The validity of this approach also only extends upto the areas in the vicinity of the contact line and becomes irrelevant for areas deep inside the droplet or well away from the contact line. This argument is limited to a 2-dimensional point of view but can be applied to any radial segment if axial symmetry is maintained [36, 37].

The surface free energy argument can also be used to calculate the conditions for the spreading coefficient for a dry flat surface. Similarly, a small displacement of the contact line of a liquid film by an amount of ΔA leads to a change in the total surface energy, ΔF,

$$\Delta F = (\gamma_{\mathrm{SL}} - \gamma_{\mathrm{SV}})\Delta A + \gamma_{\mathrm{LV}} \Delta A \tag{2.16}$$

If this lowers the overall surface energy, then the liquid film continues to advance across the surface, i.e.

$$(\gamma_{\mathrm{SL}} - \gamma_{\mathrm{SV}})\Delta A + \gamma_{\mathrm{LV}} \Delta A < 0$$

Defining $S = \gamma_{\mathrm{SV}} - (\gamma_{\mathrm{SL}} + \gamma_{\mathrm{LV}})$ (Equation 2.7) gives spreading and film formation when $S > 0$. This is the same conclusion as when simply comparing the interfacial energies of the wet and dry surfaces.

Another situation where the surface free energy approach can be used is that of

corner filling. Imagine a liquid filling one corner of a solid, as shown in Figure 2.15.

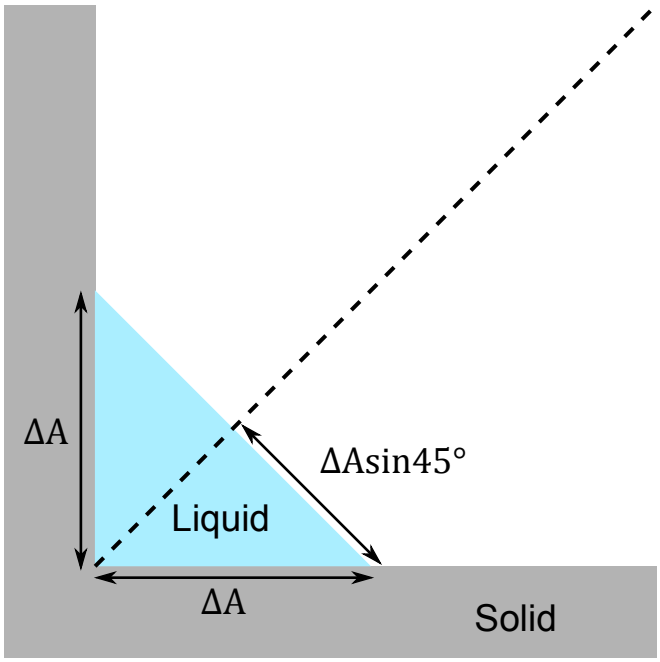

Figure 2.15: Conditions for corner filling represented as a 2-dimensional corner.

Due to symmetry, only the lower part of (below dashed line) Figure 2.15 needs to be considered. A surface free energy contribution of $\gamma_{SL}\Delta A$ is given by the solid-liquid interface. There is also a liquid-vapour area contribution to the surface surface free energy of $\gamma_{LV}\Delta A \sin 45°$. This liquid will only fill the corner if the total surface free energy is lower when it is filled than when it has no liquid for which the energy is $\gamma_{SV}\Delta A$, the condition for corner filling is therefore,

$$\gamma_{SV}\Delta A > \gamma_{SL}\Delta A + \gamma_{LV}\Delta A \sin 45° \tag{2.17}$$

Several terms can be cancelled and a more general expression is given as,

$$\gamma_{SV} > \gamma_{SL} + \gamma_{LV} \sin\left(\frac{\varphi}{2}\right) \tag{2.18}$$

where φ is the corner angle. This is valid even for extreme cases. A flat surface can be seen as a corner with $\varphi = 180°$ and gives $S = \gamma_{SV} - (\gamma_{SL} + \gamma_{LW}) > 0$ as the condition. Moreover, parallel solid surfaces form a corner with $\varphi = 0°$, which gives $\gamma_{SV} > \gamma_{SL}$.

Relating Equation 2.18 to the contact angle θ of the liquid on the solid, Equation 2.11 can then be incorporated into the equation to give the condition for corner filling,

$$\cos\theta_e > \sin\left(\frac{\varphi}{2}\right) \tag{2.19}$$

In summary, for corners with $\varphi > 0°$, liquids with θ greater than $0°$ but smaller than a θ_e dependent on φ will fill the corner. This contrasts flat surfaces where a liquid will only spread on them if $\theta_e = 0°$.

2.9 Surface Roughness

As mentioned in Section 2.6, surfaces are often non-ideal and contain roughness [1,23]. Surface roughness plays a key role in understanding the wetting properties of surfaces. Therefore, understanding how liquids behaves on different surface topographies can shed light on the possible ways to control the wetting properties of surfaces by tailoring the surface roughness.

When a water droplet is placed on a rough or topographically structured surface that is hydrophobic, it can contact the surface in two extreme fashions. One possibility is the complete wetting of the surface, where the liquid penetrates and maintains contact with the entirety of the rough surface and is known as the Wenzel state (Figure 2.16a) [38,39]. The other extreme, known as the Cassie-Baxter state, involves the droplet bridging across the tops of the surface roughness/features, leaving a partchwork of solid-liquid and liquid-vapour interfaces below it (Figure 2.16b) [40].

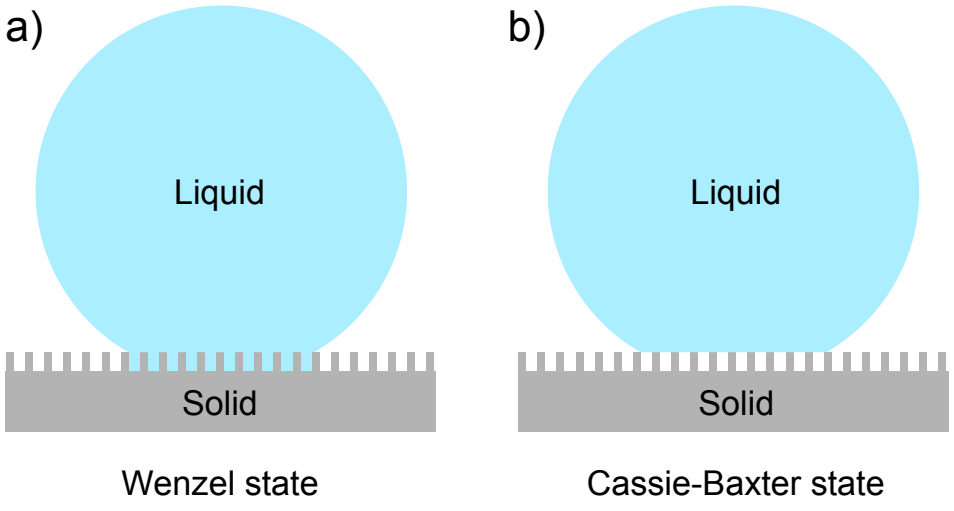

Figure 2.16: a. Wenzel state, b. Cassie-Baxter state.

For a droplet in either the Wenzel or the Cassie-Baxter state, describing its local contact angle becomes more complicated because the surface is no longer flat. Using a pillared surface as a model surface, the surface free energy argument can be applied to both cases.

Wenzel model

In the Wenzel case, when the liquid advances from the edge of one pillar to another and thus displacement of the contact line by one period, ΔA (Figure 2.17); there is a change in the surface free energy $[2h + (1 - f_s)\Delta A + f_s\Delta A](\gamma_{SL} - \gamma_{SV})$ and a gain in liquid-vapour interfacial energy of $\cos\theta\gamma_{LV}\Delta A$.

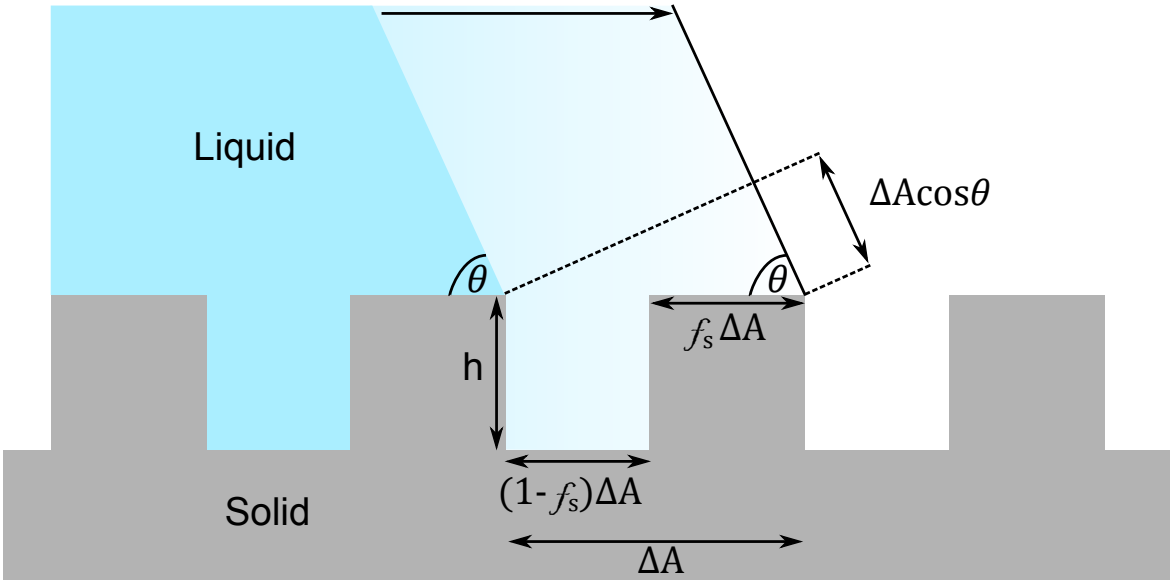

Figure 2.17: Contact angle on a rough surface using the Wenzel approach.

The change in overall surface free energy is hence,

$$\Delta F = \underbrace{[2h + (1 - f_s)\Delta A + f_s\Delta A] \overbrace{(\gamma_{SL} - \gamma_{SV})}^{\text{sub in Equation 2.11}}}_{\text{gain in solid-liquid and loss in solid-vapour}} + \underbrace{\cos\theta_w\gamma_{LV}\Delta A}_{\text{gain in liquid-vapour}}$$

where $\cos\theta_w$ is the equilibrium contact angle of a surface in the Wenzel state, Young's contact angle for smooth surface, θ_e^s can then substituted into the equation,

$$\Delta F = -[2h + (1 - f_s)\Delta A + f_s\Delta A]\cos\theta_e^s\gamma_{LV} + \cos\theta_w\gamma_{LV}\Delta A$$

$$\frac{\Delta F}{\gamma_{\mathrm{LV}} \Delta A} = -[2h + (1 - f_{\mathrm{s}}) + f_{\mathrm{s}}] \cos\theta_{\mathrm{e}}^{\mathrm{s}} + \cos\theta_{\mathrm{w}}$$

By defining roughness of the surface to be the ratio between the actual surface area and the horizontal project of the surface area, a roughness factor known as the Wenzel roughness, $r_{\mathrm{w}} = (2h + \Delta A)/\Delta A = 1 + (2h/\Delta A)$, the equation becomes,

$$\frac{\Delta F}{\gamma_{\mathrm{LV}} \Delta A} = -r_{\mathrm{w}} \cos\theta_{\mathrm{e}}^{\mathrm{s}} + \cos\theta_{\mathrm{w}}$$

At local equilibrium, $\Delta F = 0$,

$$0 = -r_{\mathrm{w}} \cos\theta_{\mathrm{e}}^{\mathrm{s}} + \cos\theta_{\mathrm{w}}$$

$$\therefore \underbrace{\cos\theta_{\mathrm{w}} = r_{\mathrm{w}} \cos\theta_{\mathrm{e}}^{\mathrm{s}}}_{\textbf{Wenzel's law}} \tag{2.20}$$

$\cos\theta_{\mathrm{e}}^{\mathrm{s}}$ is determined purely by surface chemistry and r_{w} acts to amplify its effect. Hence, changes in $\theta_{\mathrm{e}}^{\mathrm{s}}$ leads to larger changes in θ_{w} as long as complete contact is maintained between the liquid and the solid. A changeover in sign of the cosine term occurs at $\theta_{\mathrm{e}} = 90^{\circ}$. This means that, when $\theta_{\mathrm{e}} < 90^{\circ}$, increasing r_{w} further reduces the Wenzel contact angle towards 0°. Oppositely, θ_{w} is pushed towards 180° with increasing roughness when $\theta_{\mathrm{e}} > 90^{\circ}$. Thus, r_{w} pushes the surface's natural inclination towards the extreme cases of either complete wetting or complete non-wetting. In other words, if a surface is hydrophilic then it becomes more hydrophilic with additional roughness, and if a surface is hydrophobic then extra roughness renders it more hydrophobic [3, 28].

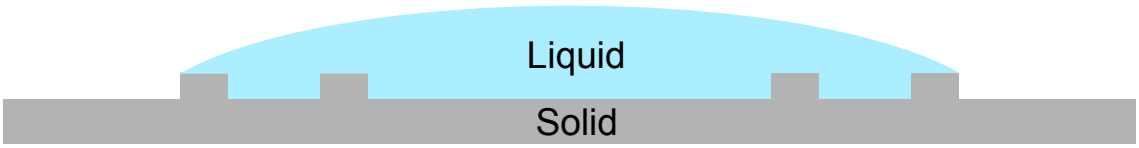

Figure 2.18: r_{w} is the roughness of the droplet edge, not the average roughness.

Note that r_w describes the roughness of the surface as sampled locally by the contact line of the liquid. If the surface topography varies with location then a local average of roughness should not be used in Wenzel's law [3].

Cassie-Baxter model

In the case where the droplet bridges across the tops of the pillars, the liquid does not penetrate the space between the surface features. Again, using the surface free energy approach, an effective contact angle of a droplet in the Cassie-Baxter state, θ_{CB}, can be evaluated in terms of the contact angle for a flat smooth surface, θ_e^s. In this approach, it is assumed that the liquid in only contact with the tops of the surface with flat meniscus below the droplet. This assumption relies on the relatively small gaps between the features compared to the curvature of the meniscus.

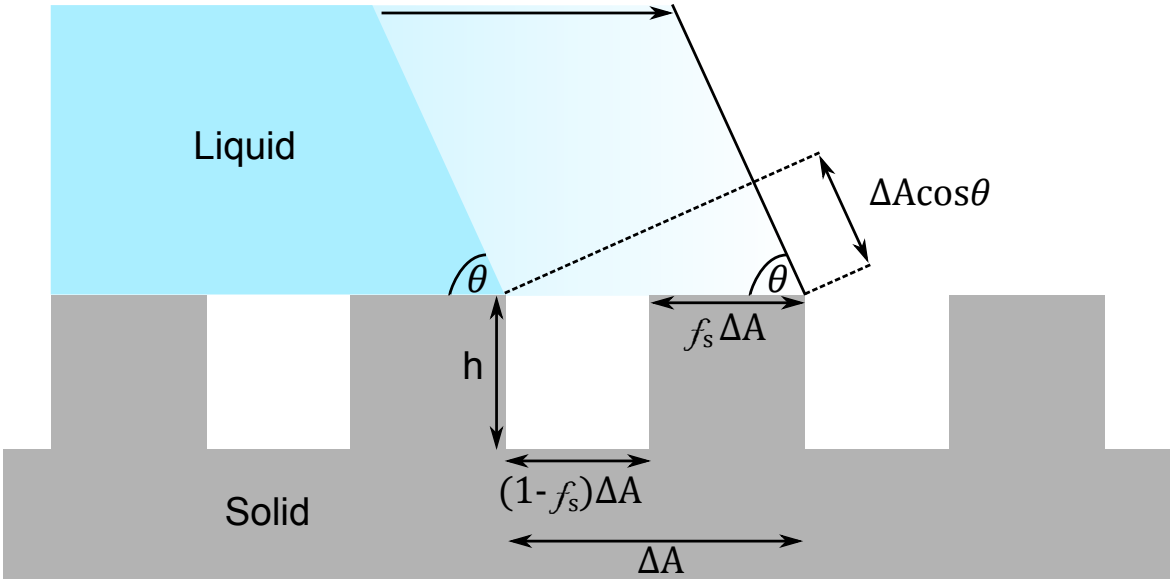

Figure 2.19: Contact angle on a rough surface in the Cassie-Baxter state.

As described earlier, an advance of the contact line by an amount of ΔA leads to a change in the total surface free energy. However, only a fraction $f_s \Delta A$ comes into contact with the liquid and the remainder results in the creation of a liquid-vapour interface by an amount of $(1 - f_s)\Delta A$ (Figure 2.19), the change in surface free energy is then,

$$\Delta F = \underbrace{\gamma_{\mathrm{LV}}(1-f_{\mathrm{s}})\Delta A}_{\text{gain in liquid-vapour}} + \underbrace{\overbrace{(\gamma_{\mathrm{SL}}-\gamma_{\mathrm{SV}})}^{\text{sub in Equation 2.11}} \quad f_{\mathrm{s}}\Delta A}_{\text{gain in solid-liquid and loss in solid-vapour}} + \underbrace{\gamma_{\mathrm{LV}}\cos\theta_{\mathrm{CB}}\Delta A}_{\text{gain in liquid-vapour}}$$

$$= \gamma_{\mathrm{LV}}(1-f_{\mathrm{s}})\Delta A - \gamma_{\mathrm{LV}}\cos\theta_{\mathrm{e}}^{\mathrm{s}} f_{\mathrm{s}}\Delta A + \gamma_{\mathrm{LV}}\cos\theta_{\mathrm{CB}}\Delta A$$

If a droplet is in equilibrium and thus $\Delta F = 0$, there is no change in surface free energy, the equation becomes,

$$0 = (1-f_{\mathrm{s}}) - f_{\mathrm{s}}\cos\theta_{\mathrm{e}}^{\mathrm{s}} + \cos\theta_{\mathrm{CB}}$$

$$\therefore \underbrace{\cos\theta_{\mathrm{CB}} = f_{\mathrm{s}}(1+\cos\theta_{\mathrm{e}}^{\mathrm{s}}) - 1}_{\textbf{Cassie-Baxter equation}} \tag{2.21}$$

In contrast to the Wenzel model, small changes in $\theta_{\mathrm{e}}^{\mathrm{s}}$ leads to even smaller changes in θ_{CB}, even though the absolute value of θ_{CB} is larger than $\theta_{\mathrm{e}}^{\mathrm{s}}$. Whilst the model surface used here is topographically structured and exhibits roughness, the roughness factor, defined as r_{w}, does not directly enter into Equation 2.21. The roughness factor does play an indirect role because the threshold value for Young's contact angle at which the Cassie-Baxter state becomes more energetically favourable compared to the Wenzel state is determined by a balance of roughness and solid surface fraction. Another way to look at Equation 2.21 is that it can be considered as the weighted mean of Young's contact angle with a contact angle with vapour of 180°, i.e. $\cos 180^\circ = -1$,

$$\cos\theta_{\mathrm{CB}} = f_{\mathrm{s}}\cos\theta_{\mathrm{e}}^{\mathrm{s}} + (1-f_{\mathrm{s}})\cos 180^\circ$$

which is equivalent to Equation 2.21. This way of thinking also reveals the possibility of the central negative sign to switch to positive if the pores of the surface is filled with the same liquid as the test liquid, with which it has a contact angle of 0°. A reduced θ_{CB} will be observed as a results of this. Although this is not an example of superhydrophobicity, it can occur on superhydrophobic surfaces under the right conditions.

More complex topography

Both models use simple flat topped surface protrusions as model surfaces and represent an idealised view of solid-liquid interaction. However, the structures of naturally occurring surfaces are comparably complex, accessing the roughness factor thus becomes less straight forward. It is also possible that droplets exists neither in a pure Wenzel nor a pure Cassie-Baxter configuration, but can instead exhibit the characteristics of both. The liquid may penetrate or bridge across the surface features [3].

Examples of a combined Wenzel and Cassie-Baxter state is that of a set of parallel fibres or any surfaces with an inward curve, i.e. "ball on a stick" (Figure 2.20).

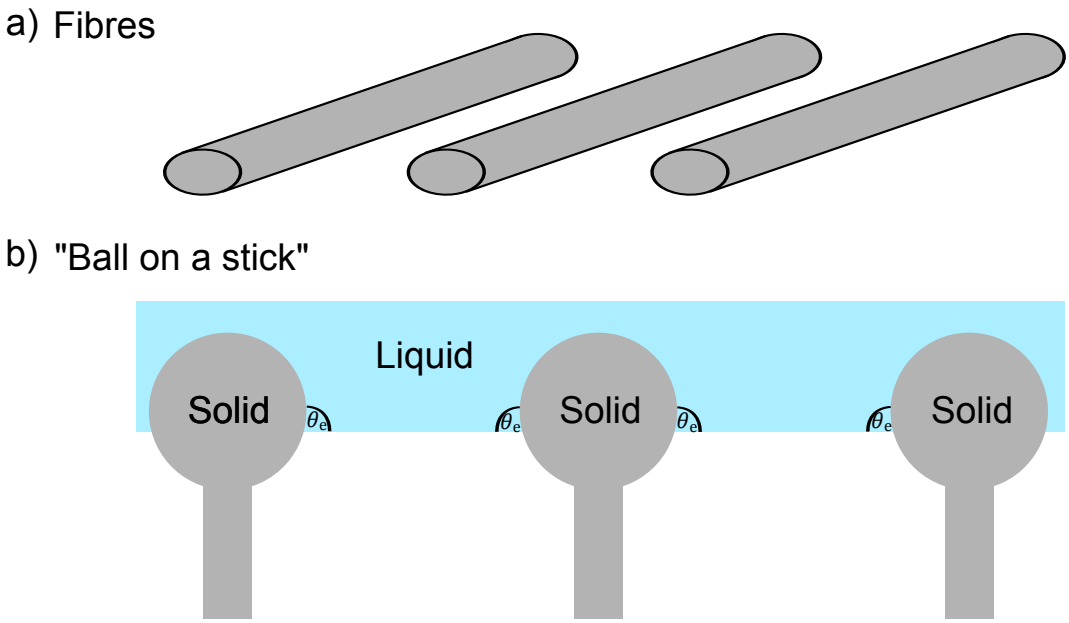

Figure 2.20: Re-entrant surfaces can support the bridging of liquids with at low contact angles: a. fibres, b. "ball on a stick".

On these surfaces, a liquid wets the surface until its local contact angle matches the value as defined by the Young's equation. Further wetting of the surface by the liquid results in a local contact angle greater than θ_e and it is not energetically favourable. This characteristic is important for constructing oil-repellent surfaces since flat surfaces with high contact angle with oils may not exist. One may estimate effect of the combined state by considering the transition of θ_e^s on a flat surface to a Wenzel state, θ_w and subsequently, the Cassie-Baxter state. i.e.

$$\cos\theta_{\mathrm{w}} = r_{\mathrm{w}} \cos\theta_{\mathrm{e}}^{\mathrm{s}}$$

$$\cos\theta_{\mathrm{CB}} = f_{\mathrm{s}}(1 + \cos\theta_{\mathrm{w}}) - 1$$

where f_{s} is dependent on the value of $\theta_{\mathrm{e}}^{\mathrm{s}}$ and the shape of the surface.

Although Wenzel and Cassie-Baxter models describe well the wetting behaviour of liquids on rough surfaces, but they can be misleading as both models ignore the effect of how shapes and patterns combine. For example, a liquid advancing on a set of triangular features which approaches the sharp points first will behave differently to one which approaches the blunt edges first.

Corners and Pinning

The sharp edges on the simple post-type surfaces are important features for the Cassie-Baxter state because it is where the contact line becomes pinned, this also applies to other surfaces with features consisting sharp edges.

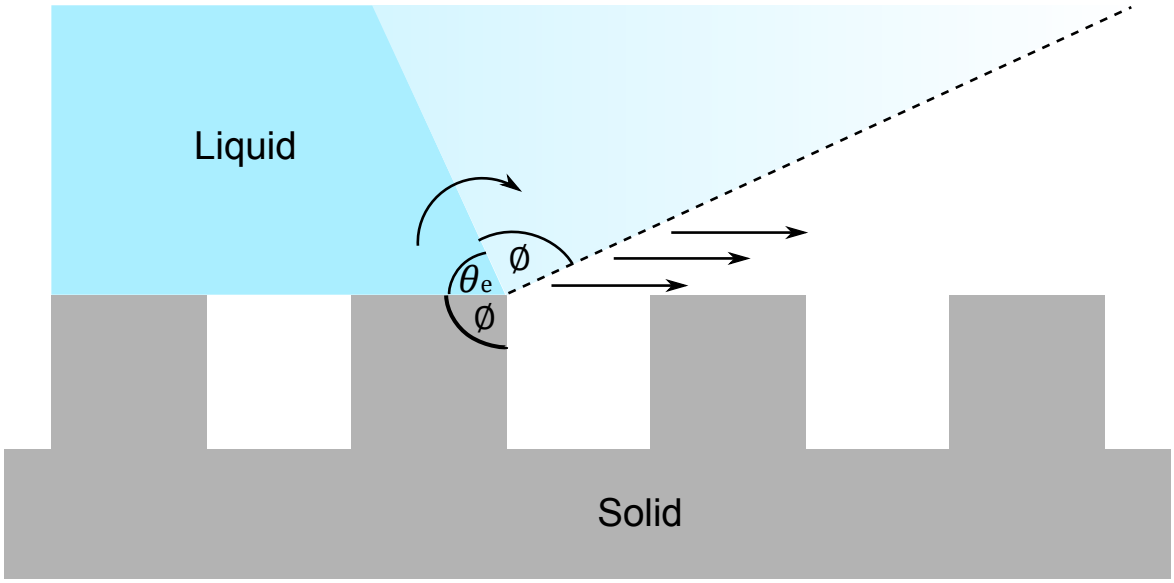

Figure 2.21: Change in the apparent contact angle as the orientation of the surface changes.

The above figure shows the pinning of the front edge of the contact line as it arrives at a sharp edge of angle ϕ. The contact line remains pinned until the θ reaches a value

of $\theta = \theta_e + \phi$, at this point the contact line advances towards the next feautre. This suggests that value of θ lies between θ_e and $\theta_e + \phi$. This is the reason the contact angle measured on rough surfaces are sometimes referred to as the apparent contact angle as it is measured from the horizontal [23, 41].

Cassie-Baxter – Wenzel transition

A comparison of the total surface free energy between the Wenzel and the Cassie-Baxter states reveals the existence of a critical value of θ_e at which a transition from one state to the other may occur. The change of surface free energy over an area of ΔA are as follow:

Wenzel:

$$\Delta F_w = r_w(\gamma_{SL} - \gamma_{SV})\Delta A + \cos\gamma_{LV}\Delta A \tag{2.22}$$

Cassie-Baxter:

$$\Delta F_{CB} = (\gamma_{SL} - \gamma_{SV})f_s\Delta A + \gamma_{LV}(1 - f_s)\Delta A + \cos\theta\gamma_{LV}\Delta A \tag{2.23}$$

For a droplet to be in the Cassie-Baxter state, it must be more energetically favourable for it to bridge across the features rather than penetrating the gaps between them, i.e., $\Delta F_w > \Delta F_{CB}$.

$$r_w(\gamma_{SL} - \gamma_{SV})\Delta A + \cos\gamma_{LV}\Delta A > (\gamma_{SL} - \gamma_{SV})f_s\Delta A + \gamma_{LV}(1 - f_s)\Delta A + \cos\theta\gamma_{LV}\Delta A$$

$$r_w(\gamma_{SL} - \gamma_{SV}) - f_s(\gamma_{SL} - \gamma_{SV}) > (1 - f_s)\gamma_{LV} + \cos\gamma_{LV} - \cos\gamma_{LV}$$

$$(r_w - f_s)(\gamma_{SL} - \gamma_{SV}) > \gamma_{LV}(1 - f_s)$$

$$\frac{(\gamma_{SL} - \gamma_{SV})}{\gamma_{LV}} > \frac{(1 - f_s)}{(r_w - f_s)}$$

which can be rearranged to substitute in Equation 2.11,

$$\underbrace{\frac{(\gamma_{SV} - \gamma_{SL})}{\gamma_{LV}}}_{\text{Sub in Equation 2.11}} < -\frac{(1 - f_s)}{(r_w - f_s)}$$

The Cassie-Baxter state is therefore favourable when

$$\cos\theta_e < -\frac{(1 - f_s)}{(r_w - f_s)} \tag{2.24}$$

Therefore, for the droplet to remain in the Cassie-Baxter state and to satisfy the condition $\cos\theta < \cos\theta_C$, the value of θ must be greater θ_C [3, 42–45], where,

$$\cos\theta_C = -\frac{(1 - f_s)}{(r_w - f_s)} = \frac{(f_s - 1)}{(r_w - f_s)} \tag{2.25}$$

Therefore, in the opposite case where the droplet transitions to a Wenzel state, the penetration of liquid into the gaps must lead to a reduced surface free energy, i.e., $\Delta F_w < \Delta F_{CB}$. During this transition, the air trapped between the surface features becomes thermodynamically unstable and the nucleation of the liquid occurs from the middle of the droplet and the liquid begins to penetrate the gaps. The front of this penetration continues to propagate until it reaches the edges of the droplet, completing the transition to the Wenzel state (Figure 2.22) [42, 46].

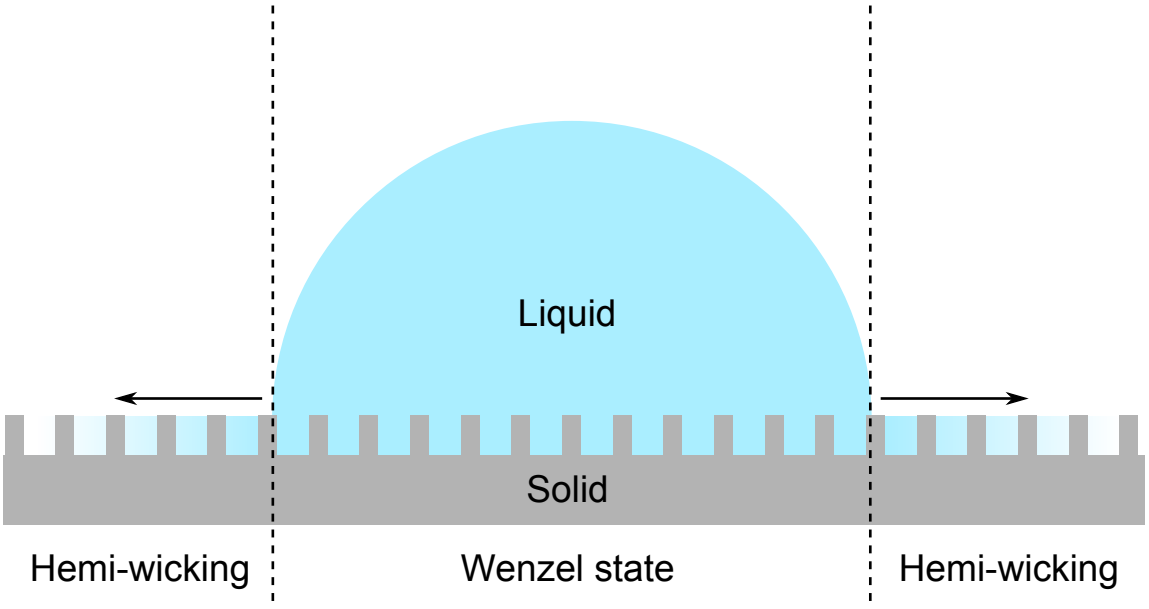

Figure 2.22: Hemi-wicking on a rough surface.

It is possible for the liquid to spread beyond the edges of the droplet, this spreading and phenomenon is known as hemi-wicking (Figure 2.22).

Hemi-wicking

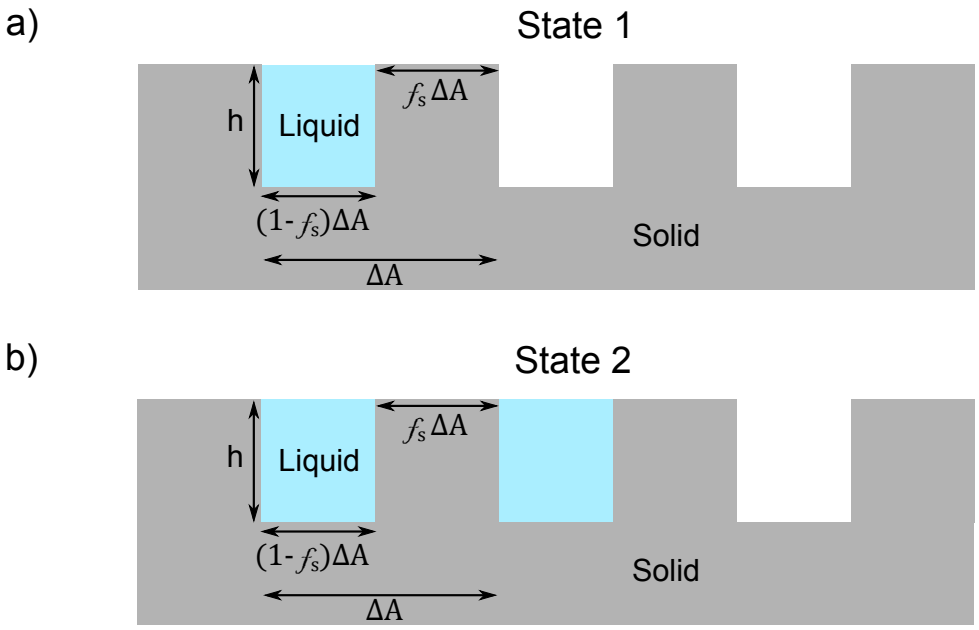

Figure 2.23: Conditions for Hemi-wicking

By considering the two states shown in Figure 2.6, for state 2 to be the preferred state and therefore the liquid to hemi-wick into the features beyond the edges of the droplet (Figure 2.22), it must have lower overall surface free energy than state 1. By comparing surface free energies for a system going from state 1(F_1) to state 2 (F_2), one can obtain a change in the surface free energy of $2(\gamma_{SL} - \gamma_{SV})h + (1 - f_s)\Delta A(\gamma_{SL} - \gamma_{SV})$ plus a gain in liquid-vapour area of $(1 - f_s)\Delta A\gamma_{LV}$. The overall change in the surface free energy is therefore,

$$\Delta F = F_2 - F_1 = 2(\gamma_{SL} - \gamma_{SV})h + (1 - f_s)\Delta A(\gamma_{SL} - \gamma_{SV}) + (1 - f_s)\Delta A\gamma_{LV}$$

$$\frac{\Delta F}{\Delta A} = \frac{2h}{\Delta A}(\gamma_{SL} - \gamma_{SV}) + (1 - f_s)(\gamma_{SL} - \gamma_{SV} + \gamma_{LV})$$

Since:

$$r_{\mathrm{w}} = \frac{2h + \Delta A}{\Delta A} = \frac{2h}{\Delta A} + 1$$

$$\frac{\Delta F}{\Delta A} = (r_{\mathrm{w}} - 1)(\gamma_{\mathrm{SL}} - \gamma_{\mathrm{SV}}) + (1 - f_{\mathrm{s}})(\gamma_{\mathrm{SL}} - \gamma_{\mathrm{SV}} + \gamma_{\mathrm{LV}})$$

$$\frac{\Delta F}{\gamma_{\mathrm{LV}} \Delta A} = (r_{\mathrm{w}} - 1) \underbrace{\frac{(\gamma_{\mathrm{SL}} - \gamma_{\mathrm{SV}})}{\gamma_{\mathrm{LV}}}}_{\text{Sub in Equation 2.11}} + (1 - f_{\mathrm{s}}) \Bigg(\underbrace{\frac{(\gamma_{\mathrm{SL}} - \gamma_{\mathrm{SV}})}{\gamma_{\mathrm{LV}}}}_{\text{Sub in Equation 2.11}} + 1 \Bigg)$$

$$= (1 - r_{\mathrm{w}}) \cos\theta_{\mathrm{e}} + (1 - f_{\mathrm{s}})(1 - \cos\theta_{\mathrm{e}})$$

$$= \left[(1 - r_{\mathrm{w}}) - (1 - f_{\mathrm{s}})\right] \cos\theta_{\mathrm{e}} + (1 - f_{\mathrm{s}})$$

Thus, hemi-wicking is favourable when,

$$= \left[(1 - r_{\mathrm{w}}) - (1 - f_{\mathrm{s}})\right] \cos\theta_{\mathrm{e}} + (1 - f_{\mathrm{s}}) < 0$$

or $\cos\theta_{\mathrm{e}} > \cos\theta_{\mathrm{C}}$, where $\cos\theta_{\mathrm{C}}$ is the critical angle for hemi-wicking [42],

$$\cos\theta_{\mathrm{C}} = \frac{1 - f_{\mathrm{s}}}{r_{\mathrm{w}} - f_{\mathrm{s}}} \tag{2.26}$$

2.10 Creating Superhydrophobic Surfaces

Over the past decade, researchers have been able create surfaces which exhibit excellent liquid shedding abilities using a combination of surface chemistry and micro-/nano-texturing. The latter adds additional roughness to the surface which acts as physical amplification to the surface chemistry. Methods to create this additional roughness involve physical modification to the solid surface and can be placed in different categories, they include:

- *Additive processes*: These processes involve the deposition of extra materials onto the solid surface, whether that be a different material or the same material as

the solid surface. Examples of such process include: lithography, deposition of particles, crystal growth, diffusion limited growth and electrospinning [47–52].

- *Subtractive processes*: These involve the removal of materials from the solid surface, ways to do this include: chemical etching, plasma etching, milling and laser machining [53–55].

- *Inherently rough surfaces*: Surfaces which are inherently rough can be superhydrophobised with the application of a hydrophobic surface chemistry. Exmaples of such surfaces include textile and fabrics, paper membranes, metallic or plastic meshes [56, 57].

Other methods to increase the roughness of a surface include phase separation of a multicomponent mixture to create three dimensional porous structures [58, 59] and templating whereby a soft or liquid material fills a rough surface and is then hardened and removed from the surface [60].

2.11 Lubricant-Impregnated Surfaces (SLIPS/LIS)

The reliance of superhydrophobic surfaces on surface roughness also means that they are prone to damages. Any discontinuation to the surface roughness could lead to pinned droplets. Moreover, even though the contact between droplet and the surface are reduced because of the surface roughness, they are nevertheless in direct contact with the surface which results in some form of pinning (see Section 2.9). This can be detrimental to studies where mobile contact lines are desired.

The main goal of surface texturing is the possibility of inducing specific effects. Whilst superhydrophobicity is one of these effects, where surface texturing is used to minimise the liquid-solid contact area and to retain a layer of air within the gaps of the features, the opposite case where the texture is impregnated by the liquid suggests another interesting application [4].

The concept of a surface impregnated with a liquid which repels other liquids was first proposed by Quéré [4]. It was suggested that a textured surface impregnated by a liquid (liquid 1) becomes hemi-solid and hemi-liquid. When a droplet of second liquid

(liquid 2) is deposited onto this type of surface, the drop can either displace liquid 1 if the surface prefers to be wetted by liquid 2 rather than liquid 1, or it can float without displacing liquid 2. It was observed in the latter situation that the contact angle hysteresis of liquid 2 is typically below 1°. This situation has two interesting implications: firstly, in the case whereby the droplets rest on the mixed substrate and do not penetrate the surface features, their tendency to adhere to the surface is reduced and thus enabling possible self-cleaning surfaces to be made. Secondly, because of the low contact angle hysteresis, these surfaces can be useful for tackling a variety of practical problems, where contact angle hysteresis can be detrimental. The importance of surface texture was emphasised because a liquid film deposited onto a simple flat surface flows and may be displaced by a more wetting liquid.

Interesting phenomenons in the field of wetting can often be seen in nature, and the concept of a liquid-impregnated surface which repels other liquids is no exception. *Nepenthes distillatoria*, also known as the pitcher plant, is capable of catching insects using a layer of liquid trapped within the cavities on its surface to repel the oils on the insects' feet (Figure 2.24).

Figure 2.24: Image of a pitcher plant.

Using the pitcher plant as an inspiration and the concept proposed by Quéré [4], new types of liquid repellent surfaces by means of a immiscible lubricating liquid impregnated into the surface features have been developed. Different names have been given to these

types of surfaces. For example, Wong *et al.* created surfaces whereby porous solids, in forms of nano-post arrays and Teflon nanofibres, are infused with perfluorinated liquids, to which they refer to as **S**lippery **L**iquid-**I**nfused **P**orous **S**urfaces (SLIPS) [14]. This study focused on the slippery characteristics of these materials, their anti-icing properties and their abilities to resist physical damage and pressure. In the same year, Lafuma and Quéré published a paper, in which they called their surfaces Slippery Pre-Suffused Surfaces, with a focus on the necessary conditions to create such surfaces and their ultra-slippery nature which gives unusual properties [61]. A more general term, **L**ubricant-**I**mpregnated **S**urfaces (LIS), was used by Smith *et al.* in their study of the mobility of droplets on these surfaces in which they demonstrated the possible thermodynamic states of droplets [15]. Presently, SLIPS and LIS are most commonly used and are used interchangeably. In the remainder of this thesis, they will be referred to as lubricant-impregnated surfaces and a combined term SLIPS/LIS will be used.

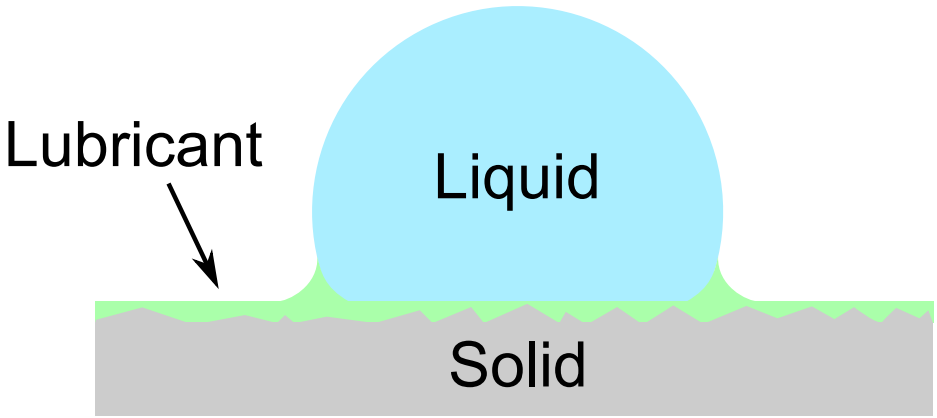

Figure 2.25: A droplet on a SLIPS/LIS.

2.12 Fundamentals of SLIPS/LIS

A lubricant-impregnated surface, by definition, is a porous or textured surface into which a layer of lubricating liquid is stabilised by capillary forces. Once impregnated,

the original solid-vapour interface is replaced by a solid-liquid interface. When a droplet is placed on a SLIPS/LIS, the interface between the droplet and the surface is no longer a simple solid-liquid interface as seen on a ordinary solid surface, instead it rests upon a layer of lubricating liquid. This configuration requires the surface to possess the ability to retain the lubricating liquid upon contact with the droplet. To achieve, it is necessary for the solid surface to prefer to be wetted by the lubricating liquid instead of the liquid of the droplet. The three essential criteria for creating SLIPS/LIS were summarised by Wong *et al.* [14]:

- The lubricating liquid must fully suffuse and adhere to the surface features.
- The solid surface must be preferentially wetted by the lubricating liquid rather than the test liquid.
- The lubricating liquid and the test liquid must be immiscible.

Wetting Ridge

When a droplet of the test liquid is placed upon a lubricant-impregnated surface, it adopts the shape of a spherical cap over the majority of its shape [15, 16, 62]. In the area near the solid surface, the shape of the lubricating liquid layer is distorted by the droplet and a wetting ridge is formed by the balance between the lubricating liquid, the droplet and the vapour, similar to the ridges that may formed for droplets on soft solids [63, 64]. The presence of the wetting ridge also means that a contact angle as described by Young can no longer be measured. Despite this, Guan *et al.* showed that it is possible to use an extrapolated contact angle to study the evaporation of sessile droplets by defining an apparent contact angle to be the intersection angle of the solid surface profile with the extrapolated profile of the droplet (see Section 3.1.5) [16]. The apparent contact angle was shown in Guan *et al.*'s subsequent study to decrease with increasing thickness of the lubricating layer [65]. This finding was consistent with the numerical analysis of the shape of droplets surrounded by a wetting ridge by Semprebon *et al.* [66]. Another relevant analysis was carried out by Neeson *et al.* in which they considered the shape of drops in contact with immiscible fluids [67]. Using confocal

microscopy, Schellenberger *et al.* performed direct observation of the wetting ridges of surfaces impregnated with different liquids and different test liquid, they found that the height of the wetting ridge is related to the thickness of the lubricating layer [62]. More recently, Tress *et al.* studied the shape of a droplet covered in a thin layer of lubricant. They showed that the height of the wetting ridge is insensitive for macroscopically thick film of lubricant, whereas the wetting ridges changes with varying film thickness when the lubricating layer is small [68]. The size of the wetting ridge is particularly relevant to the mobility of a droplet since most of the viscous dissipation in a droplet on a SLIPS/LIS occurs in the wetting ridge. The size of the wetting ridge relative to the droplet size also determine whether or not two or more droplets coalesce as demonstrated by Boreyko *et al.* [69].

Cloaking of the Droplet by the Lubricating Liquid

As mentioned in Section 2.7, a liquid (o) may spread over test liquid (w) in order to lower the total surface free energy if its spreading coefficient on the test liquid is greater than 0, i.e. $S_{ow(a)} > 0$. Therefore, the droplet can be cloaked by the lubricant providing its spreading coefficient in the presence of vapour is greater than zero. Anand *et al.* showed the two step process of the cloaking as it spreads over the droplet [70]. First, a monolayer of the lubricant spreads over the droplet and the position of the spreading front scales as $(4S_{ow(a)}/3(\mu_o\rho_o)^{1/2})^{1/2}t^{3/4}$ where $S_{ow(a)}$ is the spreading coefficient of the lubricant on water in the presence of air, μ_o and ρ_o are the viscosity and density of the lubricant, respectively. This step is then followed by the spreading of a thicker layer of the lubricant and its thickness depends on the thickness of the lubricant layer. The timescale for this stage of spreading is determined by the Ohnesorge number $\mathrm{Oh} = \mu_o(\rho_o R\gamma_{oa})^{-1/2}$ where R is the radius of the droplet and γ_{oa} is the surface tension of the lubricant in vapour. Carlson *et al.* studied the timescale τ_ρ of the detachment of a droplet from a needle upon contact with another liquid and found that $\tau_\rho = (\rho_o R^3/\gamma_{oa})$ for $\mathrm{Oh} < 1$ and $\tau_\mu = \mu_o R/\gamma_{oa}$ for $\mathrm{Oh} > 1$ [71]. The detachment of the droplet is assumed to be a result of the complete spreading of the lubricant over the droplet, these timescales therefore provide an estimate for the timescale for the second stage of

cloaking. Schellenberger *et al.* estimated the thickness of a cloak of fluorocarbon FC-70 liquid on a 1mm water droplet to be ≈ 20 nm using confocal microscopy [62]. Anand *et al.* [70] and Rykaczewki *et al.* [72] provided direct evidence for cloaking of water droplets *via* scanning electron microscopy (SEM) whilst Cheng *et al.* demonstrated the ability to visualise the cloaking using X-ray tomography [73].

Conditions for SLIPS/LIS states

Smith *et al.* described the 12 possible thermodynamic configurations a droplet of water can take when placed on a lubricant-impregnated surface depending on the properties of the surface and the lubricating liquid, the test liquid and the surrounding environment. They considered the behaviours of the lubricating liquid both outside the droplet (in the presence of air, oil-solid-air interface) and underneath the droplet (in the presence of water, oil-solid-water interface) [15].

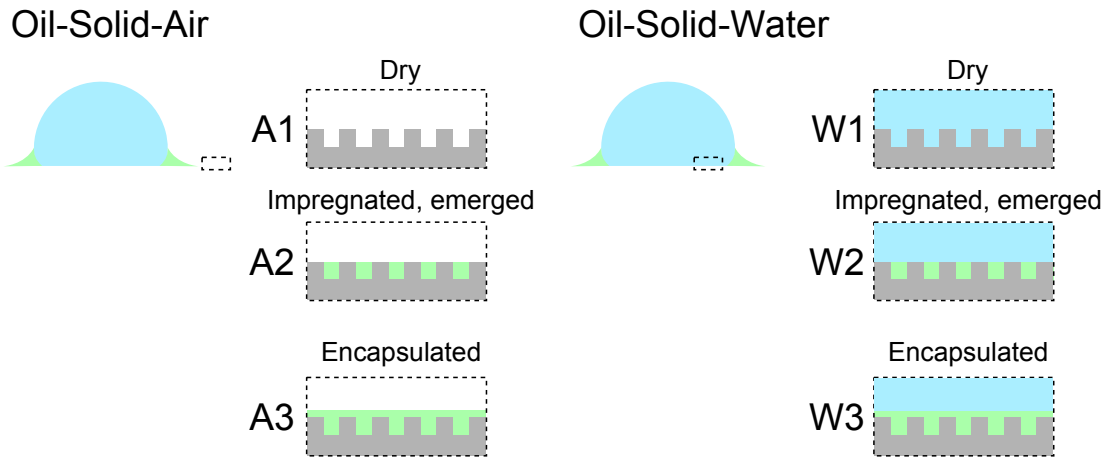

Figure 2.26: Wetting configurations outside and underneath the droplet: a. oil-solid-air, b. oil-solid-water.

A solid surface is considered as "dry" when the entirety of the surface is in contact with a semi-infinite expanse of vapour (this means that the vapour has no upper boundary)(Figure 2.26a, A1). The surface becomes "impregnated, emerged" when the gaps between the surface features are infused by a lubricant but the tops of the features are in contact with a semi-infinite expanse of vapour (Figure 2.26a, A2). The surface is said to be "encapsulated" when the lubricant liquid is in contact with both the gaps

and the tops of the surface features where the lubricating liquid has a top surface in contact with a semi-infinite expanse of vapour (Figure 2.26a, A3). Underneath the droplet, three similar situations can occur but the vapour is replaced by a semi-infinite expanse of liquid, i.e. A1 → W1, A2 → W2, A3 → W3 (Figure 2.26b).

Energetics of Oil-Solid-Air System

By comparing the interfacial energies per unit area of state A1, A2, A3, the conditions for any of them being the favourable can be obtained. They are summarised below,

$$\text{A1} \rightarrow E_{\text{A1}} = r\gamma_{\text{sa}}$$

$$\text{A2} \rightarrow E_{\text{A2}} = (r-f)\gamma_{\text{so}} + f\gamma_{\text{sa}} + (1-f)\gamma_{\text{oa}}$$

$$\text{A3} \rightarrow E_{\text{A3}} = r\gamma_{\text{so}} + \gamma_{\text{oa}}$$

where the subscript s, a and o refer to the solid, air and oil phase of the system. For state A1 to be the preferred state, it is necessary that its interfacial energy is lower than state A2 and A3:

$$E_{\text{A1}} < E_{\text{A2}} \text{ and } E_{\text{A1}} < E_{\text{A3}}$$

The first condition is therefore,

$$r\gamma_{\text{sa}} < (r-f)\gamma_{\text{so}} + f\gamma_{\text{sa}} + (1-f)\gamma_{\text{oa}}$$

$$0 < (r-f)\gamma_{\text{so}} + (r-f)\gamma_{\text{sa}} + (1-f)\gamma_{\text{oa}}$$

Grouping the f terms, the spreading coefficient for oil on the solid in the presence of air can be substituted into the equation,

$$0 < r\gamma_{\text{so}} - r\gamma_{\text{sa}} + \gamma_{\text{oa}} - f\underbrace{\left(\gamma_{\text{so}} + \gamma_{\text{oa}} - \gamma_{\text{sa}}\right)}_{S_{\text{os(a)}}}$$

$$0 < r\underbrace{\left(\gamma_{\text{so}} - \gamma_{\text{sa}}\right)}_{-(S_{\text{os(a)}}+\gamma_{\text{oa}})} + \gamma_{\text{oa}} - fS_{\text{os(a)}}$$

$$0 < -r(S_{\mathrm{os(a)}} + \gamma_{\mathrm{oa}}) + \gamma_{\mathrm{oa}} + fS_{\mathrm{os(a)}}$$

$$0 < (1-r)\gamma_{\mathrm{oa}} + (f-r)S_{\mathrm{os(a)}}$$

Since the roughness, r, is equal to or larger than 1,

$$0 < -(r-1)\gamma_{\mathrm{oa}} - (r-f)S_{\mathrm{os(a)}}$$

$$\therefore S_{\mathrm{os(a)}} < -\gamma_{\mathrm{oa}}\left(\frac{r-1}{r-f}\right) \tag{2.27}$$

Alternatively, the first condition can be rearranged as follows,

$$(r-f)\gamma_{\mathrm{sa}} < (r-f)\gamma_{\mathrm{so}} + (1-f)\gamma_{\mathrm{oa}}$$

$$\gamma_{\mathrm{sa}} < \gamma_{\mathrm{so}} + \underbrace{\left(\frac{1-f}{r-f}\right)}_{\text{Sub in Equation 2.26}} \gamma_{\mathrm{oa}}$$

By substituting the critical angle for hemi-wicking, $\cos\theta_{\mathrm{C}}$ [42], it becomes,

$$\gamma_{\mathrm{sa}} < \gamma_{\mathrm{so}} + \cos\theta_{\mathrm{C}}\gamma_{\mathrm{oa}}$$

$$\underbrace{\frac{\gamma_{\mathrm{sa}} - \gamma_{\mathrm{so}}}{\gamma_{\mathrm{oa}}}}_{\text{Sub in Equation 2.11}} < \cos\theta_{\mathrm{C}}$$

$$\cos\theta_{\mathrm{os(a)}} < \cos\theta_{\mathrm{C}}$$

which is the same as,

$$\theta_{\mathrm{os(a)}} > \theta_{\mathrm{C}} \tag{2.28}$$

The second condition $E_{\mathrm{A1}} < E_{\mathrm{A3}}$ is

$$r\gamma_{\mathrm{sa}} < \gamma_{\mathrm{so}} + \gamma_{\mathrm{oa}}$$

$$r\underbrace{\frac{(\gamma_{\mathrm{sa}} - \gamma_{\mathrm{so}})}{\gamma_{\mathrm{oa}}}}_{\cos\theta_{\mathrm{os(a)}}} < 1$$

$$r\cos\theta_{\mathrm{os(a)}} < 1$$

$$\cos\theta_{\mathrm{os(a)}} < \frac{1}{r} \tag{2.29}$$

This is satisfied if the first condition $E_{\mathrm{A1}} < E_{\mathrm{A2}}$ is satisfied because,

$$\cos\theta_{\mathrm{C}} = \frac{1-f}{r-f} < \frac{1}{r}$$

provided that r is greater than 1. In summary, the dry state (A1) is favoured if the contact angle for the lubricant on the solid in the presence of air is larger than the critical angle for hemi-wicking (Equation 2.26).

Similarly, the "impregnated, emerged" state (A2) is favoured when,

$$E_{\mathrm{A2}} < E_{\mathrm{A1}} \text{ and } E_{\mathrm{A2}} < E_{\mathrm{A3}}$$

For the first condition, $E_{\mathrm{A2}} < E_{\mathrm{A1}}$, the same algebraic manipulations can be used with the "greater" sign replacing the original "less" sign. The condition thus becomes,

$$\therefore S_{\mathrm{os(a)}} > -\gamma_{\mathrm{oa}}\left(\frac{r-1}{r-f}\right) \tag{2.30}$$

or alternatively,

$$\cos\theta_{\mathrm{os(a)}} > \cos\theta_{\mathrm{C}}$$

$$\theta_{\mathrm{os(a)}} < \theta_{\mathrm{C}} \tag{2.31}$$

The second condition, $E_{\mathrm{A2}} < E_{\mathrm{A3}}$, can be calculated as follows,

$$(r-f)\gamma_{\mathrm{so}} + f\gamma_{\mathrm{sa}} + (1-f)\gamma_{\mathrm{oa}} < r\gamma_{\mathrm{so}} + \gamma_{\mathrm{oa}}$$

$$-\gamma_{\mathrm{so}} + \gamma_{\mathrm{sa}} - \gamma_{\mathrm{oa}} < 0$$

This can be re-written using the spreading coefficient as,

$$S_{\mathrm{os(a)}} < 0$$

Using $\cos\theta_{\mathrm{os(a)}}$, it can also be written as,

$$\gamma_{\mathrm{oa}} \cos\theta_{\mathrm{os(a)}} - \gamma_{\mathrm{oa}} < 0$$

$$\cos\theta_{\mathrm{os(a)}} < 1 \text{ or } \theta_{\mathrm{os(a)}} > 0$$

Thus, the conditions for the state A2 can be written as,

$$0 > S_{\mathrm{os(a)}} > -\gamma_{\mathrm{oa}} \left(\frac{r-1}{r-f} \right) \tag{2.32}$$

or alternatively,

$$1 > \cos\theta_{\mathrm{os(a)}} > \cos\theta_{\mathrm{C}} \text{ or } 0 < \theta_{\mathrm{os(a)}} < \theta_{\mathrm{C}} \tag{2.33}$$

To summarise, the "impregnated, emerged", or hemi-wicked state (A2) occurs when the contact angle for the lubricant on the solid in the presence of air infinite, but smaller than the critical angle for hemi-wicking.

Lastly, for state A3, or the "encapsulated" state to be favoured over the state A1 and A2, the comparison of their interfacial energies per unit area should look as follows,

$$E_{\mathrm{A3}} < E_{\mathrm{A1}} \text{ and } E_{\mathrm{A3}} < E_{\mathrm{A2}} \tag{2.34}$$

The first condition for this state is similar to the consideration of condition 2 for the dry state to be favoured, but the less than sign switches to a greater sign since in this state the surface is in contact with the lubricant instead of air,

$$\cos\theta_{\mathrm{os(a)}} > \frac{1}{r} \tag{2.35}$$

The second condition is similar to the consideration of condition 2 for the hemi-wicked state to be favoured, but again with the less than sign switched to a the greater than sign,

$$S_{\mathrm{os(a)}} > 0$$

or

$$\cos\theta_{\mathrm{os(a)}} > 1$$

Thus, the first condition is automatically satisfied if the second condition is satisfied. In fact, for the state A3 to truly be the lowest energy state, the lubricant must form a film over on the tops of the surface features.

Energetics of Oil-Solid-Water System

When the vapour in state A1, A2, A3 is replaced by water, these states become states W1, W2, W3. To obtain the conditions for these states, one can start by considering whether a droplet of water on the surface displaces the oil fully (W1), partially (W2) or not at all (W3) (Figure 2.27). The previous conditions for the oil-solid-air system can be applied to describe the energetics of the oil-solid-water system, provided the index "a" for air is replaced by "w" for water, i.e. $S_{\mathrm{os(a)}} \rightarrow S_{\mathrm{os(w)}}$.

Thermodynamic States of Droplets on SLIPS/LIS and Droplet Mobility

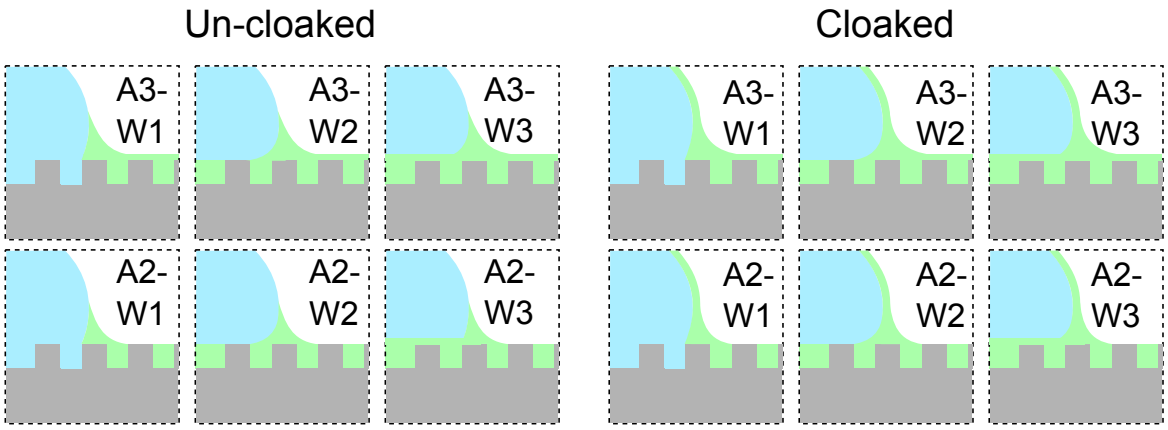

Figure 2.27: Thermodynamic states of a water droplet on a SLIPS/LIS.

A droplet on a SLIPS/LIS may or may not be cloaked by a layer of the lubricant depending on the spreading coefficient of the lubricant on the droplet. Underneath the droplet, the lubricant may be fully(W1), partially (W2) or not at all displaced (W3). Outside the droplet, the surface may remain dry (A1, no impregnation), hemi-wicked (A2) or fully covered by the lubricant (A3). Using these rationales, 12 possible thermodynamic states can be found for a water droplet placed on a SLIPS/LIS [15].

The difference in the interactions between the lubricant, the droplet and the surface in these configurations also lead to differences in the mobility of the droplets on the surface. They are summarised as follows for both cloaked and non-cloaked droplets,

Low mobility: (A3-W1) and (A2-W1) are Wenzel-like droplet states where the droplets impale the surface texture and thus are expected to have high pinning and low mobility.

Reduced mobility: (A3-W2), (A2-W2) and (A2-W3) are droplets states which do not maintain an encapsulated substrate both underneath or outside the droplet and thus have reduced mobility.

High mobility: In (A3-W3), an encapsulated substrate is maintained both under and outside the droplet, leading to high mobility.

2.13 Applications of SLIPS/LIS

The development of SLIPS/LIS and their ability to retain an immiscible layer of lubricating liquid offers a natural solution to practical applications where contact line pinning is an important issue.

Condensation

Condensation is a naturally occurring phenomenon and plays crucial roles in many practical problems. For example, steam cycles used in power plants rely heavily on condensers. On superhydrophobic surfaces, droplets forming on the surface may not shed off until they reach sizes on the order of a few millimetres. Anand *et al.* showed that, on lubricant impregnated surfaces, shedding of droplets as small as 2 μm was possible [74]. It was also observed that dropwise condensation occurs sooner on SLIPS/LIS than it does on superhydrophobic surfaces, hinting at a lower energy barrier for nucleation. Xiao *et al.* studied the condensation heat transfer on SLIPS/LIS and showed a two-fold enhancement over conventional hydrophobic surfaces [75]. In addition to water, the condensation of liquids with surface tension ranging from 12 to 20 mNm^{-1} were investigated by Rykaczewski *et al.* on both SLIPS/LIS and oleophobic surfaces. It was found that most of the liquids condensed into drops (dropwise condensation) leading to

increased heat transfer [76].

Fog Collection

Another way droplets may form on surfaces is the generation of water from the liquid drops in fog. The increased mobility of droplets on SLIPS/LIS can lead to an increased collection efficiency of fog. Boor *et al.* carried out fog collection experiments and showed an increased rate of water collection on electrospun surfaces impregnated with a lubricating liquid compared to those without [77]. They, however, observed depletion of the lubricating liquid from the surfaces during the experiments. Park *et al.* observed similar gradual loss of the lubricating liquid with time [78].

Anti-Icing

In addition to reducing water adhesion to the surface, SLIPS/LIS are useful for the reduction of ice adhesion and thus anti-icing applications. Although superhydrophobic surfaces have been used for anti-icing studies because of their ability to repel liquids, frost may still form on theses surfaces, leading to increased adhesion to ice, as shown by Varanasi *et al.* [79] Using surfaces impregnated with excess lubricating liquid, Kim *et al.* observed a significant reduction of frost formation and ice adhesion as well as the lack of residual water after defrosting [80]. The effect of the thickness of the lubricant layer on the anti-icing performance was investigated by Subramanyam *et al.* [81]. They show that the equilibrium layer led to an increased adhesion which can be lowered by increasing the density of the surface features with the same lubricant layer. Another issue in anti-icing using SLIPS/LIS is that the depletion of the lubricant occurs when ice is removed from the surface. Therefore, the major challenge in the development of SLIPS/LIS for anti-icing is durability and has been the focus of various studies [82, 83].

Fluid Mobility

The mobility of droplets is significantly enhanced when placed on SLIPS/LIS and the most slippery situation corresponds to one in which a lubricating layer is present between the droplets and the surface (Figure 2.27, A3-W3). In this situation, the velocity of a moving droplet is set by the balance of gravitational and viscous forces.

Smith *et al.* suggested three regions of viscous dissipation originating from the inside of the droplet, the lubricant layer and the wetting ridge and showed that last is the most dominant of the three [15].

The reduced hindrance to the motion of the contact line could extend beyond droplets to other moving bodies of fluids. At the interface between a solid and a fluid, no-slip is the most accepted boundary condition and has been experimentally verified under most flow conditions [84]. On a SLIPS/LIS, however, special consideration is need for the interface between the lubricating liquid and the test fluid (both in the "encapsulated" and "hemi-wicked" state) and an apparent slips may arise. Solomon *et al.* measured a drag reduction up to 16% between a lubricating liquid and a test liquid which is 260 times more viscous [55]. Analytically, Schönecker *et al.* were able to show a 20% reduction in drag with a viscosity ratio of 56 between the lubricating liquid and the test liquid [85].

Hemeda *et al.* also demonstrated drag reduction using a type of surfaces which they called Liquid-Infused Surfaces with Trapped Air (LISTA) and showed $20 - 37\%$ advantage over their SLIPS/LIS counterparts [86]. Although this type of surfaces differ slightly to SLIPS/LIS in the sense that they are infused with a lubricating liquid using re-entrant surfaces whilst trapping a layer of air underneath, the general principle behind the motivation is the same.

Self-Cleaning

Superhydrophobic surfaces are considered as self-cleaning surfaces due to their ability shed off liquid droplets which carry away contaminants. However, these surfaces maintain their self-cleaning properties by relying on a reduced contact area with the droplets and may fail when liquids with low surface tension are used. SLIPS/LIS have shown excellent self-cleaning properties because of their ability to repel a much wider range of liquids. The extremely low contact hysteresis on SLIPS/LIS also allow surfaces in more horizontal orientations to self-clean. Droplets of identical volumes also have larger footprints on SLIPS/LIS compared to their superhydrophobic counterparts, further enhancing their self-cleaning ability.

The reduced adhesion of particles on SLIPS/LIS can also be used to alter drying patterns of particle-rich droplets. A commonly seen example is the ring patterns left behind by droplets of coffee. The formation of the coffee rings can be attributed to the pinned contact lines of the droplets. Contact lines of droplets experience virtually no pinning during evaporation and thus allowing different drying patterns to be formed [16, 61].

Anti-Fouling

A major problem for surfaces in constant contact with liquids as such oil and gas piplines, turbine systems and surfaces of marine vessels is the formation of biofilms, accumulation of bacteria and the adhesion of plants and small marine animals. Using SLIPS/LIS, Epstein *et al.* demonstrated a 97.2% reduction in the accumulation of bacteria and overall film adhesion under mild flow [87]. The reduced attachment and adhesion of seaweed on SLIPS/LIS was shown by Xiao *et al.* [88]. Another problem with surfaces in contact with liquids is that they are prone to corrosion. The use of superhydrophobic surfaces as a away to minimise corrosion has limited success because the layer of trapped air will be lost over time. Yang *et al.* shown that SLIPS/LIS showed the least amount of corrosion when immersed in 3.5% NaCl solution, compared to hydrophobic surfaces and non-treated surfaces [89].

Droplet Manipulation

The ability to induce motion to small droplets are particularly relevant to microfludic related applications. Due to the lack of pinning, droplets on SLIPS/LIS are highly mobile. Using external force fields such as electric, magnetic or thermal, droplets can easily be manipulated on these surfaces. Using magnetic particles, Chen *et al.* showed that droplets infused with the particles can be moved with a magnetic field [90]. Without infusing the droplets with magnetic particles, Khalil *et al.* demonstrated motion of droplets cloaked by a superparamagnetic ferrofluid, this technique also allows droplets of other liquids to be moved, as long as they are cloaked by the ferrofluid [91]. SLIPS/LIS can also be used in electrowetting to enhance the reversibility of recovering droplets, demonstrated by Pollack *et al.* [92], Hao *et al.* [93], Verheijen *et al.* [94],

Krupenkin *et al.* [95], Bormashenko *et al.* [96] and more recently, Brabcová *et al.* [97] and Barman *et al.* [98]. Other methods to manipulate droplets include the use of thermal gradients as shown by Bjelobrk *et al.* [99], geometric confinement in the form of wedges by Ruiz-Gutiérrez *et al.* [100]. More recently, Guan *et al.* demonstrated the autonomous motion and positioning of droplets using macroscopic surface geometry rendered as SLIPS/LIS [65].

Chapter Summary

This chapter has introduced the background and underpinning theory of solid-liquid interactions including a section summarising the theory behind lubricant-impregnated surfaces (SLIPS/LIS). More specific backgrounds are included in the following chapters in order to set the scene for the specific studies.

The next chapter is the methods chapter. It summarises the general methodologies used to develop the lubricant-impregnated surfaces which are used throughout the thesis.

Chapter 3

Methods

This methods chapter summarises the general methodologies used throughout the thesis, both in the fabrication process of the lubricant-impregnated surfaces and the characterisations of these surfaces. A standard set of techniques were used throughout the entirety of the thesis, with some of the finer details having since been modified and tailored appropriately for more specific purposes as the project progressed. The development of lubricant-impregnated surfaces has allowed the behaviour of droplets with highly mobile lines on surfaces to be studied.

3.1 Development of Lubricant-Impregnated Surfaces

3.1.1 Fabrication of Micro-Textured Surfaces

In this work, the surfaces were chosen such that they could be accurately textured. Silicon wafers with a photolithographically patterned SU-8 layer were used. SU-8 is an epoxy-based negative photoresist that can be spin coated or spread over a range of thicknesses to fabricate thick patterns with smooth walls using photolithography [47]. The SU-8 becomes strong, stiff and chemically resistant after processing and has a typical static water contact angle of $\theta \approx 80^{\circ}$ on a flat and smooth surface with large contact angle hysteresis [47]. Textured surfaces were created using 4" diameter polished silicon wafers (Pi-KEM) with a thickness of 525 μm $\pm$ 25 μm. Prior to the spin coating process, the silicon wafers were first rinsed with acetone and isopropyl alcohol (IPA)

followed by a 10 minute bake at 100 °C to completely remove any remaining solvent. The substrate was then treated with an adhesion promoter HMDS (hexamethyldisilazane) prior to applying SU-8 2025 resist (MicroChem, 2025 denotes that the photoresist should spin to a thickness of 25 μm at 3000 rpm). Using a plastic pipette, the promoter was deposited onto the silicon wafers until it covered the entirety of the substrate surfaces. The silicon wafers then underwent a spin-coating process which consists of two stages. Substrates were first accelerated to 500 rpm at 164 rpm/s for 10 seconds then at 3000 rpm at 820 rpm/s for 1 minute. This was followed by another 2-step spin-coating process of the SU-8 photoresist. The amount of resist deposited onto each substrate was fixed at 4 ml. They were first accelerated to 500 rpm at 164 rpm/s for 10 seconds and further accelerated at a rate of 328 rpm/s to a final speed of 1750 rpm for 30 seconds. This speed was used to achieve a SU-8 thickness of 50 μm (See Figure 3.1 for spin curve). The data point represented by an open diamond shape corresponds to the spin speed of 1750 rpm.

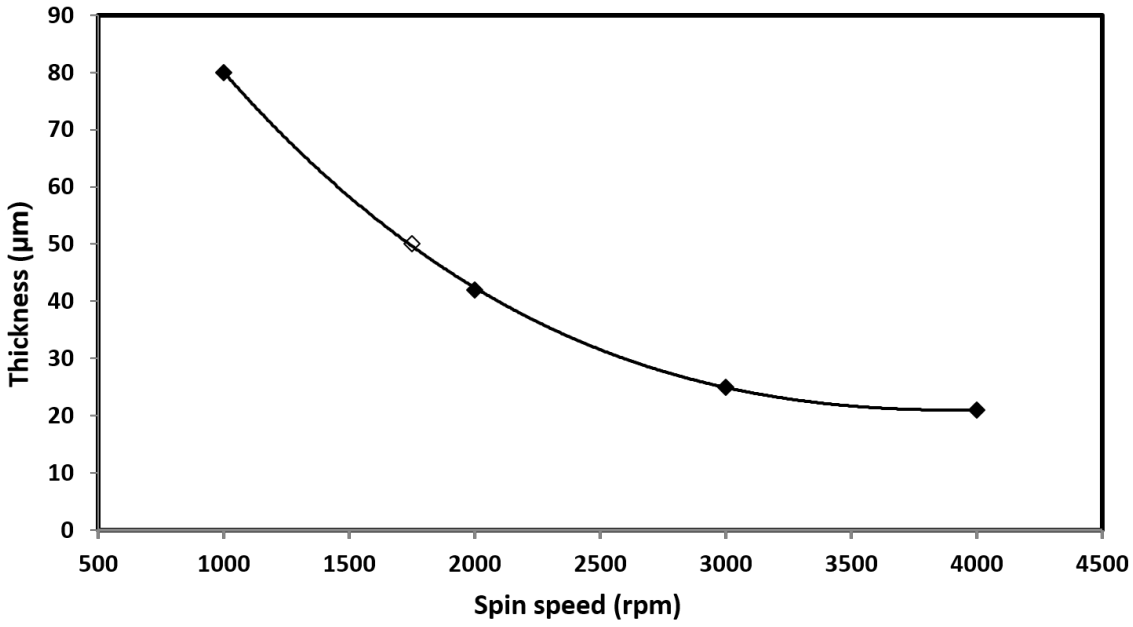

Figure 3.1: Spin curve for SU-8 2025. The data point represented by an open diamond shape corresponds to the spin speed of 1750 rpm.

Substrates were subsequently placed on a hotplate and baked for 3 minutes at 65 °C followed by a 6 minute bake at 95 °C. Substrates were then removed from the hotplate and were left to cool down to room temperature. After prebaking, the photoresist was exposed to a pattern of UV light. The exposure to UV light causes a chemical change

that allows some of the resist to be removed by a special solution, called "developer" by analogy with photographic developer. Positive photoresist, the most common type, becomes soluble in the developer when exposed; with negative photoresist, unexposed regions are soluble in the developer. The now SU-8-coated substrates underwent UV exposure in a mask aligner (EVG 620) under hard contact mode with an exposure dosage of 160 mJ/cm^2 (see Chapter 4 and 5) or 300 mJ/cm^2 (see Chapter 6). As a result of the spin-coating, these exist a circular layer of resist with a greater thickness in the outer region on the substrate due to edge bead effect, therefore only the inner portion of the substrates were patterned to minimise the inherent thickness variation in the surface features. A post-exposure bake (PEB) was performed after exposure and before developing to help ensure the homogeneity of the surface by reducing the standing wave phenomena caused by the destructive and constructive interference patterns formed between the plane wave of UV light travelling through the resist and one which is reflected from the substrate. Substrates were placed on a hotplate for 1 minute at 65 °C followed by a 6 minute bake at 95 °C before being left to cool to room temperature.

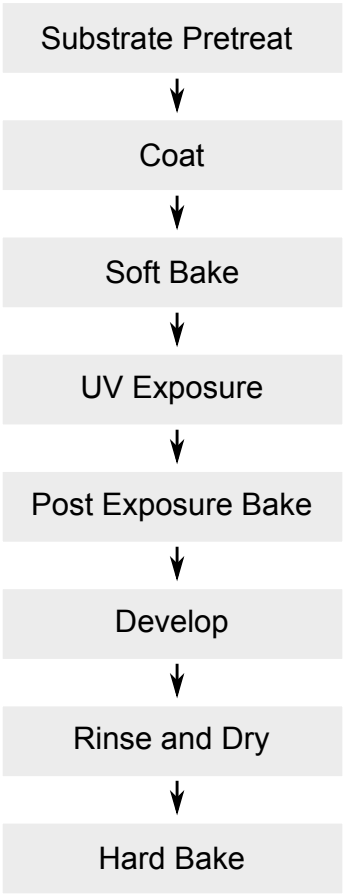

Figure 3.2: Process flow of photolithographic process.

An image of the mask should be visible on the SU-8 resist coating after 1 minute of PEB at 95 °C, the absence of a visible latent image during or after PEB would indicate insufficient exposure, heating or both. Following the post-exposure bake, the substrates were placed in a bath of EC (Ethyl lactate) solvent and agitated for 5 minutes followed by further agitation in a fresh bath for a 10 seconds. The developed substrates were then rinsed with EC solvent and IPA before being dried using nitrogen gas. Occasionally, a white film can been seen during the IPA rinse. This is an indication of underdevelopment of the unexposed photoresist. When this happens, substrates were immersed or spray with additional EC solvent. A final hard bake at 200 °C was added to ensure that the SU-8 photoresist properties did not change during actual use.

Whilst the above are the general procedures for photolithograhy used throughout the thesis (Figure 3.2), additional steps were added accordingly to better suit the specific needs of surfaces with different morphologies or to achieve a finer final finish of the surface features. Things to consider when implementing these steps include:

- **Viscosity of the photoresist** - The recommended storage temperature for SU-8 2025 according to the manufacturer's processing guidelines is 4-21 °C. In this work, the photoresist was stored at 5 °C. This relatively low temperature was seen to have a direct effect on the viscosity of the resist which is more viscous at lower temperatures and thus affect how the resist would spread. Therefore, although not mentioned in the guidelines, it was essential to allow the resist to come to room temperature before being spun onto the silicon substrates.

- **Coefficient of thermal expansion (CTE)** - During the baking processes, due to the rise in temperature, both the silicon substrates and the photoresist layer would expand but at different rates defined by their thermal expansion coefficients (52 ppm/°C for SU-8 and 2.6 ppm/°C for silicon). As a result of this relatively large discrepancy, the SU-8 resist were sometimes observed to partially or even entirely detach from the silicon substrates during baking. This was especially problematic during the cool down process from 200 °C to room temperature after the final hard bake as one material contracted significantly more rapidly than the other. To minimise the detachment of the resist from the silicon, additional

ramping steps were included in the fabrication process. Previously, substrates were first placed on a hotplate at 65 °C and moved to a second hotplate at 95 °C. This was replaced by a step in which substrates were placed on a single hotplate at 65 °C whose temperature was then slowly increased to 95 °C over a period of 3 minutes. After the final hard bake, substrates were previously removed from the hotplate immediately, this step was altered such that the hotplate was switched off and substrates were left to cool down to room temperature. The need for these additional steps depended on the type of surface features used. For example, in Chapter 4 and 5 in which square pillar surface features were used, these steps were generally not needed whereas they were crucial in Chapter 6 in which substrates consisted of large contiguous surface features.

- **Air bubble removal** - Occasionally air bubbles could form in the SU-8 resist during deposition and/or the spin-coat process. To resolve this, prior to deposition, the resist was dispensed into a small vial and de-gassed in a vacuum chamber until all of the air bubbles had disappeared. If the bubbles were still present after deposition, having undergone a degassing step, it was left alone for at least two hours or until the air bubbles were no longer present.

3.1.2 Surface Chemistry Modification

To prevent water from displacing the lubricating liquid and wetting the SU-8 features (see Figure 2.27). A hydrophobic coating was applied to the surfaces used in producing SLIPS/LIS. The purpose of making the surfaces hydrophobic/superhydrophobic is to ensure preferential adhesion of the lubricating liquid compared to water. The additional surface assists the retention of the lubricating liquid and the area combined with hydrophobicity reduces the favourability for water to displace the lubricating liquid. This is because the hydrophobic effect is caused by non-polar molecules. Water is highly polar and forms polar bonds with itself over non-polar molecules, therefore the net effect is that it is attracted to itself and beads up on non-polar surfaces [101]. Oil, on the contrary, is non-polar and tends to adhere to non-polar surfaces. This implies that a superhydrophobic surfaces are most often oleophilic.

Studies have shown that silicone oil spreads on flat, smooth surfaces coated with octadecyltrichlorosilane (OTS) in the presence of both air and water ($\theta_{os(a)} = 0°$ and $\theta_{os(w)} = 0°$) [15, 16, 55]. OTS has frequently been used to hydrophobise smooth surfaces such silicon or superhydrophobic (rough or patterned) surfaces by self-assembled monolayer formation [102, 103]

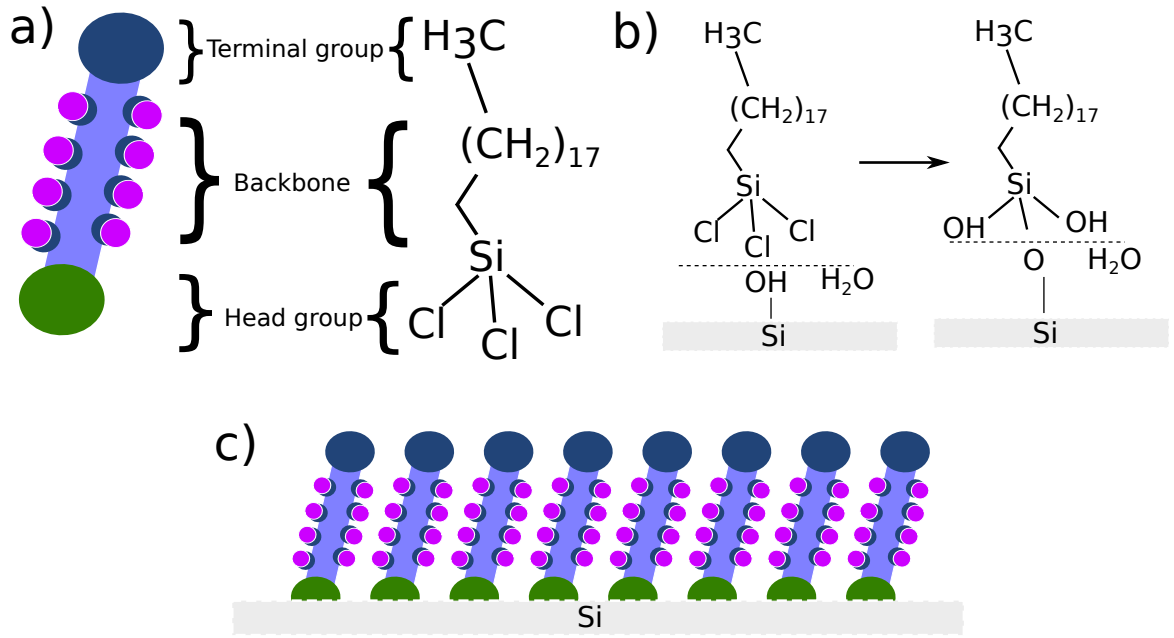

Figure 3.3: a. Schematic diagram and chemical formula of octadecyltrichlorosilane (OTS) representing three functional units; b. reaction steps of OTS with Si substrate and c. schematic diagram of OTS coated Si substrate).

This means that silicone oil will impregnate and flow atop surface features. but will be difficult to displace by water. Prior to treatment, textured silicon substrates were cleaned with acetone and IPA followed by a 10 minute bake at 100 °C to completely remove any remaining solvent. An OTS/hexane solution was prepared using 200 ml of hexane and 50 μL of OTS. A beaker containing the solution was then covered and sonicated for 20 minutes. Meanwhile, substrates were treated with oxygen plasma (Plasmalab 80Plus, Oxford Instruments) to promote adhesion of the OTS to the surface by introducing an OH groups using the following settings: Duration = 30 seconds, Power = 70W, Pressure = 150 mT, O_2 = 100 sccm. Substrates were then placed in the Hexane/OTS mixture for 1 hour. After this, substrates were placed in a fresh beaker of pure hexane immediately after being extracted from the mixture and sonicated for a

further 10 minutes prior to being baked on a hotplate for 15 minutes at 110 °C.

The OTS treatment increased the hydrophobicity of the SU-8 textured surfaces and were therefore used in Chapter 4. However, this method is inherently time consuming and is prone to inconsistency. As the project progressed, the OTS treatment was replaced by a more facile, consistent method using a commercially available product known as Glaco™Mirror Coat (Nippon Shine) which is a nano-particle based hydrophobic coating.

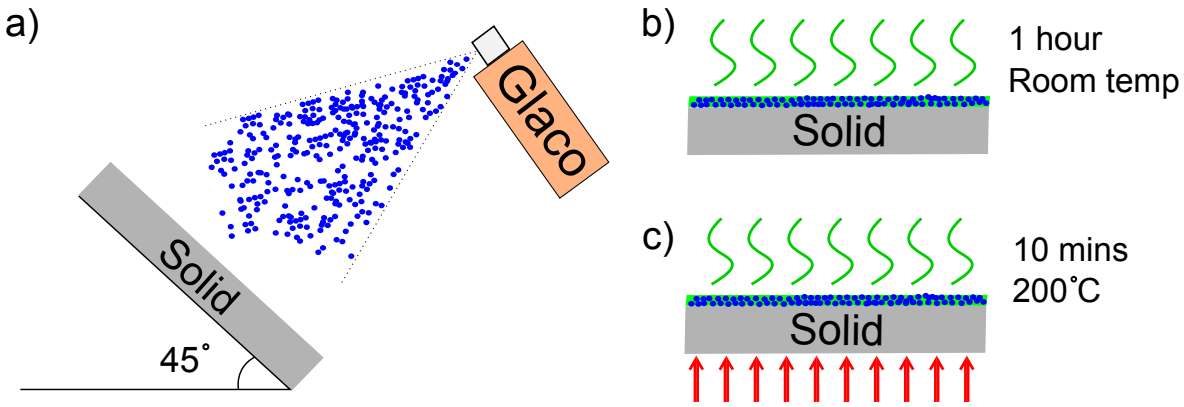

Figure 3.4: Spray coating of Glaco Mirror Coat: a. spray-process, b. solvent evaporation c. optional baking.

Substrates were placed inside a fume cupboard at an angle of 45°. The Glaco coating comes in the form of a spray can, therefore and it was sprayed twice onto the substrates from top to bottom (Figure 3.4a). Substrates were left untouched for 1 hour for the solvent within the Glaco solution to completely evaporate (Figure 3.4b). Alternatively, substrates could be baked at 200 °C for 10 minutes to shorten the duration of the evaporation process but this required the substrates to be able to withstand high temperatures (Figure 3.4c).

3.1.3 Impregnation of Textured Surfaces with Lubricating Liquid

To create a uniform impregnation layer on the surfaces (Figure 2.27), substrates were dip-coated in lubricating liquid to create the SLIPS/LIS and for this silicone oil (Sigma-Aldrich, 20cSt) was used. For a lubricating liquid to spontaneously impregnate surface features, it is necessary that its contact angle in air on a chemically identical and smooth

surface is below a critical angle,

$$\cos\theta_{\mathrm{c}} = \frac{1-\varphi_{\mathrm{s}}}{r_{\mathrm{w}}-\varphi_{\mathrm{s}}} \tag{3.1}$$

where θ_{c} is the critical angle for hemiwicking [104], φ_{s} is the Cassie solid fraction of the projected area of the textured surface, and r_{w} is the Wenzel roughness defined as the ratio of its actual surface area to its projected area. The lubricating liquid, in this case silicone oil, will impregnate the surface textures only if $\theta_{\mathrm{os(a)}} < \theta_{\mathrm{c}}$ where $\theta_{\mathrm{os(a)}}$ is the contact angle of the lubricating liquid (o) on smooth solid (s) in the presence of air (a). Similarly, the condition for impregnation under water is $\theta_{\mathrm{os(w)}} < \theta_{\mathrm{c}}$, where $\theta_{\mathrm{os(w)}}$ is the lubricant's contact angle on smooth solid in the presence of water (w). These possible thermodynamic states of a water droplet on an lubricant impregnated surface have previously been described in Section 2.12.

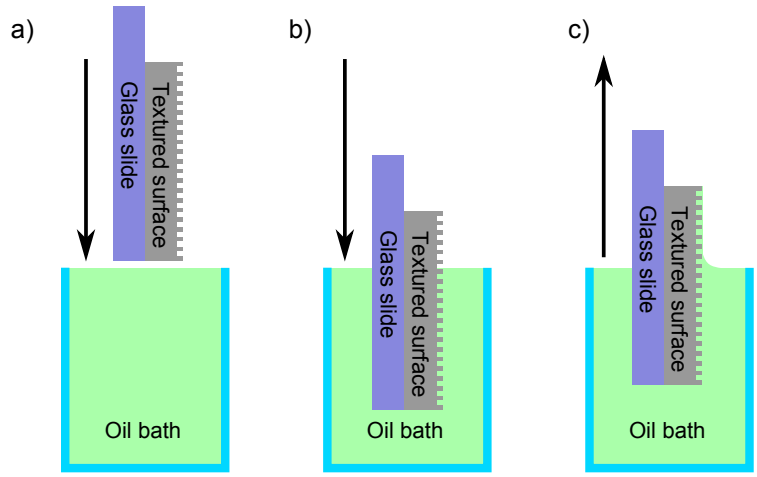

Figure 3.5: Dip-coating process: a. immersion, b. submerged, c. withdrawal.

The textured surfaces were first attached to clean glass slides and subsequently completely immersed in a bath of silicone oil (Sigma Aldrich; viscosity $\eta = 20$ mPa s, surface tension $\gamma_{\mathrm{oa}} = 20.6$ mN m^{-1}) (Figure 3.5a). They were then withdrawn vertically from the bath at speeds ranging from $0.1 - 1\,\mathrm{mm\,s^{-1}}$ (Figure 3.5c). These speeds were found to be optimal for achieving a sufficiently thin lubricant layer according to the equation

$$V_{\mathrm{crit}} = 0.12\mu_o\gamma_{LV}\left(\frac{\delta}{\kappa^{-1}}\right)^{\left(\frac{3}{2}\right)} \tag{3.2}$$

where μ_o is the viscosity of the lubricating liquid, γ_{LV} is the interfacial tension of the lubricating liquid in air, δ is the height of the surface textures and κ^{-1} is the capillary length [55, 104].

3.1.4 Surface Characterisation

To ascertain the dimensions of the textured surfaces were of desired values, a stylus profilometer (Bruker) was used to measure the height of surface features and the distance between them. Consequently, the Cassie fraction, φ_s and the Wenzel roughness, r_w (see Chapter 2.9) could be calculated. Prior to the measurements, samples were placed inside the profilometer whose levelling table is connected to a nitrogen gas supply. The stylus was lowered until it made contact with the silicon part of the samples before moving across at least 10 surface features, i.e. pillars (see Section 4).

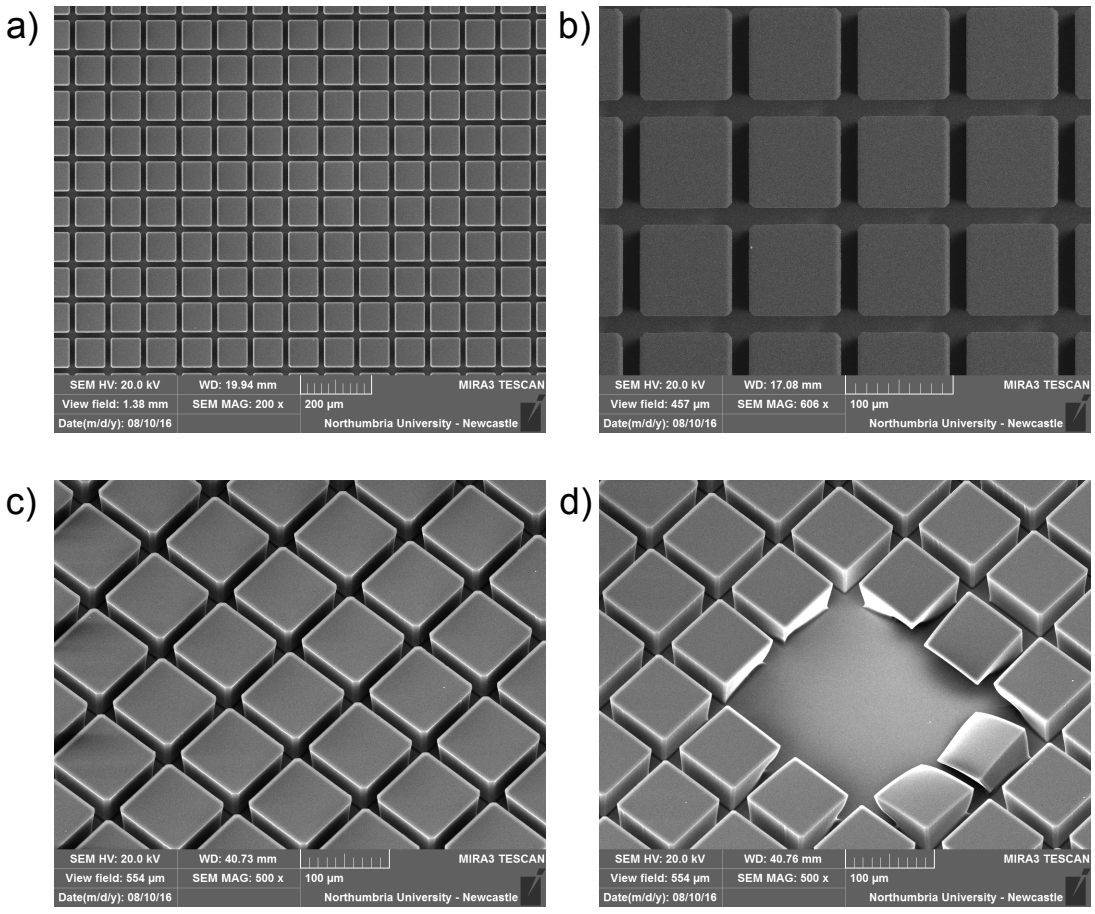

Figure 3.6: Scanning Electron Microscopy images of a surface with 80 $\mu m \times 80$ μm pillars: a. 200x magnification, b. 600 x magnification, c. image taken at 35° angle, d. surface defect.

Scanning electron microscopy (SEM) was used to check the quality of SU-8 surface features and to detect any potential defects on the surfaces due to under/over exposure during photolithograhy (Figure 3.6d). It was necessary for the samples to be coated with a thin layer of platinum before imaging, therefore sacrificial substrates were fabricated specially for this purpose. In Chapter 5, SEM was also used to confirm the existence of the hydrophobic layer in the form of nano-particles deposited on the surfaces.

Throughout the thesis, some of the most essential properties when characterising surfaces include the static contact angles of water droplets on both textured (prior to lubrication) and flat substrates were carried out using a Krüss DSA30 Contact Angle Meter. Dynamic contact angle measurements were also carried out to determine the contact angle hysteresis by measuring difference between the advancing and receding contact angles (see Figure 2.9) using droplets with volumes ranging from $1-10$ μL. The contact angle hysteresis for the substrates was also determined by measuring the sliding angle of waters droplets using the tilt table on the Krüss contact angle meter (this may differ from the different between the advancing and receding anlges because it depends on the volume of the droplet, see Section 2.6). Prior to sliding angle measurements, the tilt stage was set to its zero position and the entire machine was levelled using an Engineer's workshop level (Level Developments, 14-0.05-150) with an accuracy of 50 μm over 1 m. The tilt stage on the Krüss machine allows incremental steps of 0.1°. The sliding angle measurements for all of the samples were taken only when droplets starts to move on a surface. Average values were obtained from three separate measurements to ensure consistency.

3.1.5 Droplet Shape and Apparent Contact Angles

Droplets on lubricant impregnated surfaces in ideal conditions (see Section 2.12) sit above a layer of lubricating liquid. Therefore, strictly speaking, a contact angle as described by the Young's equation (Equation 2.11) is no longer present due to the lack of contact with the soild surface. However, for droplets on the lubricated textured surfaces, the majority of the profiles conformed to a circular arc, consistent with expectations for droplets of sizes less than the capillary length. Data points on the outer edge of

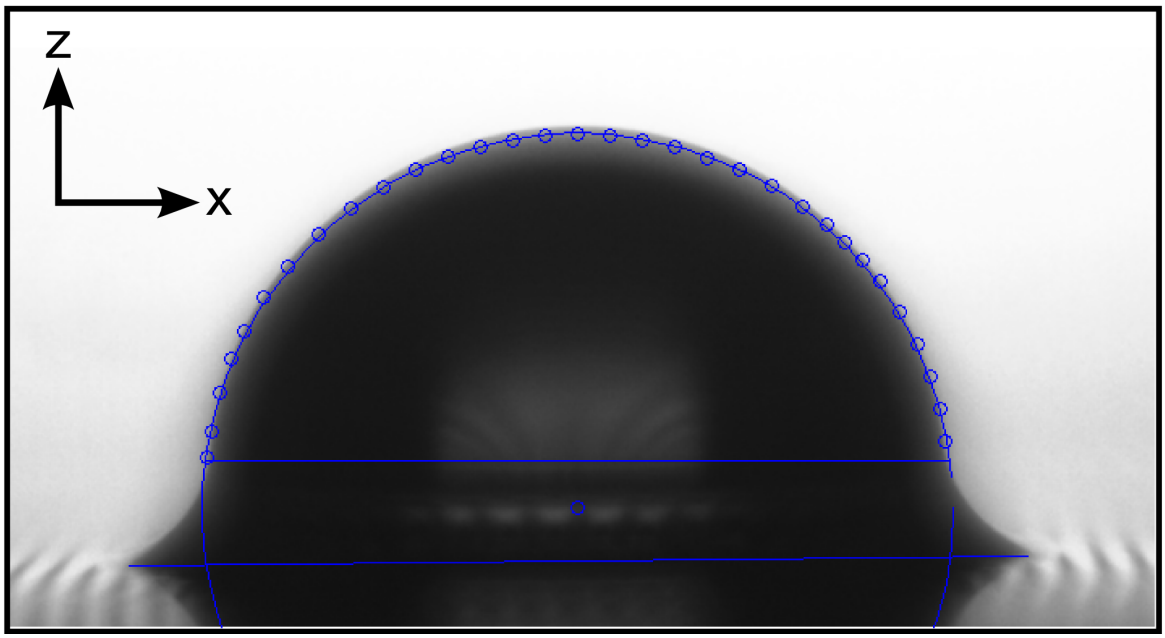

Figure 3.7: Image of a droplet on a lubricated textured surface with a sample of extracted data points on the side view profile of the spherical cap surface.

the droplet were extracted from side view images and a circular arc was fitted using a MATLAB program (a representative selection of points is shown in Figure 3.7 as an example). Baselines were fitted at the base of the droplet and the wetting ridge, and at the top of the wetting ridge. The top of the wetting ridge was determined by sampling the data points from the profile close to the substrates that lie on the wetting ridge-vapour interface and finding the point of reflection of the profile given by the data points.

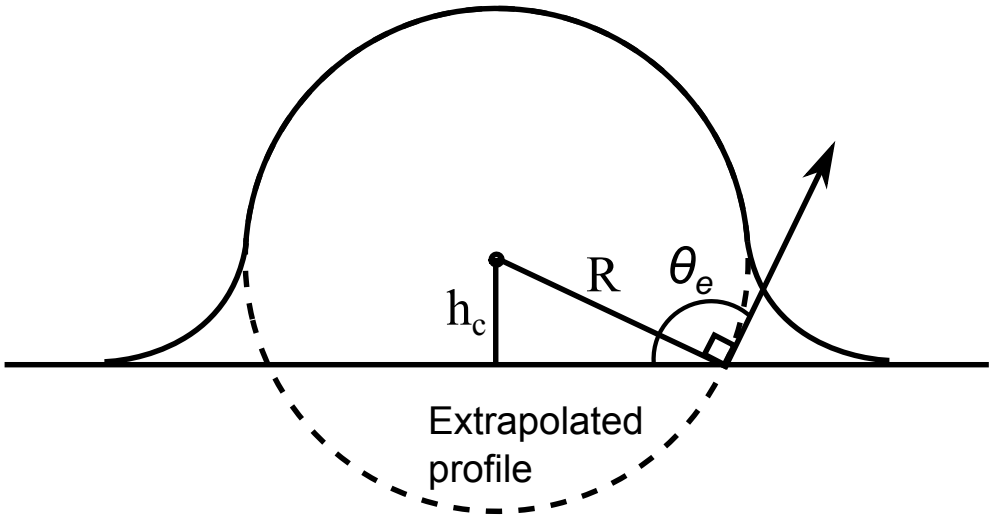

Figure 3.8: Calculating apparent contact angle.

To calculate the apparent contact angle, the following equation was used,

$$\theta_e = \pi - \arccos \frac{h_c}{R} \tag{3.3}$$

where θ_e is the apparent contact angle, h_c is the height of the centre of the fitted circle and R is the radius of the fitted circle (Figure 3.8).

3.1.6 Thickness Measurement of Lubricant Film on Surfaces

Perhaps one of the biggest hurdles, if not the biggest, in the thesis was to obtain direct measurements of the thickness of the lubricant film atop the surfaces. These measurements were particularly important in understanding the wetting ridge height because it is directly related to the amount of available lubricant on the surface. This sub-chapter will summarise various methods trialled and adapted to determine the lubricant film thickness.

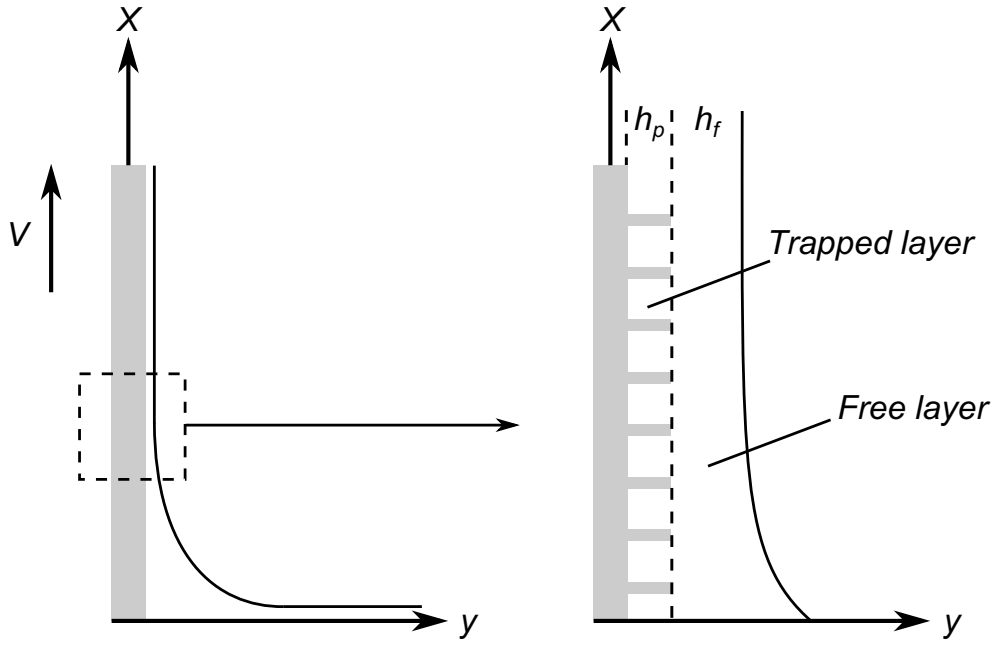

Figure 3.9: Withdrawing textured surfaces from a bath of wetting liquid.

As shown by Landau & Levinch in 1942 and Derjaguin in 1943, withdrawing the surface at a constant speed V induces the deposition of a liquid film of uniform thickness h_d [105]. The film thickness can be calculated by balancing viscous forces responsible for the coating with capillary forces, which oppose it. It is described by the

Landau-Levich-Derjaguin (LLD) equation [104],

$$h_d \approx 0.94\kappa^{-1}\mathrm{C_a}^{2/3} \tag{3.4}$$

where $\kappa^{-1} = (\gamma/\rho g)^{1/2}$ is the capillary length of the liquid, and $Ca = \mu V/\gamma$ is the capillary number. Equation 3.4 is expected to be obeyed for small capillary numbers ($Ca < 0.01$). Using this equation, values of silicone oil film thickness for flat surfaces withdrawn at $0.1 - 1\,\mathrm{mm\,s^{-1}}$ were calculated (Figure 3.11). To verify these values experimentally, various methods were tested to obtain reliable values for the thickness of deposited films of silicone oil on glass slides withdrawn at $0.1 - 1\,\mathrm{mm\,s^{-1}}$. An optical microscope was initially used. One side of glass slides were marked prior to dip-coating and a thin layer of corn flour particles were deposited onto the oil films. By focusing on markings at the bottom of the oil film and the particles above and by taking into the account the refractive index of the silicone oil of 1.403, an inferred value of the oil film thickness could be obtained. However, because of the relatively large size of the particles compared to theoretical film thickness ($\approx 3 - 13$ μm for the aforementioned withdrawal speeds) as well as the aggregation of the particles, the measured values were significantly larger than those predicted by Equation 3.4 with large errors. Alternatively, an experimental set up consisting of a micrometer onto which a 3D printed tip was attached was used. The idea behind this method was to bring the tip into contact with the top of the oil film (the presence of a oil meniscus would indicate its contact with the tip) and the top of the glass slide. This method was again found to give error values comparable to the measured values.

To obtain more accurate values, a method with much higher resolution was needed. A Nikon A1R Confocal Microscope with the ability to scan samples vertically at steps of 1μm was subsequently used. In order for the microscope to detect the silicone oil, the oil had to be dyed with a fluorescent dye prior to the measurements. To do this, 5 mg of fluorescein acrylate was added into a mixture consisting 1 g of chloroform and 1 g of methanol. The resultant mixture was agitated in a ultrasonic bath for 2 minutes. Once the dye had completely dissolved, 0.38 g of the mixture was added into 20.37 g of silicone oil. The final mixture was then agitated for another 2 minutes.

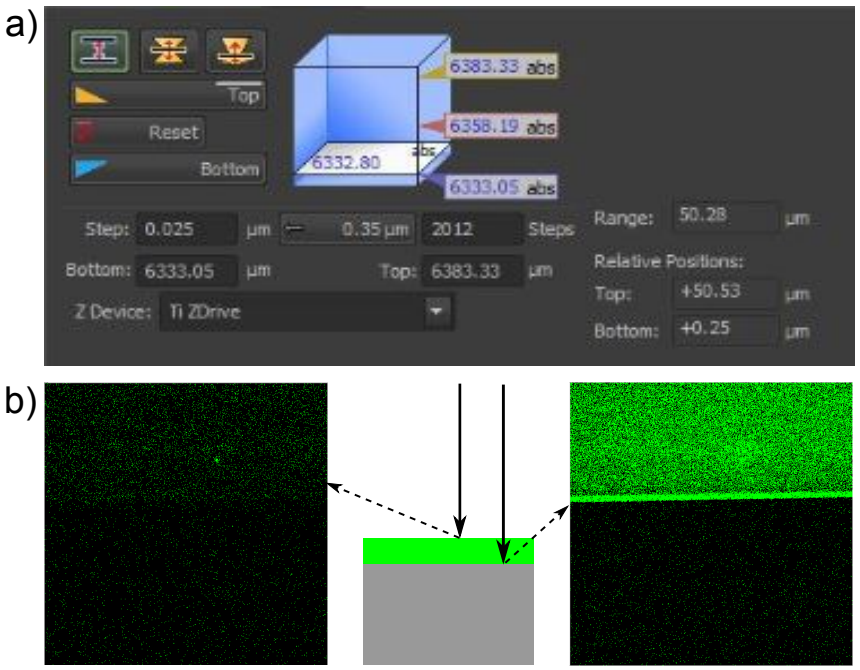

Figure 3.10: a. An example of the confocal interface showing top and bottom limit of scan, b. top of oil layer, c. top of SU-8.

To be consistent with the experimental conditions, 10 silicon substrates with a single step made using SU-8 photoresist were dip-coated with silicone oil with the fluorescent dye. Once coated, substrates were placed in a sample holder in the microscope. The fluorescent dye within the oil was excited by a 488 nm laser and showed a green colour on the screen.

Prior to the actual scan, a scan range was defined with the top of the scan being somewhere just above the oil-air interface and the bottom somewhere below the oil-solid interface(Figure 3.10a). The microscope was then set to scan through the entire range at a scan step of 1 μm. After the scan, all of the scanned layers were combined and a three-dimensional reconstruction was created. It was discovered at this point that the SU-8 photoresist was also excited by the laser and therefore also appeared green on the scan result. Despite this, a solid-oil interface was still relatively easy to find due to the scarcity of the fluorescing particles in the dye oil compared to those in the photoresist layer (Figure 3.10b,c). After carefully examining the images and with the help of the scan step (1 μm), measurements for the oil film thickness for substrates dip-coating at speeds from $0.1 - 1\,\mathrm{mm\,s^{-1}}$ were obtained and they appeared to agree well with theoretical values (Figure 3.11) [104].

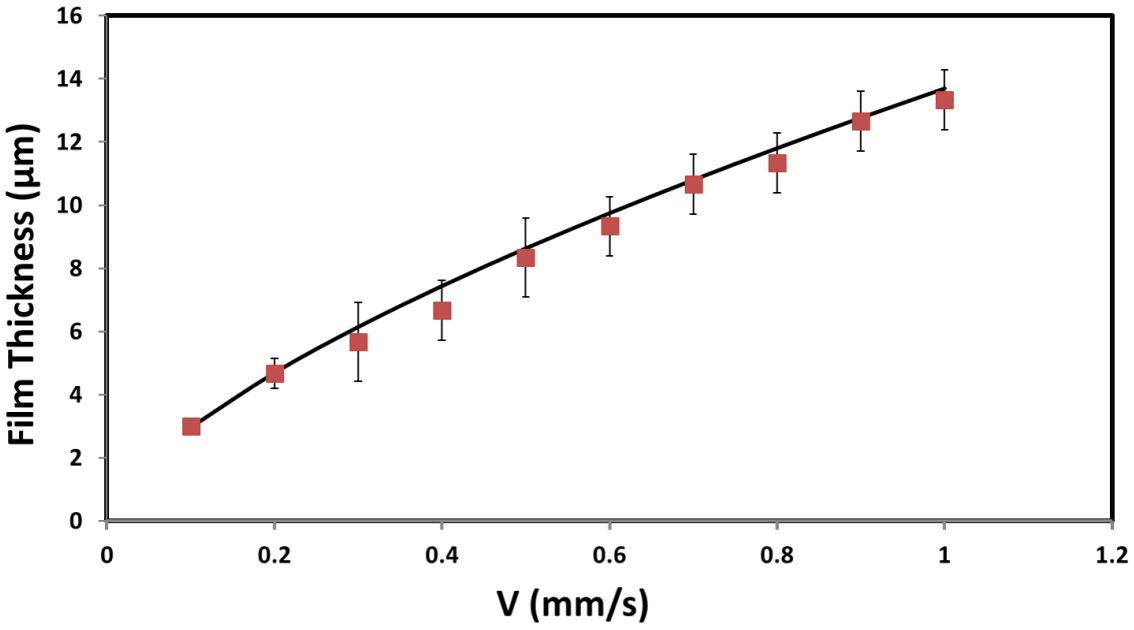

Figure 3.11: Theoretical (solid line)and measured film thickness (red squares) for silicone oil on flat surfaces dip-coated at $0.1 - 1\,\mathrm{mm\,s^{-1}}$.

Whilst Equation 3.4 predicts liquid film thickness on a smooth flat surface, studies by Chen [106] and Krechnetnikov & Homsy [107] have presented evidence that the film deposited on a rough surface is always thicker than that on a smooth surface. Seiwert *et al.* presented a study in which they discussed how well-defined microtextures entrain a film when extracted out of a bath of wetting liquid [104]. They showed experimentally the film exactly fills the gap between the surface features at low withdrawal speed, V and its thickness, h_d is independent of V but does correspond to the height of the surface features, h_p. They also showed that at faster withdrawal speeds, h_d slowly increases with V and towards the Landau-Levich-Derjaguin (LLD) thickness, h_{LLD}, as observed on a flat solid. For textured surfaces, as shown by Seiwert *et al.*, as a textured surface is withdrawn vertically from a bath of wetting liquid, a film of the liquid of thickness h_p is trapped within the surface texture of the same height, on top of which lies a free layer of the same liquid of thickness h_f, making the total thickness of liquid entrained by the textured surface a combination of two, $h_d = h_p + h_f$ (Figure 3.9).

Thickness measurements of oil film on textured surfaces (used in Chapter 4 and 5) were carried out using the aforementioned techniques. According to Equation 3.2, withdrawing at speeds of $0.1 - 1\,\mathrm{mm\,s^{-1}}$ should fill the gaps between surface features with oil as well as depositing a layer above the features and both were experimentally

verified.

3.1.7 Interfacial Tension Measurements

The term interfacial tension relates to the liquid/liquid and liquid/solid phase boundaries (as described in Section 2.1). In this project, the most prominently featured liquids are water as the test liquid and silicone oil (20 cSt) as the lubricating liquid used for the SLIPS/LIS. The interfacial tension of water in air at 25 °C has been extensively studied and the most common used value is 72.8 mN/m [108] and the silicone oil used has an interfacial tension of 20.6 mN/m. Interestingly, the spreading coefficient for oil on water in the presence of air, $S_{ow(a)}$, was calculated to be 5.4 mN/m which implies that silicone oil would spread into a thin film on water and droplets sitting on a layer of silicone oil would be cloaked with a thin layer of the oil.

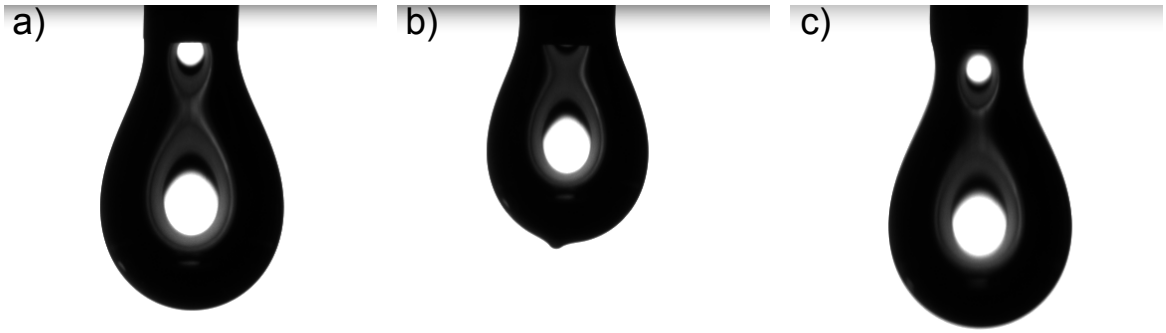

Figure 3.12: Pendant droplets: a. water, b. water cloaked in excess amount of oil, c. water cloaked in a thin layer of oil.

The Krüss DSA30 Contact Angle Meter was used to measure the interfacial tension of droplets cloaked by a thin layer of silicone oil. In pendant drop mode, the DSA software was able to measure the interfacial tension by dispensing droplets from an automated dispensing syringe. Water droplets were dispensed at a controlled rate and imaged at 24 fps. A value for the interfacial tension of water was then obtained by analysing the image captured at the moment immediately before the droplet detaches from the syringe needle (Figure 3.12a). An average value for the interfacial tension of water in the presence of air at 22 °C, $\gamma_{\mathrm{wa}} = 71.5 \pm 0.4\,\mathrm{mN/m}$, was obtained by averaging 50 measurements. To measure the effective interfacial tension of water in the presence of silicone oil, a small droplet of oil was dispensed onto the area near the tip of the syringe needle where water is dispensed. The oil was then allowed to travel freely downwards,

cloaking the water droplet. Droplets were dispensed and analysed until the surface tension measurement stabilised to a constant value $63.4 \pm 0.5\,\mathrm{mN/m}$, averaged over 10 consecutive drop counts (Figure 3.12b & c). Subsequent drops showed a systematic increase in the surface tension that stabilised to the initially measured value of γ_{wa}, indicating a depletion of the oil layer.

Chapter Summary

This methods chapter describes the general fabrication processes involved in the development of the lubricant-impregnanted surfaces. This has produced a surface on which droplets have highly mobile contact lines with the ability to hold onto the lubricant layer even when coming into contact with water.

The next three chapters report on the experiments performed with the lubricant-impregnated surfaces with different surface topography in order to achieve true constant contact angle mode of evaporation of sessile droplets, accurate droplet manipulation in wedge geometries and autonomous propulsion and positioning of droplets.

Chapter 4

Droplet Evaporation on SLIPS

This chapter will describe the work on the evaporation of sessile droplets on lubricant-impregnated surfaces. It will give an overview of the development of the field of diffusion-limited evaporation of sessile drops on solid surfaces and give a description of the different modes of evaporation and the common challenges in the study of true constant contact angle mode evaporation. It will then go on to describe the development of a general model for diffusion-limited evaporation from SLIPS/LIS.

4.1 Background of Sessile Drop Evaporation

Liquid evaporation is a widespread phenomenon and can be seen in natural processes such as rain, snow formation, dew and fog [109]. It is a type of vaporisation of a liquid that occurs from the surface of a liquid into a gaseous phase. It is basically a simultaneous heat and mass transfer operation in which heat for evaporation is transferred by conduction and convection from warm air to the drop surface from which the vapour is transferred by diffusion and convection back into the air.

A droplet of liquid evaporates when the atmosphere in the immediate vicinity is not saturated with the vapour of the same liquid as the droplet. However, evaporation may still occur for very small droplets in saturated atmosphere due to an increase in vapour pressure caused by the surface curvature of the droplet known as the Kelvin's effect. Free evaporation of small and spherical droplets of water in an ambient gas is an important topic of interest and has attracted extensive attention due to its widespread

relevance to scientific applications such as the control of deposition of particles on solid surfaces from droplets containing suspensions, ink-jet printing, thin film coatings, micro/nano material fabrication, automatic DNA mapping, spraying of pesticides and microfluidics [110–113]. These applications often involve small sessile droplets having sizes below the capillary length deposited on solid substrates whose shape is dominated by surface tension rather than gravity. The word "sessile" originated from the *Latin* word "sessilis", meaning "sitting" or "to sit". The term "sessile drops" is used to describe drops deposited on, usually a solid substrate, which is not completely spherical with a contact angle of 180° nor a complete film with a contact angle of 0°. They evaporate with time and the initial contact angle decreases depending on the vapour pressure of the liquid and external conditions in some instances. Thus, understanding the influence of evaporation on the contact angle of a sessile liquid drop in still air or controlled atmospheric conditions would lead to a better understanding of the wetting properties and surface characteristics.

The basic equations for diffusion-controlled drop evaporation in still air was first derived by Maxwell in 1877, this constituted a basis for diffusion theories that followed [114]. In his model for drop evaporation, or stationary state evaporation, Maxwell assumed that the rate of evaporating solely depends on the rate at which evaporating molecules diffused through the surrounding gaseous media [114]. He also assumed the drop to be spherical and motionless relative to an infinite uniform medium. Relating Maxwell's findings to the evaporation of hemispherical drops sitting on a plane, Sreznevsky demonstrated that rate of evaporation of a drop is approximately proportional to the vapour pressure of the liquid [109, 115]. It was later shown by Morse, by measuring the evaporation of spherical iodine drops, that the rate of evaporation was proportional to the radius of the sphere, not the surface area [109, 116]. Morse's results were analysed by Langmuir whom in turn confirmed the proportionality between the rate of evaporation and the radius of a spherical drop [117]. Langmuir also calculated the diffusivity of iodine vapour from the evaporation rate and found that the value of diffusion is lower than expected from a free hanging drop. He suggested that the reduced free diffusion in all directions due to the presence of the flat surface on which the iodine

liquid rested could have contributed to this discrepancy [117]. Picknett and Bexon considered in their foundational study of sessile drop evaporation the theory for diffusion controlled evaporation and experimentally observed the mass and profile evolution of slowly evaporating liquid (methylacetoacetate) droplets on a Teflon surface in air [118]. They showed that the evaporation rate of a completely spherical drop with a contact angle of 180° on a surface is lower than that of equivalent volume hanging spherical drop in free space due to the reduced space into which the vapour may diffuse [118].

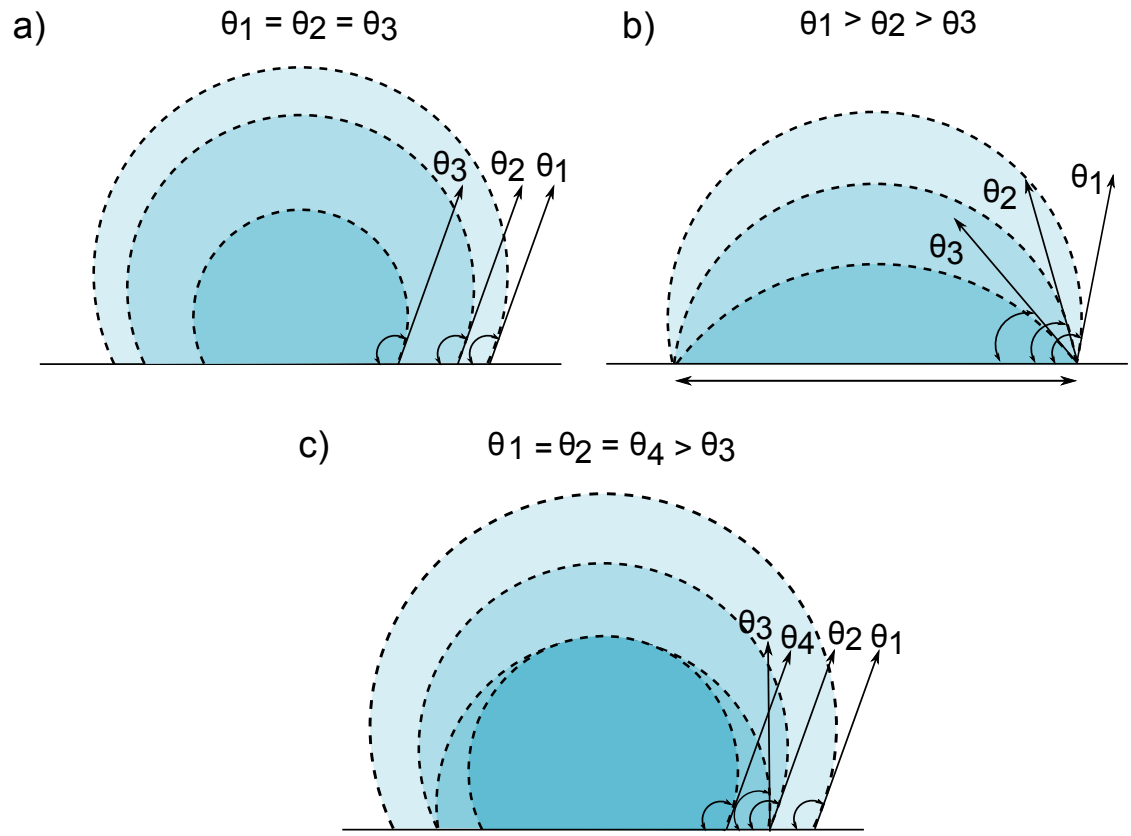

Figure 4.1: Different modes of evaporation: a. constant contact angle b. constant contact area c. mixed mode.

Using the analogy between the diffusive flux and the electrostatic potential, Picknett and Bexon derived an equation for the rate of mass loss in this situation, and it was found to be valid for droplets resting on a solid boundary with a shape of a spherical cap. In this study, two pure modes and a mixed mode of evaporation were reported [118]

- Constant contact angle with diminishing contact area (Figure 4.1a)
- Constant contact area or contact radius with diminishing contact angle (Figure 4.1b)

- A mixed mode with changes in both the contact area and the contact angle (Figure 4.1c)

In one of the earliest studies, Birdi *et al.* reported constant contact area mode of evaporation in their investigation of the evaporation rate of sessile droplets of water placed on a smooth solid surface and in which they observed a constant radius of liquid-solid interface and at the same time a decrease in the contact angle [119]. They then went on to demonstrate, in their subsequent work, the effect of wetting characteristics on the evaporation rate of droplets of liquids and showed that water on glass substrates having a contact angle $< 90^\circ$ evaporated in constant contact area mode; whereas water with a contact angle of $> 90^\circ$ Teflon was observed to have evaporated with a constant contact angle and a diminishing contact area [120]. In addition to smooth surfaces Shanahan and Bourgès also considered the evaporation of water droplets with contact angles below 90° from rough surfaces and obtained measurements of the change in contact angle, drop height and contact radius with time and provided a theoretical model [121]. In two separate studies, Rowan and co-workers observed the change of contact angle and obtained detailed measurements of various geometrical parameters on systems with $\theta < 90^\circ$ and gave a theoretical model based on a diffusion model suggested by Birdi *et al.* [119, 122, 123]. They later presented detailed measurements for evaporation of sessile drops in a system with $\theta > 90^\circ$ in which they showed that the evaporation is dominated by an initial stage with constant contact angle and a diminishing contact radius [124].

Recent reviews of sessile droplet evaporation include those by Cazabat and Guéna [125], Erbil [109], and Larson [126]. Despite extensive research, obtaining experimental systems in which sessile droplets on surfaces evaporating in true constant contact angle mode remains difficult due to the inherent contact angle hysteresis of the surfaces. Smooth solid surfaces tend to have significant contact angle hysteresis and as a droplet evaporates its contact line is often pinned and will then recede in a stick-slip stepwise fashion. Over the past decade, the most common approach to creating liquid shedding, superhydrophobic surfaces have mostly involved using micro/nanotexturing to amplify the effects of non-wetting surface chemistry. The surface textures reduces the contact of

the surface with liquid droplets. These surfaces have shown to be good candidates for studying the constant contact angle mode of evaporation due to their water shedding ability. They are often referred to as "slippery" when demonstrating a Cassie-Baxter state in which droplets bridge across the top of the surface features [40]. In 2005, McHale *et al.* were the first to report the evaporation of 1 - 2 mm diameter sessile water droplets on lithographically patterned superhydrophobic surfaces, having an initial contact angle above 150° [127]. The patterns consisted of tall and cicular pillars of SU-8 photoresist arranged in a square lattice. In their study, they observed a brief initial period in which droplets evaporated with constant contact area/radius, corresponding to the droplet evaporating while suspended across the tops of the pillars. This was followed by a depinning process which displayed a stepwise retreat of the contact line, reflecting the periodicity of the underlying surface texture. In some cases, they observed that droplets would collapse into the surface texture during the later stages of evaporation displaying a transition from Cassie-Baxter to a "sticky" Wenzel state [39], resulting in a completely pinned droplet. Zhang *et al.* studied the evaporation of sessile water droplets on superhydrophobic natural lotus and hierarchically structured polycarbonate surfaces and found that the contact line was almost pinned and droplet's contact angle vanishes to zero during the evaporation process. They attributed this behaviour to the penetration of water vapour into the rough structure and the high adhesion between the water and the lotus due to their high interaction [128].

4.2 A New Approach using SLIPS/LIS

Many studies have since looked into studying the constant contact angle mode of evaporation of droplets using superhydrophobic surfaces. Despite this, achieving true constant contact angle mode of evaporation remains challenging. Even with reduced contact, droplets nevertheless remain partially in contact with the surface which can cause pinning. A solution to this seemingly difficult problem would be to completely avoid any contact the droplets may have with the surface. At this point, the problem becomes paradoxical because a droplet in the proximity of the surface but not in contact with the surface is no longer a sessile droplet. It is no different to a hanging drop with a

distorted shape. This seemingly unsolvable conundrum does, however, have a solution.

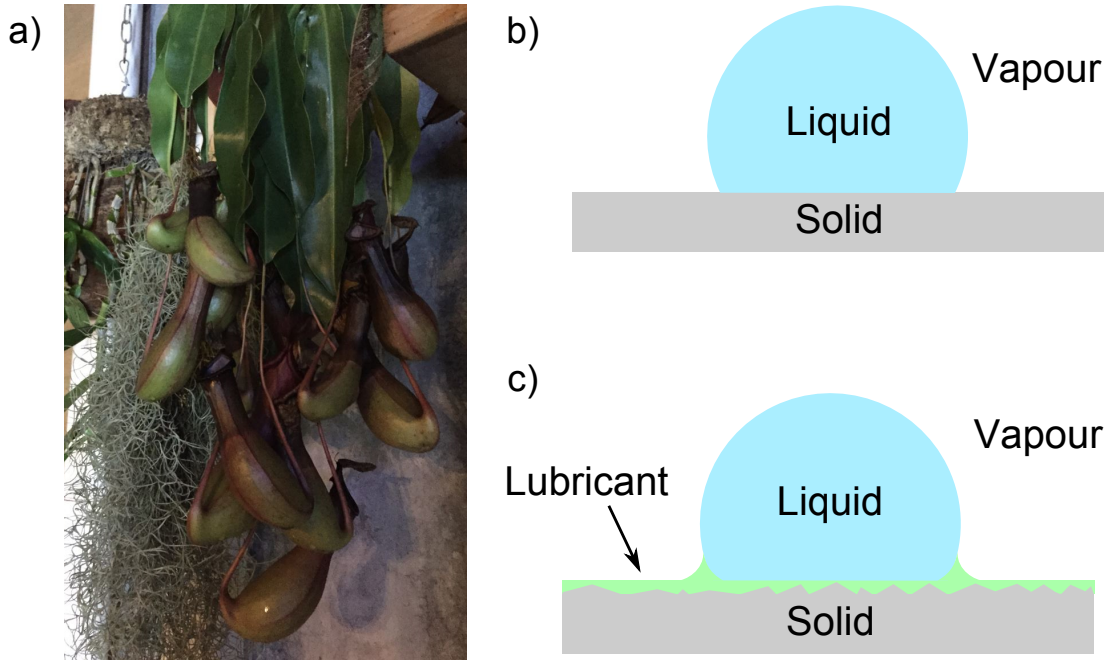

Figure 4.2: a. Pitcher plant b. droplet sitting on a solid surface c. droplet on lubricant-impregnated surface.

To prevent contact between the droplet and the surface, one can do so by replacing the original solid-vapour interface with a solid-liquid interface (Figure 4.2) which will in turn replace the original solid-liquid interface between the droplet and the surface with a new liquid-liquid interface between the droplet and a second liquid. Furthermore, this configuration must remain unaltered upon contact such that the droplet does not displace the second liquid and penetrate into the surface features. An obvious example of a surface capable of satisfying these conditions is SLIPS/LIS. As shown in Figure 2.12, there are different thermodynamically stable states which can exist when a droplet is placed on a SLIPS/LIS depending on the spreading coefficient of the lubricating liquid. The most slippery states and therefore most ideal for constant contact angle evaporation corresponds to the case whereby a lubricating liquid is present as a continuous layer between a droplet and the solid substrate underneath, completely preventing any contact the droplet has with the underlying features.

The development of SLIPS therefore offers an opportunity to study evaporation of water droplets with highly mobile contact lines not subject to the contact line pinning of previous surfaces. This, however, touches upon fundamental questions relating to wetting and conventional interpretation of contact angles. When a droplet is deposited

on a rigid solid surface, it forms a sessile droplet and its contact angle with the surface is described by the Young's equation. Whereas a droplet forms a liquid lens when deposited on a liquid sub-phase and the three phase contact line between the droplet, the liquid sub-phase, and vapour is determined by the a balance of interfacial forces often depicted pictorially using a Neumann's triangle. In between these two cases is the case whereby a droplet deposited on a soft surface and the vertical component of the droplet's surface tension deforms the surface, creating a wetting ridge.

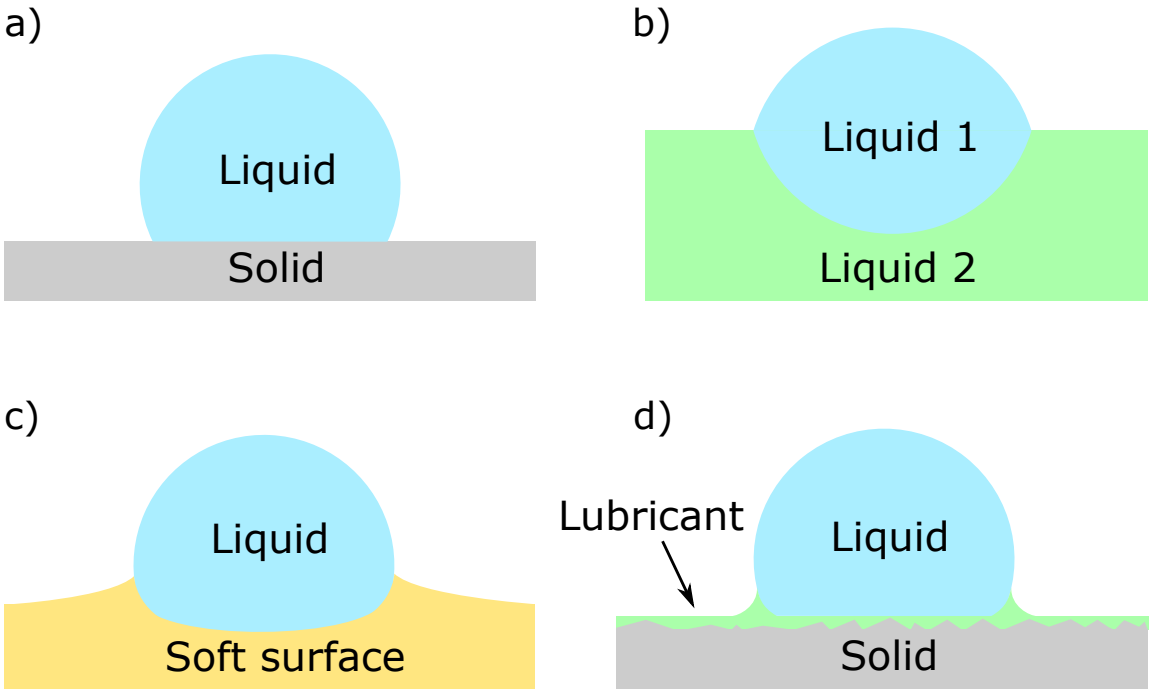

Figure 4.3: a. Droplet on a dry, rigid surface b. a liquid lens, c. a droplet on a soft surface d. droplet on a SLIPS.

In the case of a droplet on a SLIPS, the droplet appears to rest on the surface in a fashion similar to that of a sessile drop on a solid surface rather than a liquid lens, but because the droplet rests on a layer of lubricating liquid the region close to the solid surface shows a more complex shape with a wetting ridge. The lack of direct contact of the sessile droplet with the underlying solid surface makes it less clear how a contact angle as defined by Young might be defined and how previous theories, which included droplet-solid contact angle and contact area, may relate to the evaporation process.

4.3 Surface Fabrication and Characterisation

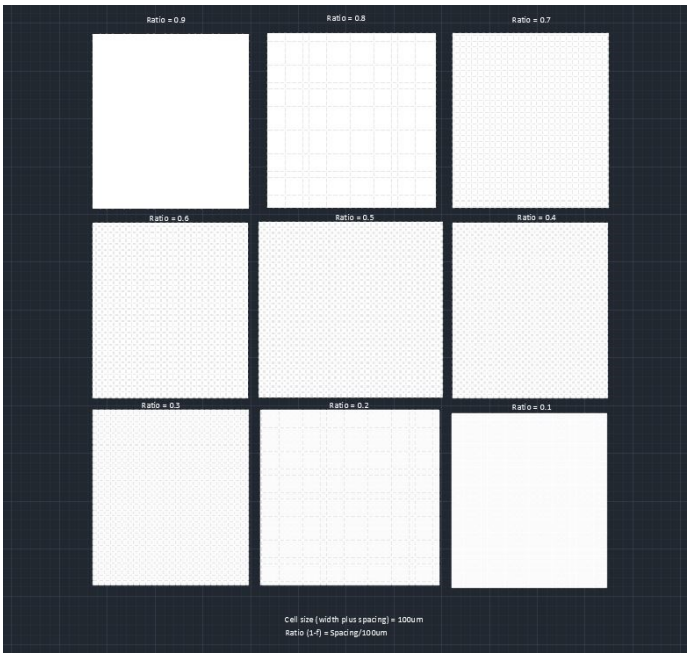

Figure 4.4: Photolithographic mask for the production of pillar surfaces.

To create surfaces suitable for studying evaporation in constant contact angle mode, the conditions as described in Section 4.2 should be satisfied. For this study, surfaces were fabricated using SU-8 2025 (MicroChem) negative photoresist deposited onto silicon wafers functionalised with OTS using the techniques described in Section 3.1.1 with a specifically designed photomask to transfer the desired final pattern onto the surfaces (Figure 4.4).

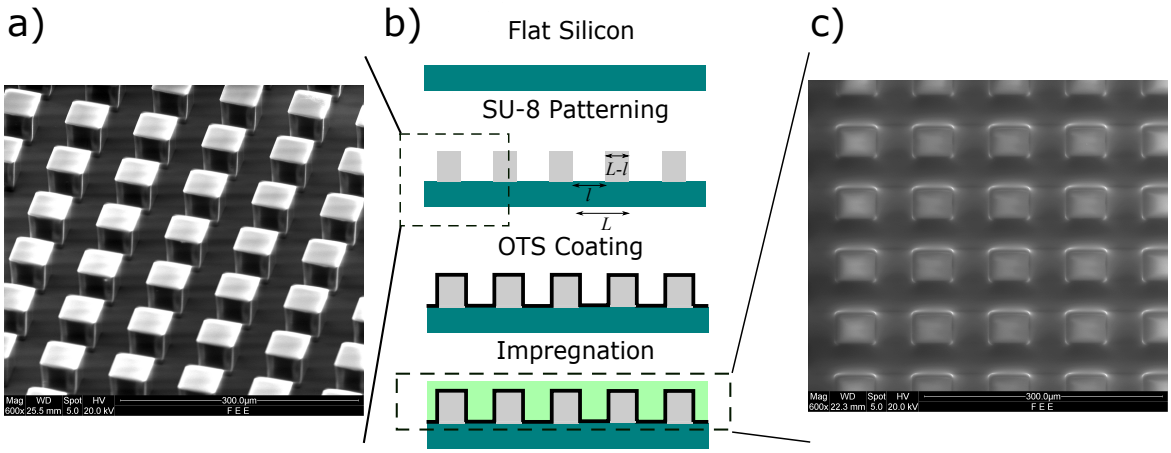

Figure 4.5: a. SEM image of surface with linear lubricant fraction $l_f = 0.5$, b. process to create the lubricant impregnated surfaces, c. image of textured surface impregnated with a lubricant.

The final surfaces consisted of square pillars of the SU-8 photoresist (Figure 4.5a,c). Dimensions of these pillars were carefully tailored to fulfil the geometrical requirements necessary for the lubricating liquid to impregnate the surface features according to Equation 3.1. The pillar widths ranged from 10 μm to 90 μm and were arranged in a square lattice with centre-to-centre separations between pillars (L) of 100 μm.

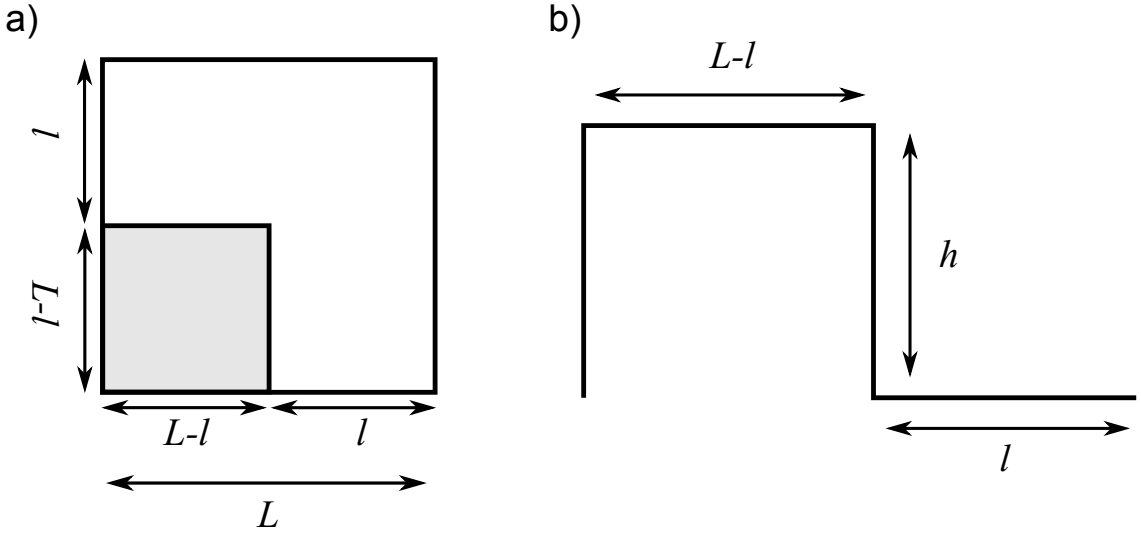

Figure 4.6: Two-dimensional a. cassie-fraction and b. wenzel roughness.

Table 4.1: Linear lubricant fraction l_f, cassie fraction φ_s, wenzel roughness r_w and critical angle for hemi-wicking

Linear lubricant fraction/l_f	Cassie fraction/φ_s	Wenzel roughness/r_w	Critical angle/$^\circ$
0.1	0.81	2.8	84.8
0.2	0.64	2.6	80.4
0.3	0.49	2.4	76.7
0.4	0.36	2.2	73.4
0.5	0.25	2	70.5
0.6	0.16	1.8	67.9
0.7	0.09	1.6	65.7
0.8	0.04	1.4	63.6
0.9	0.01	1.2	61.7

For example, a sample having 30 μm wide pillars ($L - l$) would lead to a pillar separation (l) of 70 μm (Figure 4.5). Therefore, the Cassie surface fraction (φ_s) and the their Wenzel roughness (r_w) could be calculated as follows,

$$\varphi_s = \frac{(L-l)^2}{L^2} \tag{4.1}$$

and

$$r_w = 1 + \frac{4h(L-l)}{L^2} \tag{4.2}$$

where L is kept at 100μm, $(L-l)$ is the width of the pillars and l is the separation between pillars. As a naming convention for the different samples the linear lubricant fraction (l_f) was used and it is defined as $l_f = l/L$ and therefore ranged from 0.1 to 0.9.

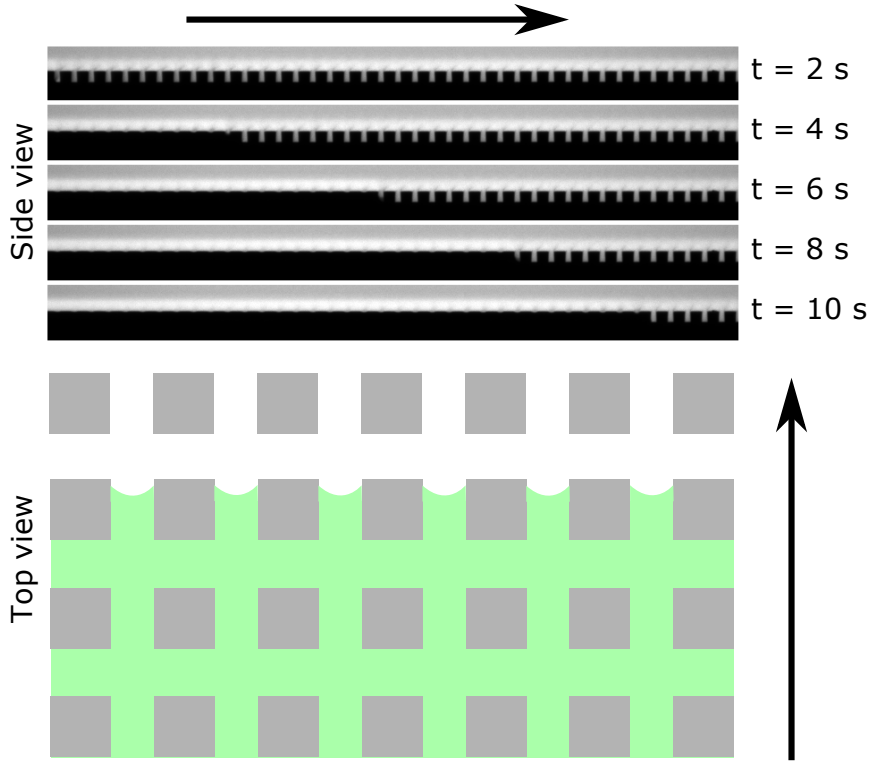

Figure 4.7: a. Silicone oil filling the surface features, b. top view illustration of oil wicking into the surface features.

Even though all samples were designed in accordance with Equation 3.1 and therefore should allow the lubricating liquid to wick into to the gap between the pillars (Figure 4.7), there exists another important factor. To create a situation in which a droplet entirely on the lubricating liquid without ever coming into contact with the underlying features, it was necessary to ascertain that the lubricating liquid spreads completely onto the SU-8 photoresist even in the presence of water. To do this, chemically identical surfaces were created by coating silicon wafers with the resist which was then coated with OTS. Measuring the contact angle of silicone oil on these surfaces in the presence of air was straight forward. However, the same measurement in the presence of water required an additional rectangular acrylic container to be built. Samples were first placed inside the container filled with water, a syringe was then brought to a point just above the

surface which then deposited silicone oil.

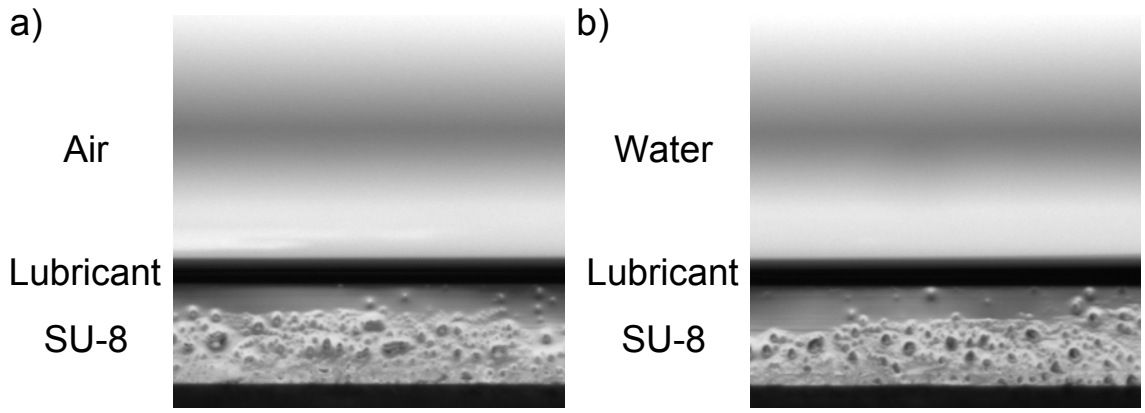

Figure 4.8: Complete spreading of silicone oil in the presence of a. air and b. water.

Studies have shown that flat, smooth surfaces treated with OTS will facilitate the spreading of silicone oil in the presence of both air and water ($\theta_{os(a)} = 0°$and $\theta_{os(w)} = 0°$) [15, 16, 55]. The same was observed experimentally on the flat silicon SU-8 coated with OTS (Figure 4.8). This means that silicone oil not only fills the gaps between the surface features but also spread atop the pillars.

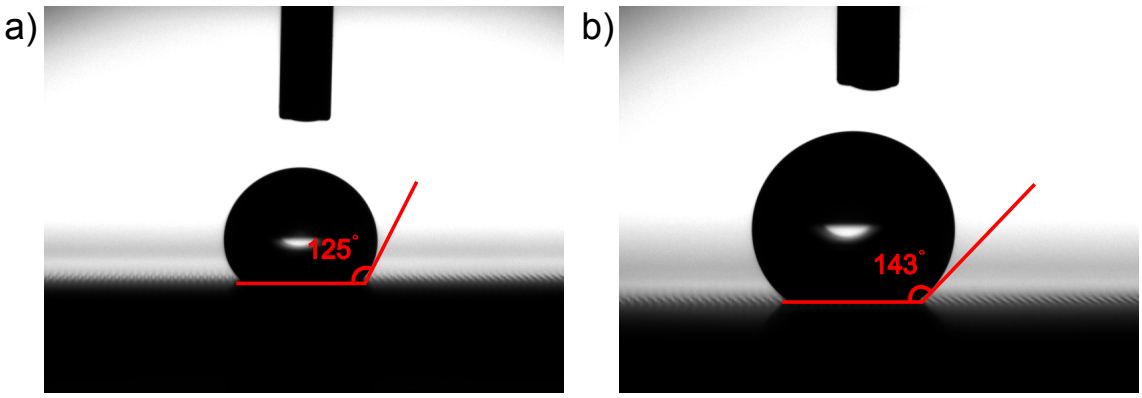

Figure 4.9: Droplets on SU-8 textured surfaces a. before and b. after OTS treatment.

Prior to impregnation, contact angle measurements were taken on surfaces before and after OTS treatment to check the effectiveness of the hydrophobic coating (Figure 4.9). Samples with greater linear lubricant fraction l_f and thus lower Cassie fraction φ_s and Wenzel roughness r_w generally showed higher values of static contact angles due to the reduced contact with the droplets. For example, surfaces with linear lubricant fraction of 0.9 consist of 10 μm by 10 μm pillars with pillar gaps of 90μm between them and

Table 4.2: Static contact angles before and after OTS treatment for surfaces with different linear lubricant fraction l_f. Stand deviation are calculated from three separate measurements.

Linear lubricant fraction/l_f	Contact angle before OTS/$^\circ$	Contact angle after OTS/$^\circ$
0.1	96 ± 5	122 ± 4
0.2	135 ± 3	142 ± 3
0.3	128 ± 2	145 ± 2
0.4	130 ± 2	136 ± 1
0.5	125 ± 3	143 ± 2
0.6	115 ± 5	128 ± 2
0.7	113 ± 1	148 ± 1
0.8	105 ± 4	155 ± 1
0.9	92 ± 4	156 ± 2

droplets bridge across the top of the pillars; whereas surfaces with $l_f = 0.1$ are covered in large, densely packed (90 μm by 90 μm) pillars, almost resembling a flat surface.

Contact angle measurements showed a consistent increase after the hydrophobic coating was applied, confirming the successful deposition of the OTS layer. Subsequently, a dip coating process was carried out to impregnate all of the surfaces with a lubricating silicone oil. Although all surfaces exhibited hydrophobic characteristics (water contact angle generally $> 120^\circ$) and possessed all necessary physical features to allow lubricant impregnation, it was not clear at this point whether they would retain the lubricant layer when droplets are placed on them (Figure 2.27). To test the effectiveness of the lubricant impregnated surfaces as SLIPS in supporting highly mobile droplets, sliding angle measurements of 1 mm diameter water droplets were carried out.

Figure 4.10 shows images of surfaces with different lubricant fractions when a droplet is placed on top. In all cases, the majority of the droplets' profile adopt a shape of a spherical cap, but it is distorted by a small wetting ridge close to the surface. Sliding angle was very low for all surfaces having $l_f = 0.1$, 0.2, 0.3, 0.4, 0.5, 0.6, 0.7, 0.8, 0.9 and were measured to be typically $\approx 1^\circ$ with some as low as 0.3°. Therefore, they were considered ideal SLIPS with highly mobile contact lines and were used in the subsequent evaporation experiments. In certain cases, some of the fabricated samples did not exhibit the same low hysteresis characteristics and were therefore classified as non-SLIPS. For example, three samples from one batch of samples with $l_f = 0.1$, 0.4, 0.6 showed significant values of sliding angle, ($25.3^\circ \pm 0.6^\circ$), ($29.8^\circ \pm 4.7^\circ$) and

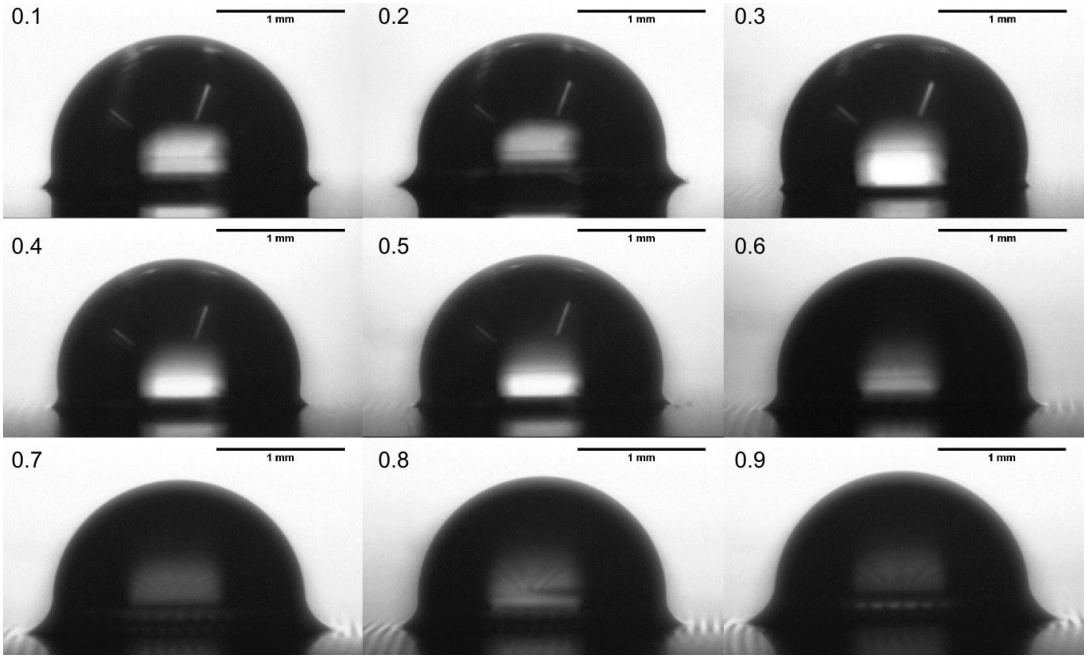

Figure 4.10: Water droplets on surfaces with different linear lubricant fractions: l_f = 0.1 - 0.9.

(16.6 $^\circ$ $\pm$ 3.5°), respectively. As described in Section 3.1.2, the OTS functionalisation process requires delicate procedures is more difficult to achieve on an SU-8 surface than surfaces such as plain silicon and glass, it is therefore more prone to failure which could have caused the droplets to come into contact with the top of the features or even penetrating into the pillar gaps.

Table 4.3: Sliding angle of water droplets for surfaces with different linear lubricant fraction, l_f, and average sliding angles from three measurements and standard deviations.

Linear lubricant fraction/l_f	Sliding angle/$^\circ$
0.1	0.9 $\pm$ 0.1
0.2	1.3 $\pm$ 0.1
0.3	0.6 $\pm$ 0.1
0.4	0.7 $\pm$ 0.1
0.5	0.7 $\pm$ 0.1
0.6	0.3 $\pm$ 0.1
0.7	0.3 $\pm$ 0.1
0.8	0.4 $\pm$ 0.1
0.9	0.5 $\pm$ 0.1

4.4 Theoretical Development

4.4.1 Model Fundamentals

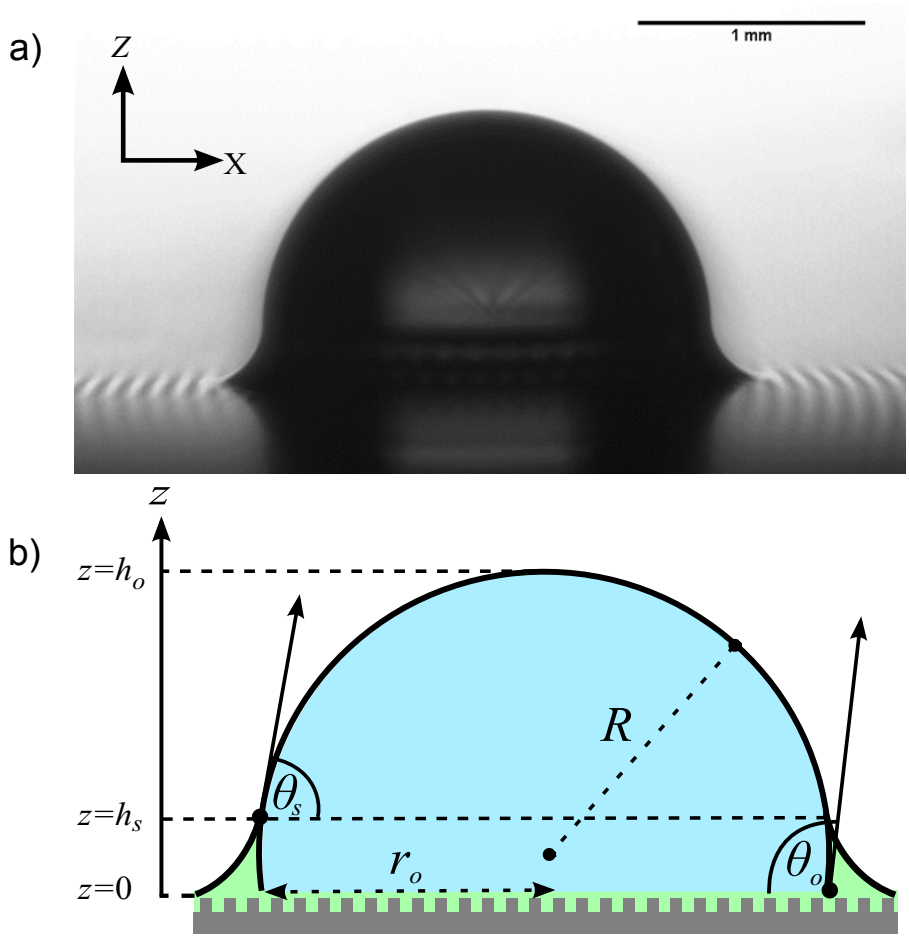

Figure 4.11: a. A droplet on a lubricant-impregnated surface b. cross section schematic of the droplet on a lubricant impregnated textured surface showing defined parameters: apparent contact angles, θ_o and θ_s, drop radius, R and drop radius, r_o.

In previous studies of evaporation of sessile droplets, measurements of the droplet's contact angle and the contact or spherical radius were used to determine the droplet shape and volume (Figure 3.8) [119–124, 127]. As Figure 4.3d shows, a droplet on a SLIPS is deposited onto a layer of liquid rather than into direct contact with the solid, the majority of its shape is described as a section of a spherical cap in the same manner as a sessile droplet resting on a solid surface, but defining and extracting a contact angle at the edge of the droplet is no longer a straight forward task. At the intersection between the infusing liquid, the water, and the surrounding air, the three interfacial forces balance often represented by a Neumann triangle at the base of the droplet and

lead to a wetting ridge around the droplet. The balance of interfacial forces determine to what extent the wetting ridge would rise, this height can be significant with respect to the overall height of the droplet and the evaporation surface area through which water molecules may diffuse through. The evaporation of the droplet at its base is hampered by a lubricant "skirt" created by the effect of a wetting ridge. It was therefore necessary for this to be taken into account in developing a model to describe the evaporation on SLIPS.

Figure 4.11a shows a droplet on a SLIPS. Its size is much less than the capillary length of the evaporating liquid, $\kappa^{-1} = (\gamma_{LV}/\rho g)^{1/2}$, where γ_{LV} is the surface tension, ρ is the density of the liquid, and g is the acceleration due to gravity [1]. The lack of direct contact between the droplet and the surface means that the idea of a contact angle must be redefined. Because of small size, the assumption that the droplet adopts a spherical cap shape remains valid; which in turn allows an apparent contact angle to be defined by extrapolating the existing spherical cap shape using the method described in Section 3.1.5. For a liquid droplet with given volume, there are therefore well-defined geometric parameters which can be measured from side profile images. These include the spherical radius R, apparent contact radius r_o, apparent contact angle θ_o, and apex height h_o above the contact surface (Figure 4.11b). In analysing an image of a spherical cap with a give spherical radius using a side profile view, the vertical placement, in the z direction, of the position of the contact surface alters the deduced volume $V(z)$, apparent contact radius $r(z)$, apparent contact angle $\theta(z)$, and apex height $h(z)$ and is therefore an important consideration. Geometrically, these parameters are related by

$$r(z) = R\sin\theta(z) \tag{4.3}$$

and

$$V(z) = \frac{\pi\beta(\theta)R^3}{3} \tag{4.4}$$

where

$$\begin{aligned}\beta(\theta) &= 2 - 3\cos\theta(z) + \cos^3\theta(z) \\ &= (1 - \cos\theta(z))^2(2 + \cos\theta(z))\end{aligned} \tag{4.5}$$

The height of the spherical cap above the position z is given by

$$h(z) = R(1 - \cos\theta(z)) \qquad \text{and} \qquad h(z) = r(z)\tan\frac{\theta(z)}{2} \tag{4.6}$$

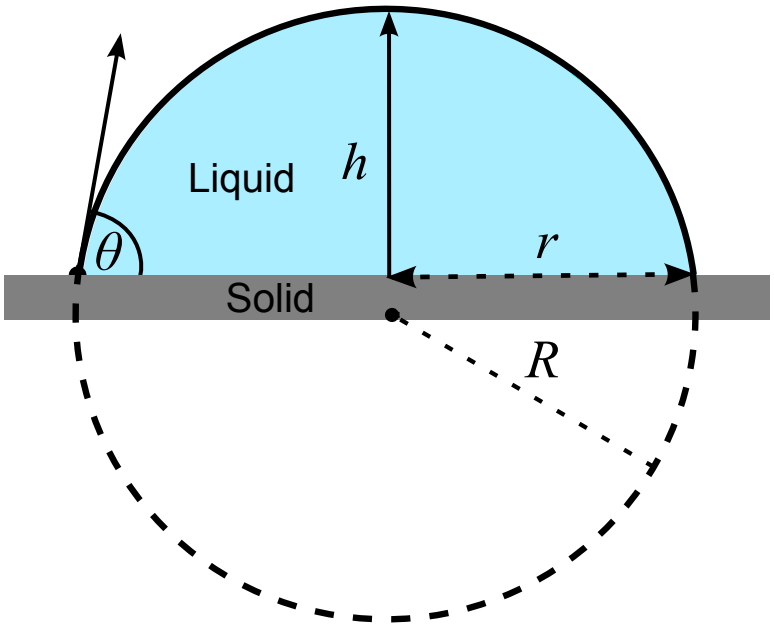

Figure 4.12: A sessile drop on a substrate: A spherical cap drop shape can be characterized by four different parameters.

In general, the rate for diffusion limited loss of liquid volume by evaporation through a liquid-vapour interface is

$$\frac{dV}{dt} = -\frac{D}{\rho}\int \nabla C \cdot dS \tag{4.7}$$

where D is the diffusion coefficient of the vapour, ρ is the density of the liquid, ∇C is the concentration gradient and its integral is taken over the surface of the spherical cap [118]. Combining the geometrical assumptions with Equation 4.7 and a concentration gradient model allows data on the evaporation of sessile droplets to be analysed.

4.4.2 General Model for Diffusion-Limited Evaporation from Lubricant-Impregnated Surfaces

One particularly simple approach used by Rowan *et al.* [122] has been to approximate the concentration gradient of vapour to be radially outward and equal to

$$(c_s - c_\infty)/R \tag{4.8}$$

where c_s is the vapour concentration at the liquid-vapour interface of the droplet and is assumed to be its saturation value, c_∞ is the concentration of vapour far removed the surface of the droplet which is assumed to be its ambient value. This approximation to the concentration gradient is intuitive and accurate for contact angles close to 90°.

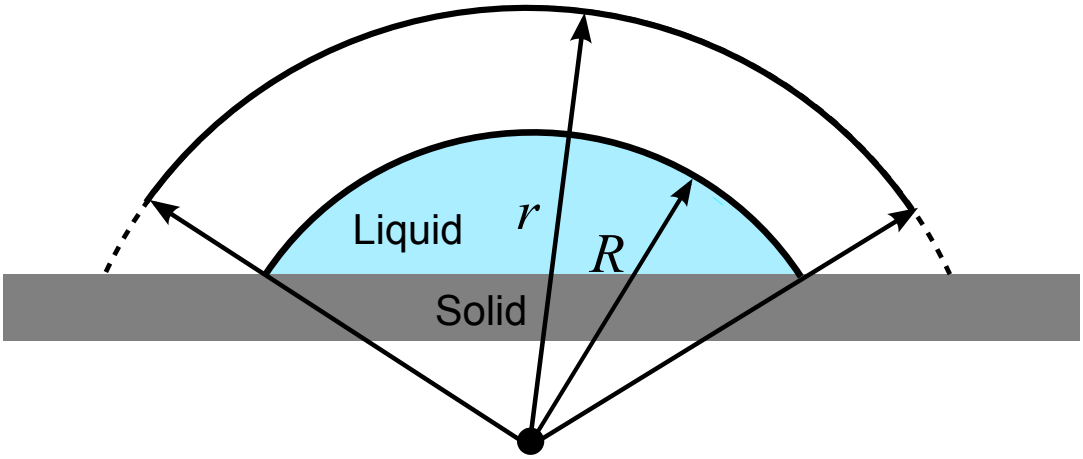

Figure 4.13: Concentration profile as modelled by Rowan *et al.* (Solid line at the distance of r and Shanahan and coworkers (Dashed line and the solid line at r.)

However, it neglects the contact angle dependence that is introduced by the presence of the substrate which restricts the available space into which vapour can diffuse. With this approximation, Equation 4.7 gives the evaporation rate to be,

$$\frac{dV}{dt} = -\lambda h_o \tag{4.9}$$

where $\lambda = 2\pi D(c_s - c_\infty)/\rho$ and $h_o = h(z = 0)$

In the case of the droplet on a lubricant-impregnated surface, the bottom of the droplet is surrounding by a layer of the non-volatile lubricating liquid (Figure 4.11). The droplet's liquid-vapour interfacial area is reduced due to the presence of a "skirt" of

lubricating liquid that rises to a height h_s, above the surface features. The presence of "skirt" modifies the liquid-vapour surface area, $A_{LV} = 2\pi R^2(1 - \cos\theta(z)) = 2\pi Rh(z)$, through which evaporation occurs which in turn modifies the rate of evaporation of the droplet as follows,

$$\frac{dV}{dt} = -\lambda h_o\left[1 - \frac{h_s}{h_o}\right] \tag{4.10}$$

Because of the existence of a skirt of lubricating liquid surrounding the base of the droplet, the evaporation rate can therefore be expected to be reduced by a factor of $[1 - h_s/h_o]$ compared to a droplet of identical volume and having the equivalent contact angle on a surface without a layer of lubricating liquid.

The evaporation rate can be re-written using the droplet volume and the contact angle, $\theta_s = \theta(z = h_s)$, deduced from the spherical cap profile, but measured at the top of the lubricant skirt,

$$\frac{dV}{dt} = -\lambda R(1 - \cos\theta_s) = -\lambda\left[\frac{3V}{\pi\beta(\theta_o}\right]^{1/3}(1 - \cos\theta_s) \tag{4.11}$$

where the spherical radius R has been replaced by the droplet volume and the contact angle, $\theta_o = \theta(z = 0)$, deduced at the top of the solid surface structure from the spherical cap profile, Assuming both the contact angle at the solid surface and the top of the lubricant skirt, as deduced from the spherical cap profile, are approximately constant, as can be expected on a SLIPS surface with no contact line pinning, this can be integrated in time, t, to give,

$$V(t)^{2/3} \approx V_i^{2/3} - \frac{2\lambda}{3}\left[\frac{3}{\pi\beta(\theta_o)}\right]^{1/3}(1 - \cos\theta_s)t \tag{4.12}$$

where V_i is the initial droplet volume and $V(t)$ is the volume contained within the spherical cap shape down to the top of the surface features at $z = 0$ at any subsequent time t. The volume therefore reduces following a $t^{3/2}$ power law and this gives a linear time dependence for the deduced solid-liquid contact area $A_{SL} = \pi r_o^2$, where $r_o = r(z = 0)$,

$$r_o^2 \approx r_i^2 - \frac{2\lambda t \sin^2\theta_o(1-\cos\theta_s)}{\pi\beta(\theta_o)} = r_i^2 - \frac{2\lambda t \sin^2\theta_o}{\pi(1-\cos\theta_o)(2+\cos\theta_o)}\left(\frac{1-\cos\theta_s}{1-\cos\theta_o}\right) \quad (4.13)$$

This is the same as previously reported by Erbil *et al.* for the constant contact angle mode of evaporation [129], but with a correction factor due to the lubricant skirt. The correction can be written using a Taylor series expansion as,

$$\left(\frac{1-\cos\theta_s}{1-\cos\theta_o}\right) \approx 1 - \frac{\Delta\theta\sin\theta_o}{1-\cos\theta_o} \quad (4.14)$$

where $\Delta\theta = \theta_s - \theta_o$ is the difference in contact angles deduced from the spherical cap profile by measuring at the top of the lubricant skirt and at the top of the solid surface features.

In previous work on sessile droplets evaporating in a constant contact angle mode, a function $f(\theta)$ was introduced by Erbil *et al.* in order to take account in a common notational format of the dependence of the concentration gradient of vapour [129], between the surface of droplet and far from the droplet, on the contact angle arising from different models, this notation was also used in studies of droplet evaporating from superhydrophobic surfaces [127]. In this notation, Equation 4.9 becomes,

$$\frac{dV}{dt} = -2\lambda R f(\theta) \quad (4.15)$$

where the simple approximation $(c_\infty - c_s)/R$ used by Rowan *et al.*, to the concentration gradient that ignores any variation with contact angle gives [122],

$$f(\theta)_{\text{Rowan et al.}} = \frac{1-\cos\theta}{2} \quad (4.16)$$

Bourgès-Monnier and Shanahan also assumed the diffusion of liquid vapour from the droplet to be radially outward (Figure 4.13) [121]. They considered a spherical cap shell of surface area $A_{LV} = f(R', \theta')$ using a coordinate system (R', θ') based on the center of the drop, their approximation to the concentration gradient therefore began with

$$\frac{dc}{dR} = -\frac{k}{A_{LV}} = \frac{k}{2\pi R'^2(1-\cos\theta')} \tag{4.17}$$

where k is a constant. Using the resultant concentration gradient, they obtained an improved self-consistent model for evaporation of small sessile droplets and it is equivalent to,

$$f(\theta)_{\text{Shanahan et al.}} = \frac{-\cos\theta}{2\log_e(1-\cos\theta)} \tag{4.18}$$

This solution is remarkably consistent with the exact solution of Picknett and Bexon except for small angles where it has a singularity and diverges. For $f(\theta)$, the physical origin of the difference between Equation 4.16 and 4.18 can be most clearly seen for the limiting case of a completely spherical drop where $\theta = 180°$. In this case, Equation 4.16 accurately reduces to the known result for the evaporation of a fully spherical drop in free space. However, in the case where a sessile droplet having a contact angle of 180° is in contact with a surface, Picknett and Bexon's solution (Equation 4.21) is more accurately approximated by Equation 4.18 than Equation 4.16. For $\theta = 180°$, Equation 4.21 gives a value of 0.694 while Equation 4.18 and Equation 4.16 give 0.721 and 1, respectively. The difference between Picknett and Bexon's exact solution and the two approximations decreases as the angle reduces from 180°. All three solutions become numerically identical at 90°. Below this, the three solutions start to diverge once again and Equation 4.18 becomes the more accurate approximation.

More recently, Stauber *et al.* studied the evaporation of droplets on strongly hydrophobic substrates with a focus on the constant contact angle and constant contact radius modes, their formulas are equivalent to [130],

$$f(\theta)_{\text{Stauber et al.}} = \frac{\sin\theta g(\theta)}{4(1+\cos\theta)^2} \tag{4.19}$$

where

$$\frac{\theta g(\theta)}{(1+\cos\theta)^2} = \tan\left(\frac{\theta}{2}\right) + \int_0^\infty \frac{\cosh^2(\theta\tau)}{\sinh(2\pi\tau)}\tanh[\tau(\pi-\theta)]d\tau \tag{4.20}$$

Using the analogy between the diffusive flux and electrostatic potential, Picknett

and Bexon derived a exact solution for Equation 4.7 for determining the evaporation rate of sessile drop and they gave a numerically accurate polynomial interpolation for $f(\theta)$ [118],

$$f(\theta)_{\text{Picknett and Bexon}} \begin{cases} \frac{1}{2}(0.6366\theta + 0.09591\theta^2 - 0.06144\theta^3) & 0^\circ < \theta < 10^\circ \\ \frac{1}{2}(0.00008957 + 0.6333\theta + 0.116\theta^2 & 10^\circ < \theta < 180^\circ \\ \quad -0.08878\theta^3 + 0.01033\theta^4) & \end{cases} \tag{4.21}$$

where θ in the series in in radians.

Following the earlier approach of using the apparent contact angle at height h_s of the lubricant skirt above the surface structure to define the droplet's liquid-vapour interfacial area through which evaporation occurs, Equation 4.15 becomes

$$\frac{dV}{dt} = -2\lambda R f(\theta_s) \tag{4.22}$$

Writing the spherical cap radius in terms of the drop volume and apparent contact angle θ_o at $z = 0$ and assuming both θ_o and θ_s are approximately constant, the volume dependence on time can be found,

$$V(t)^{2/3} \approx V_i^{2/3} - \frac{4\lambda}{3}\left[\frac{3}{\pi\beta(\theta_o)}\right]^{1/3} f(\theta_s)t \tag{4.23}$$

where V_i is the droplet's initial volume at $t = 0$. In terms of the apparent contact radius at $z = 0$, this can be re-written as,

$$\begin{aligned} r_0^2 &\approx r_i^2 - \frac{4\lambda t \sin^2\theta_o f(\theta_s)}{\pi\beta(\theta_o)} \\ &= r_i^2 - \frac{2\lambda t \sin^2\theta_o}{\pi(1-\cos\theta_o)(2+\cos\theta_o)}\left(\frac{2f(\theta_s)}{1-\cos\theta_o}\right) \end{aligned} \tag{4.24}$$

where r_i is the droplet's initial apparent contact radius.

4.5 Droplet Evaporation Experiments

All droplet evaporation experiments were carried out in constant relative humidity (30 - 50)% and at room temperature (20 - 30 °C). Although the relative humidity or the temperature were not controlled, an environmental chamber was constructed to minimise the variations in both and protect from air currents within the laboratory.

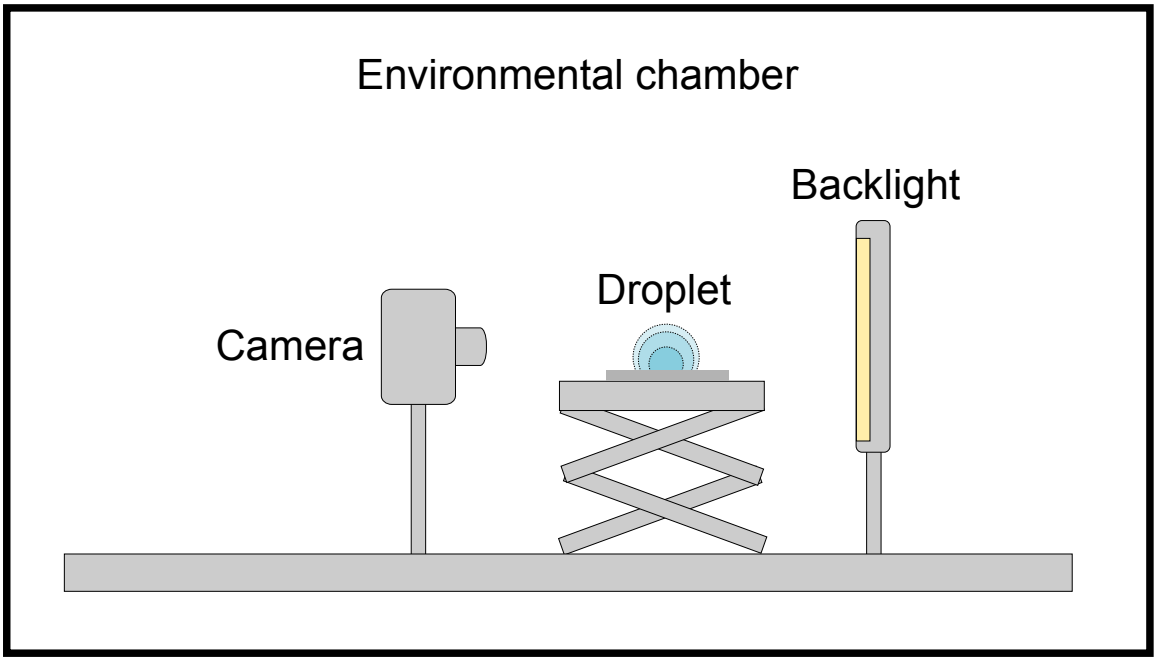

Figure 4.14: Experimental set up for evaporation experiments.

An adjustable stage was placed inside the chamber along with a diffused back light and a CCD camera. With the droplets being highly mobile and therefore extremely sensitive to any inclination, the stage was levelled before each experiment to avoid any unwanted movement during evaporation. Small droplets of water (2.5 ± 0.2 μL) having sizes below the capillary length of water were used in the evaporation experiments to avoid flattening of the droplets due to gravity. This way, droplets will adopt the spherical cap shape and their profiles can be analysed to obtain values for apparent contact angle, apparent contact radius and subsequently the diffusion coefficients. Droplets were deposited using a Proline Plus (2 - 20 μL) pipette on each surface. They were allowed to freely evaporate in a monitored enclosed environment. Images of evaporating droplets were taken at 30 s intervals for a maximum of 2500 s.

Temperature and humidity inside the chamber at any give moment was monitored and recorded by a DHT22 temperature and humidity sensor (Aosong Electronics) and

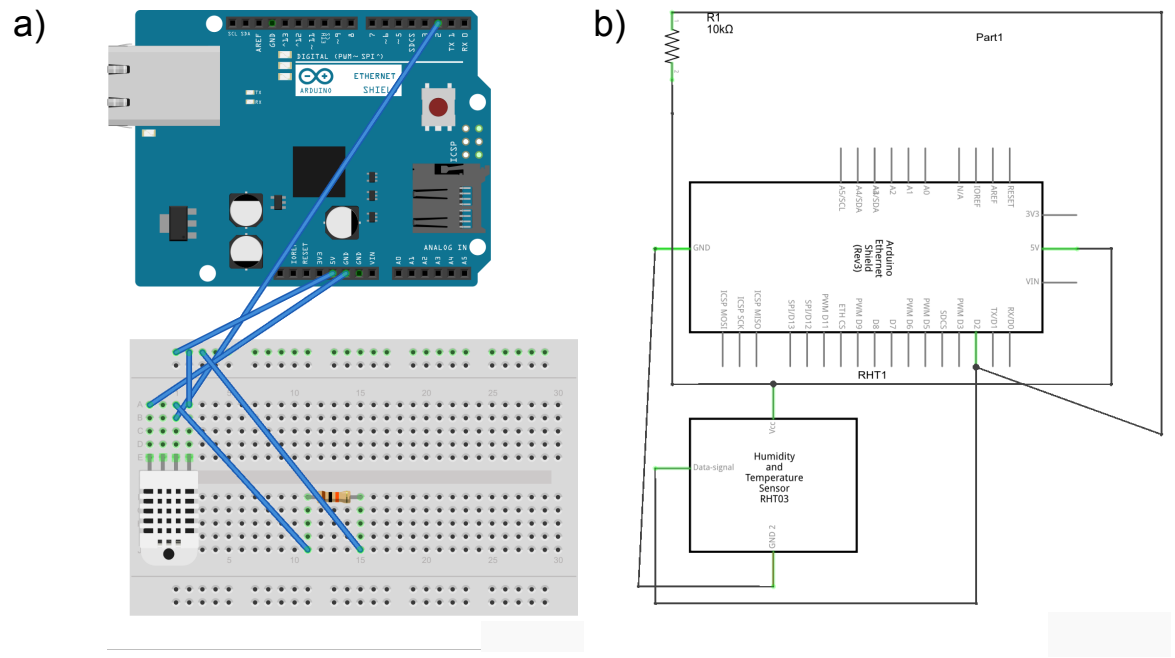

Figure 4.15: a. Configuration of the humidity & temperature sensor b. circuit diagram of the humidity & temperature sensor.

connected to a LabView program via an Arduino microcontroller. The microcontroller combined with the LabView program allowed the droplets to be imaged at specific time-lapse interval and stamped with the values of date, time, temperature and relative humidity (RH) for post-experiment analysis (Figure 4.15). Using the captured images, apparent contact angles (both above the wetting skirt θ_s and above the surface features θ_o) and apparent contact base diameter were obtained which in turn allowed the liquid-vapour surface area, spherical radius and hydrostatic pressure (using Young-Laplace equation) as a function of time to be calculated. Axial symmetry was assumed in the evaporation process and used in image processing calculations. This assumption was expected to be obeyed for a SLIPS where contact line pinning is minimised, in contrast to the case of direct droplet-solid contact. Top view images were taken to confirm this (Figure 4.16). Side view images obtained through time-lapse photography also allowed values of the height of the wetting ridge h_s and the overall droplet height h_o to be extracted using the method as described in Section 3.1.5.

All experiments were repeated three times to check reproducibility. Furthermore, images from each experiment were analysed using the same MATLAB program three times to minimise any inherent discrepancy give by the program and the results showed a variation of $< 4\%$. The average values were subsequently used in the calculations of

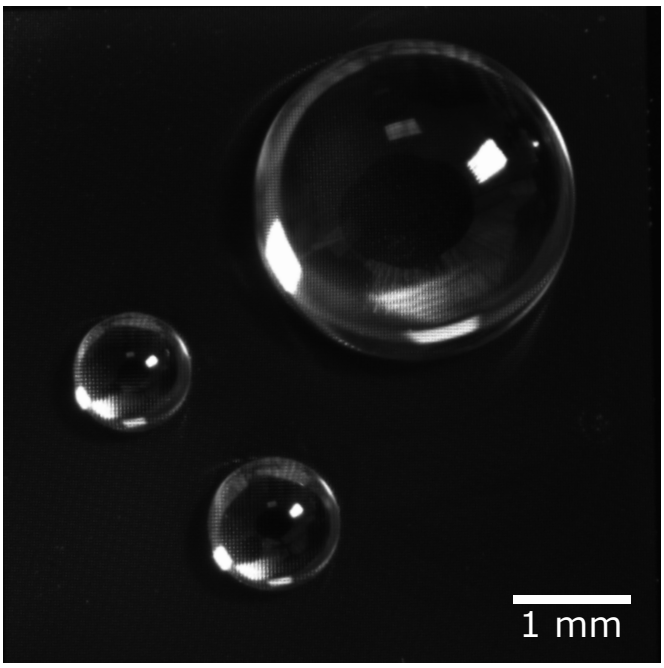

Figure 4.16: Top view image of droplets placed on a lubricant-impregnated surface with lubricant fraction $l_f = 0.2$, showing axial symmetry.

diffusion coefficients.

4.6 Results and Discussion

4.6.1 Constant Contact Angle Mode Evaporation

On surfaces with low sliding angles and therefore classified as SLIPS, droplets were expected to evaporate with constant apparent contact angle and their contact lines to move without any hindrance due to the lack of direct contact with the underlying solid surface. Captured images showed that droplets evaporating on SLIPS maintained overall spherical cap shapes throughout the evaporation process with wetting ridges close to the substrate. Visually the apparent contact angle, defined by the intersection of the spherical cap droplet profile, and the baseline appears to be above 90° and constant during evaporation as shown in Figure 4.17. Post-analysis data revealed that the evaporation of water droplets on a SLIPS proceeds with a steadily decreasing droplet volume and apparent contact area.

Side-view images of the evaporating droplets also allowed the change in the apparent contact radius with time to be measured. On a SLIPS, due to the lack of direct contact

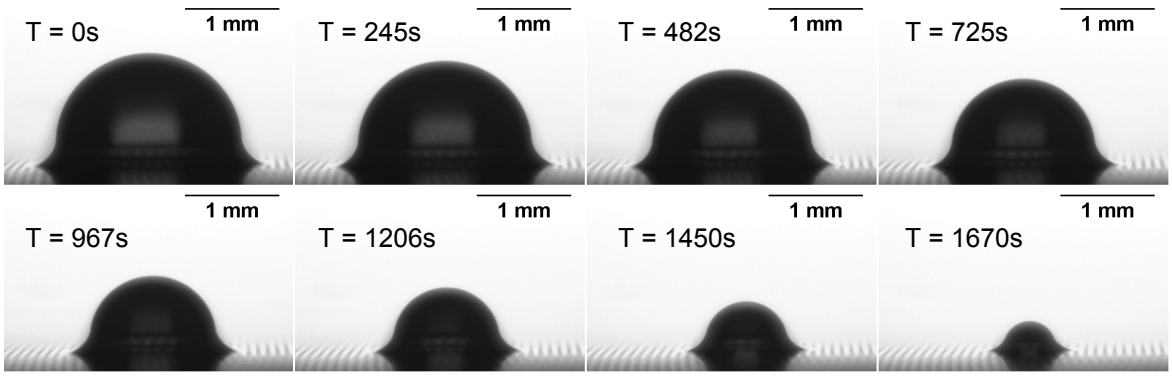

Figure 4.17: Images of a 2.5 μL droplet evaporating on a lubricant-impregnated surface ($l_f = 0.7$) with constant contact angle.

with the surface and therefore no hindrance to the motion of the contact line, droplets' apparent contact radius should display a linear decrease with time as they evaporate. Plots of r_o^2 as a function of time for the samples classified as SLIPS using the criteria of low sliding angle values show strong linear relationships over the entire range of the evaporation process (Figure 4.18). This strong linear relationship can therefore serve as evidence, in addition to the observed constancy of the apparent contact angle, that droplets are undergoing contact angle evaporation within the context of the diffusion limited evaporation model.

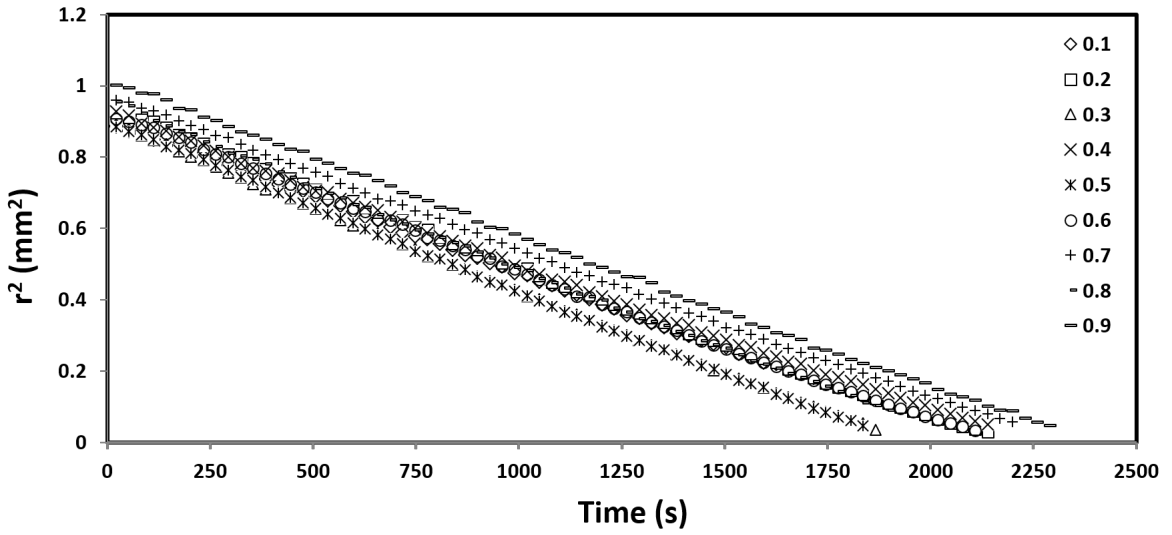

Figure 4.18: Linearity of r_o^2 during the evaporation of droplets on samples with lubricant fraction $l_f = 0.1$ - 0.9 (See legends).

To provide further confidence in the r_o^2 versus time relationship and to test the validity of the correction factor $(1 - \cos\theta_o)/(2f_{\mathrm{PB}}(\theta_s))$ to the existing model of diffusion limited evaporation of sessile droplets, the diffusions coefficients of the droplets were

calculated using the gradients, m, of the data in Figure 4.18, which, by rearranging Equation 4.24, equals to,

$$m = \frac{2\lambda \sin^2 \theta_o}{\pi(1 - \cos\theta_o)(2 + \cos\theta_o)} \left(\frac{2f(\theta_s)}{1 - \cos\theta_o} \right) \tag{4.25}$$

substituting in λ, it becomes,

$$m = \frac{4D(c_s - c_\infty) \sin^2 \theta_o}{\pi\rho(1 - \cos\theta_o)(2 + \cos\theta_o)} \left(\frac{2f(\theta_s)}{1 - \cos\theta_o} \right) \tag{4.26}$$

and D therefore becomes,

$$D = \frac{m\rho(1 - \cos\theta_o)(2 + \cos\theta_o)}{4(c_s - c_\infty) \sin^2 \theta_o} \left(\frac{1 - \cos\theta_o}{2f(\theta_s)} \right) \tag{4.27}$$

Experimentally, θ_o and θ_s were observed to have remained constant throughout the evaporation process. For the purpose of calculating the diffusion coefficients, they were measured at the start of each evaporation experiment. Complete saturation of air was assumed at the droplet-vapour interface and the value of the actual vapour density in the surrounding atmosphere was calculated using the relationship,

$$\text{Relative humidity} = \frac{\text{Actual vapour density}}{\text{Saturation vapour density}} \times 100\% \tag{4.28}$$

where c_∞ is the actual vapour density and the values of the saturation vapour density c_s were obtained from *Kaye and Laby Tables of Physical and Chemical Constants* [131].

Table 4.4: Mass of water (in grams) contained in a cubic metre (m^3) of saturated air at a total pressure of 1013.25 mbar (atmospheric).

Temperature/ °C	0	1	2	3	4	5	6	7	8	9
0	4.87	5.22	5.58	5.97	6.39	6.83	7.29	7.78	8.31	8.86
10	9.44	10.06	10.71	11.39	12.12	12.88	13.69	14.54	15.43	16.38
20	17.37	18.41	19.51	20.66	21.87	23.14	24.48	25.88	27.35	28.89
30	30.50	32.19	33.96	35.81	37.75	39.78	41.90	44.11	46.42	48.84

Table 4.4 shows the values of saturation vapour density for temperature values to the nearest integer. In order to obtain more accurate values for c_s which should in turn allow better estimates of diffusion coefficients to be obtained, the values in Table 4.4 were fitted with a polynomial function.

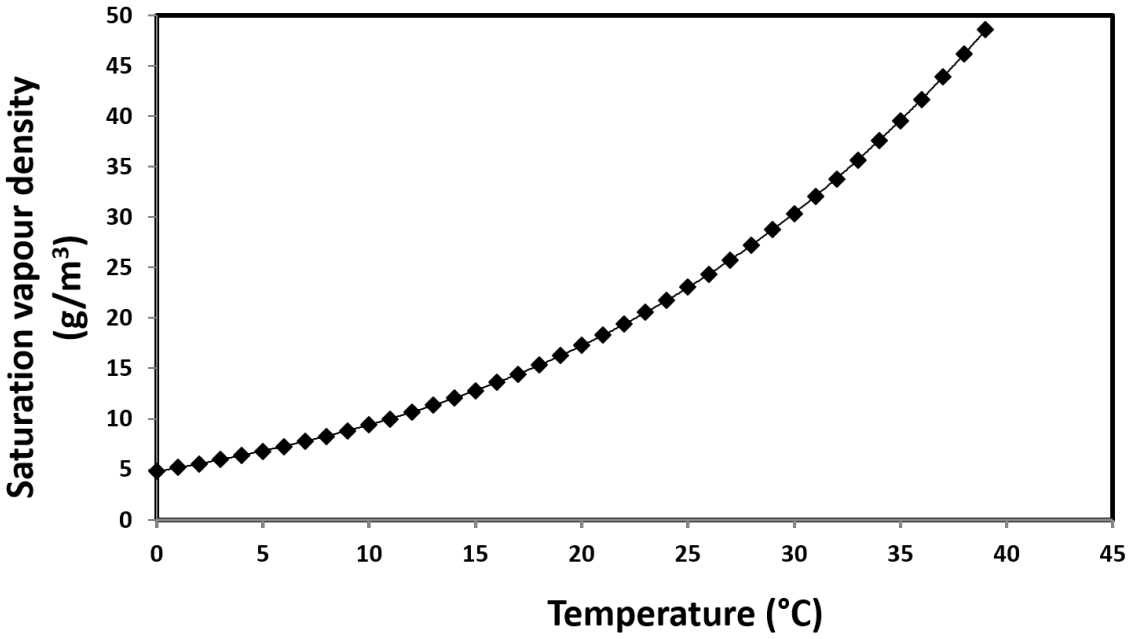

Figure 4.19: Saturation vapour density as a function of temperature.

The below relationship between c_s and temperature T was obtained,

$$\textbf{Saturation vapour density} = 0.0004T^3 + 0.0053T^2 + 0.3759T + 4.7736 \quad (4.29)$$

Equation 4.29 was assumed to be obeyed for temperature values beyond 39°C. At this point, the difference between the saturation vapour density and the actual vapour density ($c_s - c_\infty$) can be calculated using Equation 4.28 and 4.29 and the values of relative humidity (RH). Combined with slope m from the data of r_o^2 vs t, the diffusion coefficients of water into air for droplets on SLIPS can be estimated. For example, data obtained from the experiment in which droplets evaporated on the surface with the lubricant fraction l_f of 0.9, the slope is $(4.282 \pm 0.012) \times 10^{-4}$ mm^2 s^{-1}, θ_o and θ_s were measured at $101.1 \pm 1.0^\circ$ and $84.4 \pm 1.0^\circ$, respectively (all of which are averaged values from three separate measurements standard deivations are presented). Using these values, the diffusion coefficient is calculated to be $D = (2.39 \pm 0.20)\ \times 10^{-5}$ m^2 s^{-1}. To check the level of agreement between the values calculated using the modified model with reference data, values of D were obtained from the *CRC Handbook of Chemistry and Physics* for diffusion of water vapour into air (Table 4.5) [132],

The correlation between the diffusion coefficients and temperature from the reference

Table 4.5: Diffusion coefficients D for water vapour into air.

Temperature/°C	D_{Lit}/cm^2 s^{-1}
293.15	0.242
373.15	0.399
473.15	0.638
573.15	0.873
673.15	1.135

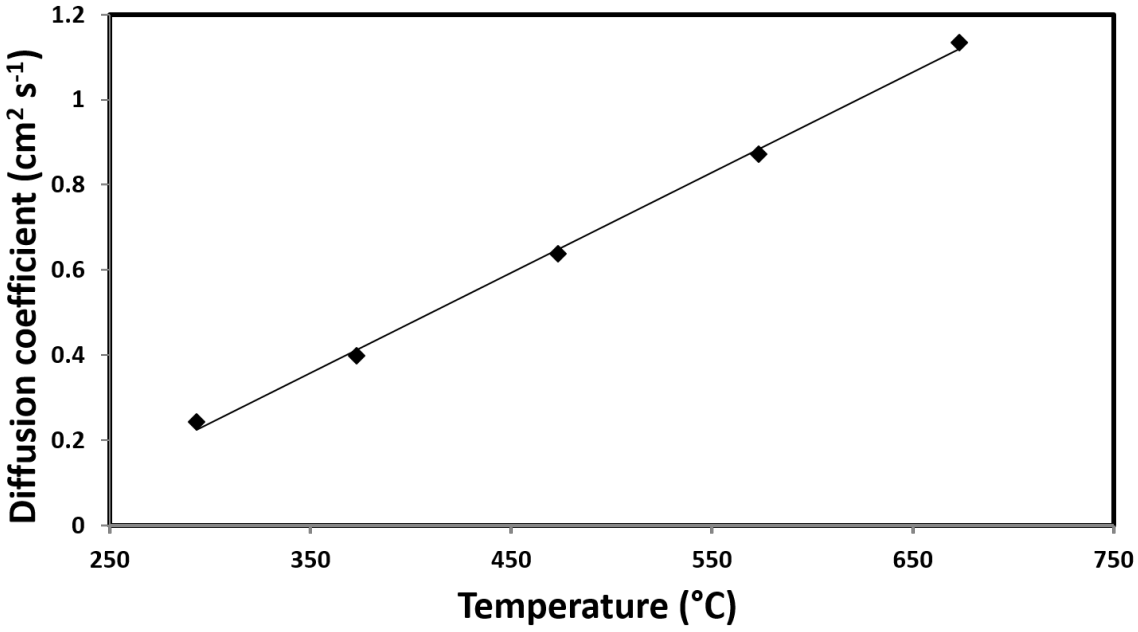

Figure 4.20: Reference data of diffusion coefficients of water vapour into air as a function of temperature from Table 4.5.

data was assumed to hold for temperature values below 293.15K. A linear fit to the data gave the following relationship (Figure 4.20),

$$D = 0.0024T - 0.4677 \tag{4.30}$$

where D is the diffusion coefficient in cm^2 s^{-1} and T is the temperature in kelvin. Using this equation, reference values diffusion coefficients D_{lit} were obtained for their experimental counterparts with the same temperature values. Table 4.6 shows the calculated values of the diffusion coefficient, D, for all droplets evaporating from surfaces classified as SLIPS by low values of sliding angles.

The error in the calculated values of D were estimated using the general equation for the propagation of error,

Table 4.6: Estimates of Diffusion Coefficients for Water into Air for Droplets on SLIPS

Lubricant fraction l_f	RH/%	T/°C	Δ_c/g m^{-3}	θ_o/°	θ_s/°	$h_s/h_{o(i)}$/%	$D/\times10^{-5}$m^{2}s^{-1}	$D_o/\times10^{-5}$m^{2}s^{-1}	D_o/D/%	D(lit)/$\times10^{-5}$m^{2}s^{-1}
0.1	48.3	26.2	13.16	105.5	86.5	13.7	2.44 ± 0.19	2.10 ± 0.19	86	2.50
0.2	34.0	22.2	12.81	98.4	90.5	13.4	2.13 ± 0.18	1.96 ± 0.16	92	2.41
0.3	34.2	22.2	12.76	102.9	97.6	6.7	2.42 ± 0.20	2.26 ± 0.19	93	2.41
0.4	47.2	26.4	13.59	107.1	87.3	16.7	2.46 ± 0.19	2.11 ± 0.19	86	2.50
0.5	34.2	22.5	12.76	103.2	94.7	8.5	2.50 ± 0.21	2.28 ± 0.19	91	2.41
0.6	46.9	26.7	13.91	105.6	88.3	13.1	2.36 ± 0.18	2.07 ± 0.18	88	2.52
0.7	38.0	22.8	12.74	99.3	87.0	19.3	2.21 ± 0.18	1.96 ± 0.16	89	2.43
0.8	37.9	23.3	12.76	102.8	90.6	13.6	2.50 ± 0.21	2.21 ± 0.18	88	2.43
0.9	38.4	23.3	12.66	101.1	84.4	20.5	2.39 ± 0.20	2.03 ± 0.17	85	2.43

$$\Delta D = \sqrt{\left(\frac{\partial D}{\partial m}\right)^2 \Delta m^2 + \left(\frac{\partial D}{\partial \rho}\right)^2 \Delta \rho^2 + \left(\frac{\partial D}{\partial \theta_o}\right)^2 \Delta \theta_o^2 + \left(\frac{\partial D}{\partial \theta_s}\right)^2 \Delta \theta_s^2 + \left(\frac{\partial D}{\partial f_{\mathrm{PB}}(\theta_s)}\right)^2 \Delta f_{\mathrm{PB}}(\theta_s)^2 + \left(\frac{\partial D}{\partial \Delta c}\right)^2 \Delta \Delta c^2} \tag{4.31}$$

where ΔD is the error in $D(m, \rho, \theta_o, \theta_s, f_{\mathrm{PB}}(\theta_s), \Delta c)$. Prior to the calculation of ΔD, the error in $f_{\mathrm{PB}}(\theta_s)$,$\Delta f_{\mathrm{PB}}(\theta_s)$, was calculated to be 0.0056 using the same method and an error of 1° for θ_s.

Values of D as shown in Table 4.6 show an excellent correlation, within an average differenct of 4% with the reference values, D_{lit}. In Equation 4.27, θ_s was used in $f_{\mathrm{PB}}(\theta)$ to account for the reduced liquid-vapour surface area available for evaporation due to the presence of a wetting skirt around the base of the droplet. To quantify the order of magnitude of the effect of the wetting skirt on estimates of D, D was re-calculated by replacing the θ_s in $f_{\mathrm{PB}}(\theta)$ in Equation 4.27 with θ_o. These estimates are shown as D_o in Table 4.6 and are systematically lower than the estimates of D. Values of D_o as a percentage of D are also shown in Table 4.6. On average, across all samples, D_o showed a 14% difference from the literature values, which is 10% higher than the average difference of 4% when using the model accounting for the wetting skirt. Thus far, evaporation experiments have been carried out on surfaces on which relatively small portions of the droplets' liquid-vapour surface area are covered by the wetting skirt, typically below 20% and these values are shown as $h_s/h_{o(\mathrm{i})}$ in Table 4.6. To further test the effect of the wetting skirt on diffusion-controlled evaporation would require SLIPS to be fabricated to allow droplets to have higher wetting skirts as a proportion of the initial droplet height, $h_{\mathrm{o(i)}}$.

Beside the wetting skirt, there exists another possible limitation on the estimates of the diffusion coefficient. The evaporation had been assumed to proceed across a water-air interface. However, Smith *et al.* have previously noted that once a droplet is in contact with the impregnated layer of lubricating liquid on a SLIPS, the lubricating liquid may spread and cloak the droplet with a thin, possibly a monolayer of the same liquid (Figure 2.27). If this cloaking were to occur, the previously assumed water-air

interface through which the droplet evaporates is replaced by a combined water-oil-air interface which could reduce the evaporation rate. For the lubricating liquid to spread over and cloak the droplet, its spreading coefficient, S, on water (w) in the presence of air (a), $S_{ow(a)} = \gamma_{wa} - \gamma_{ow} - \gamma_{oa}$ has to be greater than zero. $S_{ow(a)}$ would imply that the oil will not spread over and cloak the droplet. To calculate the value of S for the silicone oil used in this study, a value of 46.3 mN/m for γ_{ow} was obtained from literature and a value of 20.6 mN/m for γ_{oa} was provided by Dow Corning. Using these values and a value of 71.97 mN/m for γ_{wa}, $S_{ow(a)}$ is calculated to be 5.1 mN/m and this suggests that the silicone oil should cloak the drop. A simple experiment was carried out to check this, a droplet was silicone oil was dispensed onto a small bath of water and spread immediately into a thin film, covering the bath. Despite this cloaking, it was assumed in the analysis process that the oil either does not cloak the droplet or is sufficiently thin for its effect on the evaporation rate to be negligible.

4.6.2 Mixed Mode Evaporation

In contrast to the constant contact angle or constant contact area mode of evaporation, where either the contact angle or the contact area remain constant during evaporation whilst the other vanishes, in the mixed mode of evaporation changes in both the contact area (or equivalently the contact radius) and the contact angle occur during the evaporation process [130, 133, 134].

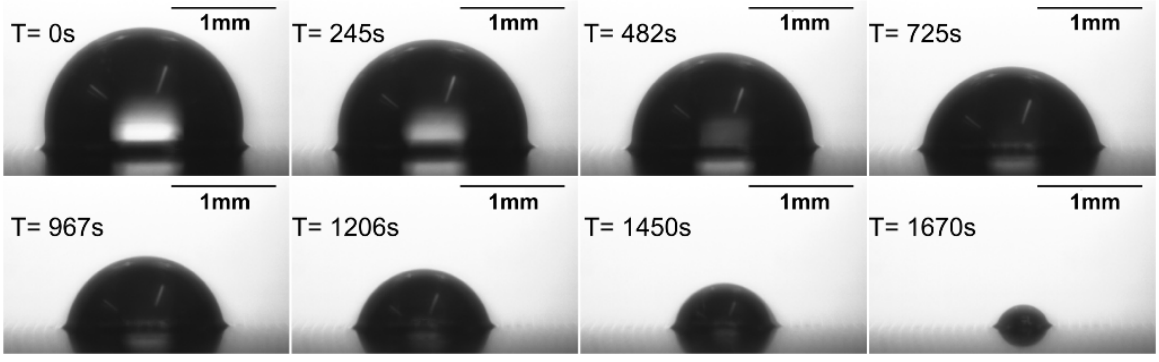

Figure 4.21: Images of a 2.5 μL droplet undergoing pinning and depinning.

Evaporation experiments were carried out on surfaces classified as non-SLIPS according to the sliding angle criteria. In these experiments, constant contact angle

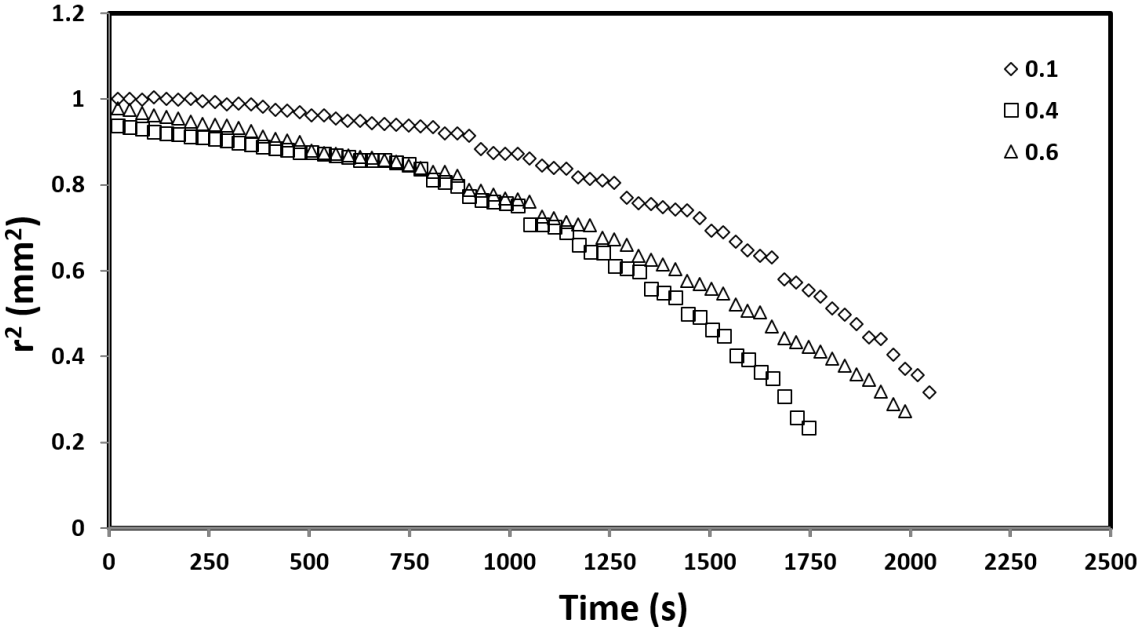

Figure 4.22: Plot of the square of the droplet's apparent contact radius as a function of time for sessile droplet evaporation on a non-SLIPS.

mode evaporation was not observed for extended times. There was, however, a brief period after the evaporation process had started that showed approximately constant contact angle evaporation. The droplet appeared to have initially evaporated with a constant contact apparent contact angle θ_o and a diminishing apparent contact radius. The droplet's contact line then appeared to get pinned and θ_o began to drop. Interestingly, the contact line appeared to have undergone a de-pinning process and showed a contraction in the apparent contact radius before becoming pinned once again. This stick-slip process repeated itself throughout the remainder of the evaporation process. Figure 4.22 shows data of the square of the apparent contact radius r_0^2 as a function of time. Unlike the evaporation of droplets on SLIPS, droplets evaporating on non-SLIPS clearly show stepping of the contact lines, which is characteristic of a stick-slip regime [62, 135, 136].

Figure 4.23 shows a portion of the data of apparent contact radius as a function of time for the surface with $l_f = 0.4$ and a sliding angle of $29.8^\circ \pm 4.7^\circ$, in which the stepping of the contact lines is highly prevalent. In this plot, r_0 is plotted as a function of time instead of r_0^2 and the data show whenever the contact lines depin the apparent contact radius would undergo a repaid drop in steps of ≈ 35 μm. This value corresponds roughly to the value 40 μm for the distance between the pillars. In order to conserve

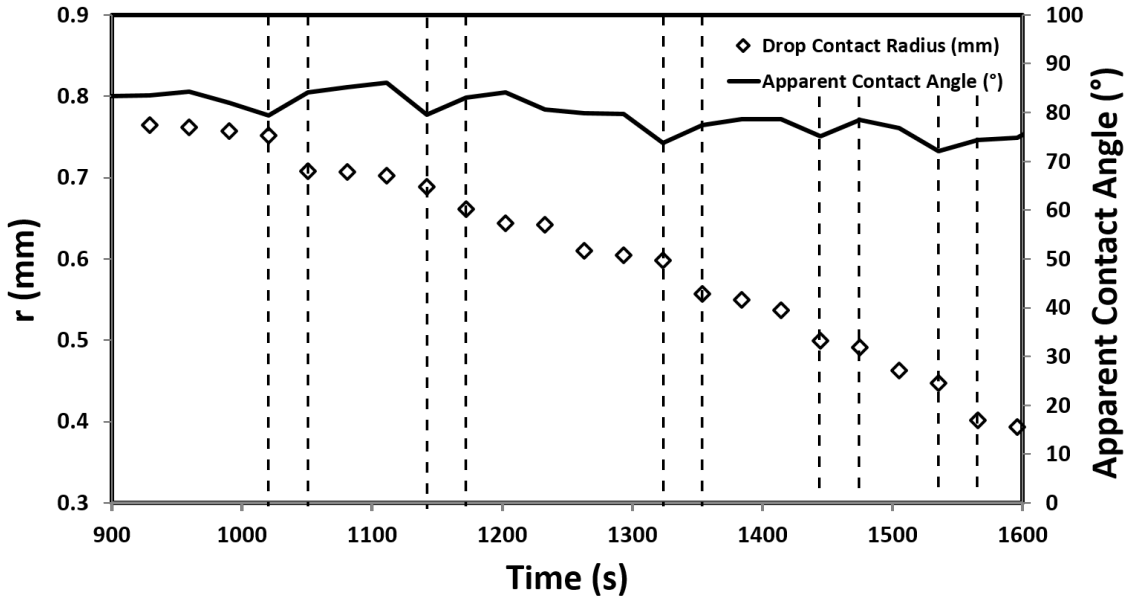

Figure 4.23: Plot of droplet's apparent contact radius and apparent contact angle during the pinning and depinning process.

volume and main the a spherical cap shape, the droplet's apparent contact angle should increase whenever a rapid drop in its apparent contact radius occurs. This was observed experimentally, and the data of apparent contact angle shows that θ_o decreases as the contact line is pinned and increases as the contact line depins (Figure 4.23).

Although constant contact angle evaporation was not observed for the entirety of the evaporation process for droplets on non-SLIPS, which was expected because, as suggested by their high sliding angles, they were sitting on the tops of the surface features. They did, however, showed a brief period of constant contact angle evaporation in the initial stage before showing a stepwise retreat. This change of behaviour could have been a result of the variations in the quality of the OTS coating and these surfaces were initially very close to becoming SLIPS, but as the droplet evaporated an increased Laplace pressure may have forced the droplet into direct contact with the solid surface at the top of the pillars. This would represent a transition from the most slippery state, in which the lurbricating liquid flows underneath the droplet and above the pillars, to a hemi-wicked Cassie-Baxter like state where the droplet rests on a combination of the solid tops of the pillars and the oil filled gas between the pillars. This transition to a more sticky state is similar to what has been observed to occur on a superhydrophobic surface when a change in the Laplace pressure causes an droplet to undergo a transition

from a Cassie-Baxter state to a Wenzel state where the droplet penetrates into the gaps between the pillars. In the SLIPS case, where the air between the pillar gaps is replaced by a lubricating liquid, a further transition to a Wenzel state where by the water in the droplet completely displaces the oil within the gaps of the texture might also be possible. This would require substantial reductions on droplet curvature to generate excess Laplace pressure necessary for displace the lubricating liquid. If substantiated, the interpretation that the water displacement of oil from the tops of the pillars could be a cause of higher sliding angles may suggest that the tilt angle method as a way to measure the sliding angle might also cause a slippery to sticky transition in some samples.

4.7 Conclusion

Previous efforts in studying evaporation of sessile droplets in true constant contact angle mode have been hampered by the contact line pinning due to the contact angle hysteresis inherent to the surfaces. A new type of surface known as SLIPS/LIS have been developed to give droplets highly mobile contact lines. They do so by introducing a layer of lubricating liquid to the space between the droplet and the surface and thus eliminating the direct contact of the droplet with the underlying surface features. The lubricating liquid is impregnated into the surface features and is not displaced when a droplet is placed on it. This type of surface allows high apparent contact angle ($\sim 100^{\circ}$) droplets with highly mobile contact lines which allows droplets to evaporate with constant apparent contact angle and a diminishing apparent contact radius. The use of the term "apparent" when describing contact angle and contact radius of droplets on SLIPS refers to their extrapolative nature. When placed on a SLIPS, a droplet adopts a spherical cap shape over the majority of their surface area but this shape is distorted near the base of the droplet by a wetting ridge. The wetting ridge is created by a balance of the three interfacial forces at the line of contact between the droplet, the lubricating liquid at the base of the droplet and the surrounding air. The lack of direct contact angle meant that it was necessary to utilise an extrapolated contact angle, and it proves possible to describe the evaporation process using all the machinery and tools

developed for sessile droplet evaporation on solid surfaces providing the effect of the wetting ridge on the evaporation rate of the droplet is accounted for. The concept that a droplet's liquid-vapour surface area available for evaporation is limited by a wetting skirt around the base of the droplet formed the basis of a modified model developed to describe the evaporation of droplets on SLIPS. This model provides linear dependence of the apparent contact surface area on time. On surfaces classified as SLIPS according to the sliding angle criteria this model has allowed the diffusion coefficients for water in air to be estimated and results showed excellent correlation, to within an average of 4% of the reference values. On lubricated textured surfaces which did not exhibit ideal low sliding angle SLIPS characteristics droplets did not demonstrate constant contact mode of evaporation throughout the entirety of the evaporation process. A brief constant contact angle period was observed during the initial stage of evaporation, followed by a stick-slip stepwise retreat of the contact line. The size of the stick-slip jumps of the apparent contact radius was measured to be roughly 35 μm, approximately corresponding to the surface texture spacing. It was suspected that this transition from an ideal SLIPS state to an oil hemi-wicked Cassie-Baxter state may have been caused by an increased excess Laplace pressure in the droplets as their spherical radius of curvature reduces, forcing the droplets to displace the lubricating liquid and thus come into direct contact with the surface texture.

Chapter Summary

This chapter focused on the evaporation of completely mobile sessile droplets on lubricant-impregnated surfaces and presented a modification to the existing theory of evaporation of sessile droplets on solid surfaces taking into account the presence of the wetting ridge. It has been shown that the presence of a lubricating liquid has made possible the study of true constant contact angle mode of evaporation.

The next chapter presents a previously unknown behaviour of droplets in wedge geometries. An improved method to create SLIPS which were used to achieve accurate manipulation of droplets in wedges with low contact angle hysteresis.

Chapter 5

Droplet Manipulation in Wedges

It was shown in Chapter 4 that micro-textured surfaces can be chemically functionalised and impregnated with a lubricating liquid to achieve low contact angle hysteresis for droplets by removing the direct contact between the droplets and the underlying solid surface. This was reflected by the lack of change in the apparent contact angle of the evaporating droplets.

This chapter explores the capillary-driven motion of droplets under confinement through the use of lubricant-impregnated surfaces and presents previously unanticipated trajectories. It will then go on to demonstrate the accurate manipulation of water droplets confined in a low-pinning wedge geometry without the need for sustained external forces.

5.1 Background of Capillary Bridges and Liquid Confinement in Wedges

The modern basis of capillary bridges studies originated as a mathematical problem set by Plateau some 140 years ago and it is known nowadays as Plateau's problem [137]. It was originally a purely mathematical problem set out to find the surface with minimal area at any given boundaries. Over the years, it has since turned into a useful tool for the description of capillary systems.

A capillary bridge is the result of the minimisation of the surface of a liquid created between two rigid bodies with an arbitrary shape. The study of capillary bridges started

when Young [5] and Laplace [18] introduced the concepts of surface tension and Laplace pressure and Delaunay calculated the solution to the profile of the capillary bridge [138]. The Laplace pressure arises from the surface tension of the liquid vapour interface and in this case refers to the difference in pressure between the liquid and vapour phase of the capillary bridges. Capillary bridges are formed when liquid droplets are brought into contact with two or more solid bodies as a way to minimise surface energy and they play an important role in our everyday life.

Depending on the shape, which depend on the wettability of the contacting surfaces, the presence of capillary bridges can either pull together or repel the solid bodies. An example of the former is the clumping of grains of sand in a sand castle on the beach. When wetted, these bridges exert attractive forces on the contacting surfaces, pulling the grains together. The earliest utilisation of such behaviour can be traced back to ancient Egypt. By pouring water onto sand, the modulus of the sand is increased by the formation of capillary bridges, which in turn facilitates the transportation of heavy statues [139]. Capillary bridges are also widely seen in living nature. Small bugs, flies, grasshoppers and tree frogs create capillary bridges between the surfaces and their feet by injecting a wetting liquid into the contact area. The formation of capillary bridges generate a relatively long-range attractive interaction, which allows them to adhere to surfaces [140]. Another excellent example of capillary bridges in nature can be seen between the beaks of a certain class of shorebirds known as Phalaropes [141, 142]. During feeding, these birds employ a peculiar feeding technique using prey laden water droplets. By opening and closing their beaks successively in a tweezering motion, they are able to transport these droplets from the tip of their beaks back into their mouths in a stepwise ratcheting fashion, often against gravity. This feeding mechanism of these shorebirds is a particularly interesting showcase of capillary bridges and shed light on how geometric confinement can be used to generate spontaneous motion of liquids by reconfiguration of boundaries [141, 142].

Perhaps the simplest example of a solid geometry that mediates the capillary transport of droplets by geometric confinement is a wedge channel. In 1712, Hauksbee observed that a drop of orange oil in contact with two non-parallel plates of a narrow

wedge spontaneously moved towards the most confined part of wedge [143]. The liquid was driven into the area of most confinement by a differential Laplace pressure established between the droplet's extremities as a result of a different curvature on its leading and trailing edges. Bouasse later suggested that a slug of wetting liquid exhibited similar behaviour and moved towards the narrow end of a tapered capillary tube [144]. Conversely, Loreanceau and Quéré studied experimentally the behaviour of a drop of wetting liquid deposited on a conical fibre and showed that it would spontaneously move toward region of lower curvature, in other words, away from the tip [145]. It has also been shown that gradients in confinement can be used to propel droplets in narrow channels. Renvoisé *et al.* presented experimental and theoretical results of the motion of wetting droplets in a tapered capillary tube and demonstrated that drops may move towards the tapered end of the tube as a result of a Laplace pressure difference along length of the droplets [146]. Capillary bridges in wedges can also be seen in microfluidic devices where the configuration of the set up can be harnessed to manipulate position of the droplets in confinement. Dangla *et al.* demonstrated the generation of droplets in microchannels [147] and Luo & Heng showed the possibility of separation of oil from water/oil mixed drop using two non-parallel plates [148]. More importantly, especially in the case of this study, the motion of capillary bridges confined in wedges can provide new ways of understanding the contact line dynamics as shown by Reyssat in the study of dynamics of drops and bubbles confined in wedges [149].

When a capillary bridge is formed between two surfaces, its shape is determined by the wettability of these surfaces which in turn determines the direction of motion of the confined droplet. In broad terms, one can identify three well-studied regimes for fluid motion depending on the wettability of the solid wedge. In the limit of complete wetting ($\theta = 0^\circ$), a liquid bridge will invade the more confined portion of the wedge, the same behaviour can also been seen in tapered capillary tubes (Figure 5.1c,g) [146, 149]. This picture still holds if the liquid has a finite contact angle with the solid, $\theta < 90^\circ$, the liquid will still completely invade the narrow portion of the wedge but will spread into an edge-blob or a cigar shape as it arrives at the apex of the wedge (Figure 5.1h) [150, 151]. On the other hand, in the complete non-wetting

limit ($\theta = 180°$), a liquid droplet confined in a wedge tends to always move away from the apex, into a the wider portion of the wedge, a situation that can be exploited to guide the formation of monodisperse droplets [149]. If enough energy is stored in the droplet from the compression, it may even "shoot" out of the wedge completely. In these regimes, control over the localisation and transport of the droplet is only possible when a sustained external force is applied which serves the purpose of counteracting the capillary-energy landscape and any pinning effects. Examples of the external forces include continuous actuation of the confining boundaries [142, 152], gravity or pressure gradients [153].

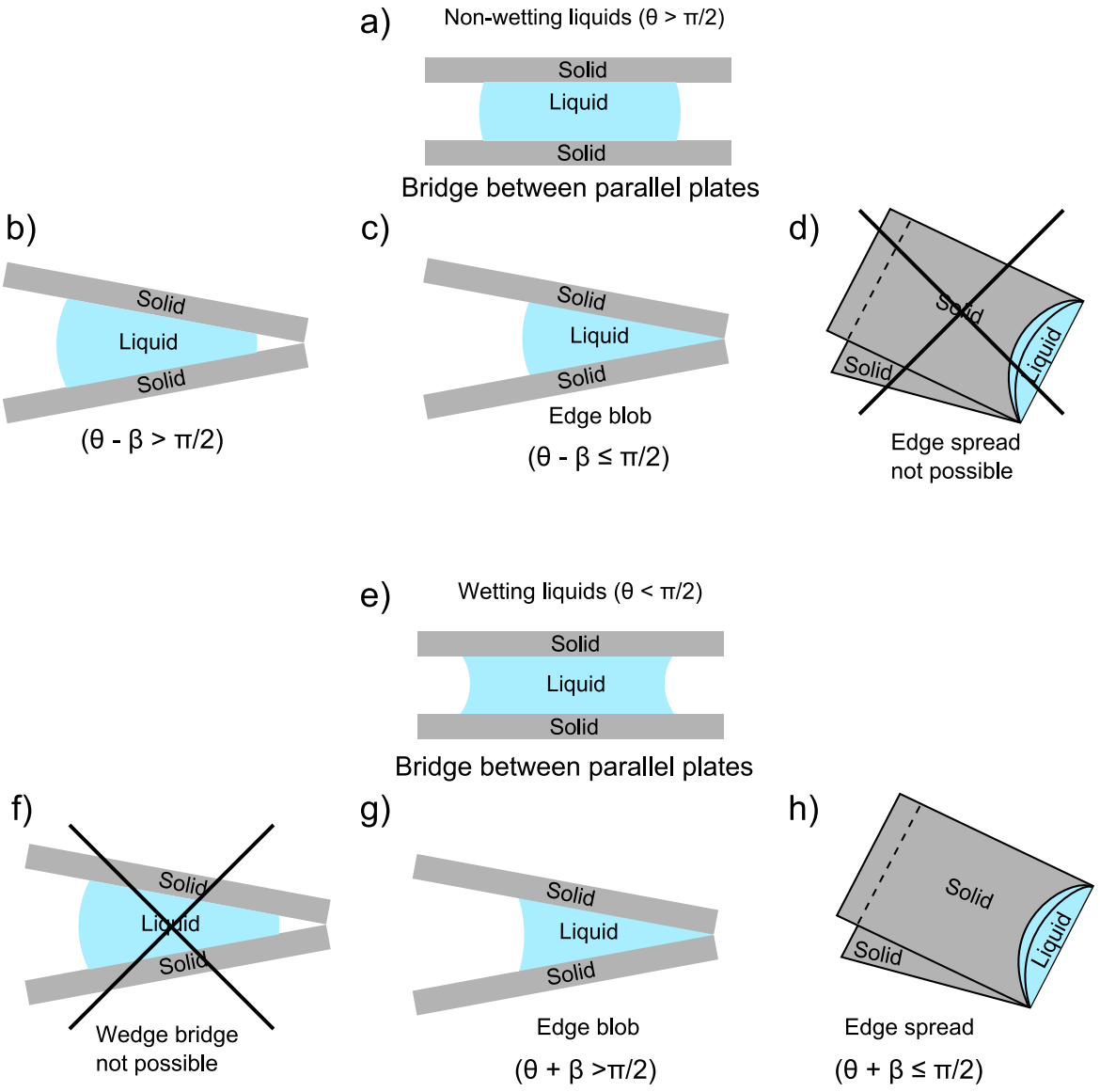

Figure 5.1: Different shapes of droplets confined in wedges, as predicted by Concus & Finn, a - d: different wetting configurations for non-wetting liquids, e - h: different wetting configurations for non-wetting liquids.

In the partial wetting regime, $0 < \theta < 180^{\circ}$, droplets can take on numerous equilibrium shapes upon contact with the confining surfaces which relates to, in absence of external forces, the contact angle and the tapering angle of the wedge [150]. It has been shown that, at a finite contact angle, a stable equilibrium can be achieved in a wedge providing the two bounding surfaces are fixed in place. Droplets in equilibrium, having contact angles with the confining surfaces of $90^{\circ} < \theta < 180^{\circ}$, would adopt the shape of a truncated sphere. In the regime where $\theta > 90^{\circ} + \beta$, where β is the half opening angle of the wedge, droplets would equilibrate away from the apex, without ever filling it (Figure 5.1b). Such a regime was observed Luo *et al.* who carried out experiments of water droplets trapped between Teflon-coated surfaces [154]. More recently, Baratian *et al.* analysed droplets confined in wedges and provided further insights into these static shapes [155]. Using a sustained electrowetting actuation, they directly observed the profiles of static droplets consistent with the shape of a truncated sphere as predicted Concus and Finn [150]. Nonetheless, the dynamics of droplets in wedges in this regime remain largely unexplored, especially in experimental approaches. Experimentally, it is relatively simple to satisfy the condition needed to create the regime of $\theta > 90^{\circ} + \beta$. Naturally, a droplet in this configuration, if in an out of equilibrium position, would tend to move to its equilibrium position. However, this motion is often hampered by the contact line pinning due to the contact angle hysteresis. By using surfaces with reduced wettability pinning can be minimised but it can result in the droplet's complete ejection from the wedge or detachment from one of the bounding surfaces upon reconfiguration of geometry. Thus, the effort in retaining control over the droplet's motion have mostly relied on the use of sustained external forces, for example, electrowetting used by Baratian *et al.* [155].

Removing contact line pinning without the need for sustained external forces whilst retaining control over the droplet in wedges is therefore of considerable interest, both from the fundamental and technological points of view. In this Chapter, the smooth transport and controlled positioning of partially non-wetting droplets purely by the reconfiguration of a wedge geometry where the pinning is virtually zero is demonstrated.

5.2 Initial Observation

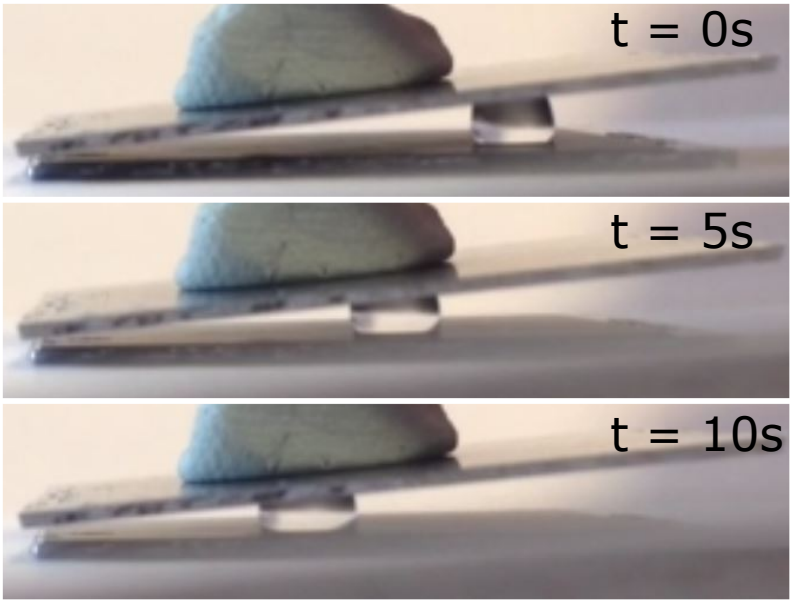

Figure 5.2: First observation of droplet confined between two lubricant-impregnated surfaces moving towards the apex of the wedge.

The study described in this Chapter began with a simple experiment in which a droplet was placed between two parallel SLIPS with the intention of observing the shape of the droplet. The upper SLIPS was held in place with a slab of putty-like adhesive and brought into contact by hand with the droplet sitting on the bottom SLIPS. Upon establishing contact with both SLIPS substrates which were unintentionally non-parallel, the droplet proceeded to migrate towards the more confined area between the surfaces and eventually came to a halt before reaching the apex (Figure 5.2). At the time of the experiment, this seemingly strange behaviour of the droplet was unanticipated and the expectation of an opposite trajectory was held for the droplet. Upon better familiarisation with the works related to the shapes of capillary bridges in wedges, this was identified as an example of a "spherical bridge" as described by Concus and Finn [150]. It was predicted by Concus and Finn that a droplet with contact angle θ with the surfaces of the wedge with a half wedge angle of β will equilibrate away from the apex if $\theta > 90^\circ + \beta$ [150]. Droplets out of their equilibrium positions will, depending on their initial positions, either move towards or away from the apex of the wedge. Interestingly, by using SLIPS, the lack of direct contact between the droplet and the underlying solid surface had led to a highly mobile contact line; allowing the

droplet to freely move to its equilibrium position. This indicates that the study of the dynamics of droplets in wedges in the partial wetting regime has been, for the first time, made possible. This would make it possible to exploit the capillary energy landscape resulting from geometric confinement to control droplet transport without the need of external forces. Furthermore, by introducing changes in the configuration of the boundaries, one could achieve a smooth dynamic actuation with precise control over the droplet's position.

5.3 Experimental Methods

5.3.1 Selecting Suitable Surfaces

The initial observation and several subsequent preliminary experiments provided strong indications that, a wedge can be constructed using a pair of lubricant-impregnated surfaces for the purpose of studying the dynamics of partially non-wetting ($\theta > 90^\circ + \beta$ in particular) and achieving of accurate control transport and positioning, in the absence of any sustained external forces. Preliminary experiments also revealed the three crucial characteristics that surfaces deemed suitable and thus used in this study must exhibit:

- **Low sliding angle characteristics ($< 1^\circ$)**, this will ensure any impediment to the motion of confined droplet due to contact line pinning is eliminated. The process to produce lubricant-impregnated surfaces has been described in Section 3.1, it was shown in the evaporation experiments Chapter 4 that surfaces showed sliding angles generally below 1°. To reduce the relatively long production time hydrophobisation process, an alternative hydrophobic coating in the form of nano-particles suspended in a solvent (Glaco Mirror Coat, Nippon Shine), along with the original OTS coating, was tested for comparison.

- **Apparent contact angle with water** greater than 90°, this way droplets will find equilibrium positions away from the apex as long as β is sufficiently small. $\theta < 90^\circ$ would lead to the formation of a capillary bridge with a negative curvature upon contact with both bounding surfaces of the wedge and eventually the complete invasion of the apex of the wedge.

- **The layer thickness of lubricating liquid** above the surface textures is sufficiently small such that the overall shape of the droplet is not altered by the presence of the large wetting ridges (Figure 5.3). As shown by Seiwert *et al.* [104], as a textured surface is withdrawn vertically from a bath of wetting liquid, a film of the liquid of thickness h_p is trapped within the surface texture of the same height, on top of which lies a free layer of the same liquid of thickness h_f, making the total thickness of liquid entrained by the textured surface a combination of two, $h_d = h_p + h_f$ (Figure 3.9). In the limit of high pillar density, the tops of the pillars act as a quasi-continuous surface, leading to the deposition of a LLD film on these tops and the effective thickness of the liquid film is close to h_f. On the other hand, the liquid film entrained by surface with lower pillar density be closer to that case of $h_d = h_p + h_f$.

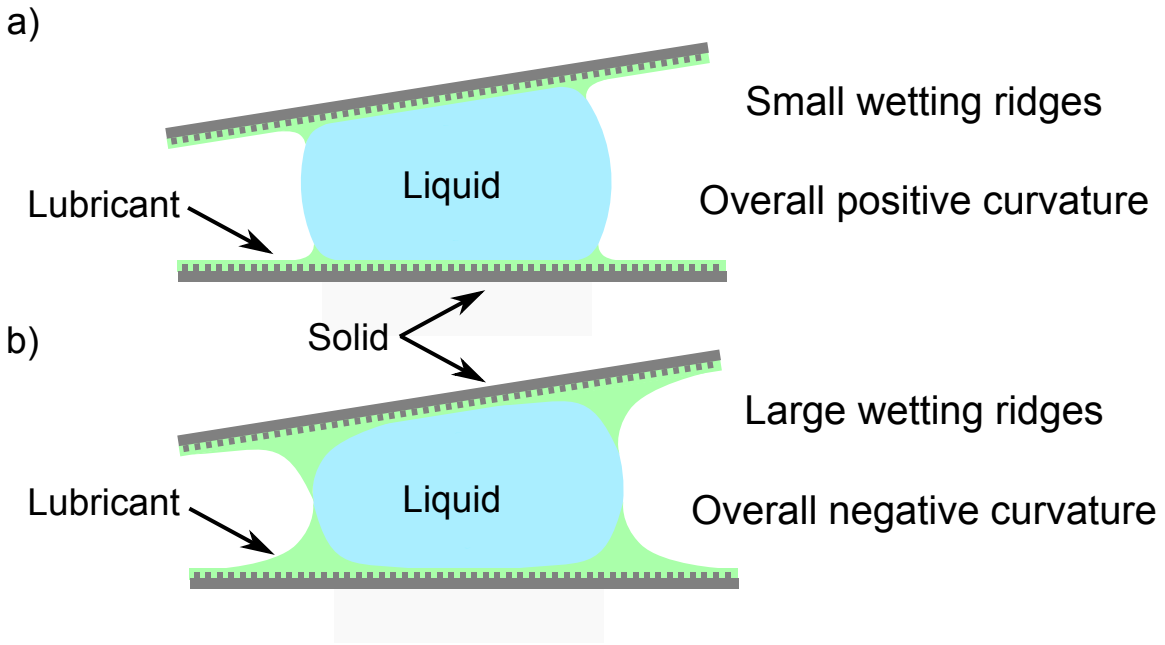

Figure 5.3: The effect of wetting ridges on the shape of droplet confined between two SLIPS: a. small wetting ridge, b. large wetting ridge.

Using the above rationale, surfaces with linear lubricant fraction l_f of 0.1 as defined in Chapter 4, once functionalised and lubricated, should give the smallest wetting ridges. To validate this assumption, ten samples with l_f ranging from 0.1 - 0.9 were fabricated using the standard photolithography (Section 3.1.1), they were then treated with OTS. 2.5 μL water droplets were placed on each of the surfaces and the height of the wetting ridges around the base of the droplets were measured on surfaces dip-coated

Table 5.1: Wetting ridge heights for droplets on surfaces with different lubricant fractions

			Wetting	Ridge	Height	/mm			
Dip Speed/mm s^{-1}	$l_f(0.1)$	$l_f(0.2)$	$l_f(0.3)$	$l_f(0.4)$	$l_f(0.5)$	$l_f(0.6)$	$l_f(0.7)$	$l_f(0.8)$	$l_f(0.9)$
1	0.20±0.01	0.30±0.01	0.33±0.02	0.32±0.01	0.28±0.02	0.26±0.01	0.25±0.01	0.24±0.01	0.25±0.01
5	0.37±0.02	0.42±0.05	0.40±0.02	0.45±0.01	0.43±0.01	0.47±0.01	0.46±0.01	0.51±0.01	0.54±0.02
10	0.55±0.04	0.56±0.03	0.55±0.03	0.57±0.01	0.57±0.01	0.62±0.02	0.57±0.04	0.62±0.02	0.60±0.02
15	0.65±0.02	0.60±0.01	0.62±0.04	0.58±0.01	0.70±0.01	0.65±0.02	0.59±0.01	0.65±0.01	0.68±0.01
20	0.69±0.02	0.66±0.02	0.65±0.01	0.62±0.02	0.70±0.01	0.68±0.02	0.64±0.01	0.67±0.03	0.72±0.01

at five different withdrawal speeds: 1, 5, 10, 15, 20 mm s^{-1}. Different speeds were used to confirm the assumed correlation between the wetting ridge height and the oil film thickness. According to Equation 3.4, faster withdrawal speeds will result in a thicker lubricant layer being deposited on the surface. Table 5.1 clearly shows an increase in the wetting ridge height as the withdrawal speed increases. From Table 5.1, one can see that surfaces with $l_f = 0.1$ dip-coated at 1mm s^{-1} showed the smallest wetting ridge.

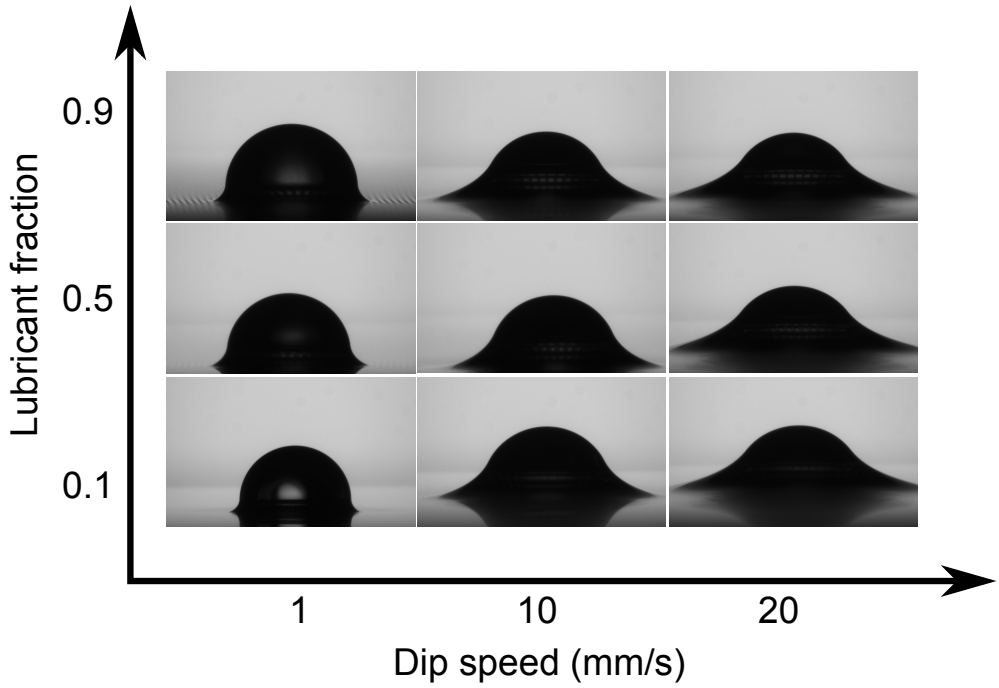

Figure 5.4: Water droplets on surface with linear lubricant fraction l_f ranging from 0.1-0.9 at different withdrawal speeds.

Table 5.2: Preliminary measurements of sliding angle, apparent contact angle, and wetting ridge heights of surfaces with linear lubricant fraction of 0.1 and treated with OTS or Glaco.

Sample	Sliding Angle/°	Apparent Contact Angle/°	h_s/mm	h_o/mm	h_s/h_o/%
SLOTS1	0.65±0.12	102.2±0.5	0.047±0.006	1.508±0.045	3.12
SLϕ1	0.61±0.11	103.3±0.6	0.067±0.011	1.518±0.034	4.41
SHϕ9	3.80±0.24	156.9±0.9	n/a	n/a	n/a

At this point, surfaces with $l_f = 0.1$ seemed to be the most suitable for this study. A fresh pair of these surfaces were fabricated on which measurements of sliding angle, apparent contact angle, and wetting ridge height were carried out. These surfaces are identical except for the method of hydrophobisation, one of them is treated with OTS whilst the other is coated with the Glaco coating. Additionally, a surface with $l_f = 0.9$

was also fabricated and coated with the Glaco coating for the purpose of validating the effectiveness of the coating itself and also to demonstrate the behaviour of a droplet confined between superhydrophobic surfaces.

Table 5.3 shows the sliding angles, apparent contact angles, wetting ridge heights (h_s), droplet heights (h_o) and the wetting ridge heights as a percentage of the droplet height, h_s/h_o for surfaces with linear lubricant fraction of 0.1 functionalised by OTS (SLOTS1) and Glaco coating (SLϕ1). (Each value shown in the table is the average value of ten separate measurements taken from ten droplets on the same surface.) Quantitatively, there does not seem to be much difference between surfaces treated with OTS or Glaco. The Glaco's effectiveness was further consolidated by the low sliding angles and large contact angle exhibited by the surface with $l_f = 0.9$ (SHϕ9) .

To check the reproducibility of the different coating methods, five fresh surfaces were fabricated for each of the methods and the same measurements were carried out. As shown in Table 5.3, droplets were pinned on all but one of the surfaces treated with OTS, due to either surface defect or the failure of the OTS in retaining the oil layer in the presence of water; whilst Glaco coated surfaces consistently exhibited extremely low sliding angles ($<0.3^\circ$).

Table 5.3: Repeated measurements of sliding angle, apparent contact angle, and wetting ridge heights of surfaces with lubricant fraction of 0.1 and treated with OTS or Glaco.

Sample	Sliding Angle/$^\circ$	Apparent Contact Angle/$^\circ$	h_s/mm	h_o/mm	h_s/h_o/%
SLOTS1(1)	2.00±0.30	105.3±0.8	0.24±0.03	1.53±0.05	15.73
SLOTS1(2)	Pinned	102.4±1.9	0.26±0.03	1.54±0.05	16.99
SLOTS1(3)	Pinned	103.1±1.1	0.22±0.03	1.50±0.03	14.81
SLOTS1(4)	Pinned	103.1±0.6	0.19±0.05	1.51±0.03	12.88
SLOTS1(5)	Pinned	92.3±3.7	0.21±0.02	1.47±0.02	14.57
SLϕ1(1)	0.24±0.05	103.2±0.6	0.14±0.02	1.53±0.05	9.17
SLϕ1(2)	0.34±0.05	103.7±0.3	0.16±0.02	1.53±0.04	10.01
SLϕ1(3)	0.26±0.05	102.9±0.5	0.17±0.02	1.53±0.04	10.97
SLϕ1(4)	0.28±0.07	103.4±0.2	0.19±0.01	1.50±0.05	12.38
SLϕ1(5)	0.28±0.07	103.4±0.2	0.15±0.02	1.53±0.04	9.70

The Glaco coated surfaces showed generally lower and more consistent values of apparent contact angles (typically $\approx 103^\circ$) than their OTS treated counterparts. As described in Section 3.1.5, the magnitude of apparent contact angle of a droplet surrounded by a wetting skirt directly relates to the height of the wetting ridge. Since

the apparent contact angle is extrapolated from the circle fitted on the points extracted from the droplet's profile above the wetting ridge, a larger wetting ridge would give a smaller apparent contact angle. Therefore, the Glaco coated surfaces showed generally smaller wetting ridges and since same volume droplets were used, smaller h_s/h_o. These measurements strongly indicate that the surfaces with linear lubricant fraction of 0.1, treated with Glaco coating would be suitable for the current study.

5.3.2 Droplets in Wedges Experiments

Experimental Set Up

To create a system where the pinning energy barrier experienced by a droplet is eliminated by the introduction of a thin liquid layer that prevents direct contact with the bounding surfaces, pairs of fresh lubricant-impregnated surfaces were used. They were rendered as SLIPS/LIS by patterning silicon wafers with square micro-pillars using standard photolithography. The height of the pillars was set to 50 μm with their cross section to 90 μm $\times$ 90 μm in area. Pillars were arranged in a square lattice with a 100 μm centre to centre separation. The resulting substrates were sprayed with a nano-particle based coating to create superhydrophobic surfaces whose contact angle with water is typically close to 150°. The surfaces were subsequently dip-coated in silicone oil, which exhibits complete spreading on the textured surface in the presence of both air and water. The dip-coating was controlled by fixing the withdrawal rate from the oil bath at 1 mm s^{-1} using a dispensing robot. This resulted in a thin layer of oil being infused both between the gaps and atop the tops of the surface textures.

Experiments were designed accordingly to allow the desired variables to be measured. These variables include:

- the half wedge angle, β.
- the width of the droplet, W which is the distance between the leading (L) and trailing (T) edges.
- the height of the droplet, H, defined as the length connecting the contact lines at the narrow end of the wedge.

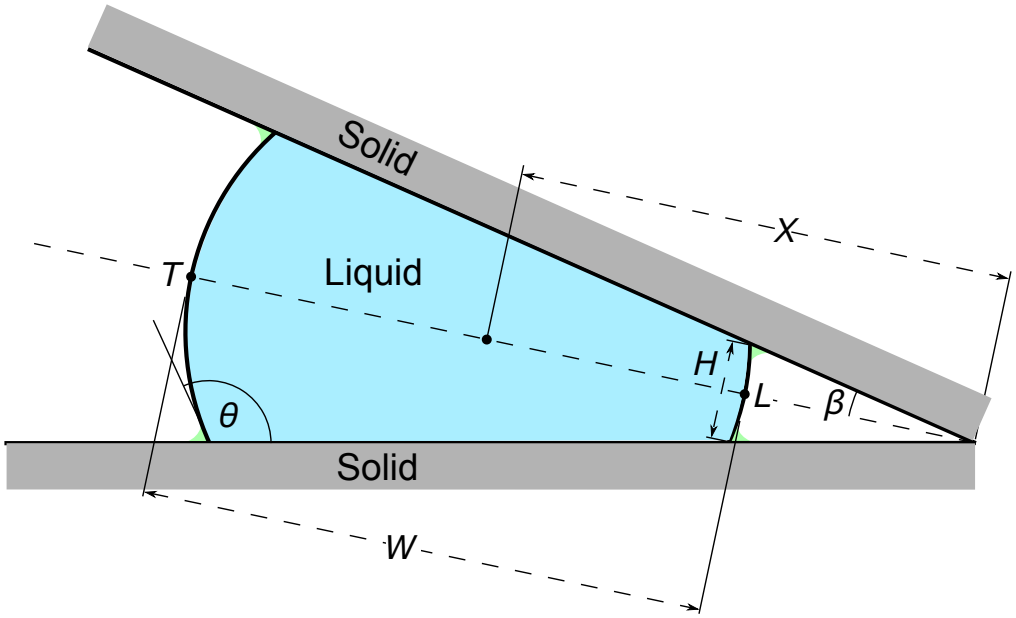

Figure 5.5: Parameters of the system.

- the droplet's position in relation to apex of the wedge at an given time, $X(t)$. Taking into account the width of the droplet, the droplet's position is defined as the average position of the leading (L) and trailing (T) edges.

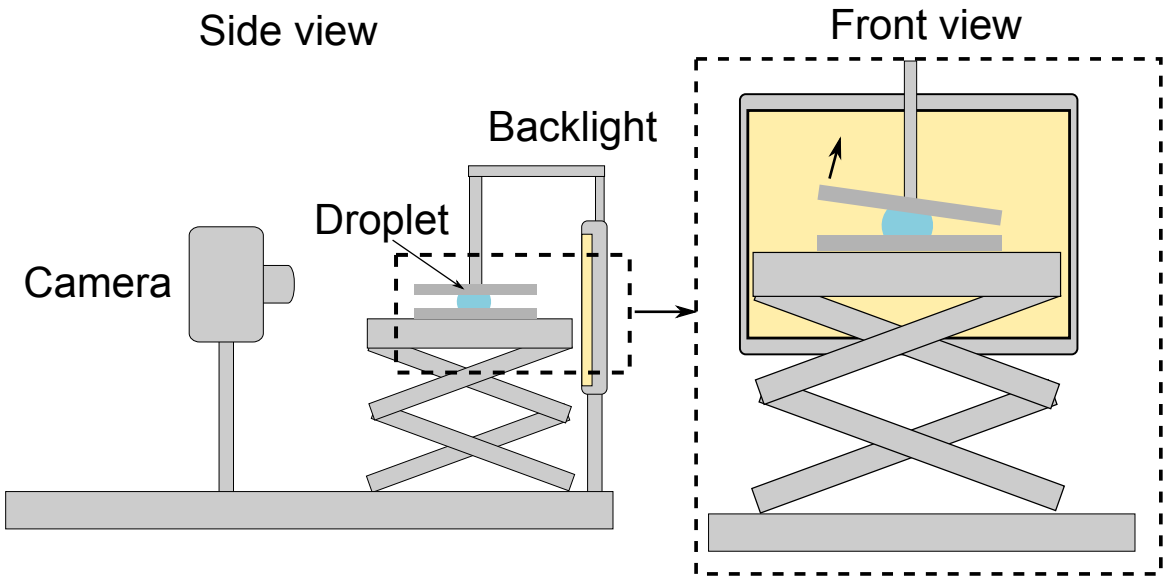

Figure 5.6: Experimental set up for droplet in wedges experiments.

An experimental set up was built specifically for the droplet in wedges experiments. Its main components include: a highly accurate levelling stage upon which the bottom substrate of the wedge is situated to prevent any unnecessary movement of the highly mobile droplets, an adjustable stage allowing movement in the z direction equipped

with a rotatable sample holder in which the upper substrate is held, a CCD camera (Thorlabs) to image the lateral cross-section of the wedge during the experiment and diffused backlight behind the stage.

Two identical lubricant-impregnated surfaces with $l_f = 0.1$ were used, one placed on the levelling stage and the other is inserted into the sample holder. To measure the equilibrium position of a droplet of a certain volume confined between two surfaces, the upper surface was initially held in place with the sample holder far from and not parallel to the bottom surface. It was then lowered until its lower edge made contact with the bottom surface.

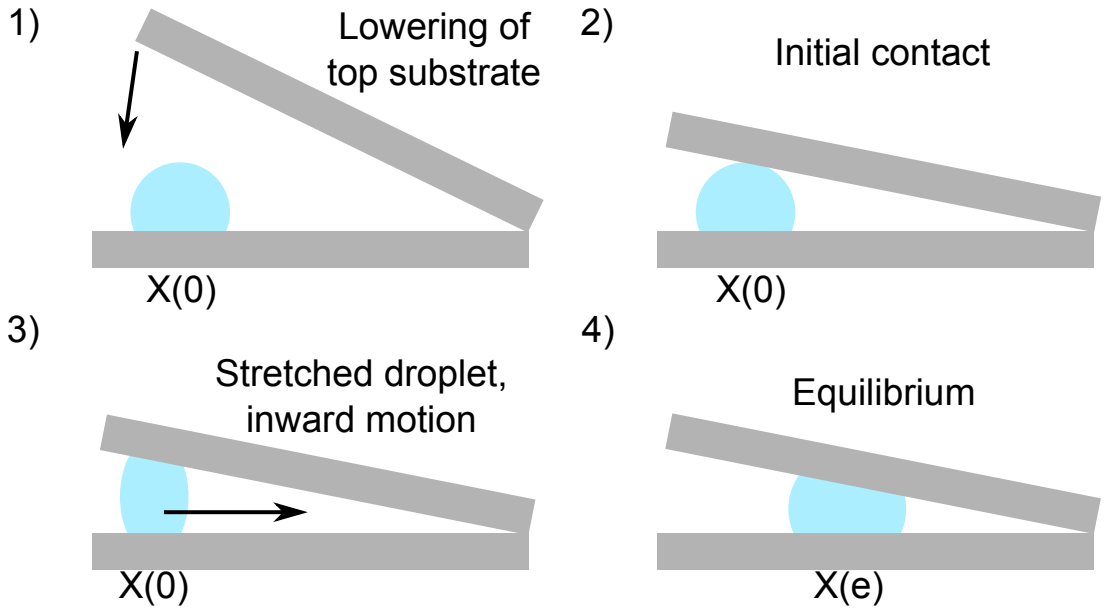

Figure 5.7: Process flow of droplets in wedges experiments going from initial position $X(0)$ to its equilibrium position $X(\mathrm{e})$.

A droplet of water of known volume was then placed on the bottom surface at a place far from the apex of the wedge. The sample holder, along with the upper surface, was then rotated about the apex of the wedge using a dial until contact was made by the droplet with both the upper and the bottom surfaces. Rotation was either immediately stopped upon contact with the droplet or was rotated quickly until a desired opening angle was achieved. The droplet was then allowed to freely move towards its equilibrium position. Time lapse photography was carried out by a CCD camera facilitated by a LabVIEW programme allowing images to be captured at a rate of 1fps. Extra care was taken to ensure that the droplet had indeed reached its equilibrium position, the

programme was left to run for a sufficient amount of time after the droplet appeared to have stopped (Figure 5.7).

Equilibrium Position and Aspect Ratio Measurements

Images captured by the CCD camera were analysed using a bespoke MATLAB programme using a standard image thresholding algorithm. For each individual image the position of the droplet at any given time $X(t)$ was determined by averaging the position of the leading and trailing edges of the droplet (Figure 5.8). The droplet's aspect ratio, $h = H/W$, was also monitored through out the experiment where H is the length connecting the contact lines at the narrow end of the wedge and W is the distance between the leading and trailing edges. Since the CCD camera was left to image the droplet after it had seemingly reached its equilibrium, equilibrium values of $X(t)$ and h were obtained by averaging the values measured from these images, typically over 100 measurements. This is to minimise the effect of systematic limitations such as the resolution of the CCD camera.

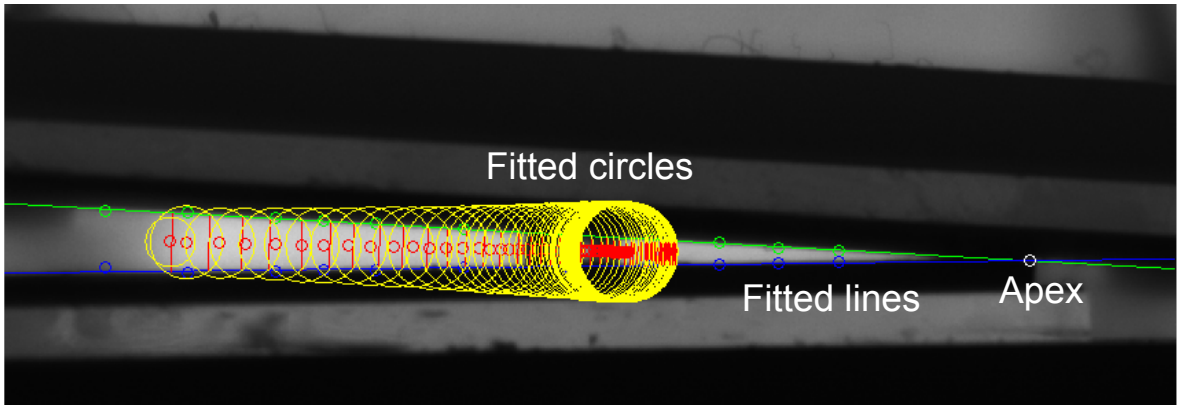

Figure 5.8: Interface of MATLAB programme used to track the position of the droplet in a SLIPS wedge.

5.4 Equilibrium

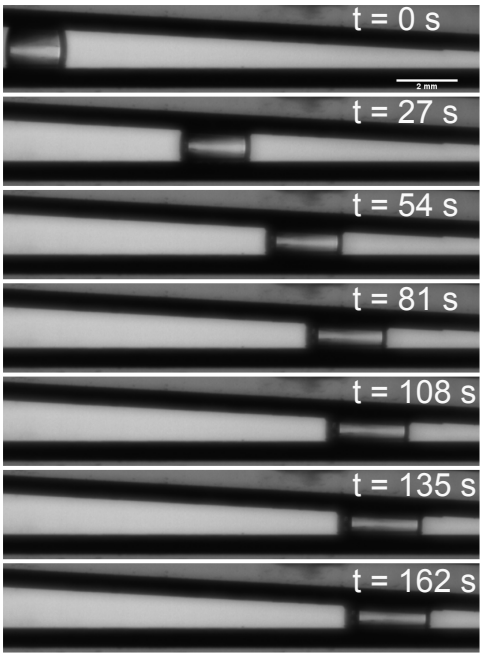

Figure 5.9: Experimental sequence of droplet moving in a wedge. Scale bars = 2 mm

The experimental set up as described in Section 5.6 allows an accurate control of the bounding geometry by adjusting the separation between the surfaces and the half opening angle, β (Figure 5.5). A single water droplet of controlled volume V ($2 - 5$ μL) was placed on the bottom surface of the wedge. The sample holder was adjusted until contact was established between the droplet and both bounding surfaces, keeping the opening angle fixed. Figure 5.9 shows a typical experimental sequence recorded using a CCD camera using time-lapse photography. If the half wedge angle β and the apparent contact angle θ_e satisfy the equation $\theta_e > \beta + \pi/2$ and according to Concus & Finn, one would expect that the droplet settles at a finite position from the wedge apex. Preliminary experiments confirmed that this is indeed the case, the droplet moves inwards until its position relative to the apex at any given time, $X(\mathrm{t})$, reaches a well-defined equilibrium value, X_e.

To test that the static state is not the result of contact line pinning, experiments were carried out in which droplets of the same volume were placed at different initial distances from the apex, $X(i)$. Droplets placed in between X_e and the apex, or in other words too close to the apex, would become compressed and move outwards, away from the apex. Conversely, droplets placed too far from the apex are stretched

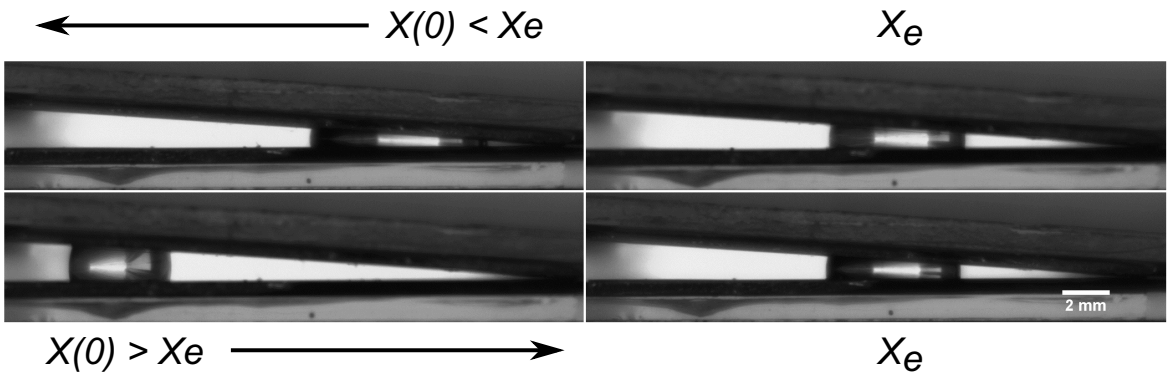

Figure 5.10: Inward and outward motion of a droplets of the same volume (v = 18 μL in identical wedges.

and therefore move inwards, towards the apex. More interestingly, regardless of the initial state, the droplets always settled at the same equilibrium position and adopt the same equilibrium shape, "intersecting" the solid at the apparent contact angle, θ_e (Figure 5.10). Measurements of the droplet's position as a function of time reveal a remarkably smooth dynamics consistent with an exponential approach to equilibrium with a time-scale, τ, which is another strong evidence of the lack of direct contact between the droplet and the solid surfaces.

5.4.1 Free Energy Approach

The minimisation of total surface free energy is the fundamental principle of modern theory of capillarity. The equilibrium of a system which consists of a of a wedge formed by two bounding surfaces and a liquid droplet that partially wets both surfaces can be understood via the variations of the Helmholtz free-energy of the arrangement.

In a situation where the mass, M, temperature, T and the volume of the confined droplet, V are held constant, the thermodynamic potential is the Helmholtz free energy, H,

$$H = U - TS \tag{5.1}$$

where U is the internal energy of the system, T is the absolute temperature of the surroundings and S is the entropy of the system.

According to the second law of Thermodynamics, the Helmholtz free energy will either remain constant or decrease upon a reconfiguration of the system, i.e., $\Delta H \leqslant 0$.

In this case, the temperature and the volume of the system are held constant, the changes in the total free energy are caused by the interfacial variations,

$$\mathrm{d}F = \gamma_{\mathrm{LV}}\mathrm{d}A_{\mathrm{LV}} + \gamma_{\mathrm{SL}}\mathrm{d}A_{\mathrm{SL}} + \gamma_{\mathrm{SV}}\mathrm{d}A_{\mathrm{SV}} \tag{5.2}$$

where γ_{LV}, γ_{SL}, γ_{SV} are the liquid-vapour, solid-liquid, and solid-vapour interfacial tensions, respectively.; and A_{LV}, A_{SL} and A_{SV} are the corresponding areas of the interfaces.

The minimisation of F yields two key equations for the shape of capillary surface. Firstly, the liquid-vapour interface must satisfy the Young-Laplace equation [5],

$$\Delta p = 2\gamma_{LV}H \tag{5.3}$$

which relates to difference between the pressure of the liquid and the vapour, Δp, to the Laplace pressure, $2\gamma_{LV}H$ where H is the mean curvature. Secondly, upon contact with the bounding surface, the profile of the interface must satisfy Young's law [5],

$$\cos\theta_{\mathrm{e}} = \frac{\gamma_{\mathrm{SV}} - \gamma_{\mathrm{SL}}}{\gamma} \tag{5.4}$$

where θ_e is the equilibrium contact angle. Substituting Equation 5.4 back into Equation 5.2, F can be rewritten as,

$$F = \gamma(A_{\mathrm{LV}} - A_{\mathrm{SL}}\cos\theta_{\mathrm{e}}) \tag{5.5}$$

5.4.2 Geometry

Concus *et al.* proved the existence of equilibrium states in the range $\theta_e > \beta + \pi/2$ which corresponds to the section of the sphere being intersected by the bounding surfaces at angles of θ_{e}. Therefore, predicting the equilibrium properties becomes a purely geometrical problem. The equilibrium shape of the droplet is a truncated sphere and for a given volume V and contact angle θ_{e}, the radius R_{e} of the sphere is fixed. R_{e} can be calculated by first calculating the volume of the sphere, V_{sphere} with the same radius R_{e} and subtracting the volumes of the two excluded caps, V_{cap}, (Figure 5.11). To

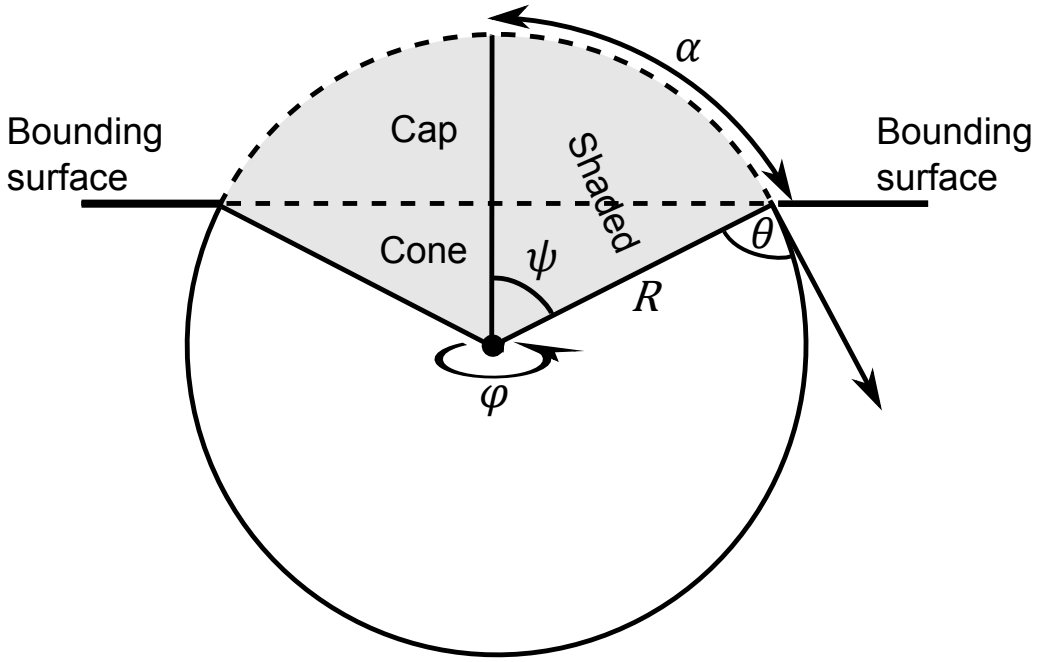

Figure 5.11: Calculating R.

calculate the volume of the excluded caps, it is necessary to first calculate the volume of the portion of the sphere which has an origin from the centre of the sphere and crosses with the intersecting plate, V_{shaded} (see shaded in Figure 5.11). Since the volume of a sphere can be calculated as,

$$\mathrm{d}V_{\text{sphere}} = R^2 \sin\psi \ \mathrm{d}R\mathrm{d}\psi\mathrm{d}\varphi \tag{5.6}$$

then the volume of the shaded portion becomes,

$$V_{\text{shaded}} = \int_0^{2\pi} \int_0^{\psi} \int_0^{R} R^2 \sin\alpha \ \mathrm{d}R\mathrm{d}\alpha\mathrm{d}\varphi \tag{5.7}$$

where R is the radius of the sphere, ψ is the azimuthal angle. After the integration and by using the relation $\psi = \pi - \theta$ where θ is the angle of contact between the droplet and the bounding surface,

$$V_{\text{shaded}} = \frac{4}{3}\pi R^3 \cos\left(\frac{\theta}{2}\right)^2 \tag{5.8}$$

The volume of the shaded area, V_{shaded} is comprised of the volume of the excluded cap, V_{cap} and the volume of a flat cone, V_{cone}, such that $V_{\text{shaded}} = V_{\text{cone}} + V_{\text{cap}}$ and V_{cone} can be calculated as,

$$
\begin{aligned}
V_{\text{cone}} &= \frac{1}{3}\pi R^2 \sin\psi^2 R\cos\psi \\
&= -\frac{1}{3}\pi R^3 \cos\theta \sin\theta^2
\end{aligned}
\tag{5.9}
$$

hence,

$$
V_{\text{cap}} = V_{\text{shaded}} - V_{\text{cone}} = -\frac{4}{3}\pi R^3 \cos\left(\frac{\theta}{2}\right)^4 (-2+\cos\theta) \tag{5.10}
$$

Since a droplet in equilibrium is a truncated sphere, therefore its volume is

$$
\begin{aligned}
V_{\text{truncated sphere}} &= V_{\text{sphere}} - 2V_{\text{cap}} \\
&= 4\pi R^3 - 2(-\frac{4}{3}\pi R^3 \cos\left(\frac{\theta}{2}\right)^4 (-2+\cos\theta)) \\
6V &= \pi R^3(-9\cos\theta + \cos 3\theta)
\end{aligned}
\tag{5.11}
$$

rearranging Equation 5.11, the radius of the truncated sphere, R_{e}, becomes,

$$
R_{\text{e}} = \left[\frac{6V}{\pi(\cos 3\theta_{\text{e}} - 9\cos\theta_{\text{e}})}\right]^{1/3} \tag{5.12}
$$

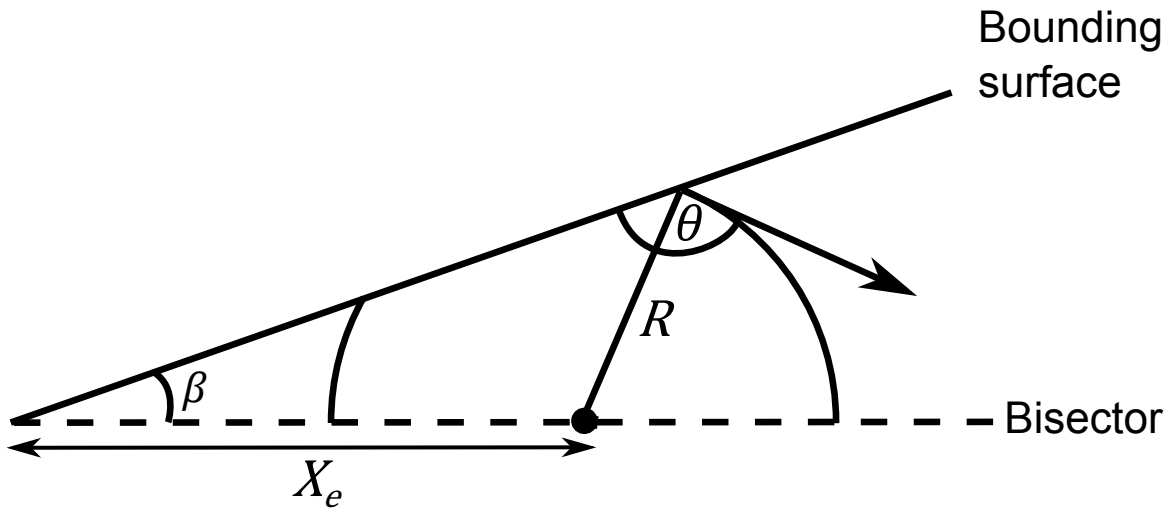

Figure 5.12: Calculating a droplet's equilibrium position.

In the system, the droplet is assumed to have a globally constant contact angle with the surfaces and therefore symmetry is assumed. Figure 5.12 shows the upper half of the truncated sphere, above the bisector. Knowing the radius R_{e} of the droplet in equilibrium, its equilibrium position in relation to the apex of the wedge, X_{e} becomes,

$$X_{\mathrm{e}} = -\frac{\cos\theta}{\sin\beta}\left[\frac{6V}{\pi(\cos 3\theta_{\mathrm{e}} - 9\cos\theta_{\mathrm{e}})}\right]^{1/3} \tag{5.13}$$

where β is the half opening angle of the wedge.

To measure how far from equilibrium the system is, another useful relation is the aspect ratio of the droplet. In equilibrium, the height-to width ratio of the droplet, $h_{\mathrm{e}} = H/W$, acts as an order parameter. For $\theta \leqslant 90^{\circ} + \beta$, corresponds to the case where the droplet complete fills the apex of the wedge and therefore h_{e} becomes 0. In the case of complete non-wetting, such that $\theta = 180^{\circ}$, h_{e} becomes $\cos\beta$. In the case of $\theta > 90^{\circ} + \beta$, the aspect ratio becomes finite.

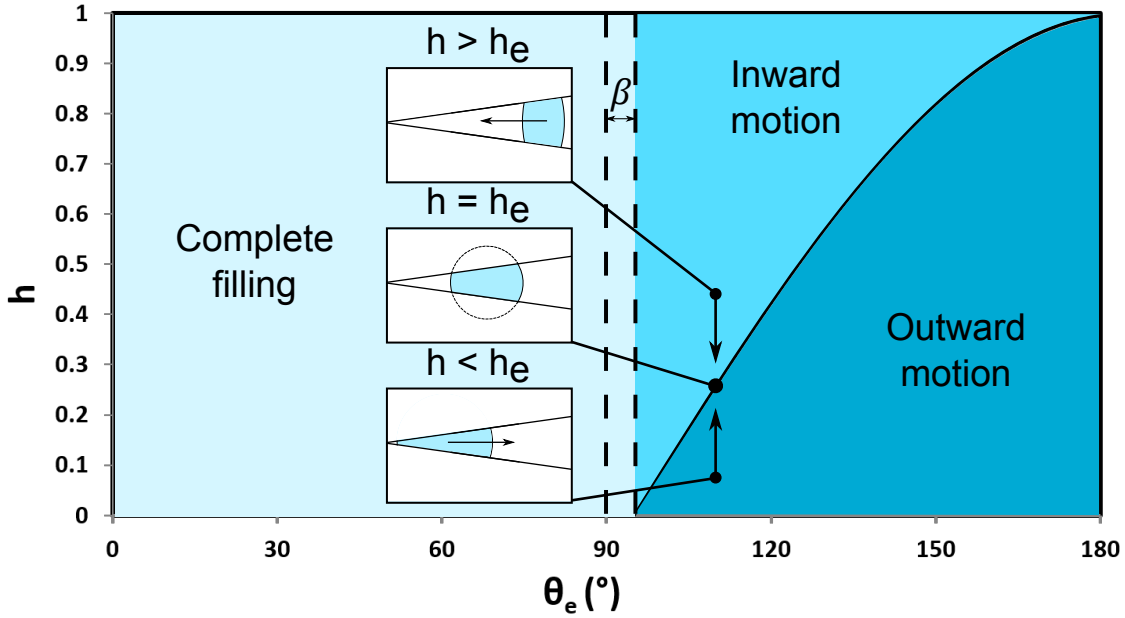

Figure 5.13: Phase diagram of the states of droplets with different values of h. Opening angle, β has been set to 5°.

In addition to the height-to-width definition of the aspect ratio, h_{e} can be re-written in terms of the droplet's equilibrium contact angle, θ_{e}, and the half opening wedge angle, β. Figure 5.14 shows the definition of the variables needed to calculate this relationship. An angle ψ was defined as the angle formed between the bisector and the line connecting the centre of the circle and the three-phase contact line at the narrow end of the wedge (Figure 5.14).

This gives, $\psi = \theta_{\mathrm{e}} - \beta - \pi/2$, and hence,

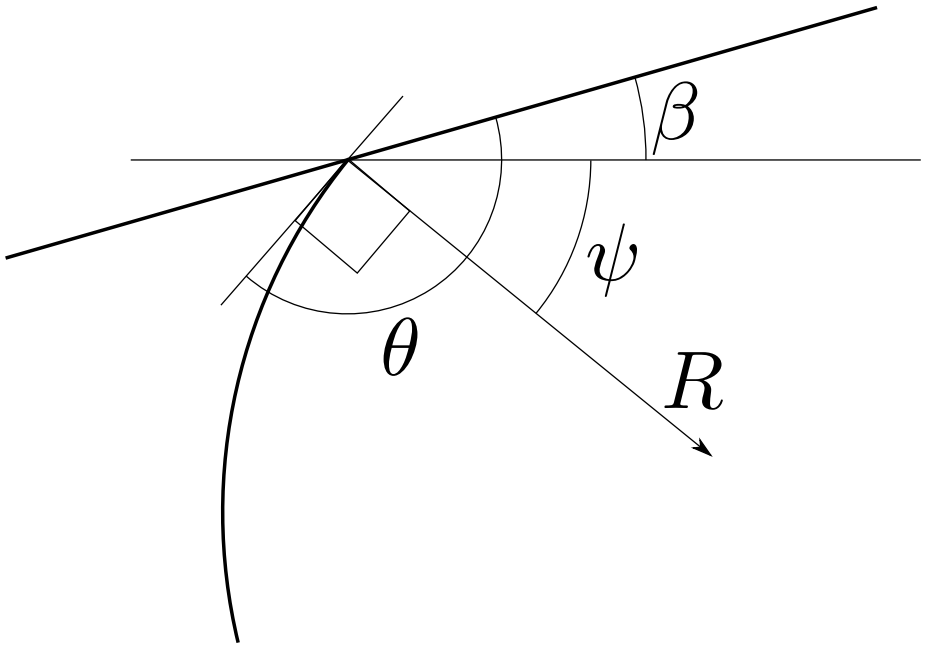

Figure 5.14: Aspect ratio of of a droplet.

$$\begin{aligned} \frac{H}{2} &= R_{\mathrm{e}} \sin\psi \\ H &= 2R_{\mathrm{e}} \sin\psi \end{aligned} \tag{5.14}$$

and since the width of the droplet in equilibrium is $W = 2R_{\mathrm{e}}$, and therefore $H = W \sin\psi$. h_{e} then becomes,

$$\begin{aligned} h_{\mathrm{e}} &= \frac{H}{W} \\ &= \sin\psi \\ &= \sin(\theta_{\mathrm{e}} - \beta - \pi/2) \\ &\therefore = -\cos(\theta_{\mathrm{e}} - \beta) \end{aligned} \tag{5.15}$$

To calculate the surface free energy of the droplet confined in a wedge in the shape of a truncated sphere, one can start by first considering the total surface free energy of a complete spherical droplet of volume V_{s} and surface area A_{s} to be $F_{\mathrm{e}} = \gamma_{\mathrm{LV}} A_{\mathrm{s}}$ where γ_{LV} is liquid-vapour interfacial tension. This geometry can be mapped to include an arbitrary number of boundaries, the total surface free energy becomes,

$$F_e = \gamma_{LV} A_s - \sum F_{xi} \tag{5.16}$$

where the first term is the surface free energy of the sphere and the second term is the energy arising from the excluded portions of the sphere due to the boundaries. F_e can be calculated using Equation 5.5 providing the area of the liquid-vapour interface, A_{LV}, and the surface area of the solid-liquid interface, A_{SL} are known and $A_{LV} = A_s - 2A_{cap}$ where A_{cap} is the area of caps excluded by the boundaries (Figure 5.11),

$$A_{cap} = 2\pi R^2 \int_0^{\psi} \sin\alpha \, d\alpha \tag{5.17}$$

and

$$A_{SL} = 2\pi R^2 \sin^2 \psi \tag{5.18}$$

Equation 5.16 therefore reduces to,

$$F_e = \gamma \frac{\pi}{3} (\cos 3\theta_e - 9\cos\theta_e) R_e^2 \tag{5.19}$$

5.5 Dynamics

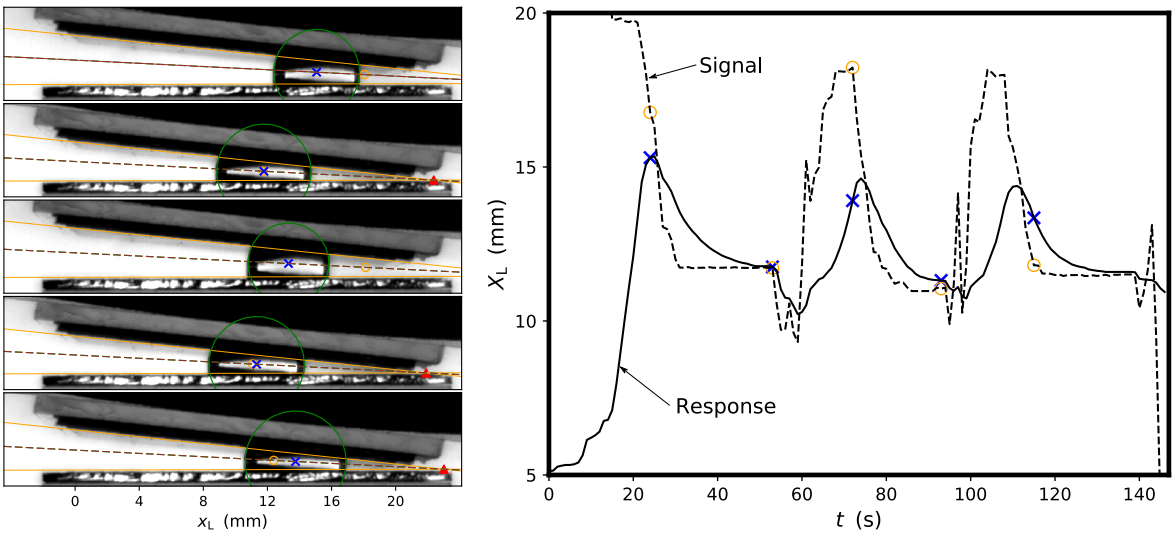

Figure 5.15: Droplet's trajectory upon a change in configuration follows an imposed signal.

In this SLIPS-wedge system, the lack of direct contact between the droplet and the bounding surfaces implies the absence of a threshold pinning force, which the droplet has to overcome. Therefore, a sudden reconfiguration of the wedge will result in the immediate motion of the droplet towards a new equilibrium position.

The droplet's trajectory follows an imposed signal (Figure 5.15 dashed line) which can be illustrated as a plot of the droplet's equilibrium position, X_e as a function of time, t (Figure 5.15). However, there exists a discrepancy between the imposed signal and the actual position of the droplet, $X(t)$ (Figure 5.15 solid line) which is determined by the friction force acting on the liquid. Furthermore, the level of agreement between the signal and the actual position of the droplet depends on the rate at which the reconfiguration occurs. In other words, the data of X_e and $X(t)$ over a certain period can be brought closer if the reconfiguration occurs slowly over time.

To test the effect of the friction force on the translational motion of the droplet, experiments were carried out in which a droplet was placed far from the apex of the SLIPS wedge such that $X(0) \neq X_e$ and $X(0) = X_e + \Delta X$, where X_e and ΔX are constants.

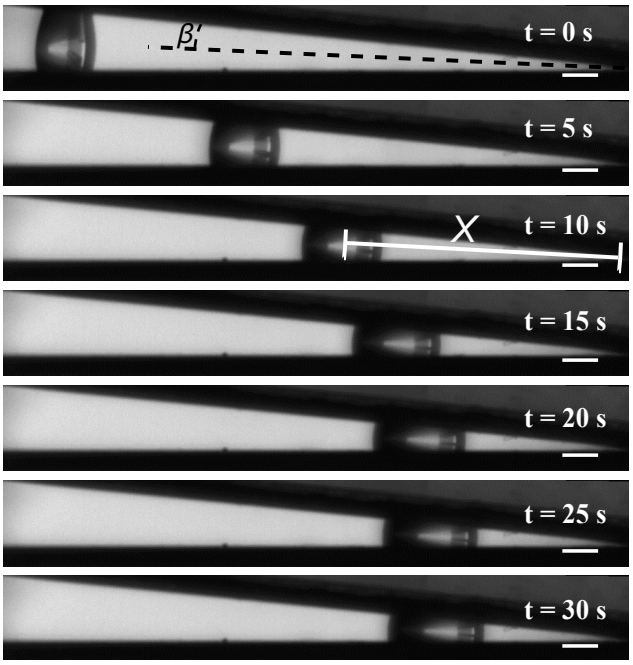

Figure 5.16: Time-lapse sequence of a 3 μL droplet moving towards the apex of a wedge where $\beta = 2.8°$.

The upper substrate was slowly brought into contact with the droplet. Once in contact with both surfaces, the droplet was allowed to relax to its equilibrium position.

Figure 5.16 shows a typical experimental sequence of the relaxation process. In these experiments, $X(0)$ was always set to be greater than X_e and droplets always moved inwards. Setting the initial condition of the experiment, to either $X(0) > X_e$ or $X(0) < X_e$, leads to inwards and outwards motion and would always, with constant volume, settle in the same equilibrium position (Figure 5.10).

From these experiments, due to the their initial positions being $X(0) > X_e$, droplets were initially stretched with aspect ratios $h(t) < h_e$. As the droplet migrated inwards towards the apex and as $h(t)$ tends towards h_e, its contact area with the two bounding surfaces, A_{SL}, or more specifically, the lubricant-water interface, $A_{water-Lubricant}$, increases. In the over-damped regime, where the driving capillary force is balanced by the frictional forces. In other words, a droplet moving towards its equilibrium position does not over-shoot. This increase in contact area was expected to cause the droplet to slow down and therefore an exponential decrease in its velocity was expected,

$$\dot{X} = -\frac{1}{\tau}(X - X_e) \tag{5.20}$$

where $-\frac{1}{\tau}$ is a constant of proportionality. Integrating for $(0, t)$, Equation 5.20 becomes,

$$X(0) = X_e + \Delta X e^{(-t/\tau)} \tag{5.21}$$

where τ is the time scale of the relaxation process which was obtained using Newton's Second Law,

$$\underbrace{m\ddot{X}}_{\text{mass} \times \text{acceleration}} = \underbrace{-\kappa(X - X_e)}_{\text{Restitution force}} - \underbrace{\nu\dot{X}}_{\text{Friction force}} \tag{5.22}$$

since $m\ddot{X} \approx 0$ in the over-damped regime, Equation 5.22 becomes,

$$\begin{aligned} -\nu\dot{X} - \kappa(X - X_e) &= 0 \\ \nu\dot{X} &= -\kappa(X - X_e) \\ \dot{X} &= -\underbrace{\frac{\kappa}{\nu}}_{\frac{1}{\tau}}(X - X_e) \\ \therefore \tau &\equiv \frac{\nu}{\kappa} \end{aligned} \tag{5.23}$$

where ν is the friction coefficient and κ is a spring constant.

The contributing factors to the friction force, $-\nu\dot{X}$, include the internal flow within the droplet, the layer of lubricant and the wetting ridge. Experimentally, the thickness of the lubricant layer was measured to be $h_{\text{lubricant}} = 13 \pm 1$ μm which agrees well with the theoretical LLD thickness (Figure 3.9) and the typical thickness of the droplet is $H \approx 1$ mm and therefore the contribution of the lubricant layer scales as $h_{\text{lubricant}}/H \approx 10^{-2}$ and is therefore negligible. On the other hand, the contribution from the wetting ridge was also expected to be small since surfaces used in this study were carefully chosen to have small wetting ridges and the apparent contact remained constant during the relaxation process. Therefore, this implies that the flow pattern within the droplet acts as the dominant contributor to the friction force.

To obtain a theoretical prediction for the relaxation time, the idea of a slip length, l, which quantifies the lubrication imparted by the SLIPS on the motion of the contact lines was used. Using l, the friction coefficient can be expressed as,

$$\nu \approx \frac{12\mu V H^2}{1 + 6\epsilon} \tag{5.24}$$

where $\epsilon = l/H$.

To obtain τ, the following relations were used,

$$\kappa \approx \frac{3\pi\gamma\beta^2}{\theta - \frac{\pi}{2}} \tag{5.25}$$

where κ was calculated using Equation 5.5, giving, to leading order in β and $\theta - \pi/2$. The dependence of κ on β shows how the driving force must vanish for droplets trapped between parallel plates. Also by using the geometrical relation,

$$H \approx \left(\frac{4V}{\pi}\right)^{\frac{1}{3}} \left(\theta - \frac{\pi}{2}\right)^{\frac{2}{3}} \tag{5.26}$$

the relaxation time can be predicted as,

$$\tau = \frac{\nu}{\kappa} \approx \left[\mu/\gamma(1 + 6\epsilon)\beta^2\right] \left[\frac{4V}{\pi(\theta - \frac{\pi}{2})}\right]^{\frac{1}{3}} \tag{5.27}$$

5.6 Results and Discussion

5.6.1 Experimental Data

Experiments were performed to measure the volume of the droplet, V, apparent contact angle, θ_e, the half wedge angle, β, droplet's equilibrium position, X_e, droplet's aspect ratio, h, and the relaxation time-scale, τ.

Table 5.4: Experimental data of V, θ_e, β, X_e, h and τ.

V/μL	θ_e/Rad	β/Rad	X_e/mm	h	τ
2.00 ± 0.06	1.823 ± 0.012	0.0261 ± 0.0006	10.57 ± 0.02	0.224 ± 0.002	28.98 ± 0.17
2.00 ± 0.06	1.803 ± 0.009	0.0257 ± 0.0005	10.57 ± 0.04	0.215 ± 0.010	28.60 ± 0.40
2.00 ± 0.06	1.824 ± 0.012	0.0261 ± 0.0006	10.33 ± 0.02	0.217 ± 0.002	30.20 ± 0.28
2.00 ± 0.06	1.802 ± 0.009	0.0314 ± 0.0004	8.23 ± 0.06	0.198 ± 0.001	21.70 ± 0.31
2.00 ± 0.06	1.857 ± 0.001	0.0355 ± 0.0008	8.17 ± 0.13	0.238 ± 0.004	- ± -
2.00 ± 0.06	1.856 ± 0.001	0.0360 ± 0.0003	8.14 ± 0.06	0.245 ± 0.002	- ± -
2.00 ± 0.06	1.839 ± 0.012	0.0394 ± 0.0014	7.17 ± 0.03	0.225 ± 0.001	10.35 ± 0.15
2.00 ± 0.06	1.840 ± 0.012	0.0393 ± 0.0008	7.23 ± 0.11	0.229 ± 0.004	9.53 ± 0.17
2.00 ± 0.06	1.832 ± 0.020	0.0399 ± 0.0008	6.86 ± 0.06	0.217 ± 0.001	9.50 ± 0.16
3.00 ± 0.09	1.817 ± 0.010	0.0242 ± 0.0003	12.95 ± 0.04	0.221 ± 0.001	36.95 ± 0.26
3.00 ± 0.09	1.817 ± 0.010	0.0256 ± 0.0002	11.99 ± 0.03	0.211 ± 0.001	30.96 ± 0.44
3.00 ± 0.09	1.810 ± 0.020	0.0253 ± 0.0008	12.12 ± 0.19	0.208 ± 0.004	33.28 ± 0.44
3.00 ± 0.09	1.796 ± 0.010	0.0296 ± 0.0005	10.12 ± 0.09	0.199 ± 0.001	30.96 ± 0.21
3.00 ± 0.09	1.795 ± 0.010	0.0303 ± 0.0007	9.86 ± 0.10	0.197 ± 0.002	26.03 ± 0.30
3.00 ± 0.09	1.796 ± 0.010	0.0302 ± 0.0003	10.02 ± 0.04	0.196 ± 0.001	24.47 ± 0.13
3.00 ± 0.09	1.810 ± 0.010	0.0377 ± 0.0005	8.11 ± 0.01	0.199 ± 0.001	14.12 ± 0.16
3.00 ± 0.09	1.802 ± 0.000	0.0373 ± 0.0003	8.24 ± 0.03	0.205 ± 0.001	13.54 ± 0.22
3.00 ± 0.09	1.817 ± 0.010	0.0381 ± 0.0006	8.21 ± 0.01	0.209 ± 0.002	12.59 ± 0.17
3.00 ± 0.09	1.782 ± 0.001	0.0383 ± 0.0001	7.33 ± 0.13	0.170 ± 0.004	14.72 ± 0.19
3.00 ± 0.09	1.788 ± 0.010	0.0391 ± 0.0004	7.38 ± 0.07	0.175 ± 0.002	13.29 ± 0.12
3.00 ± 0.09	1.788 ± 0.010	0.0395 ± 0.0004	7.31 ± 0.06	0.176 ± 0.001	12.74 ± 0.11
3.00 ± 0.09	1.781 ± 0.000	0.0467 ± 0.0004	6.17 ± 0.03	0.170 ± 0.001	8.19 ± 0.07
3.00 ± 0.09	1.781 ± 0.000	0.0471 ± 0.0002	6.10 ± 0.01	0.170 ± 0.001	8.23 ± 0.09
3.00 ± 0.09	1.781 ± 0.000	0.0471 ± 0.0004	5.93 ± 0.01	0.158 ± 0.001	8.81 ± 0.13
3.00 ± 0.09	1.784 ± 0.005	0.0505 ± 0.0009	5.52 ± 0.04	0.154 ± 0.001	7.11 ± 0.09
3.00 ± 0.09	1.788 ± 0.010	0.0507 ± 0.0004	5.63 ± 0.01	0.163 ± 0.001	7.45 ± 0.06
3.00 ± 0.09	1.788 ± 0.010	0.0510 ± 0.0005	5.59 ± 0.07	0.162 ± 0.003	6.84 ± 0.10
4.00 ± 0.12	1.779 ± 0.010	0.0181 ± 0.0012	17.32 ± 0.10	0.196 ± 0.001	- ± -
4.00 ± 0.12	1.774 ± 0.009	0.0196 ± 0.0009	16.08 ± 0.01	0.193 ± 0.000	- ± -
4.00 ± 0.12	1.779 ± 0.010	0.0233 ± 0.0001	13.49 ± 0.13	0.189 ± 0.002	53.41 ± 0.56
4.00 ± 0.12	1.792 ± 0.009	0.0235 ± 0.0006	13.81 ± 0.05	0.200 ± 0.001	47.29 ± 0.98
4.00 ± 0.12	1.786 ± 0.001	0.0232 ± 0.0005	13.62 ± 0.05	0.191 ± 0.001	72.19 ± 1.65
4.00 ± 0.12	1.772 ± 0.009	0.0303 ± 0.0005	10.00 ± 0.07	0.171 ± 0.001	25.62 ± 0.15
4.00 ± 0.12	1.773 ± 0.010	0.0295 ± 0.0010	10.26 ± 0.09	0.172 ± 0.002	27.63 ± 0.13
4.00 ± 0.12	1.776 ± 0.003	0.0299 ± 0.0010	10.23 ± 0.08	0.175 ± 0.002	25.03 ± 0.13
4.00 ± 0.12	1.755 ± 0.007	0.0348 ± 0.0004	7.97 ± 0.03	0.142 ± 0.001	25.51 ± 0.30

Table 5.5: Experimental data of V, θ_e, β, X_e, h and τ (Continued).

V/μL	θ_e/Rad	β/Rad	X_e/mm	h	τ
4.00 ± 0.12	1.772 ± 0.009	0.0347 ± 0.0001	8.33 ± 0.09	0.155 ± 0.002	18.58 ± 0.16
4.00 ± 0.12	1.765 ± 0.016	0.0341 ± 0.0003	8.62 ± 0.04	0.161 ± 0.001	19.37 ± 0.15
4.00 ± 0.12	1.740 ± 0.009	0.0401 ± 0.0000	6.51 ± 0.12	0.122 ± 0.004	15.15 ± 0.18
4.00 ± 0.12	1.741 ± 0.008	0.0398 ± 0.0004	6.39 ± 0.04	0.121 ± 0.001	14.87 ± 0.13
4.00 ± 0.12	1.747 ± 0.001	0.0397 ± 0.0000	7.06 ± 0.09	0.140 ± 0.002	14.23 ± 0.14
4.00 ± 0.12	1.766 ± 0.001	0.0492 ± 0.0004	5.99 ± 0.07	0.143 ± 0.003	9.60 ± 0.17
4.00 ± 0.12	1.773 ± 0.009	0.0486 ± 0.0002	6.24 ± 0.07	0.153 ± 0.002	- ± -
4.00 ± 0.12	1.773 ± 0.010	0.0500 ± 0.0002	5.99 ± 0.02	0.148 ± 0.000	8.58 ± 0.16
5.00 ± 0.15	1.766 ± 0.009	0.0240 ± 0.0004	12.93 ± 0.14	0.170 ± 0.002	46.96 ± 1.03
5.00 ± 0.15	1.756 ± 0.015	0.0249 ± 0.0001	11.47 ± 0.12	0.141 ± 0.002	47.00 ± 0.81
5.00 ± 0.15	1.754 ± 0.015	0.0247 ± 0.0014	12.17 ± 0.16	0.156 ± 0.003	42.25 ± 0.35
5.00 ± 0.15	1.747 ± 0.008	0.0239 ± 0.0021	11.95 ± 0.10	0.144 ± 0.002	47.59 ± 0.37
5.00 ± 0.15	1.743 ± 0.008	0.0305 ± 0.0004	8.92 ± 0.07	0.126 ± 0.001	26.02 ± 0.25
5.00 ± 0.15	1.754 ± 0.015	0.0292 ± 0.0007	9.90 ± 0.12	0.142 ± 0.002	27.81 ± 0.40
5.00 ± 0.15	1.743 ± 0.009	0.0302 ± 0.0003	9.18 ± 0.06	0.130 ± 0.001	25.33 ± 0.16
5.00 ± 0.15	1.694 ± 0.009	0.0330 ± 0.0002	6.72 ± 0.25	0.082 ± 0.006	24.77 ± 0.20
5.00 ± 0.15	1.703 ± 0.007	0.0326 ± 0.0009	7.35 ± 0.06	0.096 ± 0.001	20.73 ± 0.10
5.00 ± 0.15	1.715 ± 0.015	0.0351 ± 0.0004	7.16 ± 0.16	0.106 ± 0.004	20.54 ± 0.48
5.00 ± 0.15	1.686 ± 0.007	0.0365 ± 0.0007	5.38 ± 0.15	0.061 ± 0.004	- ± -
5.00 ± 0.15	1.668 ± 0.007	0.0378 ± 0.0004	4.94 ± 0.05	0.052 ± 0.001	- ± -
5.00 ± 0.15	1.692 ± 0.009	0.0372 ± 0.0007	5.96 ± 0.14	0.078 ± 0.004	- ± -
5.00 ± 0.15	1.730 ± 0.009	0.0523 ± 0.0000	5.28 ± 0.07	0.108 ± 0.003	7.54 ± 0.06
5.00 ± 0.15	1.713 ± 0.009	0.0582 ± 0.0005	4.35 ± 0.08	0.082 ± 0.004	- ± -
5.00 ± 0.15	1.698 ± 0.014	0.0544 ± 0.0013	4.29 ± 0.14	0.073 ± 0.004	7.79 ± 0.10

5.6.2 Superhydrophobic vs SLIPS/LIS

A wedge formed by two substrates rendered as SLIPS/LIS allow droplets to adopt numerous equilibrium shapes in the partial wetting regime. The presence of a lubricant layer eliminates the need for the droplet to overcome a threshold pinning force and thus allows it to freely move within the wedge until it reaches its equilibrium position. For comparision, a wedge was also constructed using two superhydrophobic textured surfaces (SHϕ9).

Theoretically, in the partial wetting regime ($0 < \theta < 180^\circ$), a droplet confined between two solid, flat surfaces would exhibit inward ($X(0) > X_e$), and outward ($X(0) < X_e$) motion providing that $X(0) \neq X_e$. Assuming the droplet wets the surface uniformly at an angle θ_e, it must move either in or out relative to the apex until it reaches a truncated sphere shape. With this rationale and by considering the wettability of the surfaces to be the only deciding factor to the trajectory of the droplet, the motion of droplets trapped between two hydrophobic surfaces or between two lubricant

impregnated surfaces should demonstrate similar trajectories. In reality, the motion of droplets on hydrophobic surfaces are often hampered by contact line pinning due to contact angle hysteresis which prevents droplets moving to their equilibrium positions. To reduce the effect of contact angle hysteresis, one could do so by minimising droplets' contact area with the surface by increasing the contact angle. However, to achieve a sufficiently low contact angle hysteresis, the value of θ often needs to be pushed up to near the limit of complete non-wetting, $\theta = 180^{\circ}$.

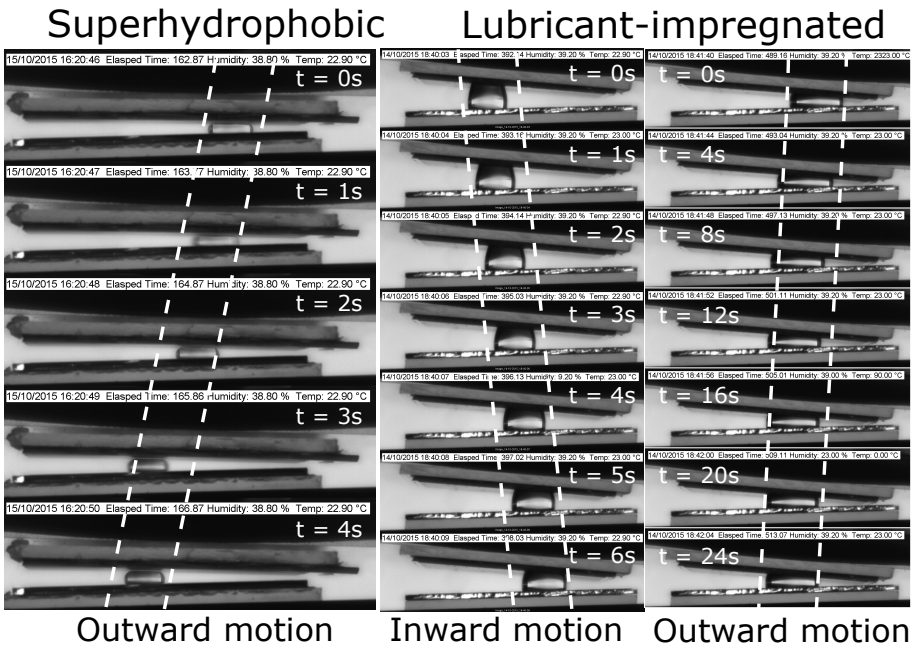

Figure 5.17: A comparison of superhydrophobic and lubricant impregnated surfaces: only outward motion of droplets between hydrophobic surfaces, both inward and outward motion of droplets between SLIPS.

The increase in the static contact angle also restricts the movement of the droplets within the wedge. For droplets having initial positions $X(0) < X_{\mathrm{e}}$, droplets would move away from the apex of the wedge and settle at X_{e}. For droplets $X(0) > X_{\mathrm{e}}$, a high contact angle implies that it would not move very far, or in other words, $X(0) \approx X_{\mathrm{e}}$. Furthermore, for the droplet to be in contact with both bounding surfaces, its opening angle must be sufficiently small such that $\beta < \tan(R/X)$. To "force" droplets inward towards the apex requires a significant increase in β. Experimentally, this often resulted in the detachment of the droplet from the upper surface. In summary, although droplets confined between superhydrophobic surfaces should theoretically exhibit the same behaviours as their SLIPS counterpart, their dependence on a reduced contact area to

minimise contact angle hysteresis imposes physical limitations which are not exhibited by SLIPS. As shown in Figure 5.17, in practise, droplets are almost always ejected from the superhydrophobic wedge but can move in or out in a SLIPS wedge.

5.6.3 Equilibrium

In the experiments, droplets of different volumes ($2-5$ μL) were allowed to relax in wedges of various opening angles ($1-4^{\circ}$). These observations support that the droplet behaviour in the SLIPS wedge is determined by apparent contact line properties (*via* the apparent contact angle), yet, in the absence of a true contact line. The equilibrium state was characterised in terms of the static position of the droplet's centre in the frame of reference of the wedge apex, X_{e}, and the height-to-width aspect ratio, $h_{\mathrm{e}} = H/W$, which are the measures of the droplet's localisation and footprint (Figure 5.5). In the absence of contact-line pinning, it is possible to control X_{e} and h_{e} by a reconfiguration of the SLIPS using the opening angle, β.

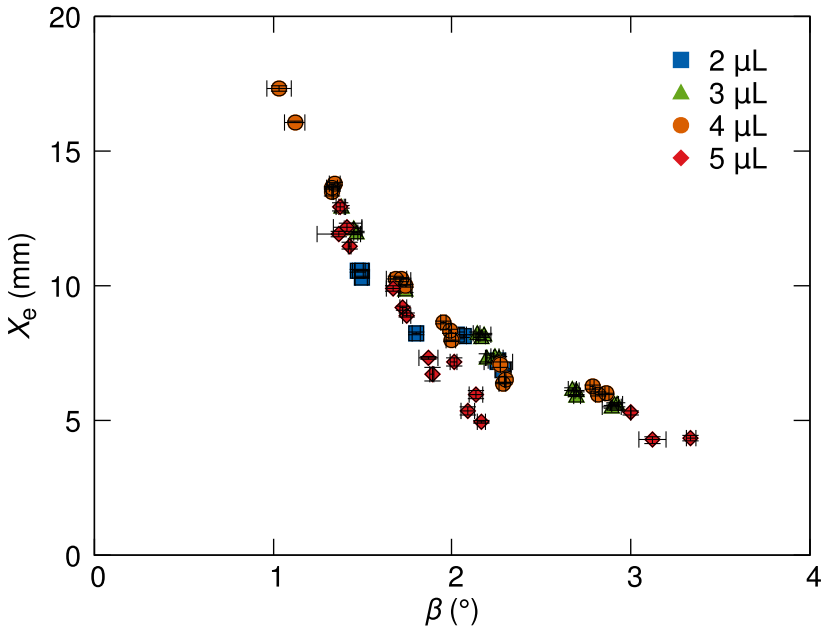

Figure 5.18: Equilibrium position X_{e} as a function of the half opening angle, β.

According to Equation 5.13, the equilibrium position of droplets X_{e} is inversely proportional to $\sin\beta$, meaning that by increasing β droplets can be positioned closer to the apex (Figure 5.18). Figure 5.18 shows the data of X_{e} for different droplet volumes as a function of β, they do not agree well with the theoretical predictions.

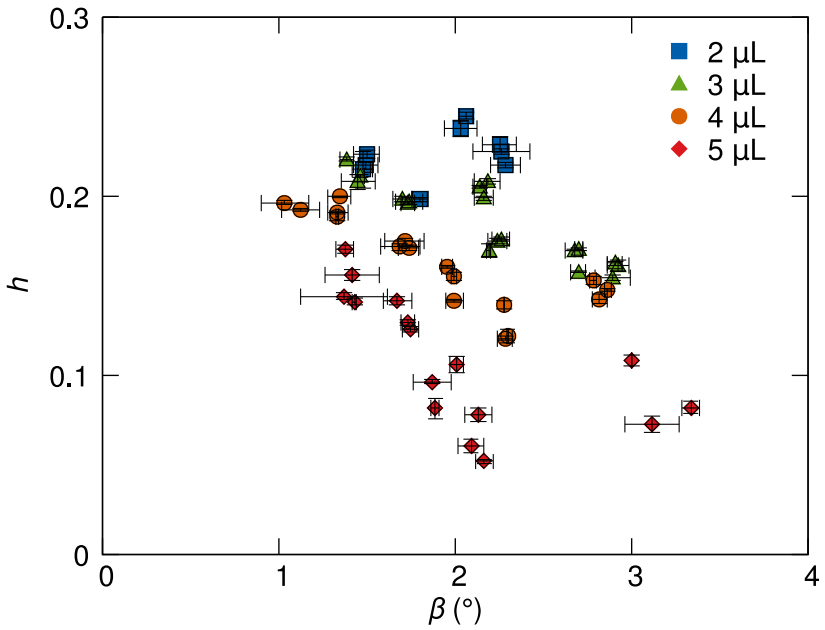

Figure 5.19: The droplet's aspect ratio, h_e, as a function of the tapering angle, β.

Figure 5.19 shows the data of droplets aspect ratio, h_e where the vertical error bars correspond to the stand deviation of the sample and the horizontal error bars are the experimental error in measuring the wedge angle. The data do not appear to show any correlation between the h_e and β.

Although Equation 5.13 and 5.15 capture the trends observed in experiments (Figures 5.18 & 5.19), the scatter in the raw data indicates that more careful consideration was needed for a quantitative comparison. After careful re-examinations of the conditions in which the experiments were carried out, it was found that the variations in θ_e and β are of the same order. Further checks revealed a possible ageing of the lubricant layer due to the presence of the droplet. It was previously found that the silicone oil (20 cSt) cloaks the droplet and as experiments were carried out one after another without a re-dipping process, it was suspected the droplet from a previous experiment could have caused a small depletion of oil. This depletion, though observed to be an effect localised to the footprint of the previous droplet, could have caused an increase in the apparent contact angle of the droplet in the experiment carried out immediately after. This reveals a delicate balance between wetting and confinement geometry which meant that the variations in the θ_e and β must be taken into account in the analysis process.

The variations in both θ and β also motivate the identification of an 'excess angle', $\delta = \theta - \beta - \pi/2$ as a natural variable for the problem. The limit $\delta = 0$, where $h = 0$ and $X_e = R_e$, corresponds to the complete invasion of the wedge, a situation that can be achieved either with sufficiently low apparent contact angles ($\theta < \pi/2 + \beta$) or by choosing a sufficiently large wedge angle ($\beta > \theta - \pi/2$). Beyond these threholds ($\delta > 0$) droplets select finite positions and aspect ratios. The initial apparent contact angles of droplet at the beginning of each experiments were re-measured, and values of δ were measured to lie in the range $0.05 < \delta < 0.25$ for which Equation 5.15 reduces to $h = \delta$. After the treatment of the data, the data shows an excellent collapse of the experimental data with this prediction (Figure 5.20).

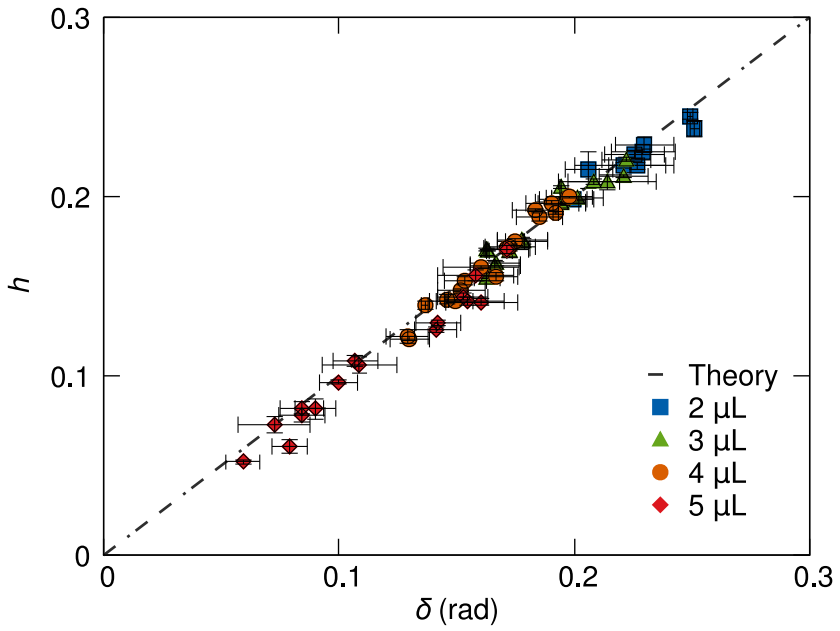

Figure 5.20: Aspect ratio h as a function of δ. Data collapse on top of the master curve $h = \delta = \theta - \beta - \pi/2$.

Since the value of X_e is derived directly from the R_e and Equation 5.12 suggests that R_e should remain the same upon a change in β, providing the both V, and θ_e remain constant. It is perhaps more meaningful to investigate the relationship between R_e and β instead of that with the droplet's equilibrium position, X_e.

Figure 5.21 shows the normalised droplet radius, taking into account the small variations in θ and β, which verifies Equation 5.12. It shows that for a given drop volume and apparent contact angle the droplet radius is independent of the wedge angle. Relating this to the Laplace pressure, $\Delta p = 2\gamma/R_e$, one can see that the independence

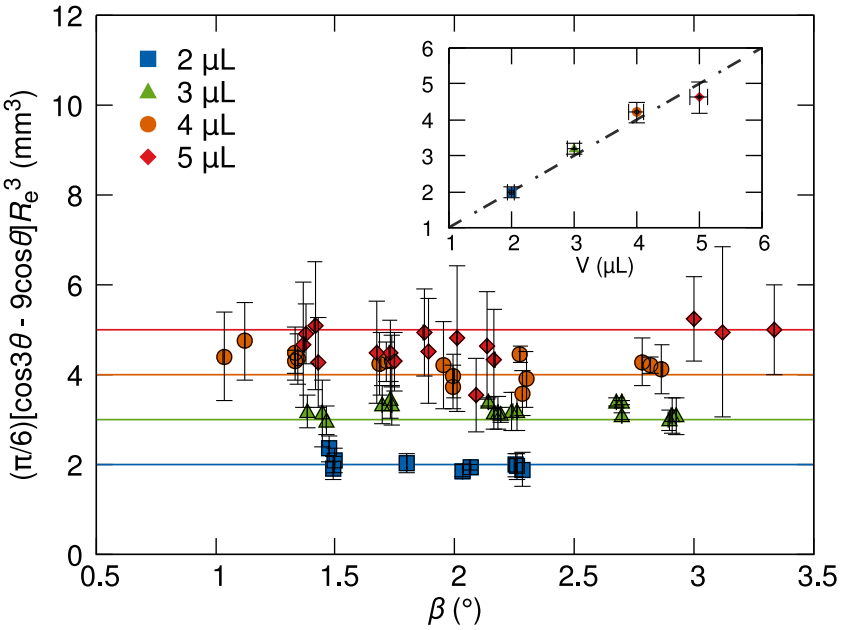

Figure 5.21: The radius of the droplet is normalised to eliminate variations in the apparent contact angle, $\theta = 100 \pm 5$ °. They are invariant upon changes in the opening angle of the wedge, β (Theoretical values are represented as solid coloured lines). The inset shows the dispensed and measured droplet volumes. Error bars correspond to the standard deviation of three experiments.

of R_e on the β leads to the vanishing of the net force acting on the droplet and a uniform Laplace pressure. A signature of the vanishing net force is the independence of the Laplace pressure on the wedge angle, which is confirmed by measurements of R_e (Figure 5.21). This further supports that pinning forces, which would arise in the presence of a contact line, have negligible effect on the configuration of the droplets.

5.6.4 Energy Invariance

The independence of droplets' equilibrium radius on the opening angle of the wedge has a more porfound implication. As described by Equation 5.19, with a given droplet volume and apparent contact angle, the surface free energy, F_e is invariant upon a change in the wedge angle, meaning that the change in internal energy caused by any reconfiguration of the wedge boundaries vanishes. This property is illustrated geometrically in Figure 5.22, where a change in the wedge angle, at fixed V and θ_e, can be visualised as the rotation of the two SLIPS boundaries about the centre of the droplet, or the rotation of the excluded spherical caps truncated by the wedge geometry about the same centre. Such rotation of boundaries does not alter the area of

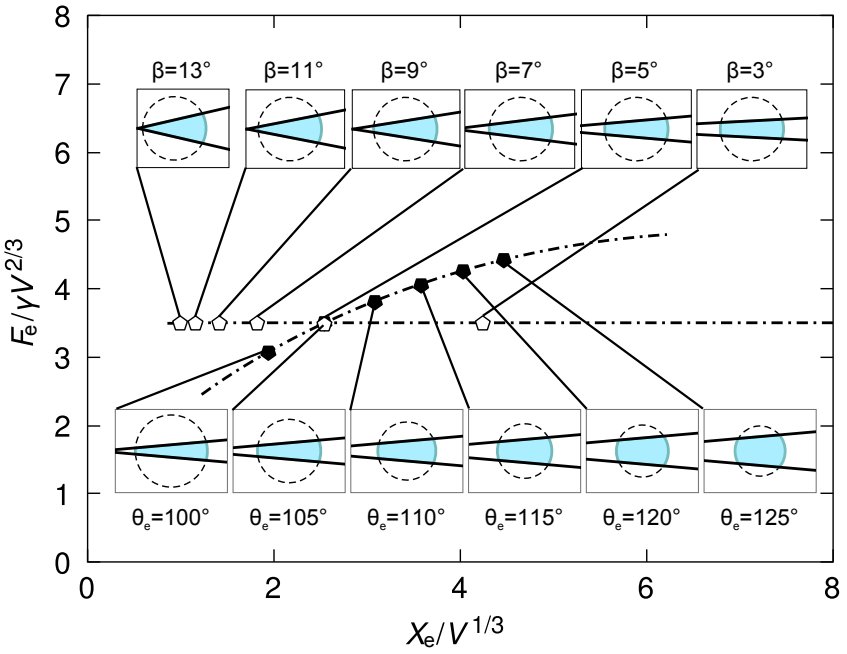

Figure 5.22: Invariance of surface free energy upon a change in β for constant apparent contact angle, θ.

the lubricant-water interface, $A_{\text{lubricant}-\text{water}}$, thus leaving the total surface free energy unaltered. A change in the apparent contact angle or the droplet volume, however, does lead to a change in the surface free energy as a change in either of them would lead to a change in $A_{\text{lubricant}-\text{water}}$(Figure 5.22).

Another important property of Equation 5.19 is that F_{e} is invariant upon a translation along the wedge. This implies that a quasi-static reconfiguration of the boundaries does not involve the surpassing of any energy barriers. Such rotation of the boundaries is equivalent to a displacement of X_{e} relative to the apex of the wedge which implies that a net translation of the droplet within the wedge could take place upon a reconfiguration of the boundaries without the system incurring in any work. The invariance in F_{e} suggests that the minimum force necessary to move the droplet along the wedge upon a reconfiguration of the boundaries is zero. This of course, is not possible to achieve in practice. Therefore, it is reasonable to infer that the only energy input the into system to move the droplet is the initial push to bring the droplet out of its equilibrium.

5.6.5 Relaxation Time

In experiments in which droplets were brought into contact with both SLIPS and migrated towards their equilibrium positions, droplets exhibited remarkably smooth

dynamics during translation (Figure 5.23). In the over-damped limit, the driving capillary force is balanced by the viscous friction originating from the motion of the drop. As mentioned in Section 5.5, the motion of a droplet trapped in a SLIPS wedge follows an imposed signal with a lag determined by the friction force acting on the liquid.

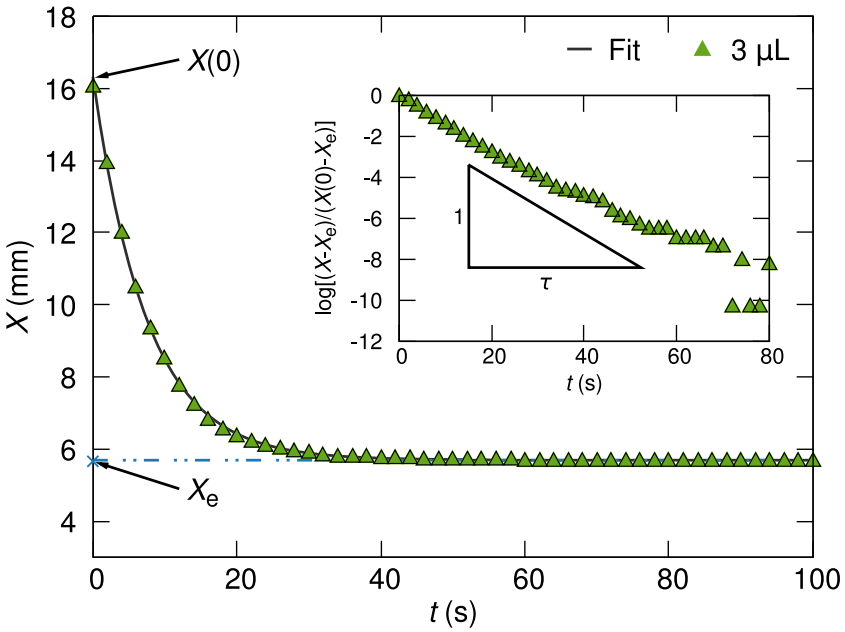

Figure 5.23: Time dependence of the position of the droplet, tracked by measuring the average distance of the leading and trailing menisci relative to the apex of the wedge $X(t)$. The time evolution obeys an exponential decay (continuous line) with a relaxation time scale τ (inset).

Figure 5.23 shows the time dependence of the position of a 3 μL droplet in a wedge of opening angle $\beta = 2.8°$. The time evolution obeys an exponential decay with a relaxation time-scale τ (Inset) which was deduced from plots of $\log[(X - X_e)]/[X(0) - X_e]$ as a function of time, t. Values of τ were obtained from all experiments except those in which droplets' motion were temporarily hindered, possibly due to impurities on the surface. All data are shown in Tables 5.4 and 5.5.

Figure 5.24 confirms the scaling of the relaxation time of the droplet with droplet volume, apparent contact angle and wedge angle data shows a good agreement with the expected linear scaling according to the theory (Equation 5.27). The pre-factor in Equation 5.27 allows a capillary speed to be defined, $U_{cap} = \gamma(1 + 6\epsilon)/\mu$ on which τ depends. Using a measure value of 63 mN m^{-}1 for the effective surface tension of the cloaked droplets (see Section 3.1.7), and the reference value of 1 mPa s for the

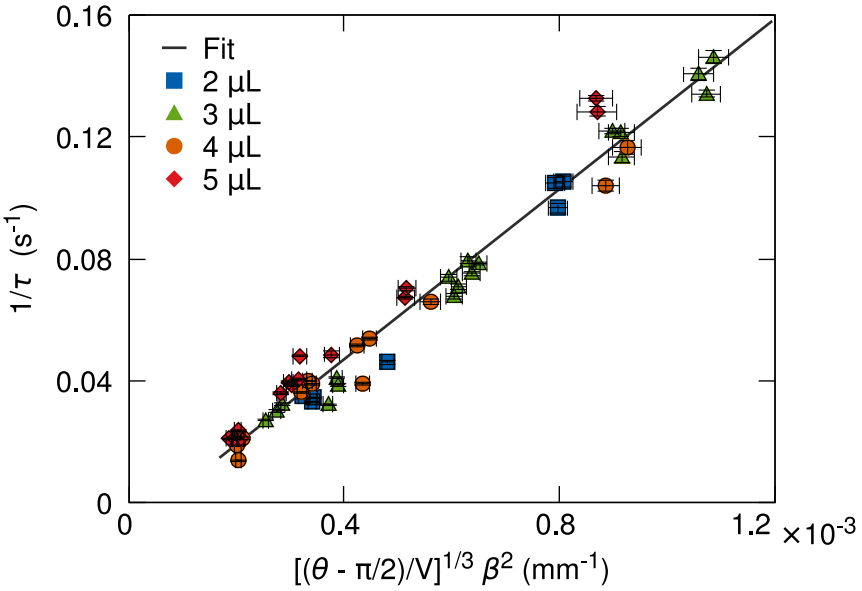

Figure 5.24: Scaling of the relaxation time with V, θ_e and β.

viscosity of water at room temperature, a best fit to the data in Figure 5.24 was found by choosing the a value of $U_{cap} \approx 140$ m s^{-1}. Since $\epsilon = l/H$, this implies a slip length - droplet height ratio of $\epsilon \approx 0.2$, or a $\approx 60\%$ drag reduction. These results highlight the faster and smoother relaxation of droplets confined between SLIPS relative to dry surfaces.

5.6.6 Manipulation of Multiple Droplets

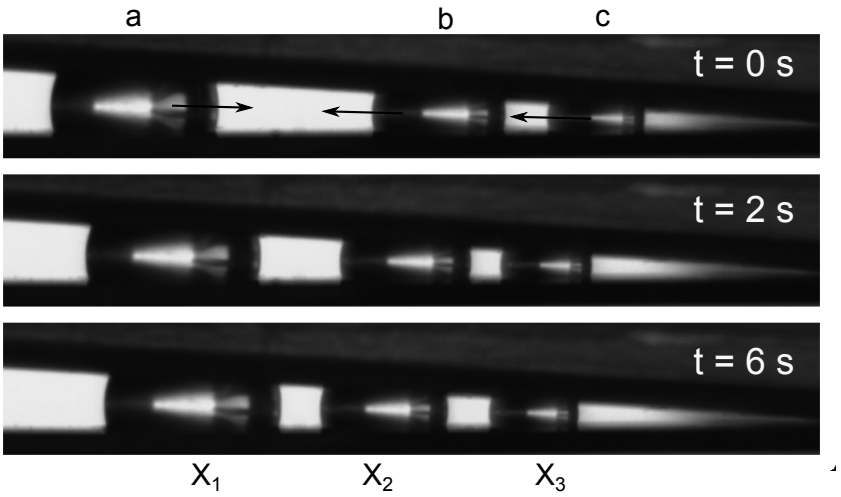

Figure 5.25: Image of droplets of different volumes in equilibrium in the same wedge: a. 14 μL, b. 5 μL, c. 2 μL.

Beyond single-droplet experiments, the manipulation of two or more droplets in wedges was also investigated. Figure 5.25 show three droplets ($V = 2\ \mu\text{L},\ 5\ \mu\text{L},\ 14\ \mu\text{L}$) placed in the same wedge but each settle in different equilibrium positions. Droplets appear to 'attract' or 'repel' each other depending on their initial position in the wedge and their volume ratio,

$$v = \frac{V_{\text{F}}}{V_{\text{N}}} \tag{5.28}$$

where V_{F} and V_{N} refer to the droplet furthest and nearest from the apex of the wedge, respectively. Two droplets having $v \leqslant 1$ will cross paths as they relax to their equilibrium positions and eventually merge into a single drop in a wedge of finite angle. This principle can be used to design paths that allow accurate positioning of droplets upon merging. For $v > 1$, droplets equilibrate with a finite distance between them. This distance reduces with increasing wedge angle up to a critical opening,

$$\beta_{\text{max}} = \left(\theta - \frac{\pi}{2}\right)\frac{v^{\frac{1}{3}} - 1}{v^{\frac{1}{3}} + 1} \tag{5.29}$$

at which point the droplets would merge in a larger drop. Figure 5.26 shows the separated-to-merged transitions for droplets with $v = 2 - 9$.

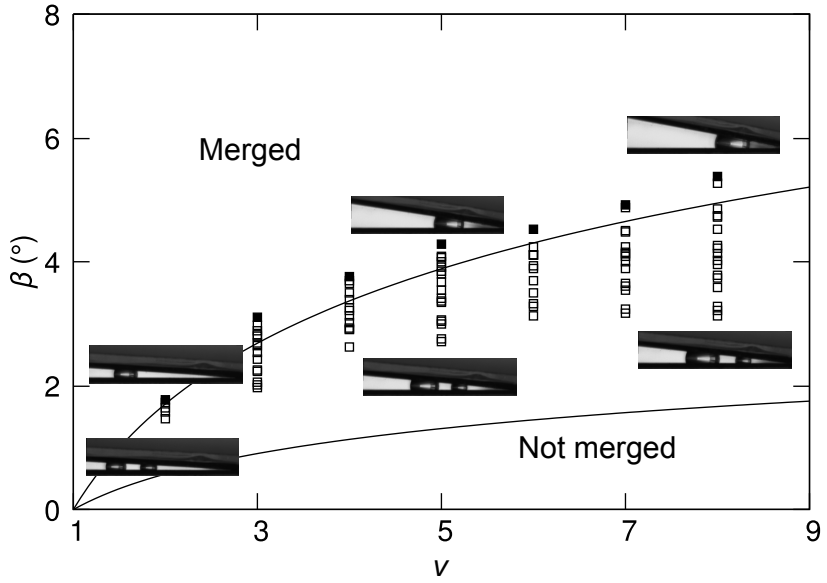

Figure 5.26: Phase diagram for drop merging. Theoretical predictions are represented as two solid lines taking into account the variations in apparent contact angles.

For a given volume ratio $v > 1$, droplets equilibrate at separated positions (open squares) but merge beyond $\beta_{\max}$ (filled squares). The solid lines correspond to the expected bounds due to variations in the apparent contact angles.

As discussed in Section 5.4, in the absence of contact line pinning, compressed droplets ($X(0) < X_e$, $h(0) < h_e$) would move away from the apex of the wedge whereas stretched droplets ($X(0) > X_e$, $h(0) > h_e$) would exhibit inward motion towards the apex. Such behaviours of droplets' trajectories implies that, by strategically placing droplets in pre-defined initial positions, one may observe the following:

- "Attraction" - A droplet placed far from the apex ($X(0) > X_e$) and one placed near the apex ($X(0) < X_e$) would move towards each other (Figure 5.27a).
- "Repulsion" - A droplet placed away from the apex ($X(0) < X_e$) and one placed near the apex ($X(0) > X_e$) would move away from each other. This requires a large volume ratio between the droplets.
- "Change of direction" - Multiple droplets within the same wedge can all initially show inward motion, but upon merging, the increased volume and thus a change in the resultant X_e could trigger a reverse motion, away from apex (Figure 5.27b).

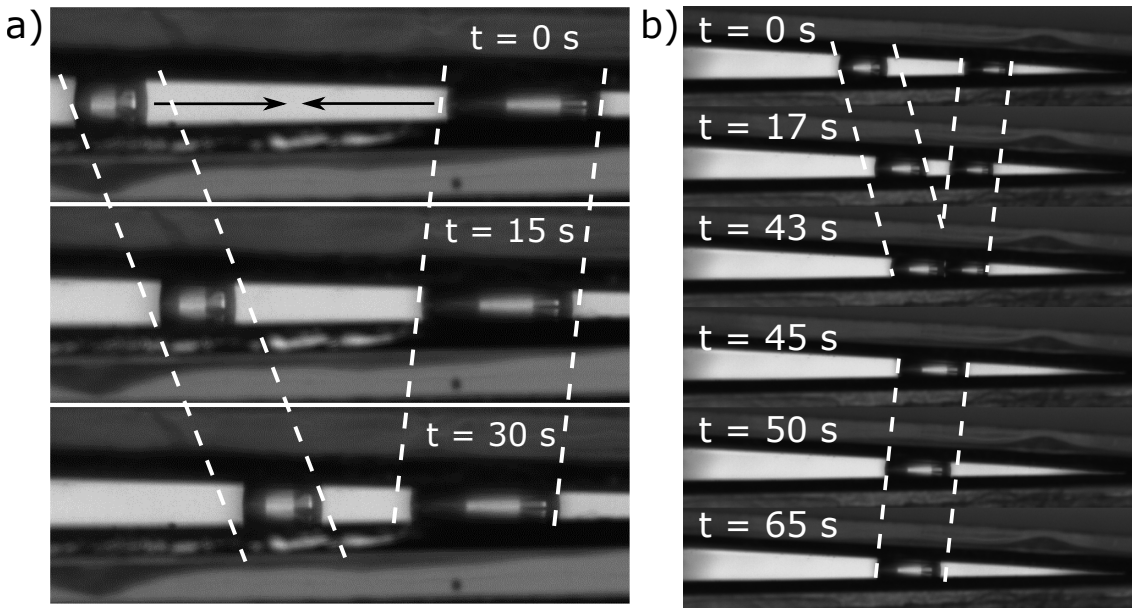

Figure 5.27: Different droplet behaviours inside a wedge.

5.7 Conclusion

Previous studies have shown the richness of shapes of liquid bridging between two solid surfaces. The shape of these capillary bridges depend on the wettability of the surfaces which in turn determines the direction of motion of the droplets confined in a solid wedge geometry. In broad terms, there exists three well-studied regimes for fluid motion in relation to the wettability of the solid wedge. In the complete wetting limit, liquid bridges completely invade the more confined portion of the wedge, the same effect can be seen when the liquid has the angle with the solid $\theta < 90^\circ$. Conversely, a liquid bridge having a contact angle of $\theta = 180^\circ$, or the complete non-wetting limit, confined liquid droplets always migrate away from the apex of wedge. To gain control over the localisation and transport of droplets in these regimes is only possible when a sustained external force is applied as a way to overcome the capillary energy landscape and any pinning effects. Concus & Finn predicted a fourth regime in which droplets having contact angles of $90^\circ < \theta < 180^\circ$ would adopt the shape of truncated spheres [150]. In the regime where $\theta > 90^\circ + \beta$, droplets will equilibrate at finite distances away from the apex. However, because of the contact line pinning inherent to solid surfaces, despite previous efforts, the dynamics of droplets in wedges in wedges in this regime were previously largely unexplored, especially experimentally.

In this study, pairs of lubricant-impregnated surfaces (SLIPS/LIS) were used to construct wedges. The SLIPS served the purpose of removing any pinning effect by eliminating the direct contact between the droplets and the wedge boundaries. It was found that, using the SLIPS wedge, smooth transport and controlled positioning of partially non-wetting droplets can be achieved purely by the reconfiguration of the boundaries, without the need for sustained external forces.

The lack of pinning allows droplets to freely move within the SLIPS wedges to their equilibrium positions. In equilibrium, droplets adopt the shape of truncated spheres, this has allowed the equilibrium radius of droplets, R_e, the equilibrium position, X_e, aspect ratio, h, and the equilibrium surface free energy, F_e to be predicted in terms on the droplet volume, V, the apparent contact angle, θ_e and the wedge opening angle, β. Initially, experimental data show scatter and a lack of correlations between these

parameters. Re-examination of experimental conditions revealed a delicate interplay between wetting properties and geometry and were thus taken into account in all theoretical predictions. The time dependence of X_e also revealed a remarkably smooth dynamics consistent with an exponential approach to equilibrium with a time-scale, τ, which is another strong evidence of the lack of direct contact between the droplet and the solid surfaces.

Last but not least, the independence of the droplets' equilibrium radius on β supports that idea that the surface free energy is invariant, for a given droplet volume and apparent contact angle, upon a change in the wedge angle or a translation along the wedge. This means that the change in internal energy caused by a reconfiguration of the wedge boundaries is zero. This opens up the possibility of unlocking pathways for droplet manipulation and actuation at no energy cost.

Chapter Summary

This chapter focused on the experimental aspects of capillary-driven motion of droplets in confinement through the use of lubricant-impregnated surfaces and presented an improved method to create SLIPS. This system has allowed smooth dynamics and accurate positioning of droplets to be achieved *via* a reconfiguration of the wedge boundaries. It has been shown that the internal energy of droplets upon reconfiguration of wedge and upon translation in the wedge remains unaltered.

The next Chapter presents a system in which autonomous propulsion and positioning of droplets can be achieved through a combination of a variations in the thickness of the lubricant and an effect similar to that of the "Cheerios effect", without the need for cumbersome micro-texturing.

Chapter 6

Droplet Transport and Positioning

This chapter presents a method of creating highly mobile droplets on lubricant-impregnated surfaces, without the need for complex micro-texturing. It will then go on to demonstrate the "proof-of-concept" of droplet motion in the presence of thickness variation in the lubricant layer *via* a series of experimental arrangements. Finally, it will describe the method used to achieve autonomous propulsion and self-positioning of droplets using macro-scale patterning on lubricant-impregnated surfaces.

6.1 Background of Droplet Motion on Surfaces

Normally, the spreading of a droplet on a smooth surface is described by the Hoffman-de Gennes law [156, 157], which gives a relationship between the contact angle and the edge speed. When a liquid drop is placed on a horizontal surface, its edges move according to Tanner's law [158] or the laws of Lopez *et al.* [159] for small or large droplets, respectively [160]. However, its centre of mass does not move horizontally and the droplet's equilibrium contact angle with the surface is determined by the surface's wettability. With uniform wettability across the surface, the droplet will spread to a static configuration dictated by its contact angle. If, however, the surface's wettability is not uniform the droplet will move towards an area of greater adherence, or equivalently, with which it has a lower contact angle. The droplet's contact line advances or recedes if its dynamical contact angle is greater or smaller than the local equilibrium value. Therefore, it is possible to induce motion to droplets by treating a surface to produce a

gradient in its wettability (Figure 6.1).

Steinberg first proposed the hypothesis of differential adhesion as a way to explain the cell organisation and showed that the cellular motion was related to an adhesion gradient [161]. Subsequently, the idea of adhesion gradient was further explored by Carter in the study of the migration of cells which showed that cells can move on surfaces where a gradient of a chemical species with which it has strong affinity is present [162]. Inspired by the works by Steinberg and Carter, this mechanism of droplet motion on heterogeneous surfaces was first identified by Greenspan who attributed the motion of liquid droplets to the differential adhesion on the droplet's leading and trailing edges [163]. He predicted that a droplet should move on a surface from a region of lower adherence to that of a greater adherence and formulated the first hydrodynamic theory to explain such motion, which was further consolidated by Brochard [164]. Experimentally, Chaudhury and Whitesides demonstrated this behaviour and observed uphill motion of water by placing water droplets on a surface having a spatial gradient in its surface free energy and found that the motion of the droplet originated from an imbalance of forces acting on the liquid-solid contact lines on two opposite sites of the droplets [165]

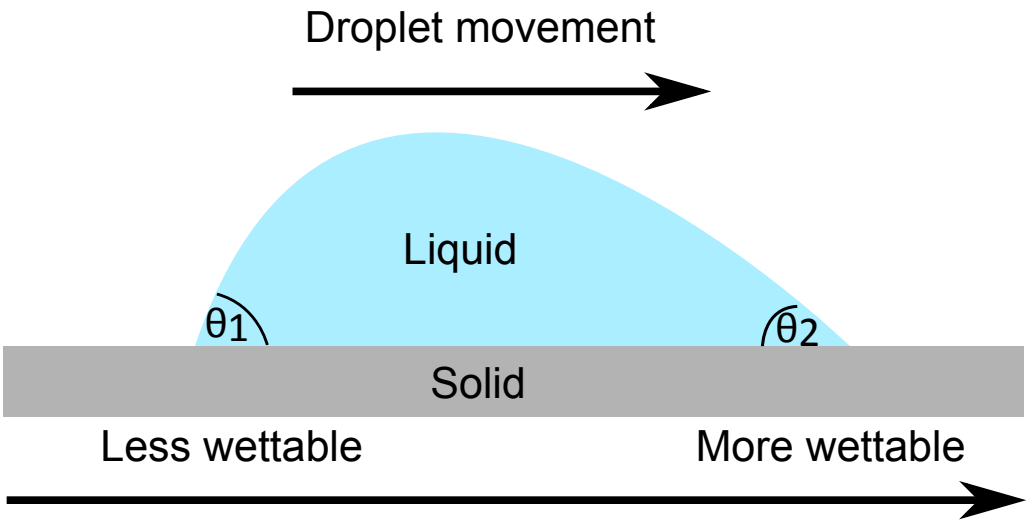

Figure 6.1: Droplet motion due to wettability gradient, i.e. $\theta_1 > \theta_2$.

Droplet motion has since been a extensively studied topic of research. The ability

to induce controlled motion to droplets and achieve self-positioning of droplets thus not only generates fascinating science, but can also lead to advances in various practical applications, such as digital microfluidics [153], inkjet printing [166], self-cleaning surfaces [23] and systems in which directional transport of liquid droplets is heavily involved [167–171].

One of the methods to create self-propelling droplets on a solid surface is to introduce an interruption to the wetting symmetry of the liquid [160, 172]. It is possible to create a Laplace pressure gradient within the droplet by introducing a wettability gradient between both sides of the droplet, which will generate a flow within the droplet, forcing it to move [173]. This type of droplet motion is described as "surface tension driven" and the movement of droplets relies on a gradient in surface energy. This surface energy depends on the surface itself as well as other parameters such as temperature. The main methods of creating such surface with surface energy gradient include:

- *Chemical gradient* - Daniel *et al.* [174], Chaudhury & Whitesides [175] and Longley *et al.* [176] prepared surfaces for their studies of droplet motion by a diffusion-controlled chemical reaction of a functional alkane with the surface. These surfaces are hydrophobic on one of the extremes and progressively hydrophilic toward the other end. Droplets placed on such surfaces would move toward a more hydrophilic region. Choi *et al.* showed that this type of surface can be created using contact printing of octadecyltrichlorosilane (OTS) [177]. Hernández *et al.* demonstrated that chemical gradients can be created on graphene to induce droplet motion [178].

- *Temperature gradient* - It is also possible to create droplet motion by introducing a temperature gradient to the surface. Bouasse performed experments with an oil drop on a slightly tilted metal wire and observed upward motion when the lower end of the wire was heated [144]. Brzoska *et al.* showed that droplet motion was feasible on hydrophobic surface with the application of a thermal gradient but motion was found to only occur above a certain droplet radius [179]. Yarin *et al.* studied the motion of droplets of different alkanes along glass fibres and observed droplets moving along a thin fibre when a temperature gradient was created along the fibre [180]. More recently, Bjelobrk *et al.* showed immensely

enhanced thermocapillary-induced droplet motion using lubricant-impregnated surfaces [99].

- *Surface topography gradient* - Surface texturing have often been used to alter the wettability of surfaces. McHale *et al.* was the first to use a gradient in superhydrophobicity to move and position droplets [181]. Reyssat *et al.* created a surface decorated with texture of variable density which caused impacting droplets to bounce off obliquely [182]. Chu *et al.* demonstrated the ability to harness the design of asymmetric nanostructured surfaces to achieve uni-directional spreading of liquid [183]. In additional to pillar arrays of varying density, self-propelling and positioning of droplets have also been shown by Li *et al.* using continuous topography gradient in the form of a radial pattern [170]. In their subsequent work, they also showed that the same radial pattern can be used to induce motion to oil droplets by rendering the surface oleophobic using table-top like features [169].

- *Electrowetting* - Electrowetting is the best-developed method to manipulate droplets [184]. By applying voltages to electrodes embedded just below the substrate surface, a charge is creating at the interface between the droplet and the surface. This applied charge adds an electrostatic energy which can be accounted for by imagining a reduced effective interfacial tension. As a result of this, a flow is created in the direction of lower interfacial tension where no voltage is applied. The applied voltage renders the surface onto which it is applied more hydrophilic and hence causes to droplet to migrate towards it. Baratian *et al.* demonstrated the control of contact angle and thereby the manipulation of droplet shape and position using a wedge geometry [155]. Pollack *et al.* reported rapid actuation of discrete droplets through direct electrical control of their solid-liquid interfacial tension [92]. Using dielectrowetting, McHale *et al.* showed that the wetting of dielectric liquids can be enhanced and controlled using non-uniform electric fields and their findings provide a non-contact electrical actuation process for meniscus and droplet control [185].

A central challenge in droplet motion and a common feature of a droplet on a surface is that its three phase contact line is often pinned by surface imperfections or defects on

the surface, which can be detrimental to the actuation of droplets. Thus, droplet motion in direct contact with the solid surface can only be achieved by overcoming a minimum static friction force arising from the contact angle hysteresis. A common method to achieve this is by the use of mechanical actuation such as vibration and repeated stretching and relaxation of the droplet. This type of droplet motion is described as "contact line driven" which occurs through an imbalance of pinning forces on the edges of the contact line. Studies by Hao *et al.* [186], Longley *et al.* [176], Duncombe *et al.* [167], Mettu *et al.* [187], Shastry *et al.* [188], Daniel *et al.* [189], Dong *et al.* [190] have demonstrated the abilities to induce motion to droplets using mechanical actuation.

Other methods of achieving droplet propulsion include the use of asymmetric surface texturing, and Leidenfrost effect but are often difficult to make and requires a huge energy input [191–193]. All of the aforementioned methods have shown the ability to induce droplet motions, but they are still plagued with problems. Since the mechanism for motion rely on the wetting properties which is dependent on the physical features on the surface, any disruption to these features could cause a discontinuity in the wettability gradient and thus hinder the motion of the droplet. Furthermore, these surfaces usually require lengthy fabrication with complicated procedures, and are expensive to produce. Another complication arises as droplets advance on these surfaces they tend to move from more hydrophobic areas to hydrophilic areas leading to a decrease in the droplet's contact angle. This happens because the droplet's footprint radius must change for it to maintain its spherical shape as a way to minimise surface energy. Last but not least, the localisation and control of droplets on these surface are only possible with sustained external forces. With or without an external stimulus the movement of a droplet on a surface is always subjected to a minimum force, due to the contact angle hysteresis, and any small defects in the surface will cause contact line pinning which hinders any motion.

Chapters 4 and 5 have shown that droplets have highly mobile contact lines when placed upon lubricant-impregnated surfaces (SLIPS/LIS) due to the lack of direct contact with the underlying solid surface. Therefore, SLIPS/LIS offer an opportunity to study the motion of self-propelling droplets in low friction situations. The rest of

this chapter will show the experiments carried out to achieve droplet motion on these types of surfaces.

6.2 Proof of Concept

To achieve droplet motion on lubricant-impregnated surfaces, both surface tension driven and contact line driven motion were considered. Due to the presence of a lubricant layer between the droplet and the surface, it is not obvious how a contact line can be defined for droplets on lubricant-impregnated surfaces. The lack of a contact line also means that it is not clear how contact line driven motion can induced.

As for surface tension driven motion, droplets move as a way to minimise the total surface free energy. A comparison of the interfacial tension of a spherical droplet in the presence of air with the interfacial tension of an identical droplet in the presence of the lubricating liquid (silicone oil) reveals a difference in their total surface free energies. The difference in the surface free energy between the two configurations can be written as,

$$\Delta E = A(\gamma_{\mathrm{wo}} - \gamma_{\mathrm{wa}}) \tag{6.1}$$

where A is the surface area of the droplet, and γ_{wo} and γ_{wa} correspond to the interfacial tensions of the water-oil interface and the water-air interface, respectively. Experimentally, γ_{wa} and γ_{wo} were measured as $\gamma_{\mathrm{wa}} = 72.8$ mN m^{-1} and $\gamma_{\mathrm{wo}} = 46.3$ mN m^{-1} using the method described in Chapter 3.1.7. Substituting these values back into Equation 6.1, one can see that the total surface free energy of a droplet in the presence of air, E_{wa}, is higher than one in the presence of the lubricating liquid, E_{wo}. This means that energetically a droplet would prefer to be immersed in the oil rather than air. However, these two values are representations of two extreme states. Droplets on SLIPS exist in an intermediate state because they are cloaked with a thin layer of the lubricating liquid (see Chapters 4 and 5) with an effective interfacial tension of $\gamma_{\mathrm{oil-cloaked}} = 63.4$ mN m^{-1}. With these values, the following relationship can be obtained,

$$E_{\mathrm{wa}} > E_{\mathrm{oil-cloaked}} > E_{\mathrm{wo}} \tag{6.2}$$

Equation 6.2 suggests that the surface free energy of the droplet is lowest in the presence of the lubricant and therefore, if possible, a droplet will tend to minimise its surface energy by moving towards a region that increases contact with an oil bath and become more encapsulated by the oil [194]. Using this rationale, it is clear to see that droplet motion may be achievable by adding a gradient to the thickness of the lubricant layer along the surface.

6.2.1 Initial Experiments

Following the work by Biswas *et al.* where droplet motion was enabled by a deforming the layer of lubricating liquid on a polymer surface *via* magnetic-field-mediated elasto-capillary transduction [194]. Two experimental arrangements were prepared to show that droplets move when a thickness gradient in the lubricant layer is introduced. In both experiments, lubricant-impregnated surfaces with micro-textured surfaces prepared using the standard method were used as the base surface to allow high mobility of droplets.

Flow System

An obvious way to show the preference of droplets to migrate towards a thicker layer of lubricant is by adding more lubricant onto one side of the droplet.

Figure 6.2a shows the experimental set up. A syringe needle held above the surface with a positioning jig is connected to a syringe pump and was used to deposit silicone oil directly onto the surface. Once deposited, the oil moved radially outwards, away from the syringe and its leading edge travelled along the surface, creating a temporary slope in the oil thickness. A droplet was placed in the middle of the surface and moved in the direction of syringe, towards the thicker bath of oil. Immediate motion was observed to occur upon contact with the advancing front of the oil, resulting in a sudden increase in the size of the wetting ridge on one side. However, the droplet came to a halt as the oil moved around the droplet due to a vanishing discrepancy between the size of the

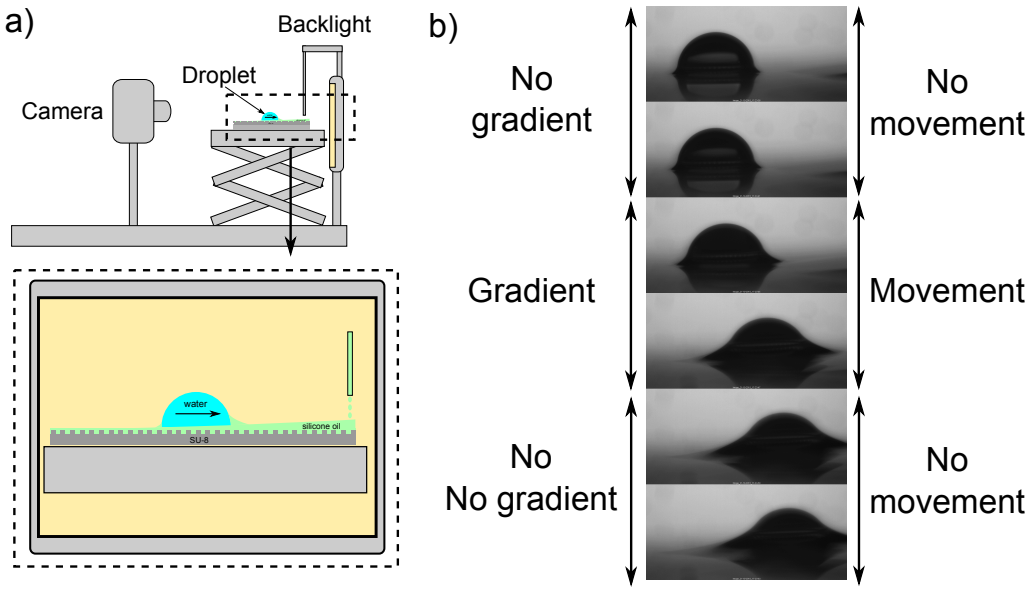

Figure 6.2: a. Experimental set up for the flow system for droplet motion on SLIPS/LIS, b. droplet moving toward deeper end of the oil bath.

wetting ridge on the opposite sides of the droplet, or the lack of a thickness gradient in the lubricant layer. This meant that to create continuous motion, a sustained gradient in the lubricant thickness was needed. In practice, this is extremely difficult to achieve and required accurate flow rate of the oil. Nevertheless, this was the first proof of droplet motion induced by the presence of a lubricant thickness gradient.

Texture Gradient

Unlike the flow system, where the lubricant thickness gradient is introduced to a surface by direct deposition of the lubricant atop of surface, a thickness gradient is created using a gradient in the pillar density on the surface based on the idea of an average lubricant thickness over a unit length.

Figure 6.3 shows a section of a pillared surface with a unit length, L, pillar spacing, l, pillar width, $L - l$, pillar height, h_p, and lubricant thickness, h_o. By considering the average lubricant thickness to be the two-dimensional volume over the unit length, L, the average lubricant thickness can be calculated as,

$$\text{Average lubricant thickness} = \frac{l(h_\mathrm{p} + h_\mathrm{o}) + (L - l)h_\mathrm{o}}{L} \tag{6.3}$$

where h_p and L have been set to 50 μm and 100 μm, respectively. Figure 6.4 shows

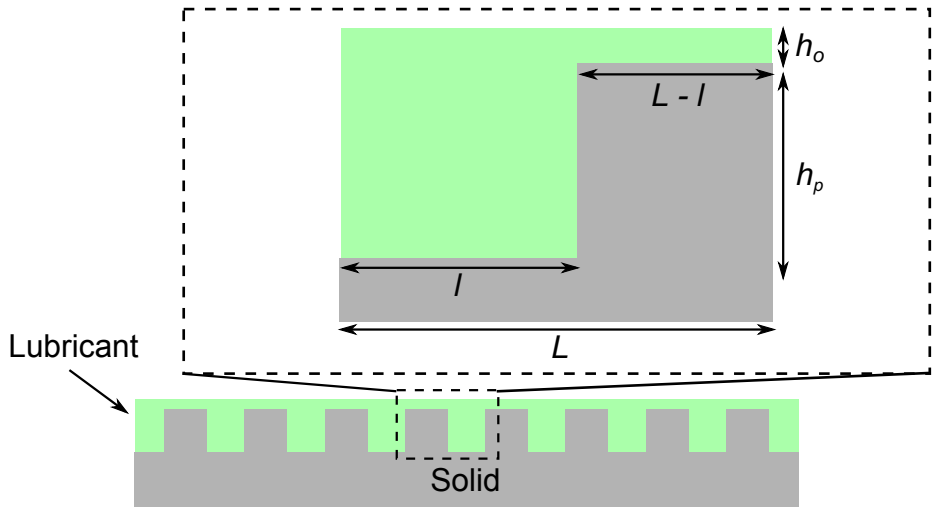

Figure 6.3: Defining the average lubricant thickness over a unit length, L.

the average lubricant thickness for surfaces having lubricant fraction l_f ranging 0.1 - 0.9 with different lubricant thickness (Figure 6.4).

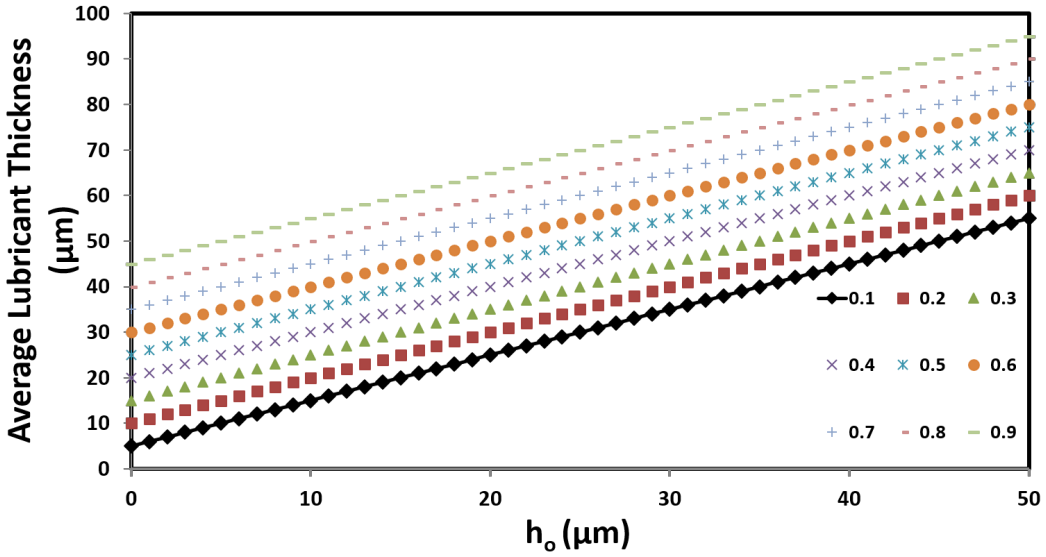

Figure 6.4: Plot of average lubricant thickness as a function of h_o.

Using the idea of an average lubricant thickness, surfaces consisting of 5 μm × 5 μm × 50 μm tall micro-pillars of variables density across the surfaces were fabricated. Figure 6.5a shows the gradient surface used in this experiment and its surface roughness is calculated and shown in Figure 6.5b. The surface roughness is directly related to the average lubricant thickness over a certain unit length (Small roughness, large average thickness).

Figure 6.6 shows droplet (2 μL) moving on a SLIPS (sliding angle $< 1^{\circ}$), it was

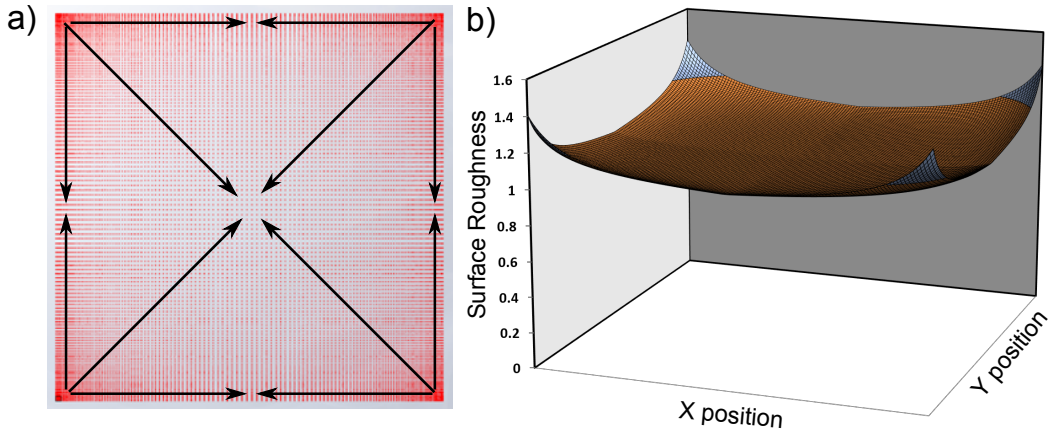

Figure 6.5: a. A representation of the gradient surface used in this experiment. The arrows indicate the direction of decreasing surface roughness and increasing average lubricant thickness. b. Surface roughness on the surface.

initially placed on an area with the smallest pillar spacing (one of the corners), it proceeded to move in a direction with an increasing pillar spacing (indicated by solid arrows). The dashed arrows in Figure 6.6b indicate the direction of droplet motion. Since the pillar spacing also increases towards the centre of the surface, the droplets appeared to have moved away from the camera and became out of focus. Prior to the experiment, the stage on which the surface was placed was levelled. To ensure that the droplet motion was not a result of a tilted surface, droplets were placed in a different corner and motion was again observed but in opposite directions (Figure 6.6).

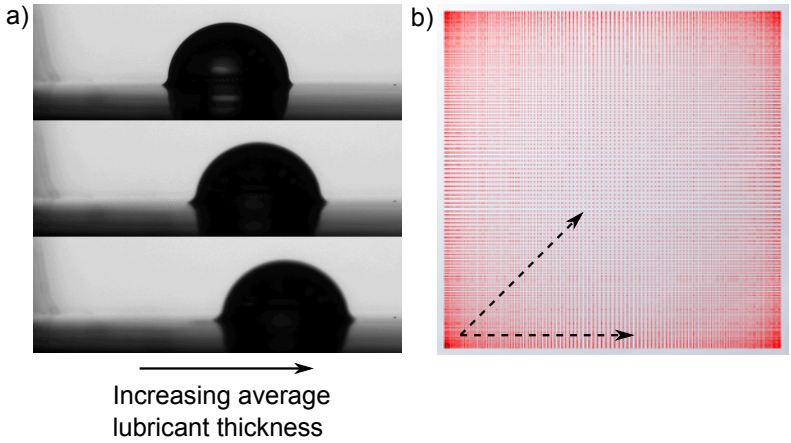

Figure 6.6: a. Droplet moving towards area with greater average lubricant thickness (solid arrows indicate increasing lubricant thickness), b. dashed arrows indicate the direction of droplet motion.

Droplets were only observed to move where there is a difference between the local

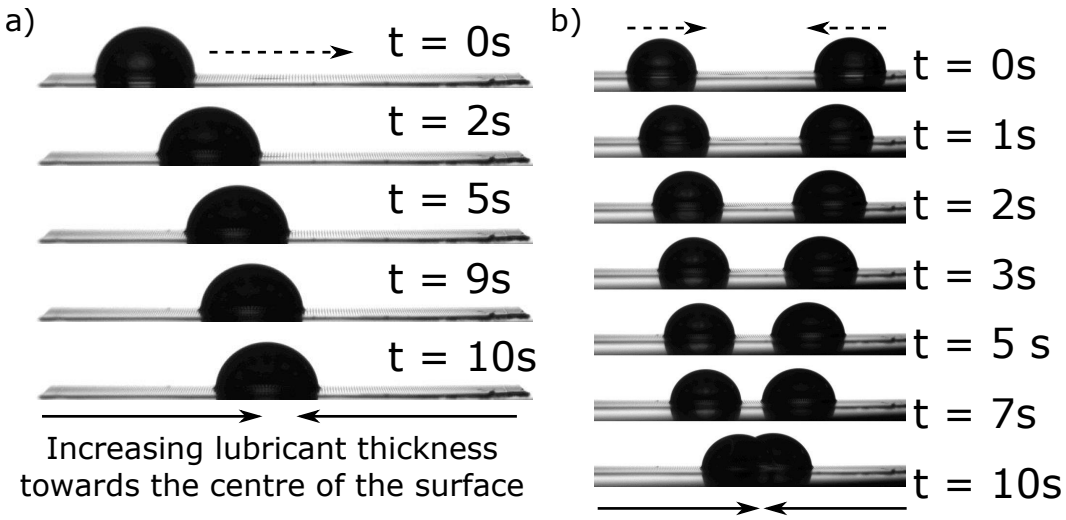

Figure 6.7: a. Droplet moving and stopping in the centre, b. droplets moving in opposite directions, both towards the centre of sample.

pillar spacing at the leading and trailing edges of the droplets. Figure 6.7a shows a droplet would move as long as a gradient in the pillar spacing or the lubricant thickness is present (indicated by solid arrows). Figure 6.7b shows two droplets of identical volumes moving towards the centre of the surface (dashed arrows).

Top view experiments was also carried out. Since the pillar spacing on this surface is the greatest in the centre, it also has the highest value of average lubricant thickness. Figure 6.8 shows that droplets placed on different corners of the surface do indeed migrate towards the centre where the lubricant thickness is at its highest.

Experiments were repeated with different droplet volumes but movement of droplets were only observed for 2 μL droplets. This suggests that there exists a volume dependence of droplet motion on surfaces using texture gradient to create a lubricant thickness gradient. Nevertheless, this experiment provides further evidence that droplet motion can be induced using a thickness gradient in the lubricant layer.

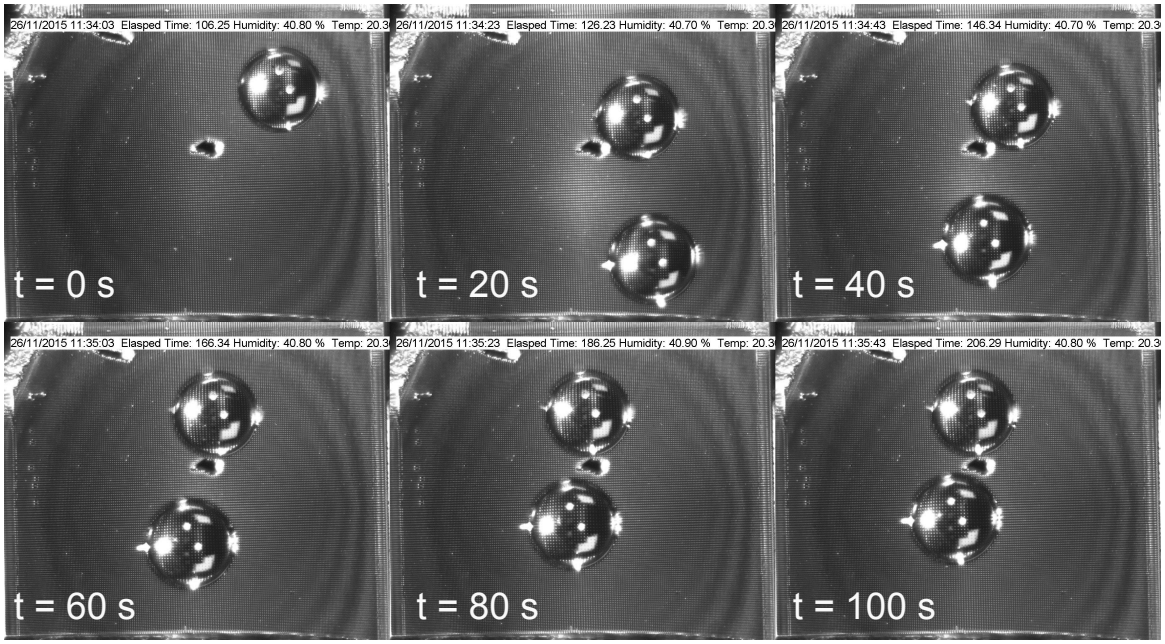

Figure 6.8: Top view sequence of droplets moving towards centre of surface with a central surface defect.

6.3 Droplets on V-Shaped Channels

Although the flow system and the gradient surfaces proved that droplet motion can be achieved, they were either unsustainable or relied on complex surface texturing to create the thickness gradient. Therefore, a surface which provides a lubricant thickness gradient without the need for complex patterning would be ideal. A good example would be that of the wedge geometry or a V-shaped channel. This type of surface pattern provides a continuous radial gradient in the Wenzel roughness, r_{w}, whilst being a significantly simple geometry compared to a pillar array.

6.3.1 A Simple Analogy

Perhaps a simple analogy of droplets moving on a wedge shaped channel would be that of a solid sphere suspended on a channel formed by two diverging walls or rods (Figure 6.9), which inspired the use of a V-shaped pattern. Because of the shape and the effect of gravity, a sphere suspended on the narrow end of the wedge shaped channel would naturally proceed to roll to the wider end of the channel. It will move as long as there is no physical obstruction to its motion, i.e. friction. Eventually, the sphere completely detaches from the two walls and arrives at a state where the potential energy

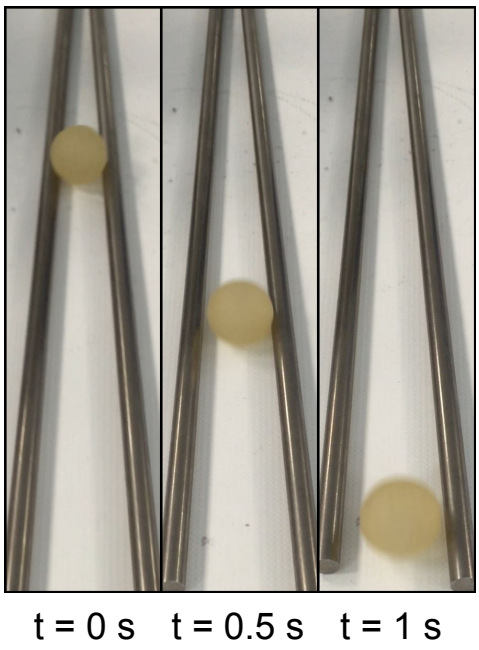

Figure 6.9: Analogy for V-Shaped channels: solid sphere suspended between two solid beams rolls towards the wider end.

is at a minimum.

This picture should hold if the solid sphere is replaced by a liquid droplet. Unlike the sphere, the shape of the droplet on a wedge channel is distorted meaning that it is no longer a sphere and instead of rolling, it would slide. For the droplet to advance to the wider portion of the channel, the state friction arising from the contact angle hysteresis must be overcome by gravity. Although the mechanisms of the moving sphere and droplet are not the same, the sphere moves because of the gravity whereas the droplet "seeks" a location to allow itself to be fully covered by the lubricant, both are examples of minimisation of energy.

It has been shown in Chapter 5 that the application of a nano-particle based coating (Glaco Mirror Coat) can facilitate the adhesion of the lubricating liquid to the surface. Later Chapters will show the ability of this coating to render surfaces with macro-scale surface patterns SLIPS.

6.3.2 Surface Preparation and Characterisation

The preparation process for samples used in this study is summarised in Figure 6.10. Fresh silicon wafers were coated with a layer of SU-8 2025 negative photoresist at a controlled thickness of 50 μm $\pm$ 5 μm *via* a spin-coat process at 1750 rpm. The

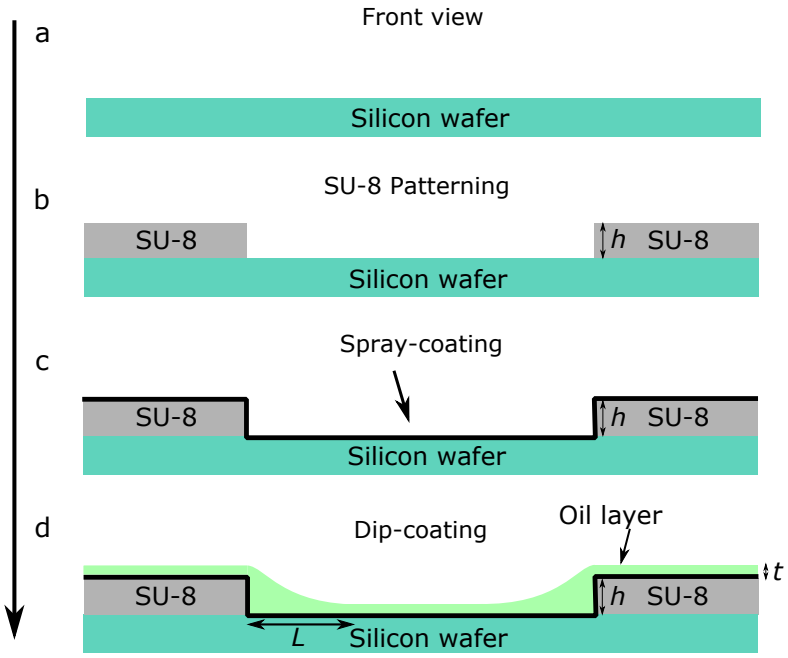

Figure 6.10: Schematics of the production process of V-shaped SLIPS.

photoresist layer was photolithographically patterned to create V-shaped channels with straight vertical walls when viewed from above. The length of all V-shaped channels were fixed at 17 mm and the geometry was controlled by varying the angle of divergence, β, from $2.7° - 5.8°$.

Table 6.1: Dimensions of V-shaped channels

Sample	h/μm	Angle of divergence, $\beta/°$
1	50±5	2.7
2	50±5	3.4
3	50±5	3.9
4	50±5	4.3
5	50±5	4.6
6	50±5	4.9
7	50±5	5.2
8	50±5	5.4
9	50±5	5.6
10	50±5	5.8

The surfaces were subsequently sprayed with a commercially available, nano-particle based hydrophobic coating (Glaco Mirror Coat, Nippon Shine) and were left to dry for at least one hour until the solvent within the coating had completely evaporated. After drying, the samples underwent a dip-coating process at various withdrawal speeds U $(0.1 - 1$ mm s$^{-1})$ in a bath of silicone oil (Sigma Aldrich; viscosity $\eta = 20$ mPa s, surface tension $\gamma_{oa} = 20.6$ mN m^{-1}, which resulted in the deposition of silicone oil on

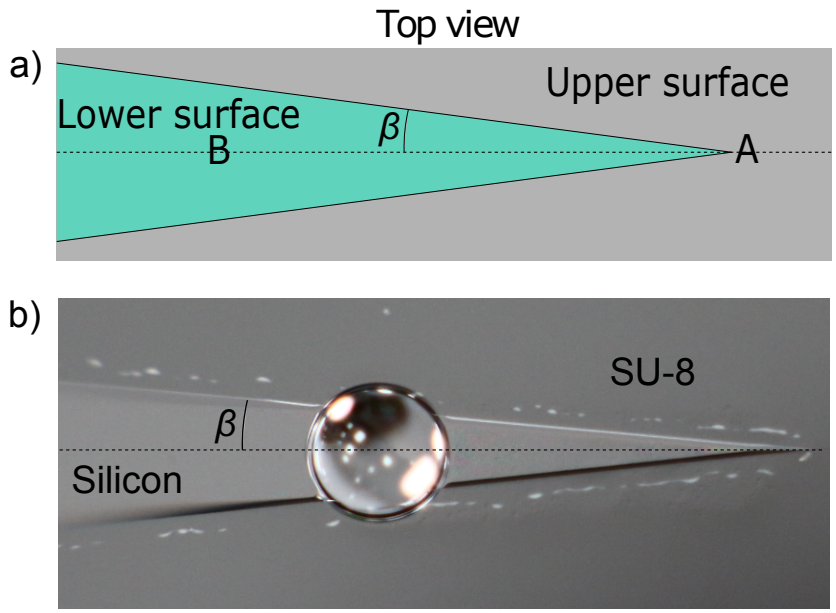

Figure 6.11: a. Top view schematic of a V-shaped channel with an angle β, b. top view image of a V-shaped channel.

the surface of various thickness (see Section 3.11).

As a consequence of the lubricant layer, a contact angle as described by Young's law is no longer present. Therefore, following the method used in Chapters 4 and 5, apparent contact angles defined as the intersection angle of the solid surface with the extrapolated spherical cap-shaped profile of the droplet were used. Measurements were carried out using 2 μL droplets of water in the Krüss contact angle meter (DSA30) on surfaces dip-coated at speeds ranging from $U = 0.1 - 1$ mm s^{-1} (Figure 6.11). Table 6.2 shows the measurements at the upper surface θ_{u}, and the lower surface (silicon wafer), θ_{l}. For a given withdrawal speed, θ_{u} was found to be larger than θ_{l}, which suggests that the lubricating liquid tends to collect within the channel, forming a thicker layer. Both θ_{u} and θ_{l} lie in the range $\approx 110^{\circ} - 115^{\circ}$ and show a slight decrease with increasing withdrawal speed.

For the lubricating liquid to spontaneously impregnate the surface, it is essential that it preferentially wets the surface in the presence of water (See Section 3.1.3). Otherwise, the lubricant may be displaced by the droplets of water and thus allow contact between the droplet and the solid surface. To check whether the Glaco coating allows the surface to retain a layer of lubricant between the droplet and the solid surface

Table 6.2: Apparent contact angles and sliding angles of water droplets placed on the upper and lower surfaces of a V-shaped channel. Standard deviation are calculated from three separate measurements.

U/mm s^{-1}	θ_u/°	θ_l/°	$\Delta\theta_u$/°	$\Delta\theta_l$/°
0.1	115.9 ± 0.4	113.9 ± 0.2	0.2 ± 0.1	0.5 ± 0.2
0.2	113.6 ± 1.1	113.4 ± 0.4	0.4 ± 0.1	0.6 ± 0.3
0.3	112.5 ± 0.3	111.9 ± 0.5	0.3 ± 0.2	0.5 ± 0.1
0.4	112.5 ± 0.3	111.3 ± 0.4	0.5 ± 0.1	0.7 ± 0.1
0.5	111.9 ± 0.8	111.2 ± 0.5	0.3 ± 0.1	0.6 ± 0.2
0.6	112.0 ± 0.2	111.4 ± 0.5	0.3 ± 0.1	0.8 ± 0.1
0.7	111.6 ± 0.1	110.2 ± 0.1	0.3 ± 0.1	0.7 ± 0.2
0.8	110.0 ± 0.6	109.4 ± 0.7	0.6 ± 0.2	0.6 ± 0.2
0.9	110.3 ± 0.7	110.1 ± 0.3	0.6 ± 0.2	0.7 ± 0.3
1	110.5 ± 0.6	108.6 ± 0.4	0.5 ± 0.2	0.9 ± 0.2

and thus be considered as SLIPS, sliding angles measurements on both the upper and lower surface were carried out using the tilt-stage on the Krüss machine, before and after impregnation. Measurements of sliding angle on the upper surface, $\Delta\theta_u$, and the lower surface, $\Delta\theta_l$ were in excess of 5° before impregnation and below 1° after impregnation Table 6.2. This low sliding angle characteristic suggests that, without complex micro-texturing, smooth surfaces can be rendered as SLIPS *via* the deposition of a hydrophobic nano-particle layer which facilitates the impregnation and adhesion of the lubricating liquid to the surface.

6.4 Experimental Methods

6.4.1 Preliminary Experiments and Identification of Equilibrium Configurations

Since the V-shaped geometry provides a continuous radial gradient in the Wenzel roughness, r_w, and it is expected to provide a radial gradient in the lubricant thickness. Therefore, droplets placed on the apex of the V-shaped were expected to move toward the wider portion of the channel and reach an equilibrium in similar manner as that of the solid sphere - completely separated from both walls (see Section 6.3.1). This was based on the assumption that a thickness gradient will no longer be present once the droplet is completely inside the channel.

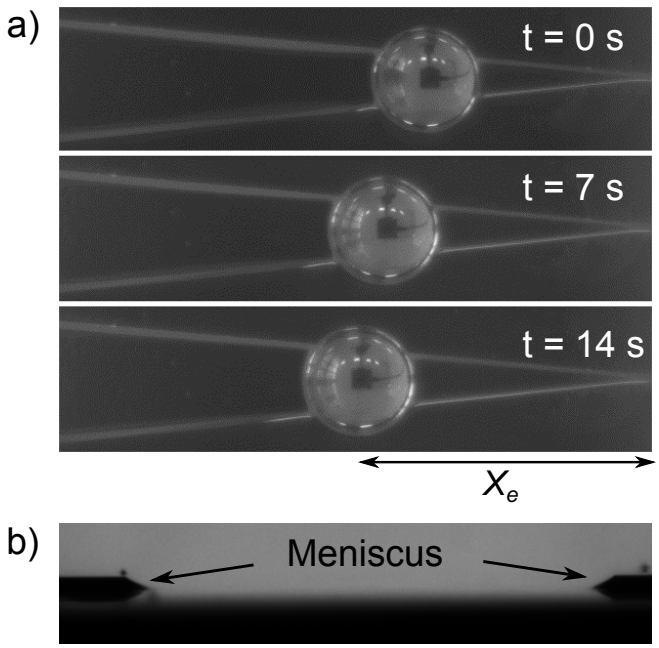

Figure 6.12: a. A 5 μL droplet moving away from the apex ($\beta = 5.6°$) but stopping before expected location, b. side view of a V-shaped channel showing distortion of the lubricant film due to the presence of the SU-8 layer.

In these preliminary experiments, it was found that droplets never completely uncoupled from the walls. Instead, they came to a stand still somewhere before, still in contact with both channel walls, contradicting with previous expectation (Figure 6.12a). After re-examination of the surface, it was discovered that the lubricant film was not flat across the entirety of the surface, but roughly follows the shape of the SU-8 walls. A closer look at the lubricant film revealed what looked like an oil meniscus on both of the walls, possibly the effect of corner filling by the lubricant into the corners formed by the flat silicon substrate and the SU-8 walls (Figure 6.12b). This finding does not completely disprove the previous explanation for droplet motion because an initial gradient in lubricant thickness would still be present in places where the two meniscus are close enough to meet, creating a thicker layer. This observation does, however, suggests that there exists another parameter which may directly influence the equilibrium position of droplets on these surfaces.

In addition to the previous equilibrium configuration in which droplets bridge across the upper and lower surfaces of the V-shaped channel. Further tests were carried out whereby droplets were placed between the channel walls, but far from any of the walls. Such droplets would remain stationary. However, when droplets are placed close to one

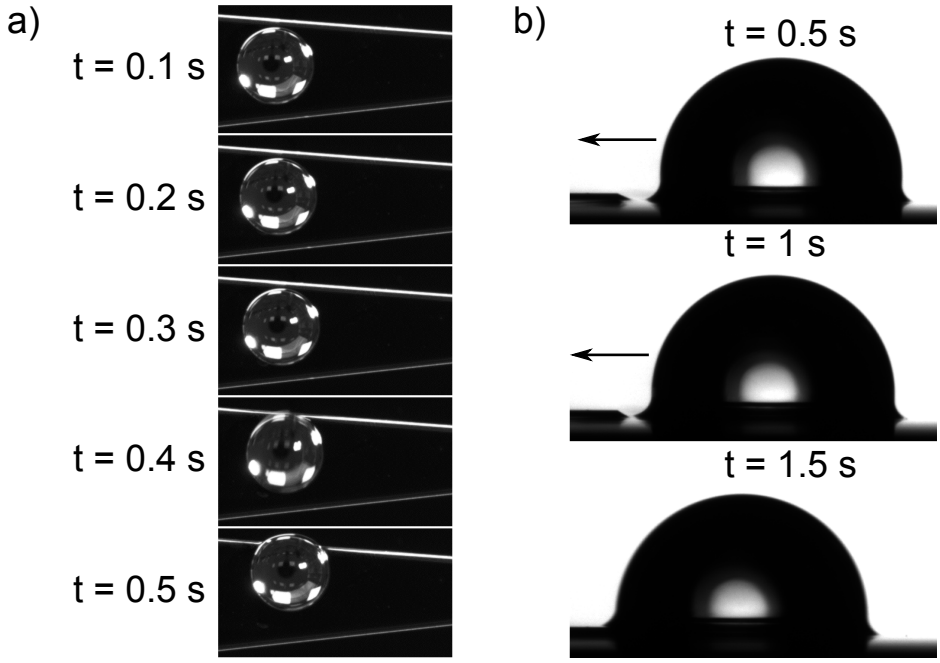

Figure 6.13: Droplet moving towards a channel wall: a. top view, b. front view

of the walls, movement towards one of the channels walls was observed. Front view images showed that droplets placed close to one of the channels walls migrated towards the wall. It was suspected that this movement was a result of the thickness gradient in the lubricant because of the lubricant meniscus created by the channel wall. This observation is a clear indication that an attractive force is present due to the distorted lubricant layer and would go on to explain droplets' equilibrium configuration observed previously (Figure 6.13).

It was found that once droplets are "attached" to one of the channel walls they would remain stationary, leading to another equilibrium configuration. Moreover, this configuration was observed to be invariant upon translation of the droplet along the channel. However, this invariance ceases to exist if droplets come close enough with the second channel wall and by this point droplets are pulled towards the second wall. Droplets in this configuration were observed to move in the opposite direction as previously observed, towards the apex of the channel, until finally settling to the first equilibrium configuration.

Figure 6.14 shows three types of final droplet configurations observed in these experiments. For clarity, in the remainder of this chapter, the following naming convention will be used for the different observed droplets equilibrium configurations:

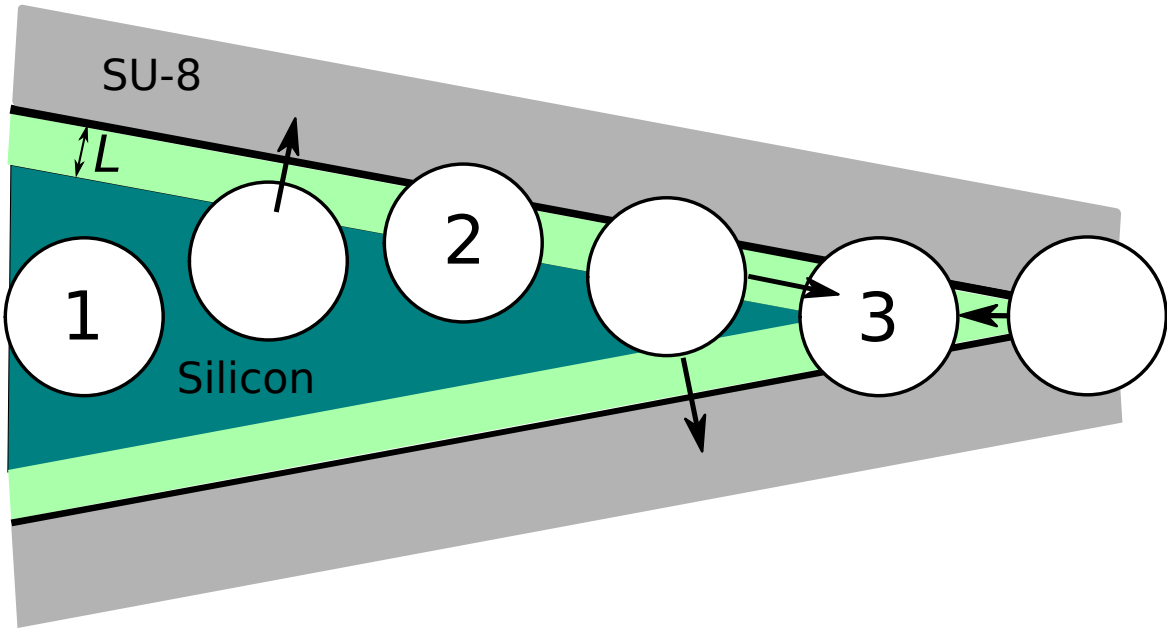

Figure 6.14: Different droplet states of sessile droplets on a V-shaped channel.

- *State 1* - refers to droplets within the channel and not in contact with any channel walls.
- *State 2* - refers to droplets attached to one of the channel walls.
- *State 3* - refers to droplets in contact with both channel walls.

6.4.2 Droplets on V-Shaped Channels Experiments

From the preliminary experiments, one can see that droplets' final states were dependent on the volume, V, and the opening angle, β. These experiments also showed droplet movement towards the channel walls due to the interaction between droplets' wetting ridges and the meniscus formed in the oil-air interface that touches the inner edges of the channel of characteristic length, L (Figure 6.10d). Experimentally, L were measured directly from images taken with an optical microscope, where L was inferred visually from the images (Table 6.3).

The value of L was expected to scale with the thickness of the lubricant layer deposited on the top of the channel walls, t (Figure 6.10d). Following the classical Landau-Levich-Derjaguin (LLD) theory of film deposition (see also Section 3.11), the scaling is $t \approx 0.94\kappa^{-1}Ca^{2/3}$, where $\kappa^{-1} \approx 1.4$ mm is the capillary length of the lubricant

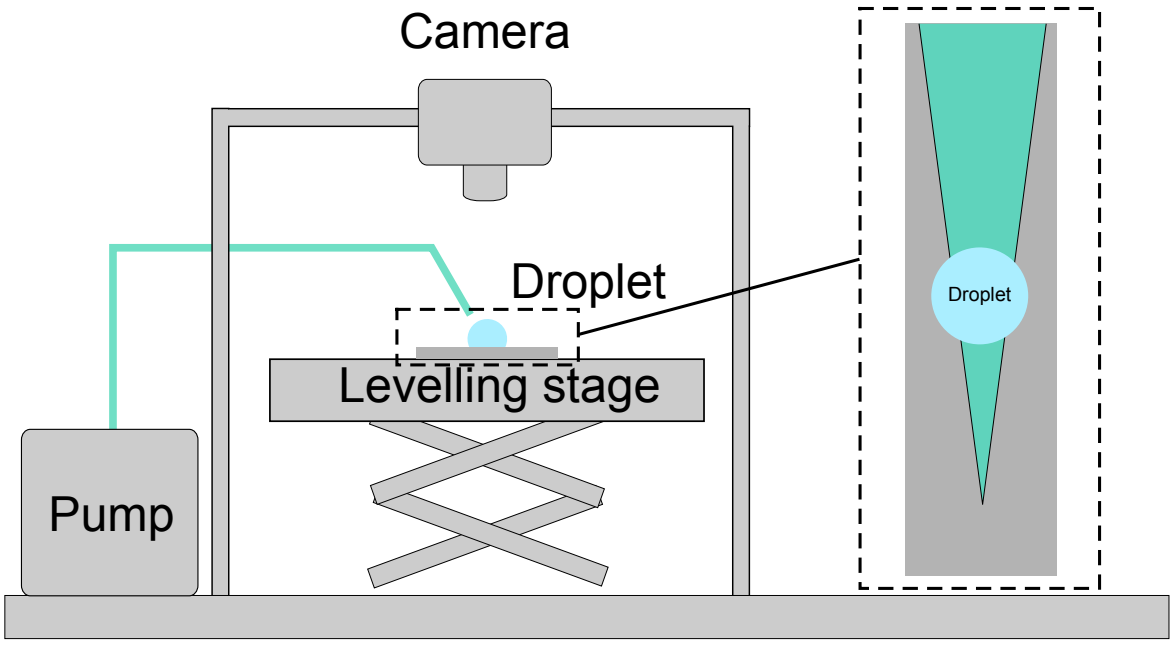

Figure 6.15: Experimental set up for droplet motion on V-shaped channels.

Table 6.3: Theoretical and measured oil film thickness and characteristic length L at different withdrawal speeds. Standard deviations were calculated from three different measurements.

U/mm s^{-1}	Theoretical Thickness/μm	t/μm	L/mm
0.1	2.95	3.33 ± 0.47	0.23 ± 0.01
0.2	4.69	4.67 ± 0.47	0.25 ± 0.01
0.3	6.14	5.67 ± 1.25	0.28 ± 0.02
0.4	7.43	6.67 ± 0.94	0.29 ± 0.01
0.5	8.63	8.33 ± 1.25	0.35 ± 0.01
0.6	9.75	9.33 ± 0.94	0.36 ± 0.01
0.7	10.80	10.67 ± 0.94	0.40 ± 0.01
0.8	11.81	11.33 ± 0.94	0.42 ± 0.01
0.9	12.77	12.67 ± 0.94	0.48 ± 0.01
1.0	13.70	13.33 ± 0.94	0.49 ± 0.01

and $Ca = \mu U/\gamma$ is the capillary number [104, 105].

Figure 6.16 shows a clear correlation between L and the withdrawal speed, U. This shows that the withdrawal speed can be used as a control factor for both the characteristic length, L, and the thickness of the lubricant layer, t.

To systematically test the effect of V, β and L on the final states of the droplets, the experimental set up as shown in Figure 6.15 was used. Single droplets of volume V ranging from $1 - 10$ μL were placed on different areas on the V-shaped channels using a syringe connected to an accurate microfluidic pump which is programmable *via* an external software. To ensure experimental consistency, the syringe was held directly

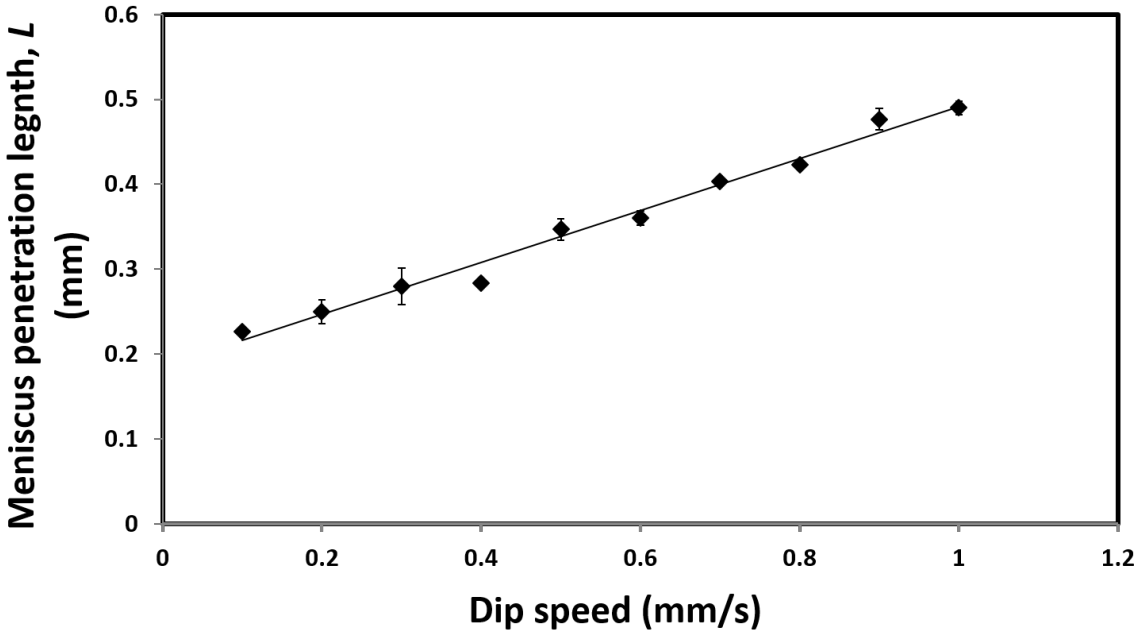

Figure 6.16: Optical microscopy measurements of the meniscus characteristic length, L as a function of dip speed. Error bars are obtained from three separate measurements.

above the surface by a positioning jig with a 25 mm wide slot, into which each surface was inserted. This allows the droplets to be consistently deposited onto the same place on a surface throughout repeated experiments. Droplets were either placed on top of the apex, or along the bisector of the channel at a distance of $X = 17$ mm from the apex (see point A and B in Figure 6.11). After deposition, all droplets were left to freely migrate to their respective equilibrium configurations. The entire process of droplets' migration was monitored with an overhead CCD camera connected to a LabView programme. Droplets' final equilibrium configurations were imaged and analysed using a MATLAB programme (especially the distance from the apex for droplets in state 3, X_e) and standard image processing software (Figure 6.17).

Figure 6.18 shows three types of equilibrium configurations of droplets of different volumes, $V = 2\ \mu\text{L}, 4\ \mu\text{L}$ and $8\ \mu\text{L}$, on a channel with fixed meniscus characteristic length, $L = 0.49$ mm and opening angle, $\beta = 5.4^\circ$. Small droplets ($\approx 2\ \mu\text{L}$) generally stayed within the V-shaped channel, between the channel walls (Figure 6.18a). At intermediate volumes, droplets migrate to one of the channel walls (Figure 6.18b). At even larger values droplets undergo a transient motion towards the second channel wall followed by a translation along the bisector and eventually settles at a distance X_e from the apex (Figure 6.18c). These experiments were repeated for different values of L and

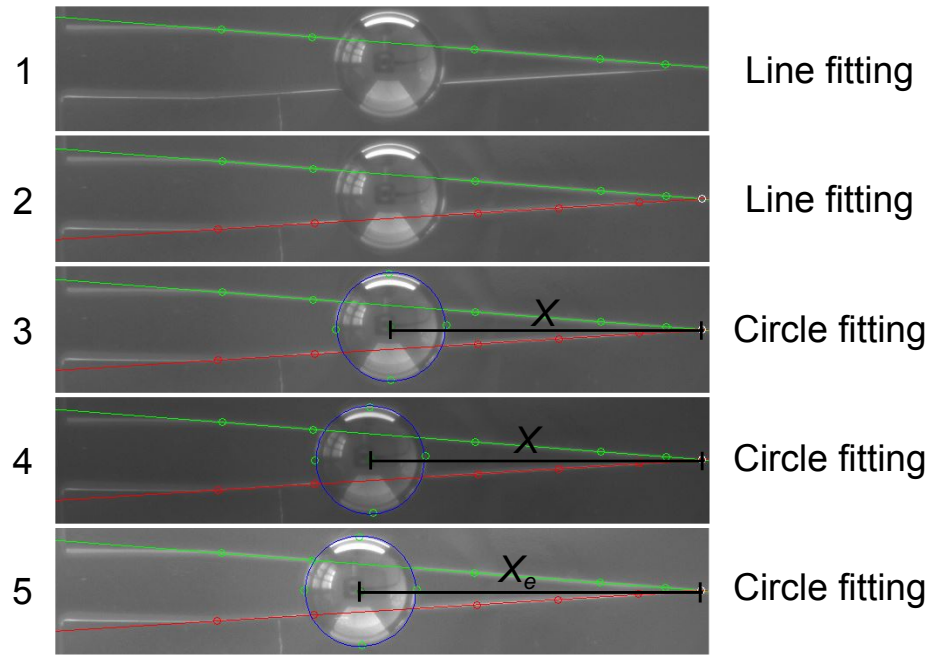

Figure 6.17: MATLAB programme used in determining X_e.

β.

6.5 Results and Discussion

6.5.1 Control Parameters and Transition between States

Experiments suggest that a droplets' tendency to selectively settle to a specific equilibrium configuration on a V-shaped SLIPS channel originated from the interplay between the extent of the wetting ridge (or skirt) around the base of the droplets and the characteristic length of the lubricant meniscus, L. For small droplet volume, V, the droplet occupies a relatively flat portion of the channel and is far from the distorted lubricant meniscus and is not "exposed" to a thickness variation in the lubricant. Therefore, the droplet would remain in this state of local equilibrium (State 1). For larger droplet volumes, the droplet's footprint is large enough and thus its wetting ridge is close enough to one of the channel walls, the interaction of the wetting ridge and the meniscus triggers a inward motion towards to the channel wall. Once the droplet is in contact with the wall the symmetry is recovered and motion ceases, leading to a second local equilibrium (State 2). At even larger volumes, the droplet footprint is large enough such that interaction occur between the droplet and both of the channel

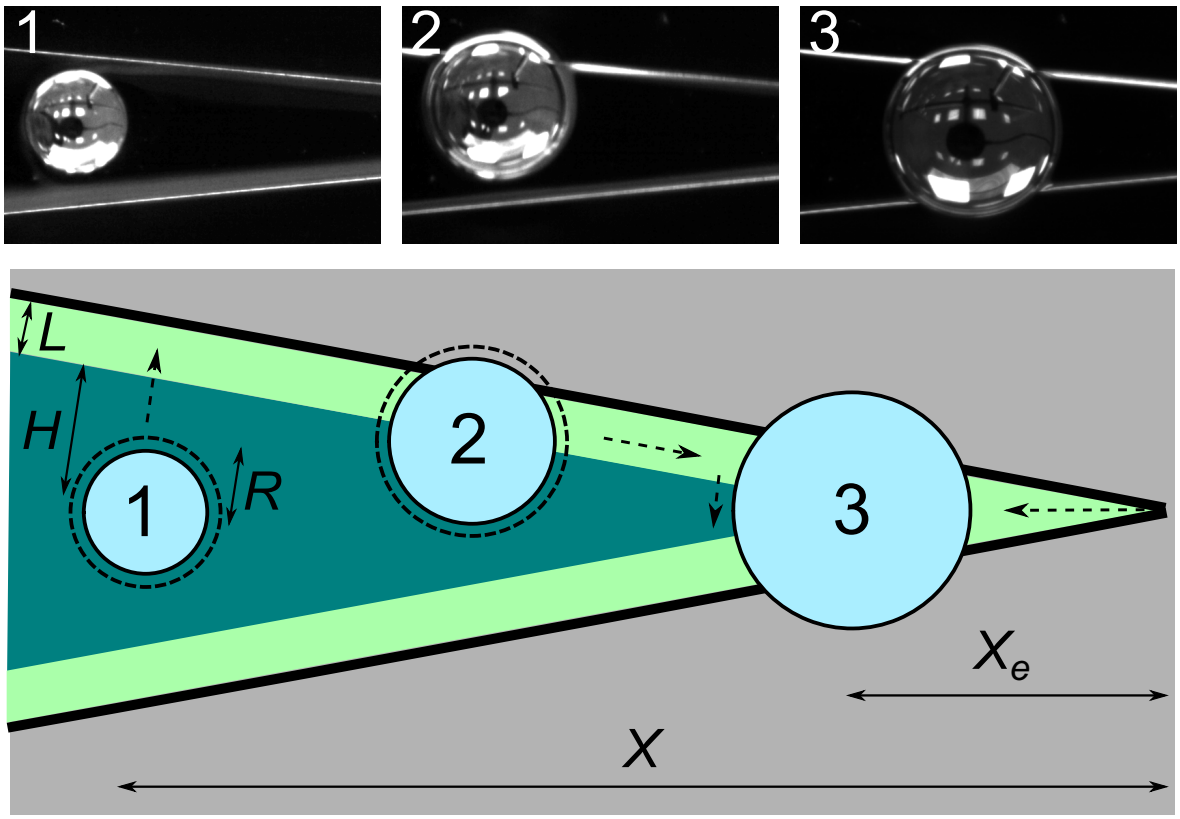

Figure 6.18: Three types of final droplet configurations

walls. This is followed by a net migration along the bisector towards the apex of the channel. The droplet eventually settles into State 3. According to previous observations, droplets initially positioned on the apex of the channel also migrated towards state 3, plus the fact that droplets in state 1 and 2 will ultimately move onto state 3 in the right experimental conditions, this suggests that state 3 corresponds to a global equilibrium configuration.

The interplay between the droplet's wetting ridge and the meniscus can be exploited for the purpose of controlling the droplet positions on the V-shaped channels using the control parameters, V, L and β. Experiments were carried out using a range of these parameters and droplets' final equilibrium configurations were examined.

In summary, for a transient motion to occur between droplets states, the droplet's wetting ridge must interact with the meniscus which can be done by varying V, L and β individually, or at the same time. Figure 6.19 shows the resulting phase diagram for the final configuration of the droplets. It was found that a droplet settles in one of the three configurations (see Figure 6.18) for any given combination of V, L and β. At small V, small L and large β (i.e. bottom right corner of Figure 6.19), droplets are far

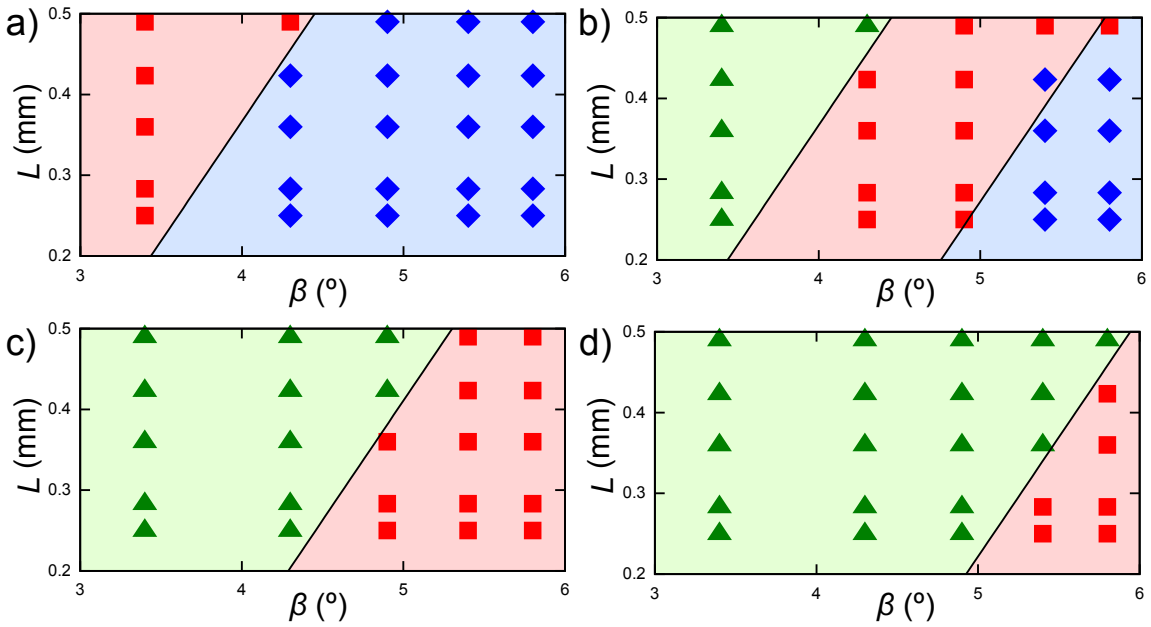

Figure 6.19: Phase diagrams for the equilibrium configurations of droplets on V-shaped SLIPS channels: a) V = 2 μL, b) V = 4 μL, c) V = 6 μL, d) V = 8 μL. Blue diamonds = state 1, Red squares = state 2, Green triangles = state 3. Solid lines represent theoretical predictions.

away from the influence of the meniscus. Therefore, without deliberate perturbation or movement due to the presence of a physical slope, droplets are seen predominantly in state 1 which are shown as blue diamonds in the Figure 6.19. To transition into state 2 (red squares), one can do so by increasing V or L, or equivalently, by decreasing β and further, into state 3 (green triangles). The data presented show a relatively small range, nevertheless it can be used to represent larger picture. Since the same range of L, and β were used, the four phase diagrams can be seen as different parts of the same data set and by increasing or decreasing the V, the data set is shifted left or right, respectively.

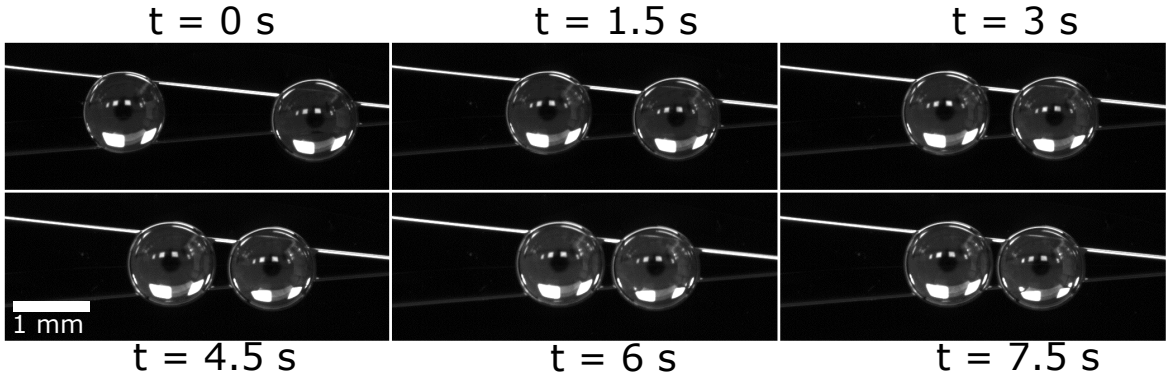

Figure 6.20: Identical droplets moving in opposite direction and reaching the same equilibrium positions

As shown in Section 6.2, when in the presence of a thickness gradient in the lubricating liquid, a droplet tends to migrate toward the area of greater thickness to minimise its surface free energy. This explains the droplets' motion towards the channel walls because of the distorted lubricant layer. However, the use of the V-shape geometry introduces further geometrical constraint to the system, and thus produces two local and one global equilibria. It is worth to note that, two droplets of identical values of V, one placed on the apex and the other moving towards state 3 from state 2 on the same channel with the same L would have the same equilibrium positions.

Mechanically, the migration of the droplets observed is similar to the so-called "Cheerios Effect" where the capillary interactions are observed between solid surfaces are mediated by a connecting interface [195]. In close proximity with each other, two menisci of the same curvature sign, an excess capillary pressure leads to a net attractive force between the solid surfaces [195]. Since a droplet on lubricant-impregnated surfaces is highly mobile and is surrounded by wetting ridge which has the same curvature sign as the distorted lubricant layer, an attractive force is to be expected when they are close enough.

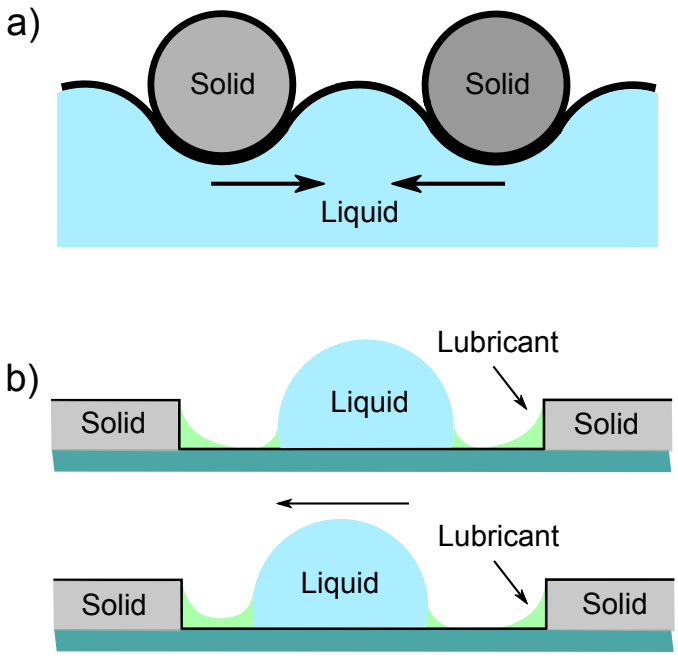

Figure 6.21: a. Cheerios effect between two solid spheres on a bath of liquid, b. droplet moving toward a distorted meniscus.

Using this principle, the transition of droplets from state 1 to state 2, and from state 2 to state 3 are therefore expected to occur when the edge of their wetting ridges come

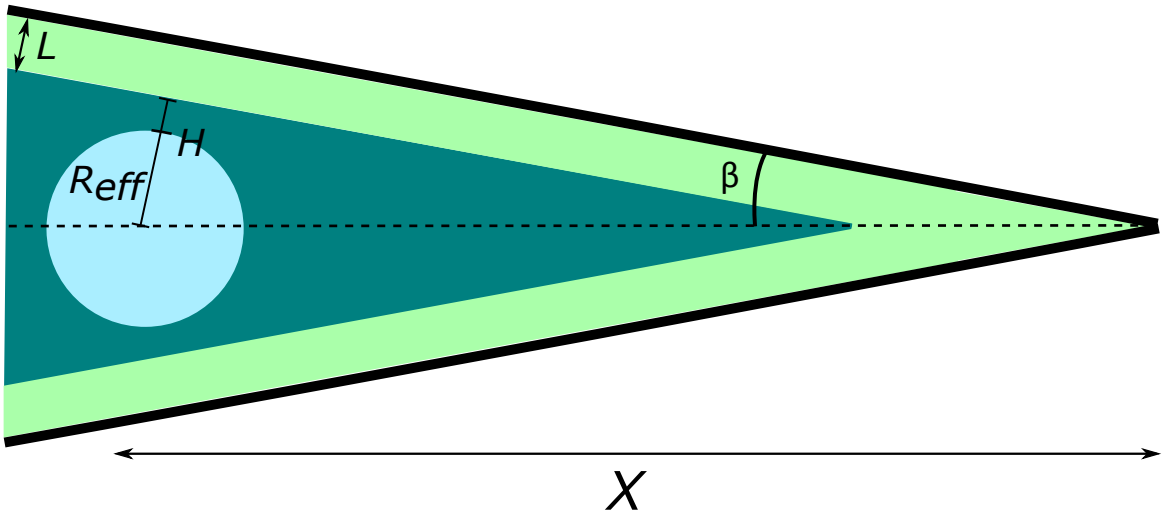

Figure 6.22: Parameters for predicting the droplets equilibrium states: the characteristic length of the meniscus, L, opening angle of the channel, β, effective radius of the droplet, R_{eff} and the lateral length scale, H.

into contact with the meniscus. To predict the transition between states, a effective radius, R_{eff} was used. It was expected to scale with $V^{1/3}$, upto a pre-factor that depends on the apparent contact angle due to the presence of the wetting ridge and the channel geometry. Droplets' transition between the states are therefore expected to occur when R_{eff} matches the lateral length scale, H, such that,

$$H \approx X \sin\beta - L \tag{6.4}$$

where X is the distance between the centre of the droplet to the apex, β is the opening angle and L is the characteristic length of the meniscus (Figure 6.22). Therefore, using the condition $R_{\text{eff}} = H$ as the threshold for droplet transitions, theoretical transition lines can be calculated,

$$L \approx X \sin\beta - R_{\text{eff}} \tag{6.5}$$

Droplets adopt spherical cap shapes when placed on lubricant impregnated surfaces, the effective radius of these droplets roughly correspond to the base radius of a hemisphere, $R_{\text{hemisphere}}$,

$$R_{\text{hemisphere}} = \left(\frac{6V}{4\pi}\right)^{\frac{1}{3}} \approx 0.78V^{\frac{1}{3}} \tag{6.6}$$

where V is the volume of the droplet with a pre-factor of 0.78 which corresponds to a contact angle of $\theta = 90°$. Due to the lubricant layer and the lack of a directly measurable contact angle, values of R_{eff} were expected to deviate , to a small degree, from $R_{\text{hemisphere}}$, leading to a variations in the pre-factor. In the experiments, values R_{eff} were expected to be dependent on the details of configuration upon contact with the lubricant layer, which in turn are dependent on droplet volumes and their locations within the V-shape channel.

Table 6.4: Different pre-factors used in the theoretical predictions for droplet transitions

Volume/μL	Pre-factor(State 1-2)	Pre-factor(State 2-3)
2	0.65	n/a
4	0.96	0.65
6	n/a	0.85
8	n/a	1

Figure 6.19 shows the comparison of the theoretical predictions (solid lines) using this model with the experimental data. Good agreement between theoretical transition lines and experimental data were obtained by setting the pre-factor for different volume droplets. Table 6.4 shows the different pre-factors used for different droplet volumes going from state 1 to 2, and from state 2 to 3. In some cases, a pre-factor was not used because droplets were never observed to undergo certain transitions. For example, 2 μL droplets were predominately seen in state 1 and state 2, but never transition into state 3. Similarly, 6 μL and 8 μL droplets were large enough to have always moved into state 2 and state 3.

6.5.2 Droplets' Global Equilibrium

Due to the symmetry and the lack of a thickness gradient in the lubricant layer, state 1 and state 2 are expected to be invariant upon translation along the bisector of the V-shaped channel and either of the channel walls, respectively (Figure 6.23). Conversely, droplets in state 3 always settled to a well-defined equilibrium positions in relation to the apex of the V-shaped channel. Such a selection in the equilibrium positions of

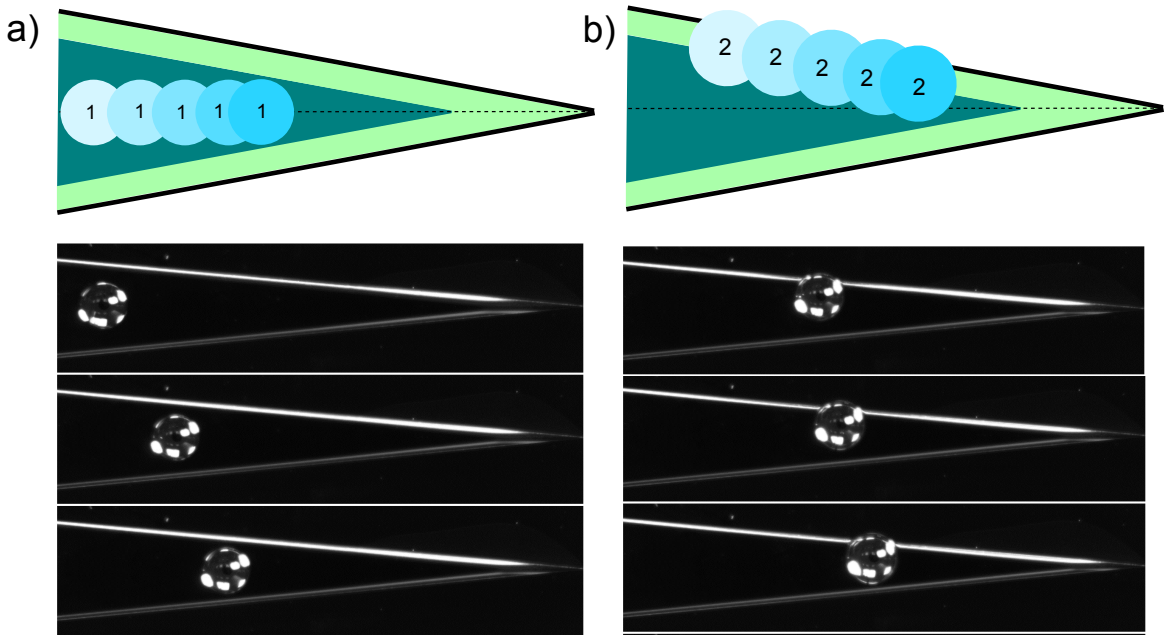

Figure 6.23: Invariance of state 1 and state 2: state 1 and state 2 are expected to be invariant upon translation along the bisector of the V-shaped channel and either of the channel walls, respectively.

droplets in state 3 is related to the net force acting on the droplet in all directions. The net lateral force was computed by integrating the tension exerted by the meniscus on the droplet over the droplet's contour, such that,

$$F = -\gamma R \int_0^{2\pi} \cos\theta \hat{\mathbf{r}} \, \mathrm{d}\varphi, \tag{6.7}$$

where $\theta(\varphi)$ is the local apparent contact angle, $\hat{r} = (\cos\varphi, \sin\varphi)$ is the local unitary normal vector to the apparent contact line and φ is an azimuthal angle (Figure 6.24).

A droplet reaches an equilibrium when $F = 0$. To calculate the total net force in the system, an approach was used whereby the apparent contact angle of the droplet takes on different values along its contour doe to the distorted lubricant and the underlying solid geometry (see Table 6.2). To model such a variation, a piecewise distribution of the apparent contact angles was used over the three regions: θ_l, θ_u and θ_a (Figure 6.24b) delimited by the angles φ_1, $\varphi_1 + \varphi_2$ and $\pi - (\varphi_1 + \varphi_2)$, respectively, such that,

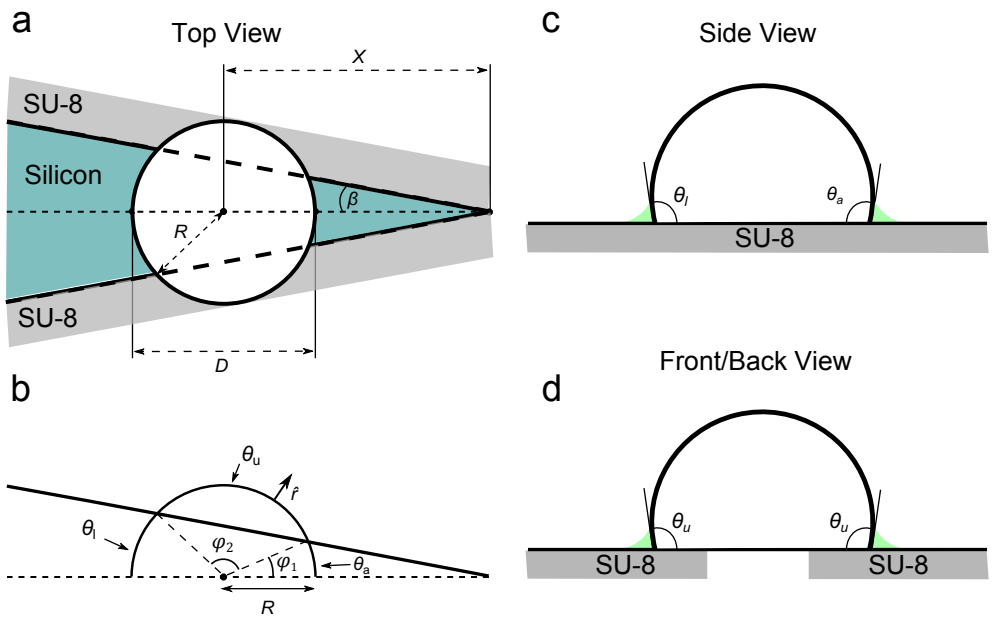

Figure 6.24: Schematics of the model for the configuration of a droplet in a V-shaped channel in state 3: a. top view showing equilibrium position, X, drop diameter, D, opeing angle, β, and droplet radius, R, c-d. the distribution of the three apparent contact angles, θ_{l}, θ_{u} and θ_{a}.

$$\theta(\varphi) = \begin{cases} \theta_{\mathrm{l}} & \text{if} \quad \varphi \in [\varphi_1 + \varphi_2, 2\pi - (\varphi_1 + \varphi_2)] \\ \theta_{\mathrm{u}} & \text{if} \quad \varphi \in [\varphi_1, \varphi_1 + \varphi_2] \bigcup [-\varphi_1 - \varphi_2, -\varphi_1] \\ \theta_{\mathrm{a}} & \text{if} \quad \varphi \in [-\varphi_1, \varphi_1] \end{cases} \tag{6.8}$$

To assign values to θ_{u} and θ_{l}, the apparent contact angles of droplets measured on top of the upper surface (SU-8) and in the wider portion of the channel, respectively. The value of θ_{a} was not so obvious to estimate, but as the lubricant tends to collect in the portion of the channel closer to the apex, which was expected to lead to an apparent contact angle $\theta_{\mathrm{a}} < \theta_{\mathrm{l}}$ [66]. With these considerations in mind, Equation 6.7 reduces to,

$$F = 2\gamma R \left[S_{-} \left(\cos\theta_{\mathrm{a}} - \cos\theta_{\mathrm{u}} \right) + S_{+} \left(\cos\theta_{\mathrm{u}} - \cos\theta_{\mathrm{l}} \right) \right] \tag{6.9}$$

where

$$S_{\pm} = \frac{\sin\beta}{R} \left(X\cos\beta \pm \sqrt{R^2 - X^2 \sin^2\beta} \right) \tag{6.10}$$

The net force F is expected to vanish as the droplet equilibrates. Therefore, setting

$F = 0$ in Equation 6.9 gives predictions for the droplet's equilibrium distance from the apex of the V-shaped channel,

$$X_{\mathrm{e}} = \frac{R(\cos\theta_{\mathrm{a}} - 2\cos\theta_{\mathrm{u}} + \cos\theta_{\mathrm{l}})}{\sqrt{\cos^2\beta(\cos\theta_{\mathrm{a}} - \cos\theta_{\mathrm{l}})^2 + (\cos\theta_{\mathrm{a}} - 2\cos\theta_{\mathrm{u}} + \cos\theta_{\mathrm{l}})^2\sin^2\beta}} \tag{6.11}$$

To test the validity of this model, experiments were carried out in which droplets were placed on the apex of V-shaped channels with different opening angle, β, ranging from $2.7^\circ - 5.6^\circ$. All samples were prepared using the standard methods (see Section 6.3.2) and dip-coated at a withdrawal speed $U = 1$ mm s^{-1}, which were expected to give values of $\theta_{\mathrm{u}} = 110.5^\circ$ and $\theta_{\mathrm{l}} = 108.6^\circ$, consistent with previous measurements. Experiments were also carried out with different droplet volumes ranging from $1-7$ μL since Equation 6.11 suggests that the droplets' equilibrium position is affected by the volume of the droplet up to a factor of $R \sim V^{1/3}$. Experimentally, all droplets placed on the apex of the channels exhibited net migration away from the apex and settled in state 3. Figure 6.25 shows a clear linear decrease in the normalised and average data of X_{e} as a function of the β. The error bars correspond to one standard deviation.

To check the level of agreement between the experimental data and the theoretical model. Measured values $\theta_{\mathrm{u}} = 110.5^\circ$ and $\theta_{\mathrm{l}} = 108.6^\circ$ were used in Equation 6.11. However, measuring the value of θ_{a} is relatively difficult. It was, therefore, treated as a fitting parameter in this model and the fitted value of X_{e} are shown in Figure 6.25 as dashed circles. The inset within Figure 6.25 shows the corresponding values of θ_{a} used in the fitting process, which shows a small decrease with as β increases. This trend is in agreement with the previous assumption that the lubricant tends to collect near in the portion closer to the apex, leading to lower apparent contact angles. For example, for channels with greater β, droplets tend to equilibrate at closer to the apex, one would expect a comparatively thicker layer of lubricant and therefore a smaller θ_{a} (Figure 6.25 inset).

The sensitivity of X_{e} on the fitting parameter is reflected by the small difference in the values of θ_{a} which suggests that a strong dependence of the equilibrium position of droplets on the details of the interplay between the shape of the wetting ridges and the

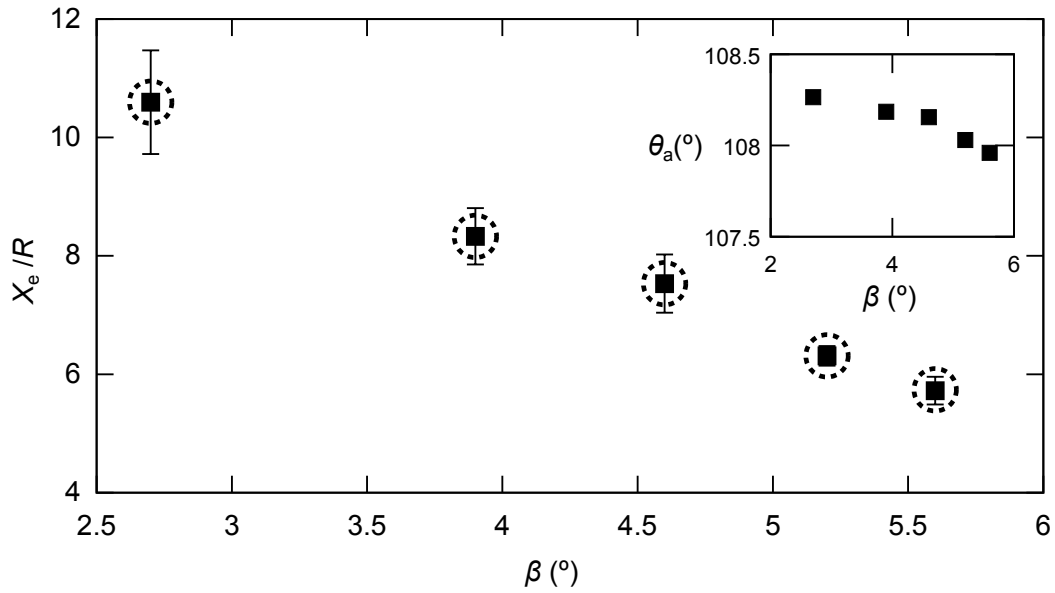

Figure 6.25: Equilibrium position of the droplet in state 3, X_e as a function of the half angle of the V-shape channel, β. The squares correspond to experimental data carried out in channels dip-coated at $U = 1$ mm s^{-1}. Each data point corresponds to normalised values averaged over different droplet volumes in the range of $1 - 7$ μL The error bars correspond to one stand deviation. The dashed circles correspond to the theoretical prediction. The inset data corresponds to the values of θ_a used to fit the experimental data.

underlying geometry. Although such characteristics are not captured by the geometrical model used in this chapter. A more complete model would involve taking into account the variations in all three of the apparent contact angles and direct observation of these angles in different positions on the V-shaped channel. Nevertheless, the model used in this study captures the basic dependence of X_e on β, supporting the validity of force balance approach in estimating the selection of droplets' equilibriums.

6.6 Conclusion

Controlled, guided transport and localisation of sessile droplets have been achieved on macro-patterned surfaces, made possible by the introduction of a slippery lubricant layer impregnated into the surface, completely removing any hindrance to the motion of droplets by eliminating the effect of contact line pinning. The mechanism behind the droplets' self propulsion has been identified as the minimisation of surface free energy through increased contact with the impregnating lubricant layer. Mechanically, the motion of droplets can be interpreted as the interplay between the droplets' wetting

ridges and the lubricant layer and the relaxation of distortions to the lubricant layer, caused by both the droplet and the macro-pattern.

Using V-shaped channels as a model system, experiments have been carried to demonstrate that droplets' specific equilibrium configurations (both local and global equilibria) can be controlled by choosing different thickness of the lubricant layer, droplet volume and the opening angle of the channels. A mathematical model for the prediction of droplet's equilibrium position has been developed by considering the net force acting on the droplet. The model captures the main features observed in the experiments and reveals strong dependence of the final equilibrium of the droplet on the specific distributions of the apparent contact angles along the droplet's contour, caused by the interaction with the surface pattern.

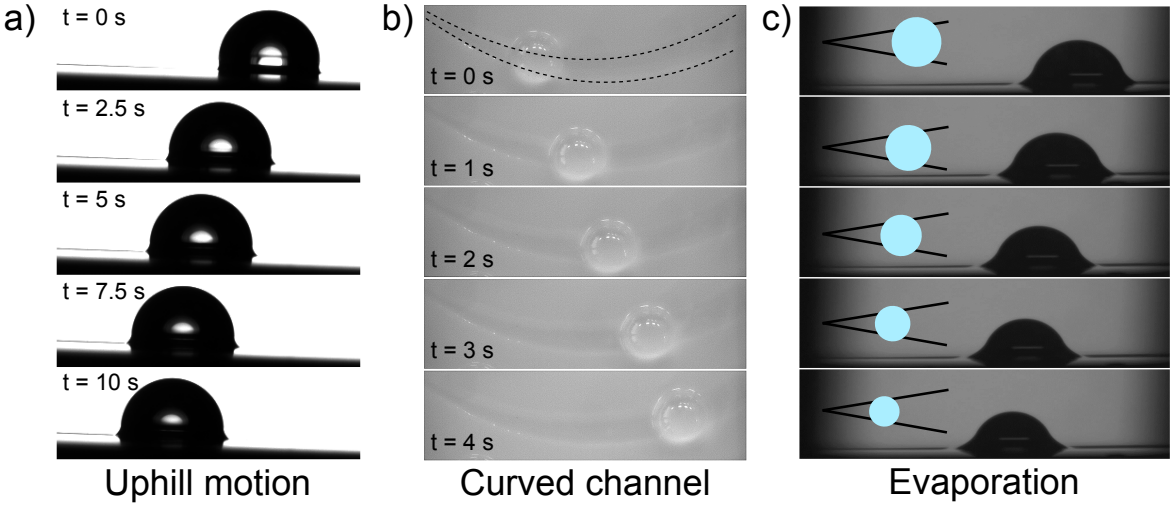

Figure 6.26: a. Droplet moving uphill against the effect of gravity on a 2° tilt, b. droplets moving on a curved V-shaped lubricant-impregnated channel, c. X_e changing with V as droplets evaporated on a V-shaped channel.

Beyond the V-shape geometry used in this study, the results also hint at the opportunity to use more generalised geometries for the purpose of guiding droplets to well-defined positions by exploiting the droplets' highly mobile contact lines offered by lubricant-impregnated surfaces and the differences in the apparent contact angles as a result of distortion to the lubricant layer in the presence of underlying geometry. An excellent example is that of a radial pattern which can guide the inwards or outwards

motion of droplets from a central position, or to induce self-centering of droplets. In this study, the interaction of the wetting ridge of droplets and the distorted lubricant layer have led to attractive interactions between the surface pattern and the droplets. This attractive force could be used for retaining droplets at specific locations on otherwise completely slippery surfaces, even under external forces, such as gravity (Figure 6.26a). As opposed to the attractive interaction which arises from the interaction of menisci of equal positive curvature, it would also interesting to explore the interactions between lubricant meniscus and droplets having different curvature signs. This could allow surfaces to be designed to guide droplets along well-defined paths with the need of ever coming into contact with the bounding surface (Figure 6.26b).

Standard photolithographic techniques have been used in this study to produce the V-shaped channels as a way to minimise any unnecessary microscopic secondary roughness inherent to the surface. However, the same effect shown by these surfaces can easily be extended to surfaces treated to become lubricant-impregnated surfaces using techniques such as 3D and or roll-to-roll printing (Figure 6.26b). It, thus, feasible to use the principles explored in this study in the developing methods for controlled liquid transport in practical applications such as microfluidic devices or in fog-harvesting devices (see demonstrative experiment of droplet's changing X_e due to changing V. in Figure 6.26c).

Chapter Summary

This chapter focused on the experiments carried out to demonstrate the controlled transport and positioning of sessile droplets on lubricant-impregnated surfaces. Experimental results were supported by theoretical predictions by taking into account small variations in the apparent contact angles caused by the underlying solid geometry.

The following chapter will round up the major conclusions of all the work described in this thesis.

Chapter 7

Summary and Future Possibilities

The major technical step reported in this thesis has been the development of low friction surfaces in the form of lubricant-impregnated surfaces. These surfaces are capable of retaining a continuous layer of lubricating liquid between a droplet and the solid substrate underneath. This leads to a complete elimination of any direct contact between the droplet and the underlying solid surface, allowing droplets to have highly mobile contact lines with virtually no hindrance to their movements.

When placed on a lubricant-impregnated surface, the spherical cap shape of a droplet is distorted near its base by a wetting ridge, created by the balance of interfacial forces. This has prevented a conventional contact angle to be measured directly and thus motivated the use of an extrapolated angle. Studies carried out in this project have shown that it is possible to use all the machinery and tools developed for sessile droplets on solid surfaces providing the presence of the wetting ridge is accounted for. The lack of contact between the droplet and the underlying surface enabled by low friction SLIPS/LIS has allowed studies of droplets in low friction situations to be carried out. This was made possible by the removal of pinning forces which would otherwise be infeasible on conventional surfaces where direct contact between the droplet and the surface is unavoidable.

In this thesis, the first major finding was the observation of the most slippery configuration as described by Smith *et al.* whereby the droplet sits completely atop a layer of lubricating liquid [15]. This was supported by sliding angle measurements as low as 0.2° and the lack of stepwise movement of the contact line as droplets moved

on the surface. This finding thus established a platform for the study of evaporation of sessile droplets under constant contact angle mode. As mentioned in Section 2.9, it is difficult to eradicate the pinning of contact line on solid surfaces due to the direct contact. This problem was solved when SLIPS/LIS were used as contact between the droplet and the surface was removed. Thus, droplets' contact lines were complete free to recede as they evaporated on SLIPS/LIS.

The second study in this report saw the accurate manipulation of droplets confined in wedge geometry with arbitrarily small forces. It was predicted by Concus and Finn that a capillary bridge with positive curvature may settle in a wedge formed by two non-parallel surfaces and take on the shape of a truncated sphere, rather than filling the apex. This prediction, however, has never been observed experimentally without the aid of external forces to overcome pinning forces. The use of SLIPS/LIS has made it possible for this to be experimentally observed since droplets experience no hindrance in their paths towards equilibrium. Droplets' localisation within the wedge can thus be manipulated accurately by controlled reconfiguration of the wedge geometry. The ability of droplets to freely move within the wedges due to the lack of pinning also enabled to study of the dynamics of barrel-shaped capillary bridges to be carried out, which has until now been a relatively unexplored area. Experimental findings in this study have also provided supports for the idea of energy invariance between droplet states and thus opening up the possibility of droplet manipulation without work being incurred.

The high mobility of droplets on SLIPS/LIS was further explored in the final study. It was found in this study that the complex micro-texturing *via* photolithography used in Chapter 4 and 5 were no longer a necessary requirement for creating SLIPS/LIS. Surfaces coated with a thin layer of nano-particle were able to retain the layer of lubricating liquid needed for slippery surfaces. This has allowed significantly less complicated macroscopic textures to be made whilst maintaining the low friction characteristics exhibited by SLIPS/LIS. It was found that the macroscopic textures caused distortions in the lubricant layer. As a result of the long-range interactions between the droplets' wetting ridge and the distortion in the lubricant, droplets migrated

towards the distorted areas *via* a mechanism similar to the "Cheerios effect". By adding extra geometrical constraints and by varying controlled parameters, droplets either settled to local or global equilibria. This study has also been a good demonstration of guided motion of droplets on otherwise complete slippery surfaces, a feature relevant to various applications in microfluidics.

These studies have served as good evidence for a continuous layer of lubricating liquid between droplets and the underlying surface. However, the presence of this layer has thus far only been inferred from the high mobility of the droplets. Obtaining a direct visual confirmation of the lubricant layer in beneath a droplet has perhaps been the biggest hurdle through the project and remains largely inconclusive. Despite these shortcomings, the current thesis has continuously demonstrated the ability to create low-friction surfaces thus creating a platform for future studies of droplets with smooth contact line dynamics which would otherwise be difficult on traditional surfaces due to their physical limitations. Perhaps it is worth noting that, although the use of SLIPS/LIS enabled the studies seen in Chapter 4 and 5, they are not exclusive to lubricant-impregnated surfaces. Should surfaces not impregnated with a lubricating liquid but with the same low-hysteresis characteristics be made, one can still study the above. Chapter 6, however, shows a unique method of inducing droplet motion using the lubricant layer.

Aside from the main findings reported in this thesis, the various experiments carried out have laid down the ground work and hinted at the possible future studies. One thing which perhaps should have received more attention in the project is the robustness of the surfaces in different environments and their ability to withstand external pressures and damages. Perhaps the biggest unanswered question from the thesis project is the reason behind the variations in the size of the wetting ridge surrounding the droplets on SLIPS/LIS. Although glimpses were caught in Chapter 4, 5 and 6 whereby the wetting ridges were observed to have increased in size when placed on thicker layers of lubricating liquid, further quantitative analysis could help to reveal a more exact correlation between the two. Moreover, the effect of the underlying solid texture on the size of the wetting ridge is worth exploring. Gaining control over the wetting ridge

height through controlled surface texturing could lead to the creation of surfaces on which droplets can self-propel (see Section 6.2.1).

The evaporation experiments showed that, with specifically designed surfaces, it is possible to achieve constant contact angle evaporation but it relies on the surface's ability to retain the lubricant layer beneath the droplet. This suggests that, by altering the surface texture, surfaces may be created to allow droplet evaporation to alternate between constant contact angle and constant contact area mode. If droplets containing particles are used, these surfaces may be used to create complex patterns, such as concentric circles, through controlled deposition of the particles.

The principles demonstrated in Chapter 5 can be extended to treat systems with multiple droplets, such as the mixing of droplets *via* controlled reconfiguration of geometry. The wedge geometry may also be replaced by any arbitrary number of boundaries, for example, liquid bridges between two spheres, or liquid marbles. The results from Chapter 5 may also be used to exploit boundary reconfiguration to achieve controlled transport under energy-invariant conditions in multiphase systems, such as encapsulated droplets, suspended particles or cells. On a more fundamental level, more in depth characterisation of properties such as the flow profile of the lubricating layer as well as the droplet may reveal further information about the system, this may be achievable using particle tracking techniques.

Finally, the ability to use the distorted lubricant layer to control the localisation of droplets on SLIPS/LIS could allow new types of microfluidic devices to be developed. By "trapping" droplets using the distorted layer, their movement can thus be controlled to follow specific tracks. These principles can be exploited for the development of methods for liquid transport in applications such as biosensors and fog-harvesting devices. The simplicity of these surfaces also suggest the possibility of mass production using techniques such as 3D printing or roll-to-roll printing. The V-shape geometry used in this study may also be replaced by other designs for specific purposes. For example, radial patterns to induce self-centering droplets. The attractive interaction between the distorted lubricant layer and the droplets may also be manipulated and a repulsive interaction can be introduced by actively altering the lubricating layer.

References

[1] P-G. De Gennes, F. Brochard-Wyart, and D. Quéré. *Capillarity and Wetting Phenomena: Drops, Bubbles, Pearls, Waves*. Springer Science & Business Media, 2013.

[2] D. Bonn, J. Eggers, J. Indekeu, J. Meunier, and E. Rolley. Wetting and spreading. *Reviews of Modern physics*, 81(2):739, 2009.

[3] N.J. Shirtcliffe, G. McHale, S. Atherton, and M.I. Newton. An introduction to superhydrophobicity. *Advances in Colloid and Interface Science*, 161(1):124–138, 2010.

[4] D. Quéré. Non-sticking drops. *Reports on Progress in Physics*, 68(11):2495, 2005.

[5] T. Young. An essay on the cohesion of fluids. *Philosophical Transactions of the Royal Society of London*, 95:65–87, 1805.

[6] G. McHale. Surface wetting: Liquids shape up nicely. *Nature Materials*, 6(9):627–628, 2007.

[7] W. Barthlott and C. Neinhuis. Purity of the sacred lotus, or escape from contamination in biological surfaces. *Planta*, 202(1):1–8, 1997.

[8] Y.Y. Yan, N. Gao, and W. Barthlott. Mimicking natural superhydrophobic surfaces and grasping the wetting process: a review on recent progress in preparing superhydrophobic surfaces. *Advances in Colloid and Interface Science*, 169(2):80–105, 2011.

[9] C. Neinhuis and W. Barthlott. Characterization and distribution of water-repellent, self-cleaning plant surfaces. *Annals of Botany*, 79(6):667–677, 1997.

[10] K-C. Park, P. Kim, A. Grinthal, N. He, D. Fox, J.C. Weaver, and J. Aizenberg. Condensation on slippery asymmetric bumps. *Nature*, 531:78–82, 2016.

[11] R.B. Suter, G.E. Stratton, and P.R. Miller. Taxonomic variation among spiders in the ability to repel water: surface adhesion and hair density. *Journal of Arachnology*, 32(1):11–21, 2004.

[12] N.J. Shirtcliffe, G. McHale, M.I. Newton, C.C. Perry, and P. Roach. Porous materials show superhydrophobic to superhydrophilic switching. *Chemical Communications*, (25):3135–3137, 2005.

[13] T. Onda, S. Shibuichi, N. Satoh, and K. Tsujii. Super-water-repellent fractal surfaces. *Langmuir*, 12(9):2125–2127, 1996.

[14] T-S Wong, S.H. Kang, S.K.Y. Tang, E.J. Smythe, B.D. Hatton, A. Grinthal, and J. Aizenberg. Bioinspired self-repairing slippery surfaces with pressure-stable omniphobicity. *Nature*, 477(7365):443–447, 2011.

[15] J.D. Smith, R. Dhiman, S. Anand, E. Reza-Garduno, R.E. Cohen, G.H. McKinley, and K. K. Varanasi. Droplet mobility on lubricant-impregnated surfaces. *Soft Matter*, 9(6):1772–1780, 2013.

[16] J.H. Guan, G.G. Wells, B. Xu, G. McHale, D. Wood, J. Martin, and S. Stuart-Cole. Evaporation of sessile droplets on slippery liquid-infused porous surfaces (slips). *Langmuir*, 31(43):11781–11789, 2015. PMID: 26446177.

[17] J.T. Luo, N.R. Geraldi, J.H. Guan, G. McHale, G.G. Wells, and Y.Q. Fu. Slippery liquid-infused porous surfaces and droplet transportation by surface acoustic waves. *Phys. Rev. Applied*, 7:014017, Jan 2017.

[18] P.S. de Laplace. *Complete works of Laplace: Volume 4*, 1805.

[19] H-J. Butt, K. Graf, and M. Kappl. *Physics and Chemistry of Interfaces*. John Wiley & Sons, 2006.

[20] A. Dupré and P. Dupré. *Théorie mécanique de la chaleur*. Gauthier-Villars, 1869.

[21] M.E. Schrader. Young-dupre revisited. *Langmuir*, 11(9):3585–3589, 1995.

[22] E.G. Shafrin and W.A. Zisman. Upper limits to the contact angles of liquids on solids. ACS Publications, 1963.

[23] D. Quéré. Wetting and roughness. *Annual Review of Materials Research*, 38(1):71–99, 2008.

[24] R.T.P. Chow. On the ability of drops or bubbles to stick to non-horizontal surfaces of solids. *Journal of Fluid mechanics*, 137:1–29, 1983.

[25] K-Y. Law. Definitions for hydrophilicity, hydrophobicity, and superhydrophobicity: getting the basics right, 2014.

[26] L.C. Gao and T.J. McCarthy. Teflon is hydrophilic. comments on definitions of hydrophobic, shear versus tensile hydrophobicity, and wettability characterization. *Langmuir*, 24(17):9183–9188, 2008.

[27] G. McHale. All solids, including teflon, are hydrophilic (to some extent), but some have roughness induced hydrophobic tendencies. *Langmuir*, 25(13):7185–7187, 2009.

[28] G. McHale, N.J. Shirtcliffe, and M.I. Newton. Super-hydrophobic and super-wetting surfaces: analytical potential? *Analyst*, 129(4):284–287, 2004.

[29] P. Roach, N.J. Shirtcliffe, and M.I. Newton. Progess in superhydrophobic surface development. *Soft matter*, 4(2):224–240, 2008.

[30] N.J. Shirtcliffe, G. McHale, and M.I. Newton. Learning from superhydrophobic plants: The use of hydrophilic areas on superhydrophobic surfaces for droplet control. *Langmuir*, 25(24):14121–14128, 2009.

[31] W. Barthlott and N. Ehler. Raster-elektronen-mikroskopie der epidermis-oberflachen von spermatophyten. *Scanning electron microscopy of epidermal surfaces of Spermatophyta.) Abh. Akad. Wiss. Lit. Mainz, Math.-Naturwiss. Klasse, Trop. Subtrop. Pflanzenwelt*, 19:367–467, 1977.

[32] P. Forbes. Self-cleaning materials. *Scientific American*, 299(2):88–95, 2008.

[33] John WM Bush, David L Hu, and Manu Prakash. The integument of water-walking arthropods: form and function. *Advances in Insect Physiology*, 34:117–192, 2007.

[34] N.R. Bernardino, V. Blickle, and S. Dietrich. Wetting of surfaces covered by elastic hairs. *Langmuir*, 26(10):7233–7241, 2010.

[35] M.L. Blow and J.M. Yeomans. Superhydrophobicity on hairy surfaces. *Langmuir*, 26(20):16071–16083, 2010.

[36] L.C. Gao and T.J. McCarthy. How wenzel and cassie were wrong. *Langmuir*, 23(7):3762–3765, 2007.

[37] G. McHale. Cassie and wenzel: were they really so wrong? *Langmuir*, 23(15):8200–8205, 2007.

[38] R.N. Wenzel. Resistance of solid surfaces to wetting by water. *Industrial & Engineering Chemistry*, 28(8):988–994, 1936.

[39] R.N. Wenzel. Surface roughness and contact angle. *The Journal of Physical Chemistry*, 53(9):1466–1467, 1949.

[40] A.B.D. Cassie and S. Baxter. Wettability of porous surfaces. *Transactions of the Faraday society*, 40:546–551, 1944.

[41] J.F. Oliver, C. Huh, and S.G. Mason. Resistance to spreading of liquids by sharp edges. *Journal of Colloid and Interface Science*, 59(3):568–581, 1977.

[42] J. Bico, U. Thiele, and D. Quéré. Wetting of textured surfaces. *Colloids and Surfaces A: Physicochemical and Engineering Aspects*, 206(1):41–46, 2002.

[43] N. Gao and Y.Y. Yan. Modeling superhydrophobic contact angles and wetting transition. *Journal of Bionic Engineering*, 6(4):335–340, 2009.

[44] Y.Q. Zu, Y.Y. Yan, J.Q. Li, and Z.W. Han. Wetting behaviours of a single droplet on biomimetic micro structured surfaces. *Journal of Bionic Engineering*, 7(2):191–198, 2010.

[45] G. Alberti and A. DeSimone. Wetting of rough surfaces: a homogenization approach. In *Proceedings of the Royal Society of London A: Mathematical, Physical and Engineering Sciences*, volume 461, pages 79–97. The Royal Society, 2005.

[46] C. Ishino and K. Okumura. Wetting transitions on textured hydrophilic surfaces. *The European Physical Journal E: Soft Matter and Biological Physics*, 25(4):415–424, 2008.

[47] N.J. Shirtcliffe, S. Aqil, C. Evans, G. McHale, M.I. Newton, C.C. Perry, and P. Roach. The use of high aspect ratio photoresist (su-8) for super-hydrophobic pattern prototyping. *Journal of Micromechanics and Microengineering*, 14(10):1384, 2004.

[48] A. Kawai and H. Nagata. Wetting behavior of liquid on geometrical rough surface formed by photolithography. *Japanese Journal of Applied Physics*, 33(9A):L1283, 1994.

[49] D. Öner and T.J. McCarthy. Ultrahydrophobic surfaces. effects of topography length scales on wettability. *Langmuir*, 16(20):7777–7782, 2000.

[50] P-S. Tsai, Y.M. Yang, and Y.L. Lee. Fabrication of hydrophobic surfaces by coupling of langmuir- blodgett deposition and a self-assembled monolayer. *Langmuir*, 22(13):5660–5665, 2006.

[51] W. Ming, D. Wu, R.A.T.M. van Benthem, and G. De With. Superhydrophobic films from raspberry-like particles. *Nano letters*, 5(11):2298–2301, 2005.

[52] N.J. Shirtcliffe, G. McHale, M.I. Newton, and C.C. Perry. Wetting and wetting transitions on copper-based super-hydrophobic surfaces. *Langmuir*, 21(3):937–943, 2005.

[53] Y.J. Kwon, N. Patankar, J.K. Choi, and J.H. Lee. Design of surface hierarchy for extreme hydrophobicity. *Langmuir*, 25(11):6129–6136, 2009.

[54] S.J. Hwang, D.J. Oh, P.G. Jung, S.M. Lee, J.S. Go, J-H. Kim, K-Y. Hwang, and J.S. Ko. Dry etching of polydimethylsiloxane using microwave plasma. *Journal of Micromechanics and Microengineering*, 19(9):095010, 2009.

[55] B.R. Solomon, K.S. Khalil, and K.K. Varanasi. Drag reduction using lubricant-impregnated surfaces in viscous laminar flow. *Langmuir*, 30(36):10970–10976, 2014. PMID: 25144426.

[56] J. Zhang, P. France, A. Radomyselskiy, S. Datta, J.G. Zhao, and W. van Ooij. Hydrophobic cotton fabric coated by a thin nanoparticulate plasma film. *Journal of Applied Polymer Science*, 88(6):1473–1481, 2003.

[57] N.R. Geraldi, G. McHale, B.B. Xu, G.G. Wells, L.E. Dodd, D. Wood, and M.I. Newton. Leidenfrost transition temperature for stainless steel meshes. *Materials Letters*, 176:205–208, 2016.

[58] A.V. Rao and M.M. Kulkarni. Hydrophobic properties of tmos/tmes-based silica aerogels. *Materials Research Bulletin*, 37(9):1667–1677, 2002.

[59] N.J. Shirtcliffe, G. McHale, M.I. Newton, and C.C. Perry. Intrinsically superhydrophobic organosilica sol-gel foams. *Langmuir*, 19(14):5626–5631, 2003.

[60] W. Lee, M-K. Jin, W-C. Yoo, and J-K. Lee. Nanostructuring of a polymeric substrate with well-defined nanometer-scale topography and tailored surface wettability. *Langmuir*, 20(18):7665–7669, 2004.

[61] A. Lafuma and D. Quéré. Slippery pre-suffused surfaces. *EPL (Europhysics Letters)*, 96(5):56001, 2011.

[62] F. Schellenberger, J. Xie, N. Encinas, A. Hardy, M. Klapper, P. Papadopoulos, H-J. Butt, and D. Vollmer. Direct observation of drops on slippery lubricant-infused surfaces. *Soft Matter*, 11(38):7617–7626, 2015.

[63] M.E.R. Shanahan and A. Carre. Viscoelastic dissipation in wetting and adhesion phenomena. *Langmuir*, 11(4):1396–1402, 1995.

[64] A. Carré, J-C. Gastel, and M.E.R. Shanahan. Viscoelastic effects in the spreading of liquids. *Nature*, 379(6564):432, 1996.

[65] J.H. Guan, E. Ruiz-Gutierrez, B. Xu, G. Wood, D.and McHale, R.A. Ledesma Aguilar, and G.G. Wells. Drop transport and positioning on lubricant impregnated surfaces. *Soft Matter*, 2017.

[66] C. Semprebon, G. McHale, and H. Kusumaatmaja. Apparent contact angle and contact angle hysteresis on liquid infused surfaces. *Soft matter*, 13(1):101–110, 2017.

[67] M.J. Neeson, R.F. Tabor, F. Grieser, R.R. Dagastine, and D.Y.C. Chan. Compound sessile drops. *Soft Matter*, 8(43):11042–11050, 2012.

[68] M. Tress, S. Karpitschka, P. Papadopoulos, J.H. Snoeijer, D. Vollmer, and H-J. Butt. Shape of a sessile drop on a flat surface covered with a liquid film. *Soft Matter*, 2017.

[69] J.B. Boreyko, G. Polizos, P.G. Datskos, S.A. Sarles, and C.P. Collier. Air-stable droplet interface bilayers on oil-infused surfaces. *Proceedings of the National Academy of Sciences*, 111(21):7588–7593, 2014.

[70] S. Anand, K. Rykaczewski, S.B. Subramanyam, D. Beysens, and K.K. Varanasi. How droplets nucleate and grow on liquids and liquid impregnated surfaces. *Soft Matter*, 11(1):69–80, 2015.

[71] A. Carlson, P. Kim, G. Amberg, and H.A. Stone. Short and long time drop dynamics on lubricated substrates. *EPL (Europhysics Letters)*, 104(3):34008, 2013.

[72] K. Rykaczewski, T. Landin, M.L. Walker, J.H.J. Scott, and K.K. Varanasi. Direct imaging of complex nano-to microscale interfaces involving solid, liquid, and gas phases. *ACS Nano*, 6(10):9326–9334, 2012.

[73] Y. Cheng, H. Suhonen, L. Helfen, J.S. Li, F. Xu, M. Grunze, P. A Levkin, and T. Baumbach. Direct three-dimensional imaging of polymer–water interfaces by nanoscale hard x-ray phase tomography. *Soft Matter*, 10(17):2982–2990, 2014.

[74] S. Anand, A.T. Paxson, R. Dhiman, J.D. Smith, and K.K. Varanasi. Enhanced condensation on lubricant-impregnated nanotextured surfaces. *ACS Nano*, 6(11):10122–10129, 2012.

[75] R. Xiao, N. Miljkovic, R. Enright, and E.N. Wang. Immersion condensation on oil-infused heterogeneous surfaces for enhanced heat transfer. *Scientific Reports*, 3(1988), 2013.

[76] K. Rykaczewski, A.T. Paxson, M. Staymates, M.L. Walker, X.D. Sun, S. Anand, S. Srinivasan, G.H. McKinley, J. Chinn, and J.H.J. Scott. Dropwise condensation of low surface tension fluids on omniphobic surfaces. *Scientific Reports*, 4, 2014.

[77] B.S. Lalia, S. Anand, K.K. Varanasi, and R. Hashaikeh. Fog-harvesting potential of lubricant-impregnated electrospun nanomats. *Langmuir*, 29(42):13081–13088, 2013.

[78] K-C. Park, S.S. Chhatre, S. Srinivasan, R.E. Cohen, and G.H. McKinley. Optimal design of permeable fiber network structures for fog harvesting. *Langmuir*, 29(43):13269–13277, 2013.

[79] K.K. Varanasi, T. Deng, J.D. Smith, M. Hsu, and N. Bhate. Frost formation and ice adhesion on superhydrophobic surfaces. *Applied Physics Letters*, 97(23):234102, 2010.

[80] P. Kim, T-S. Wong, J. Alvarenga, M.J. Kreder, W.E. Adorno-Martinez, and J. Aizenberg. Liquid-infused nanostructured surfaces with extreme anti-ice and anti-frost performance. *ACS Nano*, 6(8):6569–6577, 2012.

[81] S.B. Subramanyam, K. Rykaczewski, and K.K. Varanasi. Ice adhesion on lubricant-impregnated textured surfaces. *Langmuir*, 29(44):13414–13418, 2013.

[82] Q. Liu, Y. Yang, M. Huang, Y.X. Zhou, Y.Y. Liu, and X.D. Liang. Durability of a lubricant-infused electrospray silicon rubber surface as an anti-icing coating. *Applied Surface Science*, 346:68–76, 2015.

[83] P.W. Wilson, W.Z. Lu, H.J. Xu, P. Kim, M.J. Kreder, J. Alvarenga, and J. Aizenberg. Inhibition of ice nucleation by slippery liquid-infused porous surfaces (slips). *Physical Chemistry Chemical Physics*, 15(2):581–585, 2013.

[84] J.P. Rothstein. Slip on superhydrophobic surfaces. *Annual Review of Fluid Mechanics*, 42:89–109, 2010.

[85] C. Schönecker, T. Baier, and S. Hardt. Influence of the enclosed fluid on the flow over a microstructured surface in the cassie state. *Journal of Fluid Mechanics*, 740:168–195, 2014.

[86] A.A. Hemeda and H.V. Tafreshi. Liquid–infused surfaces with trapped air (lista) for drag force reduction. *Langmuir*, 32(12):2955–2962, 2016.

[87] A.K. Epstein, T-S Wong, R.A. Belisle, E.M. Boggs, and J. Aizenberg. Liquid-infused structured surfaces with exceptional anti-biofouling performance. *Proceedings of the National Academy of Sciences*, 109(33):13182–13187, 2012.

[88] L.L. Xiao, J.S. Li, S. Mieszkin, A. Di Fino, A.S. Clare, M.E. Callow, J.A. Callow, M. Grunze, A. Rosenhahn, and P.A. Levkin. Slippery liquid-infused porous surfaces showing marine antibiofouling properties. *ACS Applied Materials & Interfaces*, 5(20):10074–10080, 2013.

[89] S.S. Yang, R. Qiu, H.Q Song, P. Wang, Z.Q. Shi, and Y.F. Wang. Slippery liquid-infused porous surface based on perfluorinated lubricant/iron tetradecanoate: preparation and corrosion protection application. *Applied Surface Science*, 328:491–500, 2015.

[90] L.Q. Chen, A. Geissler, E. Bonaccurso, and K. Zhang. Transparent slippery surfaces made with sustainable porous cellulose lauroyl ester films. *ACS Applied Materials & Interfaces*, 6(9):6969–6976, 2014.

[91] K.S. Khalil, S.R. Mahmoudi, N. Abu-Dheir, and K.K. Varanasi. Active surfaces: Ferrofluid-impregnated surfaces for active manipulation of droplets. *Applied Physics Letters*, 105(4):041604, 2014.

[92] M.G. Pollack, A.D. Shenderov, and R.B. Fair. Electrowetting-based actuation of droplets for integrated microfluidics. *Lab on a Chip*, 2(2):96–101, 2002.

[93] C.L Hao, Y.H Liu, X.M. Chen, Y.C. He, Q.S. Li, K.Y. Li, and Z.K. Wang. Electrowetting on liquid-infused film (ewolf): complete reversibility and controlled droplet oscillation suppression for fast optical imaging. *Scientific Reports*, 4:6846, 2014.

[94] H.J.J. Verheijen and M.W.J. Prins. Reversible electrowetting and trapping of charge: model and experiments. *Langmuir*, 15(20):6616–6620, 1999.

[95] T. Krupenkin, S. Yang, and P. Mach. Tunable liquid microlens. *Applied Physics Letters*, 82(3):316–318, 2003.

[96] E. Bormashenko, R. Pogreb, Y. Bormashenko, R. Grynyov, and O. Gendelman. Low voltage reversible electrowetting exploiting lubricated polymer honeycomb substrates. *Applied Physics Letters*, 104(17):171601, 2014.

[97] Z. Brabcova, G. McHale, G.G. Wells, C.V. Brown, and M.I. Newton. Electric field induced reversible spreading of droplets into films on lubricant impregnated surfaces. *Applied Physics Letters*, 110(12):121603, 2017.

[98] J. Barman, R. Pant, A.K. Nagarajan, and K. Khare. Electrowetting on dielectrics on lubricating fluid-infused smooth/rough surfaces with negligible hysteresis. *Journal of Adhesion Science and Technology*, 31(2):159–170, 2017.

[99] N. Bjelobrk, H-L. Girard, S.B. Subramanyam, H-M. Kwon, D. Quéré, and K.K. Varanasi. Thermocapillary motion on lubricant-impregnated surfaces. *Physical Review Fluids*, 1:063902, Oct 2016.

[100] É. Ruiz-Gutiérrez, J.H. Guan, B. Xu, G. McHale, G.G. Wells, and R. Ledesma-Aguilar. Energy invariance in capillary systems. *Physical Review Letters*, 118(21):218003, 2017.

[101] D. Chandler. Interfaces and the driving force of hydrophobic assembly. *Nature*, 437(7059):640–647, 2005.

[102] M. Calistri-Yeh, E.J. Kramer, R. Sharma, W. Zhao, M.H. Rafailovich, J. Sokolov, and J.D. Brock. Thermal stability of self-assembled monolayers from alkylchlorosilanes. *Langmuir*, 12(11):2747–2755, 1996.

[103] L. Zhu, Y.Y. Feng, X.Y. Ye, and Z.Y. Zhou. Tuning wettability and getting superhydrophobic surface by controlling surface roughness with well-designed microstructures. *Sensors and Actuators A: Physical*, 130:595–600, 2006.

[104] J. Seiwert, C. Clanet, and D. Quéré. Coating of a textured solid. *Journal of Fluid Mechanics*, 669:55–63, 2011.

[105] L. Landau and V. Levich. Dragging of a liquid by a moving plate. *Acta Physicochim. USSR*, 17:42–54, 1942.

[106] J.D. Chen. Measuring the film thickness surrounding a bubble inside a capillary. *Journal of Colloid and Interface Science*, 109(2):341–349, 1986.

[107] R. Krechetnikov and G.M. Homsy. Experimental study of substrate roughness and surfactant effects on the landau-levich law. *Physics of Fluids*, 17(10):102108, 2005.

[108] W.D. Harkins and F.E. Brown. The determination of surface tension (free surface energy), and the weight of falling drops: The surface tension of water and benzene by the capillary height method. *Journal of the American Chemical Society*, 41(4):499–524, 1919.

[109] H.Y. Erbil. Evaporation of pure liquid sessile and spherical suspended drops: A review. *Advances in Colloid and Interface Science*, 170(1):67–86, 2012.

[110] J.H. Park and J.H. Moon. Control of colloidal particle deposit patterns within picoliter droplets ejected by ink-jet printing. *Langmuir*, 22(8):3506–3513, 2006.

[111] M. Kimura, M.J. Misner, T. Xu, S.H. Kim, and T.P. Russell. Long-range ordering of diblock copolymers induced by droplet pinning. *Langmuir*, 19(23):9910–9913, 2003.

[112] J.P. Jing, J. Reed, J. Huang, X.H. Hu, V. Clarke, D. Edington, J.and Housman, T.S. Anantharaman, E.J. Huff, and B. Mishra. Automated high resolution optical mapping using arrayed, fluid-fixed dna molecules. *Proceedings of the National Academy of Sciences*, 95(14):8046–8051, 1998.

[113] Y. Yu, H.P. Zhu, J.M. Frantz, M.E. Reding, K.C. Chan, and H.E. Ozkan. Evaporation and coverage area of pesticide droplets on hairy and waxy leaves. *Biosystems Engineering*, 104(3):324–334, 2009.

[114] J.C. Maxwell and W.W. Greg. *Collected papers*. Clarendon Press, 1966.

[115] H.Y. Erbil and M. Dogan. Determination of diffusion coefficient- vapor pressure product of some liquids from hanging drop evaporation. *Langmuir*, 16(24):9267–9273, 2000.

[116] H.W. Morse. On evaporation from the surface of a solid sphere. preliminary note. In *Proceedings of the American Academy of Arts and Sciences*, volume 45, pages 363–367. JSTOR, 1910.

[117] I. Langmuir. The evaporation of small spheres. *Physical Review*, 12(5):368, 1918.

[118] R.G. Picknett and R. Bexon. The evaporation of sessile or pendant drops in still air. *Journal of Colloid and Interface Science*, 61(2):336–350, 1977.

[119] K.S. Birdi, D.T. Vu, and A. Winter. A study of the evaporation rates of small water drops placed on a solid surface. *The Journal of Physical Chemistry*, 93(9):3702–3703, 1989.

[120] K.S. Birdi and D.T. Vu. Wettability and the evaporation rates of fluids from solid surfaces. *Journal of Adhesion Science and Technology*, 7(6):485–493, 1993.

[121] M.E.R. Shanahan and C. Bourges. Effects of evaporation on contact angles on polymer surfaces. *International Journal of Adhesion and Adhesives*, 14(3):201–205, 1994.

[122] S.M. Rowan, M.I. Newton, and G. McHale. Evaporation of microdroplets and the wetting of solid surfaces. *The Journal of Physical Chemistry*, 99(35):13268–13271, 1995.

[123] S.M. Rowan, G. McHale, M.I. Newton, and M. Toorneman. Evaporation of microdroplets of three alcohols. *The Journal of Physical Chemistry B*, 101(8):1265–1267, 1997.

[124] G. McHale, S.M. Rowan, M.I. Newton, and M.K. Banerjee. Evaporation and the wetting of a low-energy solid surface. *The Journal of Physical Chemistry B*, 102(11):1964–1967, 1998.

[125] A-M. Cazabat and G. Guéna. Evaporation of macroscopic sessile droplets. *Soft Matter*, 6(12):2591–2612, 2010.

[126] R.G. Larson. Transport and deposition patterns in drying sessile droplets. *AIChE Journal*, 60(5):1538–1571, 2014.

[127] G. McHale, S. Aqil, N.J. Shirtcliffe, M.I. Newton, and H.Y. Erbil. Analysis of droplet evaporation on a superhydrophobic surface. *Langmuir*, 21(24):11053–11060, 2005.

[128] X.Y. Zhang, S.X. Tan, N. Zhao, X.L. Guo, X.L. Zhang, Y.J. Zhang, and J. Xu. Evaporation of sessile water droplets on superhydrophobic natural lotus and biomimetic polymer surfaces. *ChemPhysChem*, 7(10):2067–2070, 2006.

[129] H.Y. Erbil, G. McHale, and M.I. Newton. Drop evaporation on solid surfaces: constant contact angle mode. *Langmuir*, 18(7):2636–2641, 2002.

[130] J.M. Stauber, S.K. Wilson, B.R. Duffy, and K. Sefiane. On the lifetimes of evaporating droplets. *Journal of Fluid Mechanics*, 744:R2, 2014.

[131] G.W.C. Kaye and T.H. Laby. Kaye and laby tables of physical and chemical constants. *National Physical Laboratory*, 2005.

[132] R.C. Weast, M.J. Astle, and W.H. Beyer. *CRC handbook of chemistry and physics*, volume 69. CRC press Boca Raton, FL, 1988.

[133] T.A.H. Nguyen and A.V. Nguyen. Increased evaporation kinetics of sessile droplets by using nanoparticles. *Langmuir*, 28(49):16725–16728, 2012.

[134] S. Dash and S.V. Garimella. Droplet evaporation on heated hydrophobic and superhydrophobic surfaces. *Physical Review E*, 89(4):042402, 2014.

[135] N. Anantharaju, M. Panchagnula, and S. Neti. Evaporating drops on patterned surfaces: Transition from pinned to moving triple line. *Journal of Colloid and Interface Science*, 337(1):176–182, 2009.

[136] D. Orejon, K. Sefiane, and M.E.R. Shanahan. Stick–slip of evaporating droplets: substrate hydrophobicity and nanoparticle concentration. *Langmuir*, 27(21):12834–12843, 2011.

[137] J.A.F. Plateau. *Statique expérimentale et théorique des liquides soumis aux seules forces moléculaires*, volume 2. Gauthier-Villars, 1873.

[138] C.H. Delaunay. Sur la surface de révolution dont la courbure moyenne est constante. *Journal de mathématiques pures et appliquées*, pages 309–314, 1841.

[139] B. Fall, A.and Weber, M. Pakpour, N. Lenoir, N. Shahidzadeh, J. Fiscina, C. Wagner, and D. Bonn. Sliding friction on wet and dry sand. *Physical Review Letters*, 112(17):175502, 2014.

[140] B.N.J. Persson. Wet adhesion with application to tree frog adhesive toe pads and tires. *Journal of Physics: Condensed Matter*, 19(37):376110, 2007.

[141] J.W.M. Bush, F. Peaudecerf, M. Prakash, and D. Quéré. On a tweezer for droplets. *Advances in Colloid and Interface Science*, 161(1):10–14, 2010.

[142] M. Prakash, D. Quéré, and J.W.M. Bush. Surface tension transport of prey by feeding shorebirds: the capillary ratchet. *Science*, 320(5878):931–934, 2008.

[143] F. Hauksbee. An account of an experiment touching the direction of a drop of oil of oranges, between two glass planes, towards any side of them that is nearest pressed together. by mr. fr. hauksbee, frs. *Philosophical Transactions*, 27(325-336):395–396, 1710.

[144] H. Bouasse. Capillarité et phénomenes superficiels delagrave, 1924.

[145] É. Lorenceau and D. Quéré. Drops on a conical wire. *Journal of Fluid Mechanics*, 510:29–45, 2004.

[146] P. Renvoisé, J.W.M. Bush, M. Prakash, and D. Quéré. Drop propulsion in tapered tubes. *EPL (Europhysics Letters)*, 86(6):64003, 2009.

[147] Ré. Dangla and C.N. Kayi, S.C.and Baroud. Droplet microfluidics driven by gradients of confinement. *Proceedings of the National Academy of Sciences*, 110(3):853–858, 2013.

[148] C. Luo and X. Heng. Separation of oil from a water/oil mixed drop using two nonparallel plates. *Langmuir*, 30(33):10002–10010, 2014.

[149] E. Reyssat. Drops and bubbles in wedges. *Journal of Fluid Mechanics*, 748:641–662, 2014.

[150] . Concus, R. Finn, and J. McCuan. Liquid bridges, edge blobs, and scherk-type capillary surfaces. 1999.

[151] M. Brinkmann and R. Blossey. Blobs, channels and "cigars": Morphologies of liquids at a step. *The European Physical Journal E: Soft Matter and Biological Physics*, 14(1):79–89, 2004.

[152] V. Miralles, A. Huerre, H. Williams, B. Fournié, and M-C. Jullien. A versatile technology for droplet-based microfluidics: thermomechanical actuation. *Lab on a Chip*, 15(9):2133–2139, 2015.

[153] C.N. Baroud, F. Gallaire, and Ré. Dangla. Dynamics of microfluidic droplets. *Lab on a Chip*, 10(16):2032–2045, 2010.

[154] X. Luo, C.and Heng and M.M. Xiang. Behavior of a liquid drop between two nonparallel plates. *Langmuir*, 30(28):8373–8380, 2014.

[155] D. Baratian, A. Cavalli, D. van den Ende, and F. Mugele. On the shape of a droplet in a wedge: new insight from electrowetting. *Soft matter*, 11(39):7717–7721, 2015.

[156] R.L. Hoffman. A study of the advancing interface. i. interface shape in liquid—gas systems. *Journal of Colloid and Interface Science*, 50(2):228–241, 1975.

[157] G. McHale, M.I. Newton, and N.J. Shirtcliffe. Dynamic wetting and spreading and the role of topography. *Journal of Physics: Condensed Matter*, 21(46):464122, 2009.

[158] L.H. Tanner. The spreading of silicone oil drops on horizontal surfaces. *Journal of Physics D: Applied Physics*, 12(9):1473, 1979.

[159] J. Lopez, C.A. Miller, and E. Ruckenstein. Spreading kinetics of liquid drops on solids. *Journal of Colloid and Interface Science*, 56(3):460–468, 1976.

[160] Benoit Chandesris, Ulrich Soupremanien, and Nicolas Dunoyer. Uphill motion of droplets on tilted and vertical grooved substrates induced by a wettability gradient. *Colloids and Surfaces A: Physicochemical and Engineering Aspects*, 434:126 – 135, 2013.

[161] M.S. Steinberg. Reconstruction of tissues by dissociated cells. *Science*, 141(3579):401–408, 1963.

[162] S.B. Carter. Haptotaxis and the mechanism of cell motility. *Nature*, 213:256–260, 1967.

[163] H.P. Greenspan. On the motion of a small viscous droplet that wets a surface. *Journal of Fluid Mechanics*, 84(01):125–143, 1978.

[164] F. Brochard. Motions of droplets on solid surfaces induced by chemical or thermal gradients. *langmuir*, 5(2):432–438, 1989.

[165] Manoj K. Chaudhury and George M. Whitesides. How to make water run uphill. *Science*, 256(5063):1539–1541, 1992.

[166] M. Singh, H.M. Haverinen, P. Dhagat, and G.E. Jabbour. Inkjet printing—process and its applications. *Advanced Materials*, 22(6):673–685, 2010.

[167] Todd A. Duncombe, E. Yegân Erdem, Ashutosh Shastry, Rajashree Baskaran, and Karl F. Böhringer. Controlling liquid drops with texture ratchets. *Advanced Materials*, 24(12):1545–1550, 2012.

[168] D. Soto, G. Lagubeau, C. Clanet, and D. Quéré. Surfing on a herringbone. *Physical Review Fluids*, 1:013902, May 2016.

[169] J. Li, Y.M. Hou, Y.H. Liu, C.L. Hao, M.F. Li, M.K. Chaudhury, S.H. Yao, and Z.K. Wang. Directional transport of high-temperature janus droplets mediated by structural topography. *Nature Physics*, 12:606–612, 2016.

[170] Juan Li, Xuelin Tian, Alexander Pyymaki Perros, Sami Franssila, and Ville Jokinen. Self-propelling and positioning of droplets using continuous topography gradient surface. *Advanced Materials Interfaces*, 1(3):1400001, 2014. PMID: 1400001.

[171] K.O. Zamuruyev, H.K. Bardaweel, C.J. Carron, N.J. Kenyon, O. Brand, J.P. Delplanque, and C.E. Davis. Continuous droplet removal upon dropwise condensation of humid air on a hydrophobic micropatterned surface. *Langmuir*, 30(33):10133–10142, 2014. PMID: 25073014.

[172] N.T. Chamakos, G.Karapetsas, and A.G. Papathanasiou. How asymmetric surfaces induce directional droplet motion. *Colloids and Surfaces A: Physicochemical and Engineering Aspects*, 511:180 – 189, 2016.

[173] R.S. Subramanian, N. Moumen, and J.B. McLaughlin. Motion of a drop on a solid surface due to a wettability gradient. *Langmuir*, 21(25):11844–11849, 2005.

[174] S. Daniel, M.K. Chaudhury, and J.C. Chen. Fast drop movements resulting from the phase change on a gradient surface. *Science*, 291(5504):633–636, 2001.

[175] M.K. Chaudhury and G.M. Whitesides. How to make water run uphill. Technical report, DTIC Document, 1992.

[176] J.E. Longley, E. Dooley, D.M. Givler, W.J. Napier III, M.K. Chaudhury, and S. Daniel. Drop motion induced by repeated stretching and relaxation on a gradient surface with hysteresis. *Langmuir*, 28(39):13912–13918, 2012.

[177] S-H. Choi and B-M. Zhang Newby. Micrometer-scaled gradient surfaces generated using contact printing of octadecyltrichlorosilane. *Langmuir*, 19(18):7427–7435, 2003.

[178] S.C. Hernández, C.J.C. Bennett, C.E. Junkermeier, S.D. Tsoi, F.J. Bezares, R. Stine, J.T. Robinson, E.H. Lock, D.R. Boris, B.D. Pate, J.D. Caldwell, T.L. Reinecke, P.E. Sheehan, and S.G. Walton. Chemical gradients on graphene to drive droplet motion. *ACS Nano*, 7(6):4746–4755, 2013. PMID: 23659463.

[179] J.B. Brzoska, F. Brochard-Wyart, and F. Rondelez. Motions of droplets on hydrophobic model surfaces induced by thermal gradients. *Langmuir*, 9(8):2220–2224, 1993.

[180] A.L. Yarin, W.X. Liu, and D.H. Reneker. Motion of droplets along thin fibers with temperature gradient. *Journal of Applied Physics*, 91(7):4751–4760, 2002.

[181] G. McHale, S.J. Elliott, M.I. Newton, and N.J. Shirtcliffe. Superhydrophobicity: Localized parameters and gradient surfaces. *Contact Angle, Wettability and Adhesion', Koninklijke Brill NV*, 6:219–233, 2009.

[182] M. Reyssat, F. Pardo, and D. Quéré. Drops onto gradients of texture. *EPL (Europhysics Letters)*, 87(3):36003, 2009.

[183] K-H. Chu, R Xiao, and E.N. Wang. Uni-directional liquid spreading on asymmetric nanostructured surfaces. *Nature Materials*, 9(5):413–417, 2010.

[184] F. Mugele and J-C. Baret. Electrowetting: from basics to applications. *Journal of Physics: Condensed Matter*, 17(28):R705, 2005.

[185] G. McHale, C.V. Brown, M.I. Newton, G.G. Wells, and N. Sampara. Dielectrowetting driven spreading of droplets. *Physical Review Letters*, 107(18):186101, 2011.

[186] P.F. Hao, C.J. Lv, X.W. Zhang, Z.H. Yao, and F. He. Driving liquid droplets on microstructured gradient surface by mechanical vibration. *Chemical Engineering Science*, 66(10):2118–2123, 2011.

[187] S. Mettu and M.K. Chaudhury. Vibration spectroscopy of a sessile drop and its contact line. *Langmuir*, 28(39):14100–14106, 2012.

[188] A. Shastry, M.J. Case, and K.F. Böhringer. Directing droplets using microstructured surfaces. *Langmuir*, 22(14):6161–6167, 2006.

[189] S. Daniel and M.K. Chaudhury. Rectified motion of liquid drops on gradient surfaces induced by vibration. *Langmuir*, 18(9):3404–3407, 2002.

[190] L. Dong, A. Chaudhury, and M.K. Chaudhury. Lateral vibration of a water drop and its motion on a vibrating surface. *The European Physical Journal E: Soft Matter and Biological Physics*, 21(3):231–242, 2006.

[191] T. Baier, G. Dupeux, S. Herbert, S. Hardt, and D. Quéré. Propulsion mechanisms for leidenfrost solids on ratchets. *Physical Review E*, 87(2):021001, 2013.

[192] G. Lagubeau, M. Le Merrer, C. Clanet, and D. Quéré. Leidenfrost on a ratchet. *Nature Physics*, 7(5):395–398, 2011.

[193] G.G. Wells, R. Ledesma-Aguilar, G. McHale, and K. Sefiane. A sublimation heat engine. *Nature Communications*, 6, 2015.

[194] S. Biswas, Y. Pomeau, and M.K. Chaudhury. New drop fluidics enabled by magnetic-field-mediated elastocapillary transduction. *Langmuir*, 32(27):6860–6870, 2016. PMID: 27300489.

[195] D. Vella and L. Mahadevan. The "cheerios effect". *American Journal of Physics*, 73(9):817–825, 2005.

Published works

1. **J.H. Guan**, G.G. Wells, B. Xu, G. McHale, D. Wood, J. Martin, S. Stuart-Cole. Evaporation of Sessile Droplets on Slippery Liquid-Infused Solid Surfaces (SLIPS). *Langmuir* 31, 11781—11789 (2015).

2. J.T. Luo, N.R. Geraldi, **J.H. Guan**, G. McHale, G.G. Wells, Y.Q. Fu. Slippery Liquid-Infused Porous Surfaces and Droplet Transportation by Surface Acoustic Waves, *Physical Review Applied*, 7, 014017 (2017)

3. **J.H. Guan**, É. Ruiz-Gutiérrez, B. Xu, D. Wood, G. McHale, R. Ledesma-Aguilar, G.G. Wells, Drop Transport and Positioning on Lubricant-Impregnated Surfaces, *Soft Matter*, 13.18 (2017): 3404-3410.

4. É. Ruiz-Gutiérrez, **J.H. Guan**, B. Xu, G. McHale, G.G. Wells, R. Ledesma-Aguilar. Energy Invariance in Capillary Systems, *Physical Review Letters*, 118, 218003 (2017)

Langmuir

Article

pubs.acs.org/Langmuir

Evaporation of Sessile Droplets on Slippery Liquid-Infused Porous Surfaces (SLIPS)

Jian H. Guan, Gary G. Wells,* Ben Xu, and Glen McHale

Smart Materials and Surfaces Laboratory, Faculty of Engineering & Environment, Northumbria University Newcastle, Ellison Place, Newcastle upon Tyne NE1 8ST, United Kingdom

David Wood

Microsystems Technology Group, School of Engineering and Computing Sciences, Durham University, South Road, Durham DH1 3LE, United Kingdom

James Martin and Simone Stuart-Cole

Reece Innovation, Armstrong Works, Scotswood Road, Newcastle upon Tyne, NE15 6UX, United Kingdom

Supporting Information

ABSTRACT: Over the past decade, the most common approach to creating liquid shedding surfaces has been to amplify the effects of nonwetting surface chemistry, using micro/nanotexturing to create superhydrophobic and superoleophobic surfaces. Recently, an alternative approach using impregnation of micro/nanotextured surfaces with immiscible lubricating liquids to create slippery liquid-infused porous surfaces (SLIPS) has been developed. These types of surfaces open up new opportunities to study the mechanism of evaporation of sessile droplets in zero contact angle hysteresis situations where the contact line is completely mobile. In this study, we fabricated surfaces consisting of square pillars (10−90 μm) of SU-8 photoresist arranged in square lattice patterns with the center-to-center separation between pillars of 100 μm, on which a hydrophobic coating was deposited and the textures impregnated by a lubricating silicone oil. These surfaces showed generally low sliding angles of 1° or less for small droplets of water. Droplet profiles were more complicated than on nonimpregnated surfaces and displayed a spherical cap shape modified by a wetting ridge close to the contact line due to balancing the interfacial forces at the line of contact between the droplet, the lubricant liquid and air (represented by a Neumann triangle). The wetting ridge leads to the concept of a wetting "skirt" of lubricant around the base of the droplet. For the SLIP surfaces, we found that the evaporation of small sessile droplets (~2 mm in diameter) followed an ideal constant contact angle mode where the apparent contact angle was defined from the intersection of the substrate profile with the droplet spherical cap profile. A theoretical model based on diffusion controlled evaporation was able to predict a linear dependence in time for the square of the apparent contact radius. The experimental data was in excellent quantitative agreement with the theory and enabled estimates of the diffusion constant to be obtained.

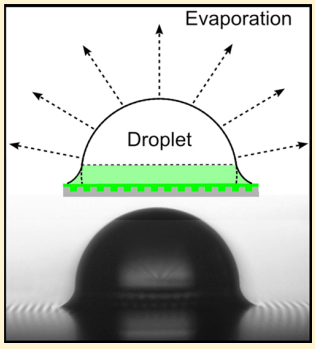

1. INTRODUCTION

Liquid evaporation is a widespread phenomenon and can be seen in natural processes such as rain, snow formation, dew, and fog.[1] Liquid evaporates if the surrounding atmosphere is not saturated with the vapor of the droplet's liquid. However, evaporation may occur in saturated conditions if the size of droplets is very small due to an increase in vapor pressure caused by the surface curvature of the droplet. Free evaporation of small and spherical droplets of water has attracted extensive attention due to its widespread relevance to engineering applications such as inkjet printing,[2] thin film coatings,[3] automatic DNA mapping,[4] and spraying of pesticides.[5] These applications often involve small droplets deposited on solid substrates and having sizes below the capillary length such that the drop shape is dominated by surface tension rather than gravity.

A foundational study of sessile drop evaporation was carried out by Picknett and Bexon[6] in which they considered the theory for diffusion controlled evaporation and experimentally observed the mass and profile evolution of slowly evaporating droplets on a Teflon surface in air. They pointed out that when a completely spherical drop on a solid substrate has a contact angle of 180° its evaporation rate is lower than that of an equivalent volume hanging spherical drop in free space due to the reduced space into which the liquid may diffuse. An exact

Received: May 19, 2015
Revised: October 7, 2015

DOI: 10.1021/acs.langmuir.5b03240
Langmuir XXXX, XXX, XXX−XXX

equation for the rate of mass loss in this situation was derived by Picknett and Bexon[6] by using the analogy between the diffusive flux and the electrostatic potential, and it was found to be valid for droplets resting on a solid boundary with a spherical cap shape. In this study, three possible modes of evaporation were reported: (i) constant contact angle with diminishing contact area, (ii) constant contact area with diminishing contact angle, and (iii) a mixed mode with changes in both the contact area and contact angle. Recent reviews of sessile droplet evaporation include those by Cazabat and Guéna,[7] Erbil,[1] and Larson.[8] Most recently, Stauber et al.[9] have theoretically considered the evaporation of droplets on strongly hydrophobic substrates with a focus on the constant contact radius and constant contact angle modes.

In one of the earliest studies, Birdi et al.[10] reported the constant contact area mode of evaporation in their investigation of the evaporation rate of sessile droplets of water placed on a smooth solid surface and in which they observed a constant radius of the liquid−solid interface and a decrease in the contact angle. In their subsequent work,[11] the effect of wetting characteristics on the rate of evaporation of droplets of liquids was demonstrated. It was shown that water on glass with a contact angle <90° evaporated in constant contact area mode; whereas water on Teflon with a contact angle of >90° evaporated with a constant contact angle and a diminishing contact area. Shanahan and Bourgès[12] also considered the evaporation of water droplets with contact angles below 90° from both smooth and rough surfaces and obtained measurements of the change in contact angle, drop height and contact radius with time. Rowan and co-workers demonstrated in two separate studies,[13,14] the change of contact angle with time via detailed measurements of various geometrical parameters on systems with $\theta < 90°$ and gave a theoretical model based on a diffusion model suggested by Birdi et al.[10] They later presented detailed measurements for evaporation of sessile drops in a system with $\theta > 90°$ in which they showed that the evaporation is dominated by an initial stage with constant contact angle and a diminishing contact radius.[15]

Despite extensive research, obtaining experimental systems that are close to a constant contact angle mode for evaporating sessile droplets remains difficult due to contact angle hysteresis. Smooth solid surfaces tend to have significant contact angle hysteresis and so as a droplet evaporates the contact line is often pinned and will then recede in a stepwise fashion. Due to their water shedding ability, superhydrophobic surfaces are often referred to as "slippery" when demonstrating a Cassie−Baxter state,[16] thus making them candidates for studying the constant contact angle mode. McHale et al.[17] were the first to report the evaporation of sessile water droplets on lithographically fabricated superhydrophobic surfaces. They observed a brief initial constant contact area period, followed by a depinning which displayed a stepwise retreat of the contact line, reflecting the periodicity of the underlying surface texture. In some cases, a collapse of the droplet into the surface texture occurred during the later stages of evaporation displaying a transition to a "sticky" Wenzel state,[18] which resulted in a completely pinned droplet.[17,19−21] Many studies have since looked into the evaporation of droplets on superhydrophobic surfaces,[19−24] but studying the evaporation of water droplets on surfaces with low contact angle hysteresis remains challenging.

Recently, new types of surfaces, slippery liquid-infused porous surfaces (SLIPS), inspired by the Nepenthes pitcher plant, have been developed.[25] These exhibit excellent non-wetting performances and provide an alternative to traditional superhydrophobic surfaces.[26−30] SLIP surfaces employ micro/nanotexture to facilitate the wicking of a nonvolatile lubricating liquid which is immiscible to the sessile droplet. These surfaces show low sliding angles,[26−30] self-healing properties through capillary wicking upon damage,[28] have anti-icing abilities[31] and are capable of withstanding external pressure.[28] Several thermodynamically stable states can exist when a droplet is placed on a SLIP surface depending on the spreading coefficient of the lubricating liquid and the test liquid as well as the surface texture.[26] These relate to whether the lubricant not only fills the texture, but whether it also exists as a film above the surface features both under the droplet and external to the droplet.[26] The most slippery states correspond to the case whereby a lubricating layer is present as a continuous layer between a droplet and the solid substrate beneath. One further complication is whether the surface energetics favors the spreading of a thin layer of the lubricant completely across the liquid−vapor interface of the sessile droplet.[26]

The development of SLIP surfaces offers an opportunity to study the evaporation of droplets of water with highly mobile contact lines not subject to the contact line pinning of previous surfaces. However, it also touches upon fundamental questions relating to wetting and interpretation of contact angles. When a droplet is deposited on a rigid solid substrate, it forms a sessile droplet and its contact angle is described in an idealized concept using Young's law; on real surfaces contact angle hysteresis is an experimental fact. When a droplet is deposited on a liquid subphase, it forms a liquid lens and the three-phase contact line between the droplet, the liquid subphase, and the air is determined by a balance of interfacial forces often depicted pictorially using a Neumann's triangle. In between these two cases is the case whereby a droplet is deposited on a soft surface and the vertical component of the droplet's surface tension deforms the surface and creates a wetting ridge. In the case of a droplet deposited on a SLIP surface, there appears to be a sessile droplet rather than a liquid lens, but because the droplet rests on a layer of liquid lubricant the region close to the solid surface shows a more complex shape with a wetting ridge due to the balance interfacial forces at the line of contact between the droplet, lubricant liquid and air, as shown in Figure 1a (see also Schellenberger et al.[32]). The lack of direct contact of the sessile droplet with the underlying solid surface makes it less clear how a contact angle might be defined and how previous theories, which included droplet-solid contact angle and contact area, may relate to the evaporation process. Compared to "slippery" superhydrophobic surfaces, which involve the sessile droplet bridging across air gaps between features, a transition to a "sticky" Wenzel state might not be anticipated when lubricant already fills the gaps between surface features.

Here we present an experimental study in which we used SLIP surfaces to create a system with an apparent contact angle greater than 90°, and where droplets of water are highly mobile with very low contact angle hysteresis. We also develop a theoretical model to estimate the diffusion coefficient based on a previous diffusion limited evaporation model modified to use apparent contact angles and apparent contact areas and to account for the presence of a wetting skirt created by the interfacial forces at the line of contact between the lubricating liquid, the evaporating droplet and the surrounding air. Thus, we report a paradoxical situation where we study an apparent constant contact angle mode of sessile droplet evaporation, but

DOI: 10.1021/acs.langmuir.5b03240
Langmuir XXXX, XXX, XXX−XXX

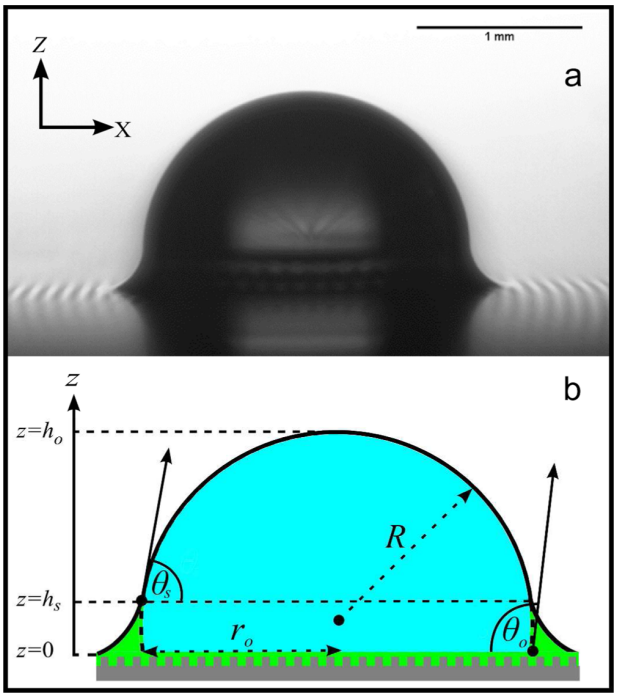

Figure 1. (a) Image of a sessile droplet of water on a SLIP surface showing a wetting ridge formed by the balance of forces between the nonevaporating lubricating liquid and the evaporating droplet. (b) Cross section schematic of the droplet on a lubricant impregnated textured surface showing defined parameters and a wetting skirt of nonvolatile lubricant created by the wetting ridge.

where the droplet is deposited on a layer of lubricant liquid rather than into direct contact with the solid. Despite that paradox, it proves possible to describe the process using all the machinery and tools developed for sessile droplet evaporation on solid surfaces providing the wetting ridge is accounted for using the concept of a wetting skirt and care is taken in defining apparent contact angles and apparent contact radii.

2. THEORETICAL DEVELOPMENT

2.1. Model Fundamentals. The surfaces in our studies use a textured solid surface into which a nonvolatile lubricant liquid has been impregnated. The solid texture locks in the lubricant, which is chosen to also coat the tops of the solid texture so that there is a continuous layer of liquid lubricant. Despite the fact that the droplet is deposited onto a layer of liquid rather than into direct contact with the solid, the majority of its shape is described as a section of a spherical cap in the same manner as a sessile droplet resting on a solid surface. The use of a SLIP surface means that there is no longer a Young's law contact angle at a liquid–solid–vapor three-phase contact line, but there is force balance between three interfacial tensions at the line of contact between the droplet, the lubricant liquid and air (described by a Neumann force triangle), which results in a wetting ridge.

In previous studies of evaporation of sessile droplets, the droplet shape and volume was determined using measurements of the contact angle and the contact or spherical radius of the droplet. However, as Figure 1a shows, on a SLIP surface, defining and extracting a contact angle at the edge of the droplet is no longer a simple concept. At the intersection between the infusing liquid, the water, and the surrounding air, the three interfacial forces balance often represented by a Neumann triangle at the base of the droplet and lead to a wetting ridge around the droplet. The height of the ridge around the droplet can be significant with respect to the overall height of the droplet and the evaporation surface area, and therefore hinders evaporation of the droplet at its base. This effect of a wetting ridge creating a lubricant skirt around the base of the droplet must be taken into account in developing any model to describe the evaporation; using a dye to dope the water droplet, we confirmed that the liquid within the skirt was lubricant.

Figure 1a shows that because the droplet size is much less than the capillary length of the evaporating liquid, $\kappa^{-1} = (\gamma_{LV}/\rho g)^{1/2}$, where γ_{LV} is the surface tension, ρ is the density of the liquid, and g is the acceleration due to gravity, the assumption that the droplet adopts a spherical cap shape remains valid away from the surface. For a given volume of liquid, there are therefore well-defined geometric parameters which can be measured from side profile images. These include the spherical radius R, apparent contact radius r_o, apparent contact angle θ_o, and the apex height h_o, above the contact surface (Figure 1b). In analyzing an image of a spherical cap with a given spherical radius using a side profile view, the vertical placement, in the z direction, of the position of the contact surface alters the deduced volume, $V(z)$, apparent contact radius $r(z)$, apparent contact angle $\theta(z)$, and apex height $h(z)$ and is therefore an important consideration. Geometrically, these parameters are related by

$$r(z) = R \sin \theta(z) \tag{1}$$

and

$$V(z) = \frac{\pi\beta(\theta)R^3}{3} \tag{2}$$

where

$$\beta(\theta) = 2 - 3\cos\theta(z) + \cos^3\theta(z) = (1 - \cos\theta(z))^2(2 + \cos\theta(z)) \tag{3}$$

The apex height measured from the position z is given by

$$h(z) = R(1 - \cos\theta(z)) \tag{4}$$

In general, the rate for diffusion limited loss of a liquid volume by evaporation through a liquid–vapor interface is

$$\frac{dV}{dt} = -\frac{D}{\rho}\int \nabla C \cdot dS \tag{5}$$

where D is the diffusion coefficient of the vapor and ρ is the density of the liquid.[6] Combining the geometrical assumptions with eq 5 and a concentration gradient model allows data on the evaporation of sessile droplets to be analyzed.

2.2. General Model for Diffusion-Limited Evaporation from SLIP Surfaces. In previous work on evaporation of sessile droplets in a constant contact angle mode Erbil et al.[33] introduced a function $f(\theta)$ to take account in a common notational format of the dependence of the concentration gradient of vapor, between the surface of the droplet and its surroundings, on the contact angle arising from different models: a notation which was also used in studies of droplet evaporation from superhydrophobic surfaces.[17] In this notation, eq 5, becomes

DOI: 10.1021/acs.langmuir.5b03240
Langmuir XXXX, XXX, XXX–XXX

$$\frac{dV}{dt} = -2\lambda R f(\theta) \tag{6}$$

One simple approach used in the literature,[13] has been to approximate the concentration gradient to be radially outward and equal to $(c_s - c_\infty)/R$, where $(c_s - c_\infty)$ is the difference in the vapor concentration at the liquid−vapor interface of the droplet c_s, which is assumed to be its saturation value, and that far removed from the droplet surface c_∞, which is assumed to be its ambient value.[13] This approximation to the concentration gradient is intuitive and accurate for contact angles close to 90°, but ignores the contact angle dependence that is introduced by the presence of the substrate which restricts the space into which vapor can diffuse. With this approximation the function, $f(\theta)$, becomes

$$f_R(\theta) = \frac{1 - \cos\theta}{2} \tag{7}$$

and eq 5 gives the evaporation rate to be

$$\frac{dV}{dt} = -\lambda h_o \tag{8}$$

where $\lambda = 2\pi D(c_s - c_\infty)/\rho$ and $h_o = h\ (z = 0)$.

In the case of the droplet on a SLIP surface, the "skirt" of lubricating liquid that rises to a height h_s, above the surface structure, reduces the droplet's liquid−vapor interfacial area, by masking the bottom of the droplet with a layer of the nonvolatile lubricating liquid (Figure 1b). The liquid−vapor surface area through which evaporation occurs is therefore modified and results in the modified evaporation rate of the droplet,

$$\frac{dV}{dt} = -\lambda h_o\left[1 - \frac{h_s}{h_o}\right] \tag{9}$$

The existence of a skirt of impregnating (lubricant) liquid around the base of the droplet can therefore be expected to reduce the evaporation rate by a factor of $[1 - h_s/h_o]$ compared to a droplet of the same volume and contact angle (equal to the apparent contact angle) on a non-SLIP surface.

An improved self-consistent model for evaporation of small sessile droplets was derived by Bourgès-Monnier and Shanahan[34] and is equivalent to,

$$f_{BMS}(\theta) = \frac{-\cos\theta}{2\log_e(1 - \cos\theta)} \tag{10}$$

In the most recent work by Stauber et al.[9] on the evaporation of droplets on strongly hydrophobic substrates and which focused on the constant contact angle and constant contact radius modes, their formulas are equivalent to,

$$f_{SWDS}(\theta) = \frac{\sin\theta g(\theta)}{4(1 + \cos\theta)^2} \tag{11}$$

where

$$\frac{g(\theta)}{(1 + \cos\theta)^2} = \tan\left(\frac{\theta}{2}\right) + 8\int_0^\infty \frac{\cosh^2(\theta\tau)}{\sinh(2\pi\tau)}\tanh[\tau(\pi - \theta)]d\tau \tag{12}$$

Most importantly for analyzing data, an exact solution for eq 5 was derived by Picknett and Bexon[6] and they gave a numerically accurate polynomial interpolation for $f(\theta)$,

$$f_{PB}(\theta) = \begin{cases} \frac{1}{2}(0.6366\theta + 0.09591\theta^2 - 0.06144\theta^3) & 0^\circ < \theta < 10^\circ \\ \frac{1}{2}(0.00008957 + 0.6333\theta + 0.116\theta^2 & 10^\circ < \theta < 180^\circ \\ \quad - 0.08878\theta^3 + 0.01033\theta^4) & \end{cases} \tag{13}$$

where θ in the series is in radians.

Following our earlier approach of using the apparent contact angle at the height h_s of the lubricant skirt above the surface structure to define the droplet liquid−vapor interfacial area through which evaporation occurs, eq 6 becomes

$$\frac{dV}{dt} = -2\lambda R f(\theta_s) \tag{14}$$

Writing the spherical cap radius in terms of the drop volume and apparent contact angle θ_o at $z = 0$, and then assuming both θ_o and θ_s are approximately constant allows the volume dependence on time to be found,

$$V(t)^{2/3} \approx V_i^{2/3} - \frac{4\lambda}{3}\left[\frac{3}{\pi\beta(\theta_o)}\right]^{1/3} f(\theta_s)t \tag{15}$$

where V_i is the initial droplet volume at $t = 0$. In terms of the apparent contact radius at $z = 0$, this can be rewritten,

$$r_0^2 \approx r_i^2 - \frac{4\lambda t \sin^2\theta_o f(\theta_s)}{\pi\beta(\theta_o)} = r_i^2 - \frac{2\lambda t \sin^2\theta_0}{\pi(1 - \cos\theta_o)(2 + \cos\theta_o)}\left(\frac{2f(\theta_s)}{1 - \cos\theta_o}\right) \tag{16}$$

where r_i is the initial apparent contact radius.

3. EXPERIMENTAL METHODS

3.1. SLIP Surfaces. For a lubricating liquid to spontaneously impregnate surface features, it is necessary that its contact angle in air on a chemically identical and smooth surface is below a critical angle defined as

$$\cos\theta_c = \frac{1 - \varphi_s}{r_w - \varphi_s} \tag{17}$$

where θ_c is the critical angle for hemiwicking,[35] φ_s is the Cassie solid fraction of the projected area of the textured surface, and r_w is the Wenzel roughness defined as the ratio of its actual surface area to its projected area. The lubricating liquid, usually an oil, will impregnate the surface textures only if $\theta_{os(a)} < \theta_c$ where $\theta_{os(a)}$ is the contact angle of the lubricating liquid (o) on smooth solid (s) in the presence of air (a). Similarly, the condition for impregnation under water is $\theta_{os(w)} < \theta_c$, where $\theta_{os(w)}$ is the lubricant's contact angle on smooth solid in the presence of water (w). These possible thermodynamic states of a water droplet on an oil-infused surface have previously been described by Smith et al.[26]

For this study, the surface was chosen such that it could be accurately textured and easily functionalized chemically. We used silicon wafers with a photolithographically patterned SU-8 photoresist layer, which was functionalized with octadecyltrichlorosilane (OTS) to add hydrophobicity, and a dip coating process to impregnate the surfaces with silicone oil (full details can be found in the Supporting Information). Studies[26,27] have shown that silicone oil spreads on flat, smooth surfaces coated with OTS in the presence of both air and water ($\theta_{os(a)} = 0°$ and $\theta_{os(w)} = 0°$). This means that silicone oil will impregnate and flow atop surface features, but will be difficult to

DOI: 10.1021/acs.langmuir.5b03240
Langmuir XXXX, XXX, XXX−XXX

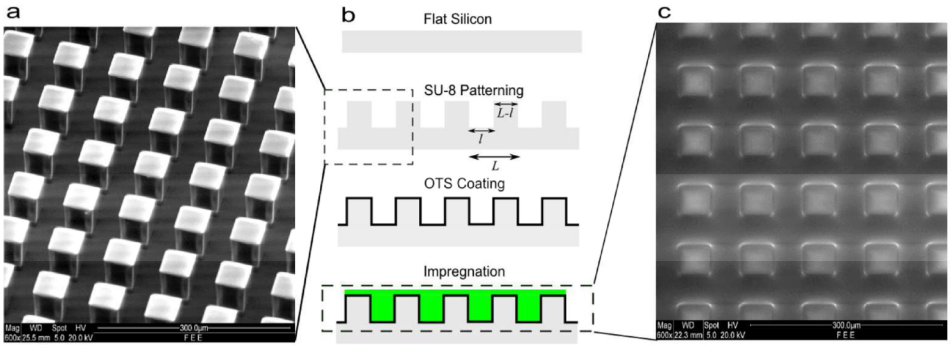

Figure 2. (a) SEM image of a lithographically patterned SU-8 surface texture. (b) Schematic showing the process to create the lubricated textured surfaces used in this study. (c) SEM image showing the surface texture impregnated with the silicone oil lubricating liquid.

displace by water. By varying the roughness of the surface we hoped to achieve the ideal case for SLIP surfaces. Figure 2a shows a SEM image of a set of pillars of dimensions 50 μm × 50 μm cross section and a height of 50 μm. Figure 2b shows a schematic of the production method and the expected impregnation regime for the SLIP surface. Figure 2c shows an, SEM image taken with a back scatter detector in low vacuum mode, of the same substrate as Figure 2a, but impregnated with silicone oil to create the lubricating layer.

3.2. Determining the Drop Shape and Contact Angle. Static contact angle measurements of water droplets on both textured (prior to lubrication) and flat substrates were carried out using a Krüss DSA30 contact angle meter. Dynamic contact angle measurements were also carried out to determine the contact angle hysteresis by calculating the difference between the advancing and receding contact angles. The contact angle hysteresis for the samples was also determined by measuring the sliding angle of water droplets using the tilt table on the Krüss contact angle meter which was initially leveled using a highly accurate spirit level (see the Supporting Information).

For droplets on the lubricated textured surfaces, the majority of the profiles conformed to a circular arc, consistent with expectations for droplets of sizes less than the capillary length. We therefore extracted data points on the outer edge of the droplet and fitted a circular arc using a bespoke MATLAB program (a representative selection of points is shown in Figure 3 as an example). To obtain the apparent

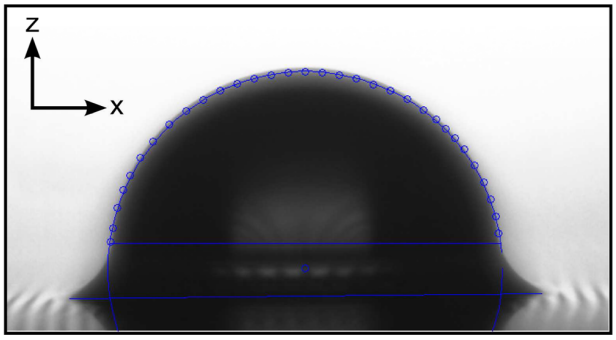

Figure 3. Image of a droplet on a lubricated textured surface with a sample of extracted data points on the side view profile of the spherical cap surface.

contact angles defined in Figure 1b, we fitted baselines at the base of the droplet and the wetting ridge, and at the top of the wetting ridge and used their intersection with the circular arc. The top of the wetting ridge was determined by sampling the data points from the profile close to the substrate that lie on the wetting ridge−vapor interface and finding the point of inflection of the profile given by the data points.

3.3. Droplet Evaporation Experiments. Small droplets of water (2.5 ± 0.2 μL) were deposited using a Proline Plus 2−25 μL pipet on each surface. These were allowed to evaporate in a monitored enclosed environment, and images of the droplets were taken at 30 s intervals for a maximum of 2500 s. All experiments in this study were carried out at room temperature (20−30 °C) and constant relative humidity (30−50%) in a bespoke environmental chamber to minimize humidity variations and protect from air currents within the laboratory. A temperature and humidity sensor (DHT22, Aosong Electronics) was placed inside of the chamber and connected to a LabVIEW program via an Arduino microcontroller. The LabVIEW program was used to image the droplet at the specified time-lapse interval and stamp the images with the time, date, temperature and relative humidity ready for postexperiment analysis. Apparent contact angles and contact base diameter were obtained from the images and the liquid−vapor surface area, spherical radius and hydrostatic pressure (using the Young−Laplace equation) as a function of time was calculated. To check reproducibility, three separate evaporation experiments were performed on each sample, these showed a variation of <4% in apparent contact radius at each time interval, and the average values of the aforementioned measurements were used in the analysis process. Axial symmetry was assumed in the evaporation process and used in image processing calculations.[17] The assumption of axial symmetry is very strongly obeyed for a SLIP surface where water droplets sit on top of a lubricating liquid in contrast to the case of direct liquid droplet-solid substrate contact which can involve contact line pinning. This was confirmed in this case with top view imaging of the droplet and image processing.

4. RESULTS AND DISCUSSION

4.1. Sliding Angles. Figure 4 shows images of droplets when placed on the different lubricated textured surfaces. In all cases the major part of the profile follows a spherical cap shape,

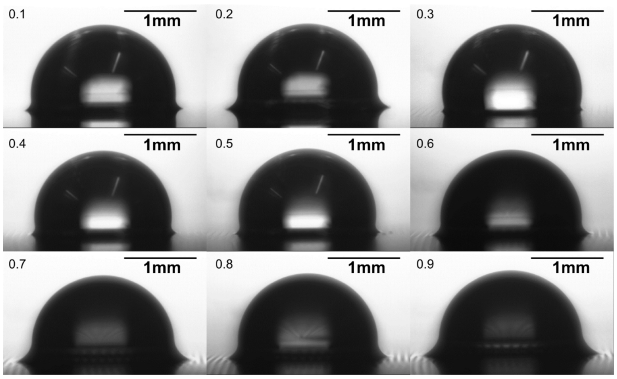

Figure 4. Water droplets on surfaces with different lubricated surface textures: l_f = 0.1−0.9 indicates the ratio of texture gap width to unit length which in this study has been set as 100 μm.

DOI: 10.1021/acs.langmuir.5b03240
Langmuir XXXX, XXX, XXX−XXX

Table 1. Sliding Angle of Water Droplets for Surfaces with Different Linear Lubricant Fraction, l_f, and Low Sliding angle

linear lubricant fraction, l_f	0.1	0.2	0.3	0.4	0.5	0.6	0.7	0.8	0.9
Cassie fraction, φ_s	0.81	0.64	0.49	0.36	0.25	0.16	0.09	0.04	0.01
Wenzel roughness, r_w	2.8	2.6	2.4	2.2	2	1.8	1.6	1.4	1.2
sliding angle (deg)	0.9 ± 0.1	1.3 ± 0.1	0.6 ± 0.1	0.7 ± 0.1	0.7 ± 0.1	0.3 ± 0.1	0.3 ± 0.1	0.4 ± 0.1	0.5 ± 0.1

but with a small wetting ridge. To test the effectiveness of the lubricated textured surfaces as SLIP surfaces in supporting mobile droplets, 1 mm diameter droplets of water were placed on each surface and the sliding angle was measured (Table 1). Here we use the linear lubricant fraction, $l_f = l/L$, as a naming convention for samples. The sliding angle for all of the nine sample designs, with l_f = 0.1, 0.2, 0.3, 0.4, 0.5, 0.6, 0.7, 0.8, 0.9, was very low (typically ~1° with some achieving as low as 0.3°) with very low contact angle hysteresis. We consider these as ideal SLIP surfaces with highly mobile contact lines. However, some of the fabricated samples did not show the same low hysteresis characteristics and where therefore classified as non-SLIP surfaces. For example, in one batch of surfaces, for three of the samples with l_f = 0.1, 0.4, 0.6, the sliding angles were much higher, (25.3° ± 0.6°), (29.8° ± 4.7°), and (16.6° ± 3.5°), respectively. This discrepancy may be due to the failure of the OTS functionalization process, which is more difficult to achieve on an SU-8 surface than surfaces such as silicon and glass.

4.2. Constant Contact Angle Mode Evaporation. On surfaces with low sliding angles, and therefore classified as SLIP surfaces, the evaporation of a water droplet proceeds with a steadily decreasing droplet volume and apparent contact area. (Note: After submission, the paper by Schellenberger et al.[32] was published reporting depinning events during evaporation-induced receding of a contact line in a system where it appears likely the evaporating droplet is in direct contact with the solid tops of their texture.) A wetting ridge is observed close to the substrate and visually the apparent contact angle, defined by the intersection of the spherical cap droplet profile and the baseline, appears to be above 90° and constant during evaporation as shown by the representative example time series of image in Figure 5.

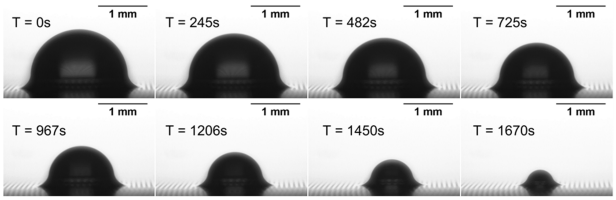

Figure 5. Images of a typical droplet evaporating on a low sliding angle SLIP surface.

Figure 6 shows the time dependence of the square of the apparent contact radius r_o^2 for the samples classified as SLIP surfaces using the criteria of low sliding angle values. The high mobility and low hysteresis of the apparent contact line provide a linear relationship from the very start of the evaporation process. This data shows a strong linear relationship over the entire range of the evaporation process and provides further confidence, in addition to the observed constancy of the apparent contact angle, that within the context of the diffusion limited evaporation model the droplet is undergoing constant contact angle evaporation.

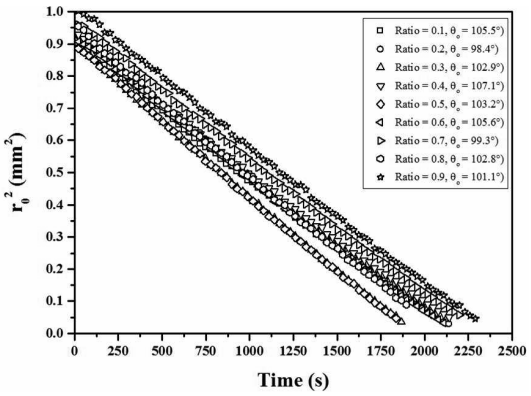

Figure 6. Linearity of r_o^2 during the evaporation of the samples with spacing/unit length ratio l_f = 0.1–0.9.

To test the validity of eq 16 and to provide further confidence in the r_o^2 versus time relationship, we estimated the diffusion coefficients of the droplets from the gradients, m, of the data in Figure 6, that is,

$$D = \frac{m\rho(1 - \cos\theta_o)(2 + \cos\theta_o)}{4(c_s - c_\infty)\sin^2\theta_o}\left(\frac{1 - \cos\theta_o}{2f_{PB}(\theta_s)}\right) \quad (18)$$

Experimentally, the two apparent contact angles, θ_o and θ_s, are observed to remain constant throughout the evaporation process. We assume complete saturation of the air at the droplet liquid/vapor interface and calculate the value of c_∞ using the relationship:

$$\text{relative humidity} = \frac{\text{actual vapor density}}{\text{saturation vapor density}} \times 100\% \quad (19)$$

where c_∞ is the actual vapor density and the value of c_s was obtained from reference data[36] for different temperatures. For example, for the droplet evaporation on a sample with the ratio l_f = 0.9, the slope is (4.282 ± 0.012) × 10^{-4} mm^2 s^{-1}, θ_o = 101.1 ± 1.0°, and θ_s= 84.4 ± 1.0°. The humidity of 38.4% and temperature of 23.3 °C gives $(c_s - c_\infty)$ = (12.66 ± 0.10) × 10^{-3} gm^{-3}. Therefore, the diffusion coefficient calculated from these values is D = (2.39 ± 0.20) × 10^{-5} m^2 s^{-1}. This compares favorably (to within 2%) with the value of D = 2.43 × 10^{-5} m^2 s^{-1} calculated from a linear fit to reference data obtained from the CRC Handbook[37] for diffusion of water vapor into air. Table 2 shows the calculated values of the diffusion coefficient, D, for all droplets on surfaces classified as SLIP surfaces by low values of sliding angles. They show an excellent correlation, within an average difference of 4% with the literature values.

It is possible to quantify the order of magnitude of the effect of the wetting skirt on estimates of the diffusion constant D, by using θ_o instead of θ_s in $f_{PB}(\theta)$ in eq 18. These estimates are shown as D_o in Table 2, and these are systematically lower than the estimates of D. On average, these estimates across all samples would have had a 14% difference from the literature values compared to an average difference of 4% when using the

DOI: 10.1021/acs.langmuir.5b03240
Langmuir XXXX, XXX, XXX–XXX

Table 2. Estimates of Diffusion Coefficients for Water into Air for Droplets on SLIP Surfaces

ratio l_f	RH (%)	T (°C)	Δc (g m^{-3})	θ_o (deg)	θ_s (deg)	$h_s/h_{o(i)}$ (%)	D (×10^{-5} m^2 s^{-1})	D_o (×10^{-5} m^2 s^{-1})	D_o/D (%)	D (lit) (×10^{-5} m^2 s^{-1})
0.1	48.3	26.2	13.16	105.5	86.5	13.7	2.44 ± 0.19	2.10 ± 0.19	86	2.50
0.2	34.0	22.2	12.81	98.4	90.5	13.4	2.13 ± 0.18	1.96 ± 0.16	92	2.41
0.3	34.2	22.2	12.76	102.9	97.6	6.7	2.42 ± 0.20	2.26 ± 0.19	93	2.41
0.4	47.2	26.4	13.59	107.1	87.3	16.7	2.46 ± 0.19	2.11 ± 0.19	86	2.50
0.5	34.2	22.5	12.76	103.2	94.7	8.5	2.50 ± 0.21	2.28 ± 0.19	91	2.41
0.6	46.9	26.7	13.91	105.6	88.3	13.1	2.36 ± 0.18	2.07 ± 0.18	88	2.52
0.7	38.0	22.8	12.74	99.3	87.0	19.3	2.21 ± 0.18	1.96 ± 0.16	89	2.43
0.8	37.9	23.3	12.76	102.8	90.6	13.6	2.50 ± 0.21	2.21 ± 0.18	88	2.43
0.9	38.4	23.3	12.66	101.1	84.4	20.5	2.39 ± 0.20	2.03 ± 0.17	85	2.43

model with the wetting skirt. To further test the effect of the wetting skirt on diffusion limited evaporation would require SLIP surfaces with lower apparent contact angles and higher wetting skirts as a proportion of the initial droplet apex height, $h_{o(i)}$.

Another possible limitation on the estimates of the diffusion constant is the assumption that evaporation proceeds across a water−air interface. Smith et al.[26] have previously noted that a lubricating liquid impregnated into a SLIP surface may spread and cloak the droplet with a thin layer, possibly a monolayer, of the lubricating liquid. If this were to occur, the evaporation would proceed through a combined water−oil−air interface and this could reduce the evaporation rate. To spread over and cloak the droplet, the spreading coefficient of the lubricating liquid, S, on water (w) in the presence of air (a), $S_{ow(a)} = \gamma_{wa} - \gamma_{ow} - \gamma_{oa}$, has to be greater than zero, whereas $S_{ow(a)} < 0$ implies the oil will not cloak the droplet. Using the value of γ_{ow} obtained from literature[38] and the value of γ_{oa} provided by Dow Corning for the silicone oil gives $S_{ow(a)}$ = 5.1 mN/m. This implies that the oil should cloak the droplet, although we did not observe such an effect. In our analysis, we assume the layer of oil either does not cloak the droplet or is sufficiently thin for its effect on the evaporation rate to be negligible.

4.3. Mixed Mode Evaporation. In the mixed mode of evaporation changes in both the contact area (equivalently the contact radius) and contact angle occur (for recent work see, e.g., Nguyen and Nguyen,[39] Stauber et al.,[40] and Dash and Garimella[41]). Figure 7 shows an example of a droplet

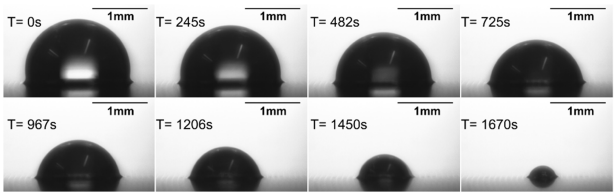

Figure 7. Images of a typical droplet evaporating on a non-SLIP surface.

evaporating on a lubricated textured non-SLIP surface classified as such according to having a high sliding angle. Under these lighting conditions the underlying texture of the surface is almost visible, but the constant contact angle mode evaporation was not observed for extended times on these samples deemed to be non-SLIP surfaces according to the sliding angle criteria. There was, however, a brief initial stage during the evaporation process that showed approximately constant contact angle evaporation. The droplet appeared to initially evaporate with a constant apparent contact angle θ_o and a diminishing apparent contact radius. The contact line then appeared to pin and θ_o began to drop. Interestingly, the contact line subsequently appeared to depin and show a contraction in apparent contact radius before becoming pinned once again. This stick−slip process repeated itself throughout the remainder of the evaporation process.

Figure 8 shows example data for a droplet on one of the non-SLIP surface and clearly shows stepping, which is characteristic

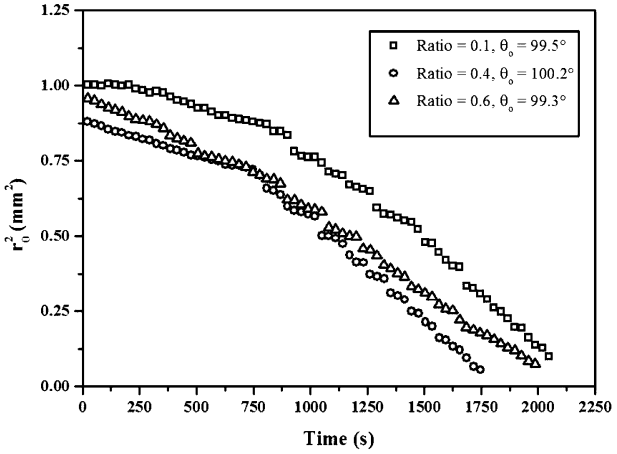

Figure 8. Plot of the square of drop apparent contact radius as a function of time for sessile droplet evaporation on a non-SLIP surface.

of a stick−slip regime.[32,42,43] Figure 9 shows a plot of a portion of the time sequence data for the lubricated texture with l_f = 0.4 and a sliding angle of 29.8° ± 4.7°, where this stepping is highly prevalent. The steps in the data appear to rapidly change the apparent contact radius by approximately 35 μm. This value corresponds approximately to the value for the gaps between pillars of 40 μm for this texture's value of linear lubricant fraction. When a drop in apparent contact radius occurs, an increase in the contact angle, θ_o, is also observed. θ_o decreases as the contact line is pinned and increases as the contact line depins (Figure 9).

Although non-SLIP samples did not exhibit constant contact angle evaporation throughout the entirety of the experiments, it is interesting to note that a brief constant contact angle period was observed in the initial stage before showing a stepwise retreat. It is therefore possible that, due to variations in the quality of the OTS coating, these surfaces were initially very close to becoming SLIP surfaces and the increase in the Laplace pressure as the droplet evaporated may have forced the water in the droplet into direct contact with the solid surface at the top of the pillars. This would represent a transition from a true SLIPS state to a hemiwicked Cassie−Baxter type state where

DOI: 10.1021/acs.langmuir.5b03240
Langmuir XXXX, XXX, XXX−XXX

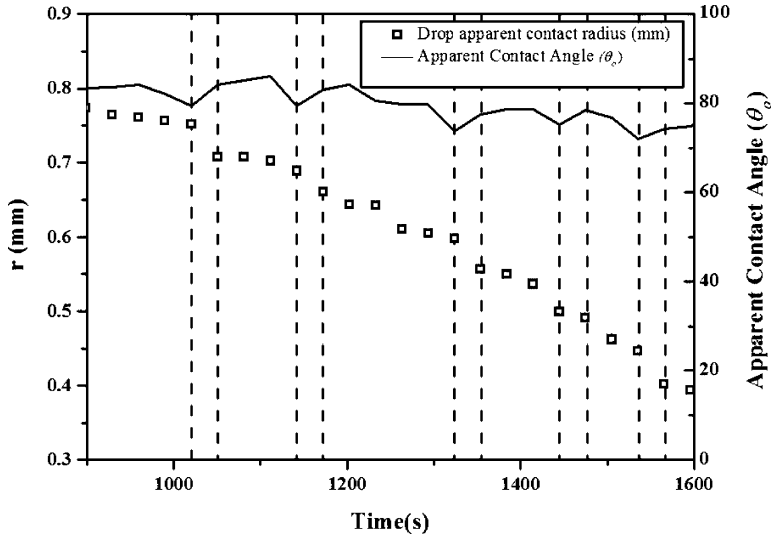

Figure 9. Plot of drop apparent contact radius and apparent contact angle as a function of time for non-SLIPS sample with $l_f = 0.4$ where the width of pillars is 60 μm and the gap between pillars is 40 μm and a sliding angle of 29.8° ± 4.7°. The sudden changes in drop apparent contact radius roughly correspond to spacing of 40 μm as the contact line jumps across pillar gaps. Vertical dashed lines indicate increases in apparent contact angle where a sudden drop in apparent contact radius occurs.

the droplet rests on a combination of the solid tops of pillars and the oil-filled gaps between pillars. This transition to a more sticky state would be analogous to what has been observed to occur on a superhydrophobic surface when an evaporating drop undergoes a transition from a Cassie–Baxter state to a Wenzel state. In the SLIPS case, a further transition to a Wenzel state whereby the water fully displaces oil within the gaps of the texture might also be possible, although this would require substantial reductions on droplet curvature to generate excess Laplace pressure. An interpretation of water displacement of oil from the tops of pillars, if substantiated, would suggest that the tilt angle method of making a sliding angle measurement might also cause a slippery to sticky transition in some samples.

5. CONCLUSION

The diffusion-limited evaporation of small droplets of water placed on lubricated textured surfaces, classified as slippery liquid-infused porous surfaces (SLIPS) by their low sliding angles, has been studied. This type of surface allows for high apparent contact angle (~100°) droplets, and gives a highly mobile apparent contact line which allows a constant contact angle mode type of evaporation. The presence of a wetting ridge created by the balance of the three interfacial forces at the line of contact between the droplet, the infusing liquid at the base of the droplet and air (often represented by a Neumann triangle) has been accounted for by extrapolating an apparent contact angle with the surface. A model has been developed which accounts for the wetting ridge by the concept of a wetting skirt limiting the droplet liquid–vapor surface area available for the evaporation. This model provides a linear dependence of the apparent contact surface area on time. On surfaces which showed ideal low sliding angle SLIPS characteristics this model has allowed us to calculate the diffusion coefficients for water in air and excellent correlation, to within an average of 4% of reference values was obtained. On lubricated textured surfaces which did not show ideal low sliding angle SLIPS characteristics the droplets did not demonstrate constant contact angle evaporation during extended times. They did, however, show evidence of the droplet transitioning into a stick–slip regime. The size of the stick–slip jumps of the apparent contact radius data was 35 μm which approximately corresponds to the surface texture spacing. This transition is possibly due to droplets transitioning from an ideal SLIPS state to one with direct droplet contact with the tops of pillars or to an oil hemiwicked Cassie–Baxter state under increased excess Laplace pressure as their spherical radius of curvature reduces, displacing the lubricating liquid and coming into contact with the surface texture.

■ ASSOCIATED CONTENT

Supporting Information

The Supporting Information is available free of charge on the ACS Publications website at DOI: 10.1021/acs.langmuir.5b03240.

Experimental procedures in detail: fabrication of textured surfaces, surface chemistry modification, impregnation with lubricating liquid and leveling Krüss meter for sliding angle measurements (PDF)

■ AUTHOR INFORMATION

Corresponding Author

*E-mail: gary.wells@northumbria.ac.uk.

Notes

The authors declare no competing financial interest.

■ ACKNOWLEDGMENTS

J.H.G. gratefully acknowledges financial support from Reece Innovation and the University of Northumbria at Newcastle via a postgraduate research studentship. The authors also acknowledge Dr. Linzi E. Dodd, Dr. Michael Cooke, and Dr. Pietro Maiello for valuable advice and technical support.

DOI: 10.1021/acs.langmuir.5b03240
Langmuir XXXX, XXX, XXX–XXX

REFERENCES

(1) Erbil, H. Y. Evaporation of Pure Liquid Sessile and Spherical Suspended Drops: A Review. *Adv. Colloid Interface Sci.* **2012**, *170* (1−2), 67−86.

(2) Park, J.; Moon, J. Control of Colloidal Particle Deposit Patterns within Picoliter Droplets Ejected by Ink-Jet Printing. *Langmuir* **2006**, *22* (8), 3506−3513.

(3) Kimura, M.; Misner, M. J.; Xu, T.; Kim, S. H.; Russell, T. P. Long-Range Ordering of Diblock Copolymers Induced by Droplet Pinning. *Langmuir* **2003**, *19* (23), 9910−9913.

(4) Jing, J.; Reed, J.; Huang, J.; Hu, X.; Clarke, V.; Edington, J.; Housman, D.; Anantharaman, T. S.; Huff, E. J.; Mishra, B.; Porter, B.; Shenker, A.; Wolfson, E.; Hiort, C.; Kantor, R.; Aston, C.; Schwartz, D. C. Automated High Resolution Optical Mapping using Arrayed, Fluid-Fixed DNA Molecules. *Proc. Natl. Acad. Sci. U. S. A.* **1998**, *95* (14), 8046−8051.

(5) Yu, Y.; Zhu, H.; Frantz, J. M.; Reding, M. E.; Chan, K. C.; Ozkan, H. E. Evaporation and Coverage Area of Pesticide Droplets on Hairy and Waxy Leaves. *Biosystems Engineering* **2009**, *104* (3), 324−334.

(6) Picknett, R. G.; Bexon, R. The Evaporation of Sessile or Pendent Drops in Still Air. *J. Colloid Interface Sci.* **1977**, *61*, 336−350.

(7) Cazabat, A.-M.; Guéna, G. Evaporation of Macroscopic Sessile Droplets. *Soft Matter* **2010**, *6* (12), 2591−2612.

(8) Larson, R. G. Transport and Deposition Patterns in Drying Sessile Droplets. *AIChE J.* **2014**, *60* (5), 1538−1571.

(9) Stauber, J. M.; Wilson, S. K.; Duffy, B. R.; Sefiane, K. Evaporation of Droplets on Strongly Hydrophobic Substrates. *Langmuir* **2015**, *31* (12), 3653−3660.

(10) Birdi, K. S.; Vu, D. T.; Winter, A. A Study of the Evaporation Rates of Small Water Drops Placed on a Solid Surface. *J. Phys. Chem.* **1989**, *93* (9), 3702−3703.

(11) Birdi, K. S.; Vu, D. T. Wettability and the Evaporation Rates of Fluids from Solid Surfaces. *J. Adhes. Sci. Technol.* **1993**, *7* (6), 485−493.

(12) Shanahan, M. E. R.; Bourgès, C. Effects of Evaporation on Contact Angles on Polymer Surfaces. *Int. J. Adhes. Adhes.* **1994**, *14* (3), 201−205.

(13) Rowan, S. M.; Newton, M. I.; McHale, G. Evaporation of Microdroplets and the Wetting of Solid Surfaces. *J. Phys. Chem.* **1995**, *99* (35), 13268−13271.

(14) Rowan, S. M.; McHale, G.; Newton, M. I.; Toorneman, M. Evaporation of Microdroplets of Three Alcohols. *J. Phys. Chem. B* **1997**, *101* (8), 1265−1267.

(15) McHale, G.; Rowan, S. M.; Newton, M. I.; Banerjee, M. K. Evaporation and the Wetting of a Low-Energy Solid Surface. *J. Phys. Chem. B* **1998**, *102* (11), 1964−1967.

(16) Cassie, A. B. D.; Baxter, S. Wettability of Porous Surfaces. *Trans. Faraday Soc.* **1944**, *40* (0), 546−551.

(17) McHale, G.; Aqil, S.; Shirtcliffe, N. J.; Newton, M. I.; Erbil, H. Y. Analysis of Droplet Evaporation on a Superhydrophobic Surface. *Langmuir* **2005**, *21* (24), 11053−11060.

(18) Wenzel, R. N. Resistance of Solid Surfaces to Wetting by Water. *Ind. Eng. Chem.* **1936**, *28* (8), 988−994.

(19) Tsai, P.; Lammertink, R. G. H.; Wessling, M.; Lohse, D. Evaporation-Triggered Wetting Transition for Water Droplets upon Hydrophobic Microstructures. *Phys. Rev. Lett.* **2010**, *104* (11), 116102.

(20) Gelderblom, H.; Marín, Á. G.; Nair, H.; van Houselt, A.; Lefferts, L.; Snoeijer, J. H.; Lohse, D. How Water Droplets Evaporate on a Superhydrophobic Substrate. *Phys. Rev. E* **2011**, *83* (2), 026306.

(21) Jung, Y. C.; Bhushan, B. Wetting Behaviour during Evaporation and Condensation of Water Microdroplets on Superhydrophobic Patterned Surfaces. *J. Microsc.* **2008**, *229* (1), 127−140.

(22) Tan, S. X.; Zhang, X. Y.; Zhao, N.; Xu, J. Simulation of Sessile Water-Droplet Evaporation on Superhydrophobic Polymer Surfaces. *Huaxue Wuli Xuebao* **2007**, *20* (2), 140.

(23) Zhang, X.; Tan, S.; Zhao, N.; Guo, X.; Zhang, X.; Zhang, Y.; Xu, J. Evaporation of Sessile Water Droplets on Superhydrophobic Natural Lotus and Biomimetic Polymer Surfaces. *ChemPhysChem* **2006**, *7* (10), 2067−2070.

(24) Kulinich, S. A.; Farzaneh, M. Effect of Contact Angle Hysteresis on Water Droplet Evaporation from Super-Hydrophobic Surfaces. *Appl. Surf. Sci.* **2009**, *255* (7), 4056−4060.

(25) Quéré, D. Non-Sticking Drops. *Rep. Prog. Phys.* **2005**, *68* (11), 2495.

(26) Smith, J. D.; Dhiman, R.; Anand, S.; Reza-Garduno, E.; Cohen, R. E.; McKinley, G. H.; Varanasi, K. K. Droplet Mobility on Lubricant-Impregnated Surfaces. *Soft Matter* **2013**, *9* (6), 1772−1780.

(27) Solomon, B. R.; Khalil, K. S.; Varanasi, K. K. Drag Reduction using Lubricant-Impregnated Surfaces in Viscous Laminar Flow. *Langmuir* **2014**, *30* (36), 10970−6.

(28) Wong, T.-S.; Kang, S. H.; Tang, S. K. Y.; Smythe, E. J.; Hatton, B. D.; Grinthal, A.; Aizenberg, J. Bioinspired Self-Repairing Slippery Surfaces with Pressure-Stable Omniphobicity. *Nature* **2011**, *477* (7365), 443−447.

(29) Huang, X.; Chrisman, J. D.; Zacharia, N. S. Omniphobic Slippery Coatings Based on Lubricant-Infused Porous Polyelectrolyte Multilayers. *ACS Macro Lett.* **2013**, *2* (9), 826−829.

(30) Manna, U.; Lynn, D. M. Fabrication of Liquid-Infused Surfaces Using Reactive Polymer Multilayers: Principles for Manipulating the Behaviors and Mobilities of Aqueous Fluids on Slippery Liquid Interfaces. *Adv. Mater.* **2015**, *27* (19), 3007−3012.

(31) Kim, P.; Wong, T.-S.; Alvarenga, J.; Kreder, M. J.; Adorno-Martinez, W. E.; Aizenberg, J. Liquid-Infused Nanostructured Surfaces with Extreme Anti-Ice and Anti-Frost Performance. *ACS Nano* **2012**, *6* (8), 6569−6577.

(32) Schellenberger, F.; Xie, J.; Encinas, N.; Hardy, A.; Klapper, M.; Papadopoulos, P.; Butt, H.-J.; Vollmer, D. Direct Observation of Drops on Slippery Lubricant-Infused Surfaces. *Soft Matter* **2015**, *11* (38), 7617−7626.

(33) Erbil, H. Y.; McHale, G.; Newton, M. I. Drop Evaporation on Solid Surfaces: Constant Contact Angle Mode. *Langmuir* **2002**, *18* (7), 2636−2641.

(34) Bourges-Monnier, C.; Shanahan, M. E. R. Influence of Evaporation on Contact Angle. *Langmuir* **1995**, *11* (7), 2820−2829.

(35) Bico, J.; Thiele, U.; Quere, D. Wetting of Textured Surfaces. *Colloids Surf., A* **2002**, *206* (1−3), 41−46.

(36) Kaye, G. W. C.; Laby, T. H. *Kaye and Laby Tables of Physical and Chemical Constants*; National Physical Laboratory: Teddington, U.K., 2005.

(37) Weast, R. C.; Astle, M.; Beyer, W. *CRC Handbook of Chemistry and Physics*; CRC Press, Inc., Boca Raton, FL, 1985.

(38) Wang, C. Y.; Calabrese, R. V. Drop Breakup in Turbulent Stirred-Tank Contactors. Part II: Relative Influence of Viscosity and Interfacial Tension. *AIChE J.* **1986**, *32* (4), 667−676.

(39) Nguyen, T. A. H.; Nguyen, A. V. Increased Evaporation Kinetics of Sessile Droplets by Using Nanoparticles. *Langmuir* **2012**, *28* (49), 16725−16728.

(40) Stauber, J. M.; Wilson, S.; Duffy, B.; Sefiane, K. On the Lifetimes of Evaporating Droplets. *J. Fluid Mech.* **2014**, *744* (R2), 1−12.

(41) Dash, S.; Garimella, S. V. Droplet Evaporation on Heated Hydrophobic and Superhydrophobic Surfaces. *Phys. Rev. E* **2014**, *89* (4), 042402.

(42) Anantharaju, N.; Panchagnula, M.; Neti, S. Evaporating Drops on Patterned Surfaces: Transition from Pinned to Moving Triple Line. *J. Colloid Interface Sci.* **2009**, *337* (1), 176−182.

(43) Orejon, D.; Sefiane, K.; Shanahan, M. E. R. Stick−Slip of Evaporating Droplets: Substrate Hydrophobicity and Nanoparticle Concentration. *Langmuir* **2011**, *27* (21), 12834−12843.

DOI: 10.1021/acs.langmuir.5b03240
Langmuir XXXX, XXX, XXX−XXX

Slippery Liquid-Infused Porous Surfaces and Droplet Transportation by Surface Acoustic Waves

J. T. Luo,[1,2] N. R. Geraldi,[2] J. H. Guan,[2] G. McHale,[2] G. G. Wells,[2] and Y. Q. Fu[2,*]

[1]*College of Physics and Energy, Shenzhen Key Laboratory of Sensor Technology, Shenzhen University, Shenzhen 518060, People's Republic of China*

[2]*Smart Materials and Surfaces Laboratory, Faculty of Engineering and Environment, Northumbria University, Newcastle upon Tyne NE1 8ST, United Kingdom*

(Received 9 September 2016; revised manuscript received 26 December 2016; published 24 January 2017)

On a solid surface, a droplet of liquid will stick due to the capillary adhesion, and this causes low droplet mobility. To reduce contact line pinning, surface chemistry can be coupled to micro- and/or nanostructures to create superhydrophobic surfaces on which a droplet balls up into an almost spherical shape, thus, minimizing the contact area. Recent progress in soft matter has now led to alternative lubricant-impregnated surfaces capable of almost zero contact line pinning and high droplet mobility without causing droplets to ball up and minimize the contact area. Here we report an approach to surface-acoustic-wave- (SAW) actuated droplet transportation enabled using such a surface. These surfaces maintain the contact area required for efficient energy and momentum transfer of the wave energy into the droplet while achieving high droplet mobility and a large footprint, therefore, reducing the threshold power required to induce droplet motion. In our approach, we use a slippery layer of lubricating oil infused into a self-assembled porous hydrophobic layer, which is significantly thinner than the SAW wavelength, and avoid damping of the wave. We find a significant reduction (up to 85%) in the threshold power for droplet transportation compared to that using a conventional surface-treatment method. Moreover, unlike droplets on superhydrophobic surfaces, where interaction with the SAW induces a transition from a Cassie-Baxter state to a Wenzel state, the droplets on our liquid-impregnated surfaces remain in a mobile state after interaction with the SAW.

DOI: 10.1103/PhysRevApplied.7.014017

I. INTRODUCTION

A fundamental problem in any situation requiring mobility of liquid droplets is the contact line pinning caused by the inherent contact angle hysteresis (the difference between the advancing and receding contact angles) of liquids on solid surfaces [1–3]. Contact line pinning determines the formation of coffee-ring stains during the drying of droplets containing solute [4], which is an effect that has to be carefully controlled in droplet microarrays [5] and inkjet printing [6]. It also causes barriers to droplet transport in microfluidics where a large surface-area-to-volume ratio generally exists [7]. To minimize the effect of contact angle hysteresis on droplet mobility, the surface chemistry can be made hydrophobic, and by manipulating the surface topography, superhydrophobic surfaces can be created [8–12]. A droplet in a Cassie-Baxter state [as shown in Fig. 1(a)] bridging between the tips of the surface features on a superhydrophobic surface balls up into an almost spherical shape. This increase in hydrophobicity minimizes the contact area and the effect of contact line pinning, thereby resulting in highly mobile droplets, unless the droplet transitions into a Wenzel state [see Fig. 1(b)] with liquid penetrating between the surface features [11].

A. Acoustofluidics

Recently, there has been increased interest in surface-acoustic-wave- (SAW) based microfluidics (often called acoustofluidics) and biosensors due to their promising applications in the fields of lab-on-a-chip and point-of-care diagnosis [13–18]. For these applications, it is essential to develop strategies for reliable and efficient microfluidic functions and manipulation of particles and biomolecules in the liquid, such as in droplet digital microfluidics [19–21]. For such small volumes of liquid down to micro- and nanoliters, it is a challenge to efficiently manipulate and actuate droplets or liquid in microchannels due to the large surface-area-to-volume ratio in microsystems and, therefore, the dominance of surface-tension forces. The movement of small droplets becomes particularly problematic with even modest levels of contact angle hysteresis, which results in contact line pinning [7,22–24]. So far, various techniques have been employed to drive microscale fluids, including pressure gradients, capillary forces, electrical and magnetic fields, and SAWs [13,19,25]. SAW microfluidic actuation has significant advantages over other technologies, such as simple device structures, easy processing and low fabrication

*Corresponding author.
richard.fu@northumbria.ac.uk

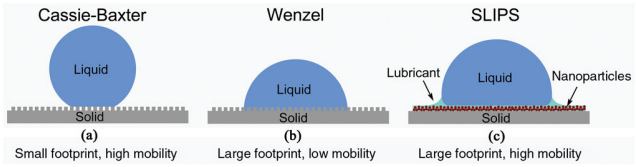

FIG. 1. Three states of surface wetting influenced by topography. (a) The Cassie-Baxter state involves the droplet bridging between the tips of the surface features, thus, reducing the solid-liquid interfacial area. The droplet has a small footprint and high mobility. (b) The Wenzel state involves the droplet penetrating between the surface features, thus, increasing the solid-liquid interfacial area. The droplet sticks to the surface and has low mobility. (c) The lubricant-impregnated surface retains lubricant due to it wetting a high-surface-area nanoparticle porous structure whose hydrophobic properties ensure the lubricant is not displaced by water. The droplet has a large footprint and high mobility.

cost, tunable frequency response, and the ability to manipulate liquids on a flat surface with precision [26].

For microfluidic applications, Rayleigh SAWs, which propagate along a solid surface with their energy confined to within one wavelength of the surface, are often used [13,15,27,28]. These are generated by applying a radio-frequency (rf) signal to interdigital transducers (IDTs), which are patterned on top of a piezoelectric substrate [Fig. 2(a)]. When the propagating SAW comes into contact with a droplet along its path, a leaky SAW with a decaying amplitude is launched and dissipated into the droplet at an angle called the Rayleigh angle (θ_R) [see Fig. 2(b)], following Snell's law of diffraction [14]

$$\theta_R = \sin^{-1}\left(\frac{c_l}{c_s}\right), \tag{1}$$

where c_l and c_s are the speeds of sound in the liquid and in the substrate, respectively. For SAW-induced droplet actuation on the substrate surface, coupling of the acoustic wave energy and transfer of momentum to the droplet are required. The energy and momentum of the longitudinal wave dissipated into the droplet provide a pressure or a body force on the droplet in the direction of propagation of the SAW. This energy dissipation provides the basis for droplet movement, pumping and mixing, streaming, manipulation, and jetting or nebulization [13,15,26,27,29].

The piezoelectric materials used for SAW devices are mostly hydrophilic in nature (e.g., with low contact angles from 40° to 60°), and so to enhance the transportation of droplets on planar substrates, a hydrophobic treatment of the SAW device is often used. The application of a hydrophobic layer reduces the length of the droplet–solid-surface contact line, but also reduces the solid-liquid contact area critical to the acoustic wave–droplet interaction. Various hydrophobic polymer coatings such as octadecyltrichlorosilane, Teflon AF®, and CYTOP™ have previously been used to increase the contact angle of the

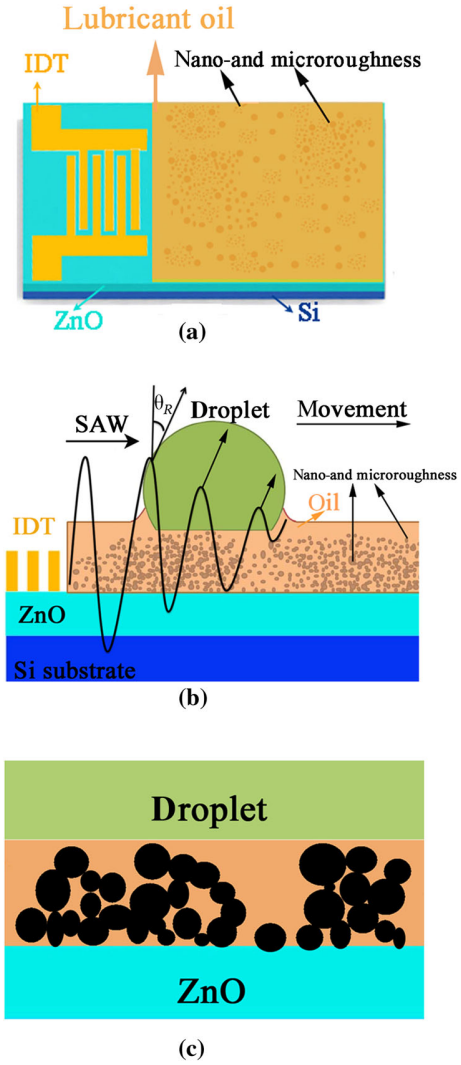

FIG. 2. (a) Schematic illustration of a SAW device with a SLIP surface. (b) Schematic illustration of the interaction between a SAW and a liquid droplet on a SLIP surface. The Rayleigh angle θ_R and a larger droplet footprint enabling effective transfer of SAW energy to drive the droplet motion are indicated. (c) Illustration of the enlarged interface between the droplet and the lubricant oil.

droplet on the surface [13,27–29]. Most of the hydrophobic polymers coated onto SAW device surfaces have contact angles of between 90°–120° [13,29–30]. Surfaces with such contact angles retain a sufficiently large footprint for the applied SAW power to be dissipated into the droplet through the wave–liquid interaction area. However, the relatively large contact area when combined with the contact angle hysteresis, as we describe below, often results in large power required to transport the droplet.

B. Contact line pinning and superhydrophobicity

The SAW-induced pressure gradient or a body force inside the droplet is dependent on the solid-liquid contact

area and the input SAW power. A sufficient area is required for an effective acoustic wave–droplet interaction and, thus, the associated microfluidic functions. Increasing the input SAW power beyond a critical value causes the pressure-gradient-induced body force on the droplet to be larger than the pinning forces arising from solid-liquid interfacial interactions, thus, moving the droplet along the wave propagation direction.

For a small liquid droplet resting on a smooth solid surface, the force that must be overcome to create motion is related to the horizontal component of the solid-liquid surface-tension force, $\gamma_{LG}\cos\theta$, where γ_{LG} is the liquid-gas interfacial tension, which is 72.8 mNm^{-1} for water in air at room temperature, and θ is the contact angle. On all solid surfaces, some level of contact angle hysteresis is observed such that when the droplet volume increases, the initial effect is that the contact angle increases without motion of the contact line until an advancing contact angle θ_A is exceeded. Similarly, when the droplet volume decreases, the initial effect is that the contact angle decreases without motion of the contact line until the contact angle becomes less than a receding contact angle, θ_R. To set a droplet into motion, the critical pinning force F_c that must be overcome is related to the difference in forces at the advancing and receding edges of the droplet, i.e.,

$$F_c \sim 2\pi R\sin\theta\gamma_{LG}(\cos\theta_R - \cos\theta_A), \tag{2}$$

where the factor $2\pi R\sin\theta$ arises from the integration of forces around the droplet-solid contact line, and R is the spherical radius of the droplet. The spherical radius of the droplet can be calculated from its volume V,

$$R = \left[\frac{3V}{\pi(2+\cos\theta)(1-\cos\theta)^2}\right]^{1/3}. \tag{3}$$

To overcome the droplet transportation problem, one strategy is to use small-scale, micro- and/or nanosurface texture or roughness to create a superhydrophobic surface to cause a droplet to ball up with a large contact angle θ, and small droplet-solid contact line length (also referred to as the *lotus* effect). In the ideal Cassie-Baxter state, the droplet bridges between surface features, as shown in Fig. 1(a) [31], and this has a small droplet footprint [8–12]. Moreover, the bridging between the surface features also results in a high receding contact angle, and, since $\theta_R < \theta < \theta_A$, the contact angle hysteresis is low, and the droplet is highly mobile on the surface. However, this approach also reduces the area of droplet contact needed for an effective acoustic wave–liquid interaction. In addition, this Cassie-Baxter state itself can be unstable under a significant external perturbation such as SAW agitation, which can cause a rapid transition from a Cassie-Baxter state into a Wenzel state with the droplet penetrating between the surface features, as shown in Fig. 1(b) [32]. In the Wenzel state, the droplet maintains complete contact with the surface features rather than bridging between them, and the receding contact angle reduces substantially causing high values of contact angle hysteresis and low droplet mobility.

C. Slippery liquid-infused porous surfaces

An alternative approach to facilitate droplet transportation is to focus on reducing the contact angle hysteresis [22]. In the absence of contact angle hysteresis, contact line pinning is removed, and a droplet will be highly mobile irrespective of its equilibrium contact angle and droplet–solid-surface contact area [33,34]. It is our hypothesis that reducing contact angle hysteresis and increasing droplet mobility, without increasing the equilibrium contact angle towards 180°, can enable the twin objectives of ease of droplet actuation and large droplet contact area for acoustic wave interaction.

Recent advances in wetting research have seen the development of slippery liquid-infused porous surfaces (SLIPS) inspired by the *Nepenthes pitcher* plant. These surfaces offer the high droplet mobility of superhydrophobic surfaces, while maintaining a large apparent droplet footprint [see Fig. 1(c)] [33]. The physical strategy is to create a large-area surface texture using micro- and/or nanoscale features which can be infused with a completely wetting nonvolatile lubricating liquid but which is hydrophobic to water, thus, preventing the lubricant from being displaced. The high surface area of this textured surface means it is energetically favorable for the lubricant to spread into and be retained by the surface while also forming a stable thin film across the surface. In such a situation, a water droplet rests on the lubricant layer, thus, entirely removing direct contact between the droplet and the solid surface and the associated contact angle hysteresis which causes contact line pinning.

Smith *et al.* [35] previously derived the absolute equilibrium thermodynamic states of a water droplet on a lubricant-impregnated surface and described their relationship to the concept of hemiwicking [36]. First, consider a textured surface in air. The total interface energy per unit area for a lubricant oil to impregnate the surface and coat across the tops of the surface features is $E_{(a)} = \gamma_{OA} + r_w\gamma_{OS}$, where γ_{OA} and γ_{OS} are the interfacial tensions (energies per unit area) of the oil-air and oil-solid interfaces. For this oil impregnation to be the lowest-energy state possible, the spreading power of the oil on the solid in the presence of air $S_{OS(a)}$ must satisfy the condition

$$\begin{aligned} S_{OS(a)} &= \gamma_{SA} - (\gamma_{OS} + \gamma_{OA}) \\ &= \gamma_{OA}(\cos\theta_{OS(a)} - 1) \geq 0, \end{aligned} \tag{4}$$

where $\theta_{OS(a)}$ is the contact angle of oil on the solid in the presence of air. Thus, the equivalent condition is that the oil

must completely wet the solid in air, i.e., $\theta_{OS(a)} = 0°$ so that the oil is film forming on the solid in air.

Next, consider the textured surface under water. The total interface energy per unit area for a lubricant oil to impregnate the surface and coat across the tops of the surface features is $E_w = \gamma_{OW} + r_w\gamma_{OS}$, where γ_{OW} is the interfacial tension (energy per unit area) of the oil-water interface. For this oil impregnation to be the lowest-energy state possible, the spreading power of the oil on the solid in the presence of water $S_{OS(w)}$ must satisfy the condition

$$\begin{aligned} S_{OS(w)} &= \gamma_{SW} - (\gamma_{OS} + \gamma_{OW}) \\ &= \gamma_{OW}(\cos\theta_{OS(w)} - 1) \geq 0, \end{aligned} \tag{5}$$

where $\theta_{OS(w)}$ is the contact angle of the oil on the solid in the presence of water. Thus, the equivalent condition is that the oil must completely wet the solid in water, i.e., $\theta_{OS(w)} = 0°$ so that the oil is film forming on the solid in water.

In our previous work on droplet evaporation from SLIPS surfaces, we have observed that a droplet will inherently have a very low contact angle hysteresis [37] and be highly mobile, typically moving when a surface is tilted from horizontal by less than 1°, due to the existence of the lubricating layer. Ensuring the conditions in Eqs. (3) and (4) are satisfied means that any motion of the droplet contact line always occurs on top of a lubricant film, which is retained by the solid surface in both air and water.

D. New design of SLIPS for SAW microfluidics

In the present work, we propose a method for SAW-induced droplet actuation, which is built on our understanding of SLIP surfaces [22,33,34,37,38]. In our case, the infused liquid is chosen to be a lubricant oil, and by designing the SLIP-surface layer to be significantly thinner than the SAW wavelength, we ensure that little damping of the acoustic wave occurs by the lubricant in the SLIP layer. The resulting surfaces support highly mobile droplets, while uniquely retaining the large footprint necessary for efficient dissipation of acoustic wave energy and momentum into the droplet. Furthermore, the lubricant-impregnated surface structure ensures the droplet state is robust and less prone to the type of transition from a Cassie-Baxter state to a Wenzel state, which can be observed on superhydophobic surfaces [11] due to interaction with an acoustic wave. Our approach using the SLIPS-enabled SAW droplet transportation offers low-power actuation with a stable droplet state when a droplet is located within the SAW propagation path.

II. EXPERIMENTAL METHODS

To prove our concept and the key physical insight that slippery lubricant-impregnated surfaces enable SAW-induced droplet transport due to their ability to also simultaneously maintain a large contact area, we coat SAW substrates with a thin self-assembled porous superhydrophobic layer infused with lubricating silicone oil [as illustrated in Figs. 2(a)–2(c)]. This surface treatment design provides a 3D porous topography with microscale and nanoscale features coexisting with hydrophobic nanoparticles, thus, forming a superhydrophobic surface. Silicone oil spreads completely on these hydrophobic nanoparticles and into the porous structure in the presence of both air and water ($\theta_{OS(a)} = 0°$ and $\theta_{OS(w)} = 0°$) [39]. The lubricant oil impregnates and flows atop the surface features in air, but it is not displaced by the water in a deposited droplet [as shown in Figs. 2(b) and 2(c)]. Thus, silicone oil impregnation converts the superhydrophobic surface into a SLIP surface. By controlling the roughness of the surface texture and the oil-impregnation process, one can achieve the ideal case of a SLIP surface with high droplet mobility but which also allows efficient SAW-induced droplet transportation.

ZnO films with a thickness of about 3.5 μm are deposited onto Si substrates using rf magnetron sputtering. Aluminum IDTs with a thickness of 150 nm are then fabricated using conventional lithographic and lift-off technology. The IDTs consist of 30 pairs of fingers with a wavelength of 200 μm and an aperture of 4.9 mm. Rayleigh modes with a resonant frequency of 22.44 MHz with the same return loss are obtained for all the SAW devices.

The SAW device surfaces are treated using a commercially available water-repellent agent (Glaco™ Mirror Coat Zero, SOFT99 Corp.), which is an alcohol-based suspension of silica nanoparticles. The IDTs are covered by a Kapton tape during the coating process. The SAW devices are placed with a tilt angle of around 45° from horizontal and then sprayed with the hydrophobic coating. The particle suspensions are left for 10 min to allow the solvent to evaporate. The device is then heated to 200 °C for 20 min. The process is repeated to produce SAW devices with between one and five coatings of the hydrophobic Glaco coating. Scanning electron microscopy (SEM) is used to characterize the surface morphology of the Glaco coating on the ZnO/Si SAW devices. A Krüss DSA30 contact angle meter is used to measure the advancing and receding contact angles to characterize the hydrophobic nature of the surfaces.

To create the SLIP surfaces, all of the samples are dip coated with silicone oil [Sigma-Aldrich, with a viscosity of 20 centistokes (25 °C) and a surface tension of 20.6 mNm^{-1}] by vertically withdrawing them from an oil reservoir at a speed of either 1 $mm\,s^{-1}$ or 0.1 $mm\,s^{-1}$. We use the confocal laser scanning microscope to characterize the thickness of the oil. The thickness of the oil is proportional to the withdrawal speed, and the measured thickness of the oil layers for the two withdrawal speeds (1 $mm\,s^{-1}$ or 0.1 $mm\,s^{-1}$) are 13.3 ± 0.94 μm and 2.67 ± 0.47 μm, respectively, which agrees well with the

estimated values based on the reported work [39–41]. To characterize the droplet pinning on the surfaces of the SAW devices, sliding-angle measurements for water droplets on the SLIP surface of all the samples are carried out using the Krüss DSA30 contact angle meter equipped with a tilt stage. For a comparison of microfluidic performance, a CYTOP layer (with a composition of 1, 3, 5, 7-tetramethyl-2, 4, 8-trioxa-6-phenyl-6-phosphaadamantane) is used as an alternative surface coating of the SAW devices. The spin-coating process is used to coat a CYTOP (Asahi Glass Co., Ltd.) layer with a rotational speed of 2000 r/ min. After baking at 100 °C for 60 s, a CYTOP layer with the thickness of 500 nm is obtained.

For the SAW droplet transportation experiments, the device IDTs are excited using a rf of 22.44 MHz from a signal generator (Agilent Technologies, N9310A) with different powers which are amplified using a broadband power amplifier (Amplifier Research, 75A250). The output power is measured using a rf power meter (Racal 9104). Deionized (DI) water droplets of 2 μl are placed onto the SAW devices, 2 mm in front of the SAW IDTs. The movement of the water droplets is recorded using a video camera. The droplet transport velocities are calculated from the recorded videos. The data on contact angles, tilt angles for sliding, threshold powers for droplet transportation (i.e., the minimum power required to initiate droplet motion), and velocity of droplet motion are determined from the average of three repeated tests.

Figures 3(a)–3(c) show three typical SEM images of the ZnO/Si surfaces coated with one, two, and four Glaco layers. Figure 3(a) is an image of a SAW device with a single coating of Glaco, and this suggests the surface has an evenly dispersed layer of silica nanoparticles. Figure 3(b) shows that the twice-Glaco-coated surface possesses many stacked and accumulated silica nanoparticle structures making the surface increasingly rough and porous. Figure 3(c) shows that the fourfold-Glaco-coated surface possesses self-assembled clustered nanoparticle features and suggests that there are two scales of roughness and porosity: (i) a coarse scale of 0.5–2.0 μm composed of clusters or agglomerates of nanoparticles with average microscale holes of approximately 1 μm and (ii) nanoscale roughness that is characteristic of the size of the nanoparticles of around 40–50 nm together with nanopores of approximately 50 nm. A combination of a microscale and nanoscale 3D porous morphology and superhydrophobic properties is obtained through multiple coatings. Similar surface morphology is reported by Vakarelski *et al.* [41].

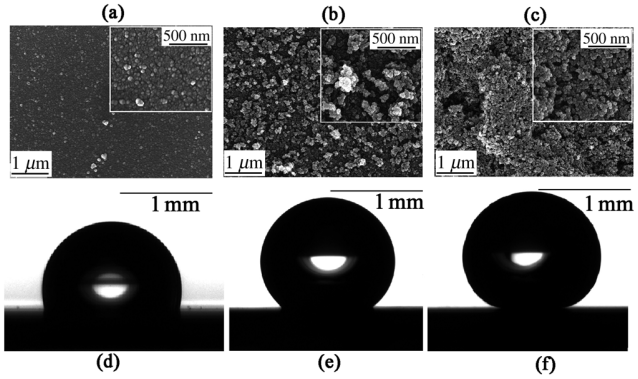

FIG. 3. SEM images of hydrophobic silica nanoparticle surfaces created using different numbers of Glaco coatings: (a) single coating, (b) double coating, and (c) four coats. Insets are the larger magnification SEM images. (d)–(f) The corresponding images for a 2-μl droplet of water on each of the above surfaces.

Figures 3(d)–3(f) show 2-μl droplets of water placed on the surfaces. With increasing numbers of coated layers, the advancing and receding contact angles of the DI droplet increase, as shown in Fig. 4. An advancing contact angle as large as 170° is achieved for a fivefold-coated surface together with a receding contact angle that indicates a low contact angle hysteresis and, thus, demonstrates excellent superhydrophobic properties for the surface. Figure 4 also shows the static apparent contact angle of 2-μl DI water on the SLIP surface created using an oil withdrawal speed of 0.1 mm/s as a function of the number of Glaco coatings. With an increasing number of coated layers from one to five, the static apparent contact angle of 2 μl DI water on the SLIP surface increases from approximately 97° to approximately 109° before oil impregnation. The droplet pinning for each sample after converting to a SLIP surface by infusion with oil at a withdrawal speed of 0.1 mm/s is illustrated by the tilt angle for sliding of water droplets in Fig. 4 as a function of the number of coated layers. On the SLIP surface created using an oil withdrawal speed of 1 mm/s, the sliding angles at the same number of coated

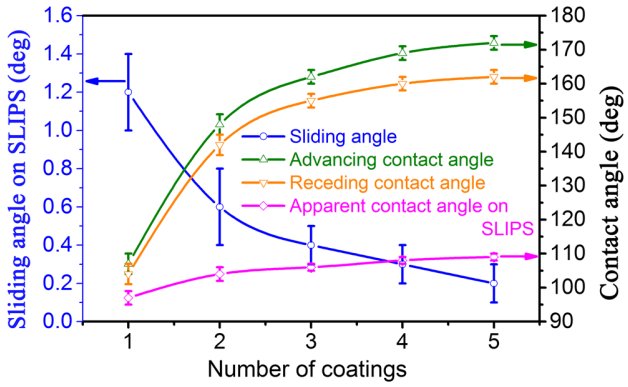

FIG. 4. Left-hand y axis shows the sliding angles (i.e., angles of the substrate tilt needed to initiate the droplet sliding) of 2 μl DI water on a SLIP surface created using an oil withdrawal speed of 0.1 mm/s as a function of the number of Glaco coatings. Right-hand y axis shows the advancing and receding contact angles of 2 μl DI water on the surface before oil impregnation as a function of the number of Glaco coatings and also shows the apparent contact angle of 2 μl DI water on a SLIP surface created using an oil withdrawal speed of 0.1 mm/s as a function of the number of Glaco coatings.

layers show similar values to those in Fig. 4. With an increasing number of coated layers, the sliding angle decreases significantly below 1°.

From the SEM observations, it appears that the surfaces coated threefold or more with the Glaco layer develop self-assembled porous structures, which become more evenly distributed on the surface by increasing the number of coatings. This type of structure may improve the retention of the lubricating oil on the surface, thus, resulting in the progressive decrease of the sliding angle [40]. We believe that for four or more coatings, the surface may become saturated with the nanoparticles causing the sliding angle to saturate to a minimum. A sliding angle of 0.2° is observed on the fivefold-coated SLIP surface. The standard deviations of the sliding angles decrease by increasing the number of coatings, indicating that the SLIP surfaces become uniform.

III. RESULTS AND DISCUSSION

The droplet transportation performance of the SAW devices with two coatings of the Glaco suspension with and without infusion with the lubricating oil is investigated. Figures 5(a)–5(e) show a 2-μl droplet on a surface not infused with oil (i.e., nonlubricated surface) before and after interaction with a SAW at a rf of 22.44 MHz and an rf power of 2.5 W for various durations. Before applying the SAW power, the droplet shows a large contact angle [Fig. 5(a)]. After applying the SAW power, the acoustic pressure applied to the droplet causes the droplet to deform into a conical shape whose trailing edge leans according to the Rayleigh angle, as shown in Fig. 5(b). However, the droplet collapses quickly, and the contact angle decreases significantly. In this case, the interaction with the SAW appears to cause the droplet to change from a Cassie-Baxter state to a Wenzel state after applying the rf SAW power [12]; i.e., the water penetrates the surface features, thus, reducing the contact angle significantly and converting the surface into one with large contact angle hysteresis and droplet pinning. The droplet is observed to vibrate significantly but without any movement, as shown in Figs. 5(b)–5(d) because of the large contact angle hysteresis of the Wenzel state. When the SAW power is turned off, the contact angle reduces to approximately 60° [see Fig. 5(e)].

Figures 5(f)–5(j) show the effect of SAW interaction with a 2-μl droplet on a similar surface but infused with silicone oil created using an oil withdrawal speed of 0.1 mm/s. Before applying a rf SAW power of 2.5 W, the droplet shows a large footprint on the SLIP surface [see Fig. 5(f)] because of the silicone oil infused into the surface. After applying the SAW power, the apparent contact angle remains almost constant, and the droplet moves smoothly across the surface as shown in Figs. 5(g)–5(i). By using the Glaco coating, the surface of the SAW devices has a combined microroughness structure and nanoscale-roughness structure which make it superhydrophobic with a large contact angle [see Fig. 3(f)], and this porous structure then facilitates the retention of the lubricating oil on the surface. The droplet has a low surface friction when moving on the oil-infused surface, and it, therefore, slides easily [36,39,42,43]. Moreover, the SLIP surface provides a sufficiently large footprint [see Figs. 1(c) and 2(b), and 5(f)–5(j)] to facilitate the transfer of SAW energy into the droplet, enhancing its transportation efficiency. When the SAW power is turned off, the apparent contact angle (approximately 110°) is similar to that before the SAW power is applied [see Figs. 5(f) and 5(j)].

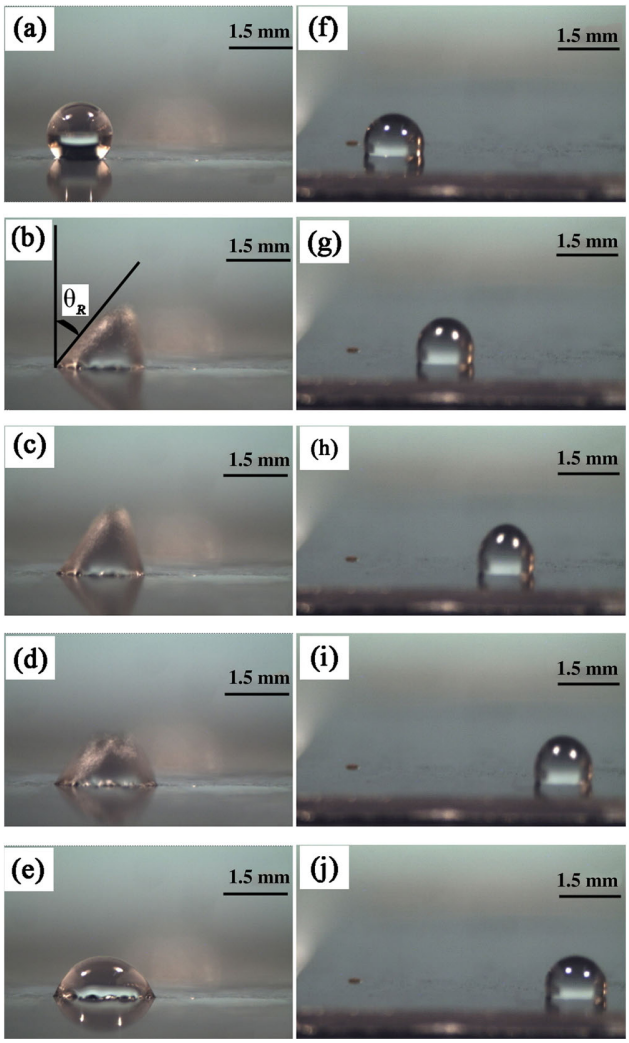

FIG. 5. The SAW microfluidic performance of a 2 μl DI water droplet on SAW devices with double Glaco coatings and an applied SAW power of 2.5 W at a frequency of 22.44 MHz after various durations. (a)–(e) show the SAW device without silicone oil. (a) Before applied SAW power, (b) applied SAW power of 0.05 s, (c) 0.12 s, (d) 0.19 s, and (e) after turning off the SAW power. (f)–(j) show the SAW device impregnated with silicone oil and the oil treatment of 0.1 mm/s. (f) Before applied SAW power, (g) applied SAW power 0.05 s, (h) 0.12 s. (i) 0.19 s, and (j) after turning off the SAW power.

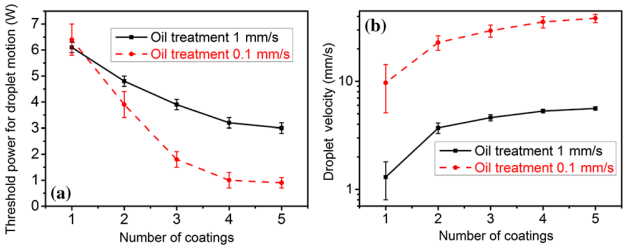

FIG. 6. (a) The threshold powers for droplet transportation of 2 μl DI water using a frequency of 22.44-MHz rf signal for surfaces created with two oil withdrawal speeds depending on the number of Glaco coatings. (b) Droplet velocity of 2 μl DI water on SAW devices using rf power of 7 W at the frequency of 22.44 MHz as a function of the number of coatings.

The SAW microfluidics performance of 2 μl DI water on the SLIP surfaces treated with different numbers of coated layers and silicone-oil-layer thickness was investigated. As seen from Fig. 6(a), the threshold power required to move a droplet decreases with increasing the number of coated layers. With increasing the number of coated layers, the contact angle θ of the non-oil-infused SAW surface increases (Fig. 4). Moreover, because of the decrease in the sliding angle and the existence of a large droplet footprint on the SLIP surface, the threshold powers for the droplet transportation decrease with the increase in the number of coated layers. A power as low as 0.9 W is capable of driving the droplet motion on the SAW devices treated with five Glaco layers and an oil withdrawal speed of 0.1 mm/s. In comparison, the threshold power to move a droplet with the same droplet volume on a standard CYTOP-coated SAW device is 6 W. Therefore, the threshold power of droplet transportation for the SLIP surface SAW devices treated with fivefold-coated Glaco layers and the oil withdrawal speed of 0.1 mm/s reduces over 85% compared to CYTOP-coated SAW devices.

As shown in Fig. 6(a), the threshold power to initiate droplet motion for the SLIP SAW device with the oil withdrawal speed of 0.1 mm/s is much smaller than that of the SLIP surface with the oil withdrawal speed of 1 mm/s for the same number of coated layers. According to the literature, the faster the withdrawal speed, the thicker the layer [36,40,43]. Therefore, the results in Fig. 6(a) are consistent with expectations, as the SAW vibration and energy should be damped by increasingly thick layers of oil.

Figure 6(b) shows the velocity of 2 μl DI water droplet moving on the SLIP surface actuated using a rf power of 7 W as a function of the number of Glaco coatings. The droplet velocity increases as the number of coats increases. A velocity of more than 38 mm/s is observed on a SLIP surface coated with five layers of Glaco and an oil withdrawal speed of 0.1 mm/s, which is more than 14 times larger than that of a single-layer-coated SLIP surface with the same oil thickness. With the increase in the number of coatings, the surface friction decreases, and the threshold power for droplet motion decreases; therefore, at the same power, the droplet velocity increases dramatically. The droplet velocity for the SLIP surface with the oil withdrawal speed of 0.1 mm/s is much larger than that of the SLIP surface with the oil withdrawal speed of 1 mm/s and the same number of Glaco coats due to the decreased attenuation of the SAW with the thinner oil layer on the SLIP surface.

We tested the SAW microfluidics performance on the same devices more than 100 times. The results show almost the same phenomena without increase of the threshold power for droplet transportation or decrease of the droplet velocity. Furthermore, we left the devices in air without protection and tested their SAW microfluidics performance frequently after more than three weeks. The threshold powers for droplet transportation and the droplet velocity remain nearly the same. The results show that the SLIP surface is robust and that the SAW microfluidics on the SLIP surface show good repeatability and long-term stability.

IV. CONCLUSION

In brief, a strategy to reduce droplet contact line pinning and enable SAW-induced droplet transportation has been developed. By creating ZnO/Si SAW devices with a SLIP surface achieved by infusing a superhydrophobic porous nanoparticulate surface with a lubricating oil, efficient droplet movement with significant reductions in the threshold power and higher droplet velocities are achieved. In this approach, the contact angle hysteresis is reduced to overcome contact line pinning, while retaining a sufficiently large droplet footprint to facilitate SAW energy to be dissipated into the droplet. To enable the SLIP-surface coating approach to be combined with effective propagation of SAWs on the device surfaces without large acoustic wave attenuation, the oil layer due to the SLIP surface has to be designed to be much thinner than the SAW wavelength. The SLIP surfaces on SAW devices presented in this work are easy to fabricate, inexpensive, and reproducible, which is promising for droplet microfluidics based on SAWs.

ACKNOWLEDGMENTS

The authors acknowledge financial support from National Natural Science Foundation of China (Grant No. 51302173), National Key Research and Development Program of China (Grant No. 2016YFB0402705), Basic Research Program of Shenzhen (Grant No. JCYJ20140418091413493), and the Royal Academy of Engineering: Research Exchange between the United Kingdom and People's Republic of China is acknowledged. We thank the UK Engineering and Physical Sciences Research Council for support under Grants No. EP/L026899/1 and No. EP/P018998/1 and Knowledge Transfer Partnership Grant No. KTP010548.

[1] P. de Gennes, Wetting: Statics, and dynamics, Rev. Mod. Phys. **57**, 827 (1985).

[2] J. Joanny and P. de Gennes, A model for contact angle hysteresis, J. Chem. Phys. **81**, 552 (1984).

[3] A. W. Adamson and A. P. Gast, *Physical Chemistry of Surfaces*, 6th ed. (Wiley-Blackwell, New York, 1997), ISBN 10: 0471148733.

[4] R. D. Deegan, O. Bakajin, T. F. Dupont, G. Huber, S. R. Nagel, and T. A. Witten, Capillary flow as the cause of ring stains from dried liquid drops, Nature (London) **389**, 827 (1997).

[5] G. McHale, Surface free energy and microarray deposition technology, Analyst **132**, 192 (2007).

[6] M. Singh, H. M. Haverinen, P. Dhagat, and G. E. Jabbour, Inkjet printing-process and its applications, Adv. Mater. **22**, 673 (2010).

[7] S. Y. Teh, R. Lin, L. H. Hung, and A. P. Lee, Droplet microfluidics, Lab Chip **8**, 198 (2008).

[8] T. Onda, S. Shibuichi, N. Satoh, and K. Tsujii, Super-water-repellent fractal surfaces, Langmuir **12**, 2125 (1996).

[9] W. Barthlott and C. Neinhuis, Purity of the sacred lotus, or escape from contamination in biological surfaces, Planta **202**, 1 (1997).

[10] C. Neinhuis and W. Barthlott, Characterization and distribution of water-repellent, self-cleaning plant surfaces, Ann. Bot. **79**, 667 (1997).

[11] D. Quéré, Wetting, and roughness, Annu. Rev. Mater. Res. **38**, 71 (2008).

[12] N. J. Shirtcliffe, G. McHale, S. Atheron, and M. I. Newton, An introduction to superhydrophobicity, Adv. Colloid Interface Sci. **161**, 124 (2010).

[13] L. Y. Yeo and J. R. Friend, Ultrafast microfluidics using surface acoustic waves, Biomicrofluidics **3**, 012002 (2009).

[14] Y. Q. Fu, J. K. Luo, X. Y. Du, A. J. Flewitt, Y. Li, G. H. Markx, A. J. Walton, and W. I. Mine, Recent developments on ZnO films for acoustic wave based bio-sensing and microfluidic applications: A review, Sens. Actuators B Chem. **143**, 606 (2010).

[15] X. Ding, P. Li, S. C. S. Lin, Z. S. Stratton, N. Nama, F. Guo, D. Slotcavage, X. L. Mao, J. J. Shi, and F. Costanzo, Surface acoustic wave microfluidics, Lab Chip **13**, 3626 (2013).

[16] J. T. Luo, M. Xie, P. X. Luo, B. X. Zhao, K. Du, and F. Pan, A sensitive glucose biosensor without using glucose test strips based on $ZnO/SiO_2/Si$ surface acoustic wave device, Mater. Lett. **130**, 14 (2014).

[17] L. Y. Yeo and J. R. Friend, Surface acoustic wave microfluidics, Annu. Rev. Fluid Mech. **46**, 379 (2014).

[18] J. T. Luo, P. X. Luo, M. Xie, K. Du, B. X. Zhao, F. Pan, P. Fan, F. Zeng, D. P. Zhang, Z. H. Zheng, and G. X. Liang, A new type of glucose biosensor based on surface acoustic wave resonator using Mn-doped ZnO multilayer structure, Biosens. Bioelectron. **49**, 512 (2013).

[19] J. J. Xu, Z. J. Lei, J. K. Guo, J. Huang, W. Wang, U. Reibetanz, and S. Y. Xu, Trapping and driving individual charged micro-particles in fluid with an electrostatic device, Nano-Micro Lett. **8**, 270 (2016).

[20] A. Barani, H. Paktinat, M. Janmaleki, A. Mohammadi, P. Mosaddegh, A. Fadaei-Tehrani, and A. Sanati-Nezhad, Microfluidic integrated acoustic waving for manipulation of cells and molecules, Biosens. Bioelectron. **85**, 714 (2016).

[21] M. C. DeSantis and W. Cheng, Label-free detection and manipulation of single biological nanoparticles, WIREs Nanomed. Nanobiotechnol. **8**, 717 (2016).

[22] T. S. Wong, T. Sun, L. Feng, and J. Aizenberg, Interfacial materials with special wettability, MRS Bull. **38**, 366 (2013).

[23] Z. Wang, M. Elimelech, and S. Lin, Environmental applications of interfacial materials with special wettability, Environ. Sci. Technol. **50**, 2132 (2016).

[24] H. Chen, T. Tang, H. Zhao, K. Y. Law, and A. Amirfazli, How pinning and contact angle hysteresis govern quasi-static liquid drop transfer, Soft Matter **12**, 1998 (2016).

[25] J. Yang and D. Y. Kwok, Analytical treatment of electrokinetic microfluidics in hydrophobic microchannels, Anal. Chim. Acta **507**, 39 (2004).

[26] J. K. Luo, Y. Q. Fu, Y. Li, X. Y. Du, A. J. Flewitt, A. J. Walton, and W. I. Milne, Moving-part-free microfluidic systems for lab-on-a-chip, J. Micromech. Microeng. **19**, 054001 (2009).

[27] X. Y. Du, M. E. Swanwick, Y. Q. Fu, J. K. Luo, A. J. Flewitt, D. S. Lee, S. Maeng, and W. I. Milne, Surface acoustic wave induced streaming and pumping in 128 Y-cut $LiNbO_3$ for microfluidic applications, J. Micromech. Microeng. **19**, 035016 (2009).

[28] S. Girardo, M. Cecchini, F. Beltram, R. Cingolani, and D. Pisignano, Polydimethylsiloxane-$LiNbO_3$ surface acoustic wave micropump devices for fluid control into microchannels, Lab Chip **8**, 1557 (2008).

[29] X. Y. Du, Y. Q. Fu, J. K. Luo, A. J. Flewitt, and W. I. Milne, Microfluidic pumps employing surface acoustic waves generated in ZnO thin films, J. Appl. Phys. **105**, 024508 (2009).

[30] Y. Liu, Y. F. Li, A. M. el-Hady, C. Zhao, J. F. Du, Y. Liu, and Y. Q. Fu, Flexible and bendable acoustofluidics based on ZnO film coated aluminium foil, Sens. Actuators B Chem. **221**, 230 (2015).

[31] A. B. D. Cassie and S. Baxter, Wettability of porous surfaces, Trans. Faraday Soc. **40**, 546 (1944).

[32] R. N. Wenzel, Resistance of solid surfaces to wetting by water, Ind. Eng. Chem. **28**, 988 (1936).

[33] T.-S. Wong, S. H. Wong, S. K. Y. Tang, E. J. Smythe, B. D. Hatton, A. Grinthal, and J. Aizenberg, Bioinspired self-repairing slippery surfaces with pressure-stable omniphobicity, Nature (London) **477**, 443 (2011).

[34] M. Nosonovsky, Materials science: Slippery when wetted, Nature (London) **477**, 412 (2011).

[35] J. D. Smith, R. Dhiman, S. Anand, E. Reza-Garduno, R. E. Cohen, G. H. McKinley, and K. K. Varanasi, Droplet mobility on lubricant-impregnated surfaces, Soft Matter **9**, 1772 (2013).

[36] J. Bico, U. Thiele, and D. Quere, Wetting of textured surfaces, Colloids Surf. A **206**, 41 (2002).

[37] J. H. Guan, G. G. Wells, B. Xu, G. McHale, D. Wood, J. Martin, and S. Stuart-Cole, Evaporation of sessile droplets on slippery liquid-infused porous surfaces (SLIPS), Langmuir **31**, 11781 (2015).

[38] C. Semprebon, G. McHale, and H. Kusumaatmaja, Apparent contact angle and contact angle hysteresis on liquid infused surfaces, Soft Matter, **13**, 101 (2017).

[39] B. R. Solomon, K. S. Khalil, and K. K. Varanasi, Drag reduction using lubricant-impregnated surfaces in viscous laminar flow, Langmuir **30**, 10970 (2014).

[40] J. C. Seiwert, C. Clanet, and D. Quéré, Coating of a textured solid, J. Fluid Mech. **669**, 55 (2011).

[41] I. U. Vakarelski, N. A. Patankar, J. O. Marston, D. Y. C. Chan, and S. T. Thoroddsen, Stabilization of Leidenfrost vapour layer by textured superhydrophobic surfaces, Nature (London) **489**, 274 (2012).

[42] X. Huang, J. D. Chrisman, and N. S. Zacharia, Omniphobic slippery coatings based on lubricant-infused porous polyelectrolyte multilayers, ACS Macro Lett. **2**, 826 (2013).

[43] F. Schellenberger, J. Xie, N. Encinas, A. Hardy, M. Klapper, P. Papadopoulos, H. J. Butt, and D. Vollmer, Direct observation of drops on slippery lubricant-infused surfaces, Soft Matter **11**, 7617 (2015).

Soft Matter

PAPER

View Article Online
View Journal | View Issue

Cite this: *Soft Matter*, 2017, **13**, 3404

Drop transport and positioning on lubricant-impregnated surfaces

Jian Hui Guan,[a] Élfego Ruiz-Gutiérrez,[a] Ben Bin Xu,[a] David Wood,[b] Glen McHale,[a] Rodrigo Ledesma-Aguilar[a] and Gary George Wells*[a]

Received 10th February 2017,
Accepted 4th April 2017

DOI: 10.1039/c7sm00290d

rsc.li/soft-matter-journal

We demonstrate the transport and positioning of water droplets on macro-patterned lubricant-impregnated surfaces. The macro-patterning produces menisci features in the impregnating liquid layer which interact with a droplet *via* a capillary mechanism similar to the Cheerios effect. These interactions control the droplet motion and positioning on an otherwise completely slippery surface. We present experimental results using a V-shape channel geometry as a model system. The interaction between deformations on the lubricant layer induced by the droplet and the underlying V-shape geometry leads to both local and global equilibrium positions for the droplet within the channel. We present a mathematical model to quantify the transition from local equilibrium states to the global equilibrium state and show that the latter can be described on the basis of a force balance along the apparent contact line of the droplet. We highlight possible applications where lubricated macro-patterned surfaces can be used to control the motion and localisation of droplets.

Introduction

The ability to induce controlled motion and positioning of droplets not only generates interesting science, but can also lead to significant advances in various practical applications, such as digital microfluidics,[1] inkjet printing,[2] self-cleaning surfaces[3] and systems in which directional transport of liquid droplets is of high importance.[4–8]

One method to create drop propulsion on a solid surface is to break the wetting symmetry of the liquid.[9,10] By creating a wettability gradient between both sides of the droplet it is possible to create a Laplace pressure gradient inside the droplet, forcing it to move.[11] Such surfaces can be created by either introducing a gradient in the surface chemistry[12] or in the surface topography.[13–16] Drop transport can also be achieved by means of an external field, such as a gradient in temperature,[17,18] by applying an electric field[19–21] or using mechanical actuation.[22–25]

A central challenge in drop self-propulsion is the fact that motion in direct contact with a solid can only be achieved after overcoming a minimum static friction force due the contact angle hysteresis. Furthermore, it is often the case that small surface defects can hamper the motion of a droplet altogether due to contact-line pinning. Recently, new types of surfaces, Slippery Liquid-Infused Porous Surfaces (SLIPS) or Lubricant-Impregnated Surfaces (LIS), inspired by the Nepenthes pitcher plant, have been developed.[26–28] SLIPS/LIS surfaces add a lubricating liquid layer which minimises contact of a droplet with the solid surface, leading to very low contact angle hysteresis, low sliding angles and almost pinning-free droplet mobility.[25,29–32] Therefore, SLIPS/LIS offer an opportunity to study the motion of self-propelling droplets in low friction situations, for example in the context of evaporation and condensation.[33,34] However, because of the lubricating layer, it is not obvious how to achieve the self propulsion of a droplet on a SLIPS/LIS surface. Moreover, due to the absence of contact-line pinning, it is not clear how to design a SLIPS/LIS surface which is able to guide the positioning of droplets.

In this paper we propose an approach for creating self-propulsion and positioning of droplets on SLIPS/LIS surfaces. We describe a simple fabrication method for lubricant-impregnated surfaces that includes a macroscopic solid pattern that induces surface deformations on the lubricating liquid layer. On these surfaces, menisci caused by the macro-pattern and by a sessile droplet lead to capillary interactions similar to the Cheerios effect.[35] We report experimental results using V-shaped channels as a model geometry, where droplets tend to migrate towards the lubricant-rich edges of the channel as a means of minimising the total surface energy. Motion is triggered whenever the typical length scale of the meniscus surrounding the droplet is comparable to the length scale of the distortion to the lubricant layer close to the channel walls. Motion stops at different positions within the channel, which can be controlled by choosing the size

[a] *Smart Materials and Surfaces Laboratory, Faculty of Engineering and Environment, Northumbria University, Ellison Place, Newcastle upon Tyne NE1 8ST, UK. E-mail: gary.wells@northumbria.ac.uk*
[b] *Microsystems Technology Group, School of Engineering and Computing Sciences, Durham University, South Rd, Durham DH1 3LE, UK*

of the droplet, the typical thickness of the lubricant layer and the pattern geometry. We provide a mathematical model that quantifies the different equilibrium states observed in the experiments. Using a force balance, we quantify the equilibrium position of the droplet in relation to the V-shape pattern. Beyond the specific geometry used in our experiments, we highlight future opportunities for exploiting the combination of low-pinning and low-friction features inherent to SLIPS/LIS surfaces and our approach to surface macro-patterning to control droplet motion and localisation.

Methods and materials

V-shaped SLIPS

The sample preparation process is summarised in Fig. 1a. Fresh silicon wafers (Pi-KEM) were spin-coated with a SU-8 negative photoresist layer of thickness, $h = 50 \pm 5$ μm, at 1750 rpm. The photoresist layer was then patterned using standard photolithography to create a V-shaped channel with straight edges when viewed from above. The geometry of the V shape was controlled by choosing the angle of divergence, β, which we varied in the range 2.7°–5.8° (Fig. 1b). The surfaces were then treated with a nanoparticle based hydrophobic coating (Glaco Mirror Coat, Nippon Shine) using a spray coating process. After drying, the samples where dip-coated in a bath of silicone oil (Sigma Aldrich; viscosity $\eta = 20$ mPa s, surface tension $\gamma_{oa} = 20.6$ mN m^{-1}) and withdrawn at a speed U ranging from 0.1 to 1 mm s^{-1}, resulting in the deposition of a layer of silicone oil on the hydrophobic surface.

After dip-coating the samples, we observed the formation of a meniscus in the oil–air interface that touches the inner edges of the channel of characteristic length L (see Fig. 1a). Fig. 1c shows measurements of L at different withdrawal speeds obtained by direct imaging using an optical microscope, where L is inferred visually from the images. We expect that L scales with the thickness of the oil layer deposited at the top of the channel walls, t. Following the classical Landau–Levich–Derjaguin (LLD) theory of film deposition,[36] we expect a scaling $t \approx 0.94a\mathrm{Ca}^{2/3}$, where $a \approx 1.4$ mm is the capillary length of the oil and $\mathrm{Ca} = \eta U/\gamma$ is the capillary number.[37] Fig. 1d shows confocal microscopy measurements of t as a function of the withdrawal speed, U, and indicates a good agreement with the LLD theory. Moreover, L and t show a clear correlation as seen by comparing Fig. 1c and d. Therefore, the withdrawal speed can be used to control both the penetration length, L, and the thickness of the oil layer, t.

SLIPS properties of V-shaped channels

2 μL water droplets were placed on the upper (u) and lower (l) surfaces of a V-shape SLIPS sample (see Fig. 1b). The apparent contact angle and sliding angles of the droplet were measured using a contact angle meter (Krüss DSA30). The upper portion of the droplets is well described by a spherical cap shape, thus ruling out gravitational effects. As a consequence of the oil layer, the shape of the sessile droplet is distorted by a small wetting ridge close to the solid[27] and therefore it is not possible to identify a contact angle as described by Young's Law. Here, we follow Guan *et al.*[30] and define the apparent contact angle to be the intersection angle of the solid surface profile with the extrapolated profile of the droplet, which we fit to a spherical cap. Table 1 reports the measured apparent contact angles at the upper and lower surfaces, θ_u and θ_l, respectively, for different withdrawal speeds. For a given withdrawal speed, we find that $\theta_u > \theta_l$.

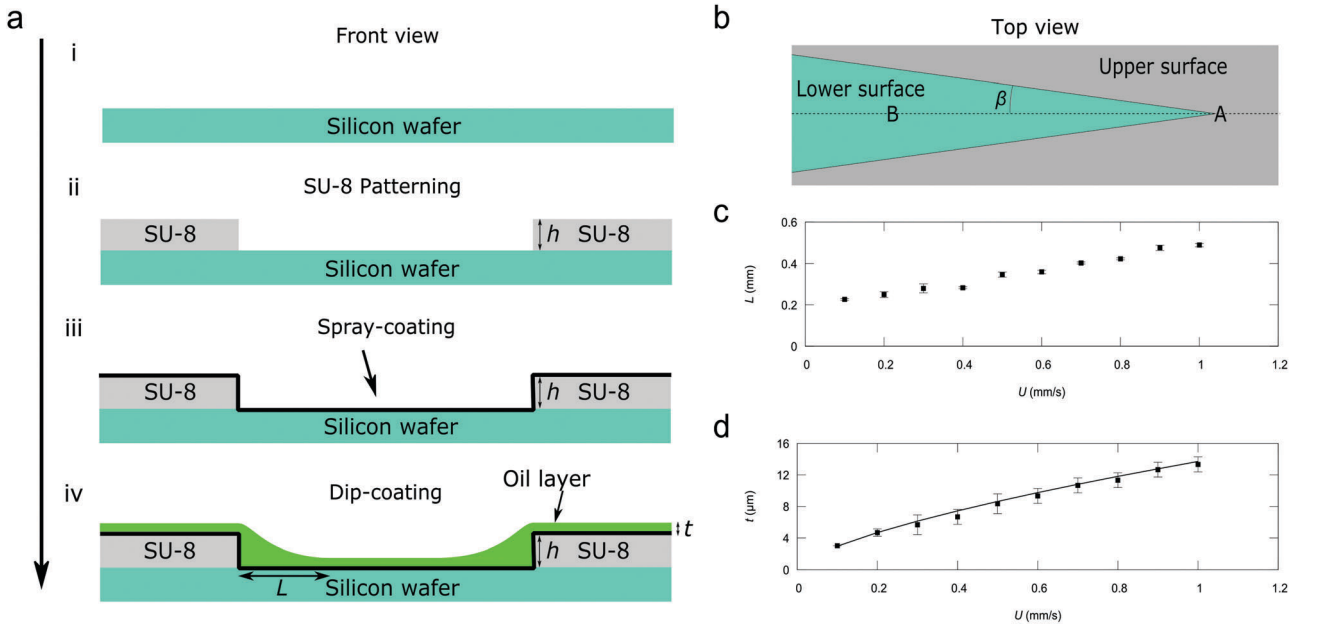

Fig. 1 Production process and characterisation of V-shaped SLIPS channels. (a) Schematics of the production process. (b) Schematic of a V-shaped channel with an angle β. (c) Optical microscopy measurements of the meniscus penetration length, L, as a function of the withdrawal speed from the oil bath, U. (d) Confocal microscopy measurements (symbols) and LLD prediction (solid line) of the thickness of the silicone oil layer on the upper surface as a function of the withdrawal speed from the oil bath.

Table 1 Apparent contact angles of 2 μL water droplets placed on the upper and lower surfaces of a V-shaped channel

U (mm s^{-1})	θ_u (°)	θ_l (°)
0.1	115.9 ± 0.4	113.9 ± 0.2
0.2	113.6 ± 1.1	113.4 ± 0.4
0.3	112.5 ± 0.3	111.9 ± 0.5
0.4	112.5 ± 0.3	111.3 ± 0.4
0.5	111.9 ± 0.8	111.2 ± 0.5
0.6	112.0 ± 0.2	111.4 ± 0.5
0.7	111.6 ± 0.1	110.2 ± 0.1
0.8	111.0 ± 0.6	109.4 ± 0.7
0.9	110.3 ± 0.7	110.1 ± 0.3
1	110.5 ± 0.6	108.6 ± 0.4

Because the silicone oil tends to collect within the channel, this suggests that the local contact angle is lower in regions of a thicker oil layer. This observation is consistent with a recent numerical analysis of the shape of droplets in contact with a wetting ridge.[38] Both θ_u and θ_l lie in a range $\approx$110°–115° and show a slight decrease with increasing withdrawal speed. The sliding angles prior to impregnation for all samples were in excess of 5°. After impregnation, the sliding angle of a droplet on a flat part of any given sample was below 1°.

Results and discussion

Single droplets of volume V ranging from 1 to 10 μL were deposited on the V-shaped channels using a syringe connected to a programmable pump (Cellix). The syringe was held in place directly above the samples by a positioning jig to ensure that droplets were consistently deposited onto the same position relative to the apex of the channel. Droplets were either deposited on top of the apex, or at a distance X = 17 mm from the apex along the axis of the channel (points A and B in Fig. 1b) and left to equilibrate. After any migration of the deposited droplet, the final equilibrium configuration was imaged and analysed using standard imaging processing software. To ensure reproducibility of the final equilibrium states, including ruling out effects from surface pinning, each experiment was repeated three times.

Fig. 2 shows three types of final droplet configurations obtained by tracking the motion of droplets of increasing volume, V = 2 μL, 4 μL and 8 μL, on a channel of fixed meniscus penetration length, L = 0.49 mm, and angle, β = 5.4°. Droplets of small volume consistently stay within the wider portion of the channel along the symmetry line of the channel (Fig. 2a). This symmetry is broken at intermediate volumes, for which the droplet migrates towards either wall of the channel (Fig. 2b). Increasing the volume of the droplet further leads to a transient motion towards either wall followed by a translation along the edge of the wall until the droplet settles along the symmetry axis of the channel at a distance X_e from the apex (Fig. 2c). Placing the droplet at the apex of the channel results in an outwards motion along the bisector line until the droplet equilibrates at the same distance X_e. In the following, we refer to these equilibrium configurations as "state 1", "state 2" and "state 3", as depicted in Fig. 2d.

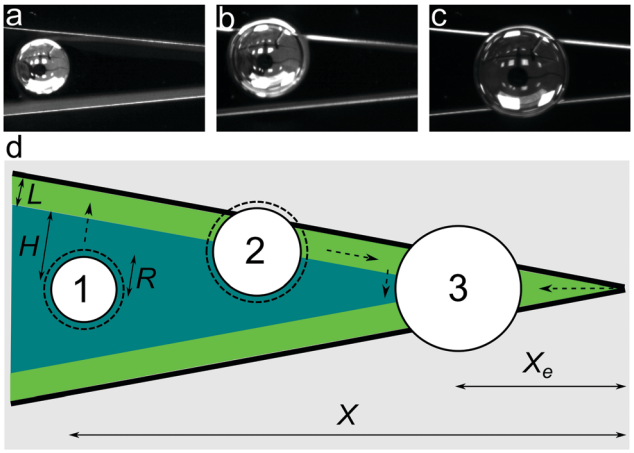

Fig. 2 Equilibrium states of sessile droplets of different volumes deposited at a distance X = 17 mm from the apex of a V-shaped SLIPS channel of angle β = 5.4° and meniscus penetration length L = 0.49 mm. (a) V = 2 μL; the droplet stays away from the channel walls on the bisector line of the channel. (b) V = 4 μL; the droplet migrates to either wall of the channel. (c) V = 8 μL; the droplet migrates to either wall and then moves towards the apex of the channel, setting at a finite distance from the apex along the bisector line. (d) Schematic illustration of the three equilibrium configurations identified, labelled "1", "2" and "3", respectively. The dashed arrows indicate typical migration paths of droplets as they equilibrate.

Control parameters and phase diagrams

Our initial observations suggest that the selection of a specific equilibrium configuration of a droplet on a V-shape SLIPS channel is controlled by the interplay between the size of the wetting ridge surrounding the drop and the typical penetration length of the meniscus, L. For a small volume, V, the droplet occupies a relatively flat portion of the V-shaped channel, and thus is in a state of local equilibrium (state 1). For intermediate volumes, however, one of the edges of the drop is close enough to the channel walls, and travels towards that wall. Once the droplet touches the wall the symmetry is recovered leading to a second equilibrium configuration (state 2). For larger volumes both edges are able to interact with the channel walls, and this leads to a net migration towards the apex of the channel, until the droplet settles in state 3. The fact that droplets initially positioned at the apex of the V-shape geometry also migrate towards state 3 suggests that this corresponds to a global equilibrium configuration.

Following this principle, the interplay between the droplet and the meniscus can be controlled *via* the droplet volume, V, the meniscus length, L, and the angle, β. To prove this assertion, we examined the equilibrium configuration of droplets placed on V-shaped channels over a range of these parameters. Fig. 3 shows the resulting phase diagrams for the equilibrium configuration of the droplet. For a given combination of V, L and β, we found that the droplet equilibrates in one of the three configurations identified in Fig. 2d. State 1, shown as blue diamonds in the figure, is predominant at small V, small L and large β, a situation arising for sufficiently small droplets, thin menisci or wide channels. Increasing V or L, or equivalently, decreasing β, gives way to state 2 (red squares) and, further, to state 3 (green triangles).

It is interesting to note that a droplet will always equilibrate in state 3 when sufficiently close to the apex, thus showing that state 1 and state 2 are local equilibria.

Physical mechanism for droplet motion and equilibration

To better understand the equilibrium configurations observed in our experiments, we first consider the limiting case of free water droplet that is brought into contact with an oil bath and neglect the effect of the solid geometry. In such a situation, the equilibrium configuration can be inferred by comparing the surface energy of a spherical droplet in contact with air to the surface energy of a droplet of the same volume in contact with silicone oil. The difference in surface energy between the two configurations is given by $\Delta E = A(\gamma_{wo} - \gamma_{wa})$, where A is the surface area of the droplet, and γ_{wa} and γ_{wo} are the surface tensions of the water–air and water–oil interfaces, respectively. In our experiments $\gamma_{wo} = 46.3$ mN m^{-1} and $\gamma_{wa} = 72.8$ mN m^{-1}. Therefore, a droplet will tend to minimise its surface energy by moving towards a region that increases contact with an oil bath.[39] However, the presence of the V-shape channel introduces a further geometrical constraint, which determines the specific configuration of the droplet.

Mechanically, the migration of the droplet can be understood in terms of the interplay between the oil meniscus surrounding the droplet and the oil meniscus adjacent to the wall of the V-shape channel. Similarly to the capillary interactions observed between solid surfaces mediated by a connecting interface,[40,41] also known as the Cheerios effect,[35] whenever two menisci of the same curvature sign come into close proximity, one expects a net attractive force arising from an excess capillary pressure. Based on this principle, we expect that the transition from state 1 to state 2, and from state 2 to state 3, is triggered whenever the rim of the droplet touches the wall meniscus. For both transitions, this will occur when the effective contact radius of the droplet, R_{eff}, matches the lateral length scale, $H \approx X\sin\beta - L$ (see Fig. 2d). We expect that R_{eff} scales with $V^{1/3}$, up to a prefactor that depends on the apparent contact angle and on the details of the specific configuration of the droplet relative to the channel geometry. Matching R_{eff} and H then leads to the transition lines

$$L \approx X\sin\beta - R_{eff}, \quad (1)$$

which reveal the interplay between R_{eff} and L as the relevant length scales in the problem.

For a spherical-cap shaped droplet, the effective radius matches the base radius, which in our system roughly corresponds to the base radius of a hemisphere, $R_{hemi} = (6V/4\pi)^{1/3} \approx 0.78V^{1/3}$. In the experiments, however, we expect that R_{eff} depends on the details of the interface configuration upon contact with the lubricant layer, which will change for droplets of different volumes and locations within the V-shape channel.

Fig. 3 shows a comparison of this model with the experimental data. The transition line from state 1 to state 2 shows a good agreement with the experimental data by setting $R_{eff} = 0.65V^{1/3}$ and $R_{eff} = 0.96V^{1/3}$ for $V = 2$ μL and $V = 4$ μL, respectively. Similarly, we obtain a good prediction for the transition from state 2 to state 3 by fixing $R_{eff} = 0.65V^{1/3}$, $R_{eff} = 0.85V^{1/3}$ and $R_{eff} = 1.0V^{1/3}$ for $V = 4$ μL, $V = 6$ μL and $V = 8$ μL, respectively.

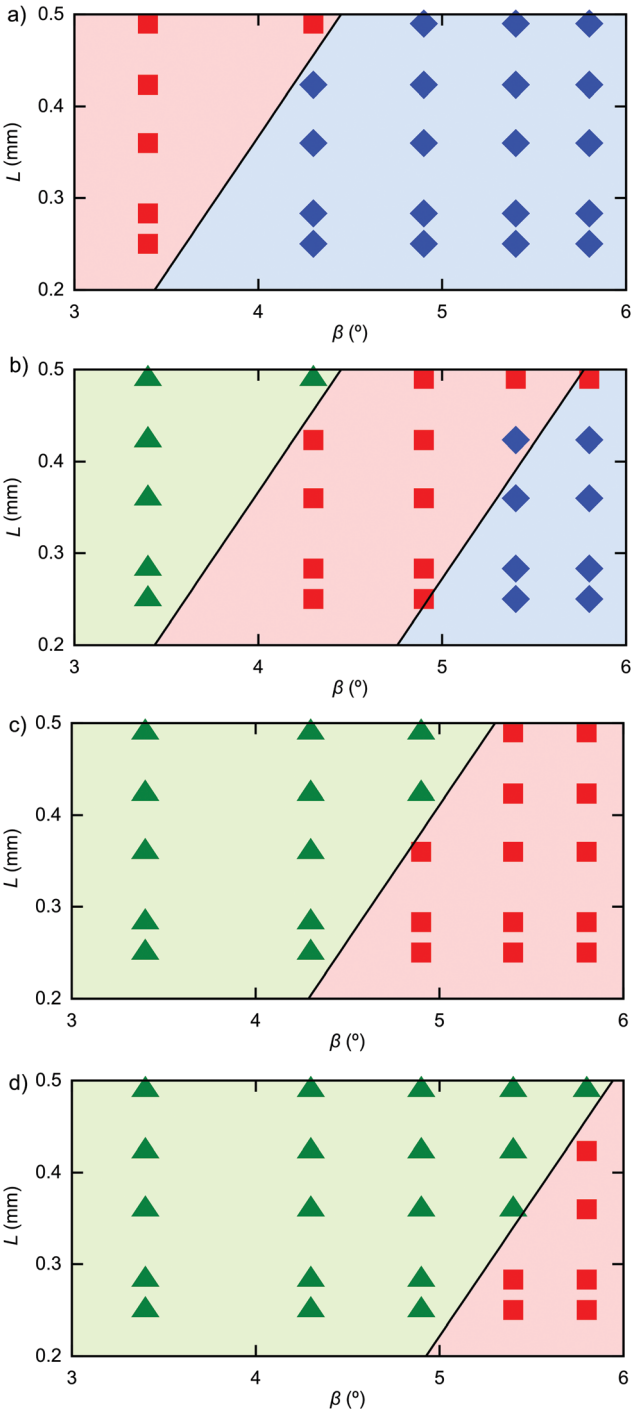

Fig. 3 Phase diagrams for the equilibrium configurations of droplets on V-shaped SLIPS channels. (a) $V = 2$ μL, (b) $V = 4$ μL, (c) $V = 6$ μL, and (d) $V = 8$ μL. The symbols indicate the final equilibrium configuration observed after allowing a droplet to equilibrate starting from an initial distance $X = 17$ mm from the apex of the channel: state 1 (diamonds), state 2 (squares) or state 3 (triangles). The solid lines separating the shaded areas correspond to the transition lines predicted by the theoretical model (see text).

Due to symmetry, states 1 and 2 are expected to be invariant upon translations of the droplet along the bisector line (state 1)

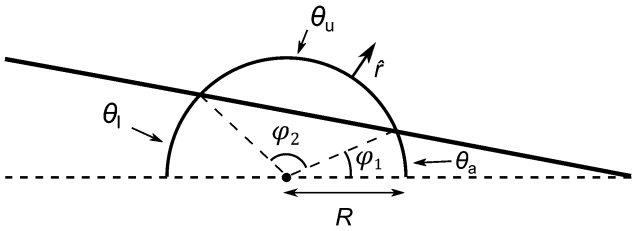

Fig. 4 Schematics of the model for the equilibrium configuration of a droplet in a V-shaped channel. The solid and dashed straight lines depict the edge and bisector line of the channel, respectively. The circular profile depicts the apparent contact line of the droplet, of contact radius R and local normal unit vector $\hat{r}$. The apparent contact angle is assumed to take three different values, θ_a, θ_u and θ_l, in the regions delimited by the angles φ_1 and φ_2 and $\pi - (\varphi_1 + \varphi_2)$, respectively.

and the channel wall (state 2). This contrasts with the configuration of the droplet in state 3, which is characterised by a well-defined equilibrium distance from the apex of the channel, X_e. In order to understand such a selection in the configuration of the droplet, we analyse the net force acting on the droplet in state 3. We assume a spherical-cap droplet shape in contact with the lubricant layer, which has a non-uniform thickness (caused by the underlying topography). The net lateral force is computed by integrating the tension exerted by the meniscus on the droplet over the droplet's contour, *i.e.*,

$$F = -\gamma R \int_0^{2\pi} \cos\theta \hat{\mathbf{r}}\, \mathrm{d}\varphi, \tag{2}$$

where $\theta(\varphi)$ is the local apparent contact angle, $\hat{\mathbf{r}} = (\cos\varphi, \sin\varphi)$ is the local unitary normal vector to the apparent contact line and φ is an azimuthal angle (see Fig. 4).

Because the surface of the lubricant layer is distorted by underlying solid geometry, the apparent contact angle will vary along the droplet's contour. To model such a variation, we consider a piecewise distribution of the contact angle over three regions. First, the portion of the droplet in contact with the upper surface of the channel will have a local contact angle close to θ_u. On the same basis, we assume that the portion of the droplet facing the wider part of the channel will have a contact angle approximately equal to θ_l. Finally, we expect that the oil collects in the portion of the channel closer to the apex, leading to an apparent angle $\theta_a < \theta_l$ in this region.

With these considerations in mind eqn (2) reduces to

$$F = 2\gamma R[S_-(\cos\theta_a - \cos\theta_u) + S_+(\cos\theta_u - \cos\theta_l)] \tag{3}$$

where

$$S_\pm = \frac{\sin\beta}{R}\left(X\cos\beta \pm \sqrt{R^2 - X^2\sin^2\beta}\right) \tag{4}$$

In equilibrium the net force vanishes. Therefore, setting $F = 0$ in eqn (3) gives a prediction for the equilibrium distance

$$X_e = \frac{R(\cos\theta_a - 2\cos\theta_u + \cos\theta_l)}{\sqrt{\cos^2\beta(\cos\theta_a - \cos\theta_l)^2 + (\cos\theta_a - 2\cos\theta_u + \cos\theta_l)^2\sin^2\beta}}. \tag{5}$$

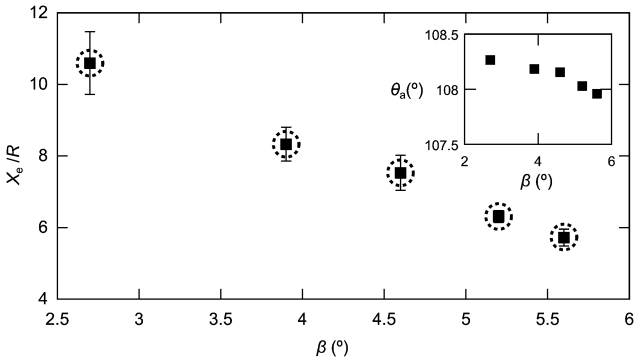

Fig. 5 Equilibrium position of the droplet in state 3, X_e as a function of the V-shape channel angle, β. The squares correspond to experimental data carried out in channels dip-coated at U = 1 mm s^{-1}. Each data point corresponds to normalised values averaged over different droplet volumes in the range 1–7 μL. The error bars correspond to one standard deviation. The dashed circles correspond to the theoretical prediction. The inset data corresponds to the values of θ_a used to fit the experimental data (see text).

In order to test this prediction, we carried out further experiments by placing droplets on the apex of channels of different angle β, in the range 2.7°–5.6°. To keep θ_l and θ_u constant, all samples were dip-coated at the same withdrawal speed U = 1 mm s^{-1}, for which we expect θ_u = 110.5° and θ_l = 108.6°. Eqn (5) suggests that the volume of the droplet affects the equilibrium position up to a factor $R \sim V^{1/3}$. Therefore, we carried out experiments with different droplet volumes, in the range 1–7 μL. In all cases, the droplet migrates towards the wider portion of the channel and settles in state 3. The normalised, averaged data for X_e *vs.* β is shown in Fig. 5. In order to compare this model to our experimental data, we used θ_u = 110.5° and θ_l = 108.6° in eqn (5). The typical apparent angle close to the apex, θ_a, is difficult to measure, and therefore we treated this as a fitting parameter in our model. The dashed circles in Fig. 5 correspond to the fitted values of X_e. The corresponding values of θ_a are reported in the inset, and show a weak decrease with increasing β. This is consistent with our previous argument that the oil collects near the apex of the channel, setting the typical value of θ_a. For wide channels, where the droplet tends to migrate closer to the apex, one expects a comparatively thicker oil layer, leading to a smaller apparent angle. The strong sensitivity of X_e on the apparent contact angle, θ_a, reflects the dependence of the final equilibrium position on the details of the interplay between the meniscus shape and the channel geometry, which is not captured by our simple geometrical model. Nevertheless, our model captures the typical value of X_e and the dependence on β, thus supporting the validity of the force balance in determining the selection of the equilibrium state.

Conclusions

We have presented a method to guide the transport and localisation of droplets on liquid-impregnated surfaces patterned with macroscopic features. Using a V-shaped channel as a model system, we have demonstrated the transport of a sessile droplet

to well-defined equilibrium positions on the channels *via* a mechanism that reduces the overall surface energy by increasing contact with an impregnating lubricant liquid layer. Mechanically, the motion of the droplet can be understood in terms of the relaxation of distortions to the impregnating oil layer, caused both by the droplet and by surface macro-pattern. This is similar to the capillary mediated interactions between solid surfaces,[35,40–42] but is also akin to the recently observed elastic mediated interactions of single and multiple droplets on soft solids.[43,44]

Here, we have presented experiments that demonstrate that the specific equilibrium configuration of the droplet within the channel can be controlled by choosing the typical thickness of the impregnating layer, the size of the droplet or the geometry of the channel. Our theoretical model captures the main features observed in the experiments, and reveals a strong dependence of the final equilibrium configuration of the droplet on the specific distribution of the apparent contact angle along the apparent contact line caused by the interaction with the underlying surface pattern. Beyond the specific geometry studied in this paper, our results highlight the opportunity to use different pattern geometries to guide droplets to prescribed equilibrium positions by exploiting the combination between small differences in the apparent contact angle caused by the underlying geometry and the low friction offered by a lubricant impregnated surface. For example, radial patterns could be used to guide the inwards or outwards motion of droplets from a central position, or to induce the self-centring of droplets within a surface pattern. Here we have explored the interaction of menisci of equal positive curvature, which leads to attractive interactions. These could be exploited to retain droplets at prescribed positions under the action of external forces, such as gravity. However, it would also be interesting to explore macroscopic pattern geometries that induce repulsive interactions between menisci of different curvature sign. This could allow the guiding of droplets along prescribed trajectories without the need of direct contact with solid walls.

Here we have used standard photolithography as a means of surface patterning. This allows us to minimise any unnecessary microscopic secondary roughness inherent to the surface. However, millimetre-scale surface textures that can be treated to become lubricant-impregnated surfaces can be easily produced using techniques such as 3D printing or roll-to-roll printing, thus making it feasible to use the principles explored in this paper to develop methods for liquid transport in technological applications, such as microfluidics or in fog-harvesting devices.

Acknowledgements

J. H. G. gratefully acknowledges financial support from Reece Innovation. J. H. G. and E. R.-G. acknowledge the University of Northumbria at Newcastle for its support *via* postgraduate research studentships. The authors also acknowledge Dr Michael Cooke for valuable advice and technical support.

References

1 C. N. Baroud, F. Gallaire and R. Dangla, *Lab Chip*, 2010, **10**, 2032–2045.
2 M. Singh, H. M. Haverinen, P. Dhagat and G. E. Jabbour, *Adv. Mater.*, 2010, **22**, 673–685.
3 D. Quéré, *Annu. Rev. Mater. Res.*, 2008, **38**, 71–99.
4 T. A. Duncombe, E. Y. Erdem, A. Shastry, R. Baskaran and K. F. Böhringer, *Adv. Mater.*, 2012, **24**, 1545–1550.
5 D. Soto, G. Lagubeau, C. Clanet and D. Quéré, *Phys. Rev. Fluids*, 2016, **1**, 013902.
6 J. Li, Q. H. Qin, A. Shah, R. H. A. Ras, X. Tian and V. Jokinen, *Sci. Adv.*, 2016, **2**, e1600148.
7 J. Li, X. Tian, A. P. Perros, S. Franssila and V. Jokinen, *Adv. Mater. Interfaces*, 2014, **1**, 1400001.
8 K. O. Zamuruyev, H. K. Bardaweel, C. J. Carron, N. J. Kenyon, O. Brand, J.-P. Delplanque and C. E. Davis, *Langmuir*, 2014, **30**, 10133–10142.
9 N. T. Chamakos, G. Karapetsas and A. G. Papathanasiou, *Colloids Surf., A*, 2016, **511**, 180–189.
10 B. Chandesris, U. Soupremanien and N. Dunoyer, *Colloids Surf., A*, 2013, **434**, 126–135.
11 R. S. Subramanian, N. Moumen and J. B. McLaughlin, *Langmuir*, 2005, **21**, 11844–11849.
12 S. C. Hernández, C. J. C. Bennett, C. E. Junkermeier, S. D. Tsoi, F. J. Bezares, R. Stine, J. T. Robinson, E. H. Lock, D. R. Boris, B. D. Pate, J. D. Caldwell, T. L. Reinecke, P. E. Sheehan and S. G. Walton, *ACS Nano*, 2013, **7**, 4746–4755.
13 A. Shastry, M. J. Case and K. F. Böhringer, *Langmuir*, 2006, **22**, 6161–6167.
14 M. Reyssat, F. Pardo and D. Quéré, *EPL*, 2009, **87**, 36003.
15 J. Li, Y. Hou, Y. Liu, C. Hao, M. Li, M. K. Chaudhury, S. Yao and Z. Wang, *Nat. Phys.*, 2016, **12**, 606–612.
16 G. McHale, S. J. Elliott, M. I. Newton and N. J. Shirtcliffe, *Contact Angle, Wettability Adhes.*, 2009, **6**, 219–233.
17 N. Bjelobrk, H.-L. Girard, S. Bengaluru Subramanyam, H.-M. Kwon, D. Quéré and K. K. Varanasi, *Phys. Rev. Fluids*, 2016, **1**, 063902.
18 M. Chakraborty, U. U. Ghosh, S. Chakraborty and S. DasGupta, *RSC Adv.*, 2015, **5**, 45266–45275.
19 D. Baratian, A. Cavalli, D. van den Ende and F. Mugele, *Soft Matter*, 2015, **11**, 7717–7721.
20 M. G. Pollack, R. B. Fair and A. D. Shenderov, *Appl. Phys. Lett.*, 2000, **77**, 1725–1726.
21 G. McHale, C. V. Brown, M. I. Newton, G. G. Wells and N. Sampara, *Phys. Rev. Lett.*, 2011, **107**, 186101.
22 S. Daniel, M. K. Chaudhury and P.-G. de Gennes, *Langmuir*, 2005, **21**, 4240–4248.
23 J. E. Longley, E. Dooley, D. M. Givler, W. J. Napier, M. K. Chaudhury and S. Daniel, *Langmuir*, 2012, **28**, 13912–13918.
24 T. A. Duncombe, E. Y. Erdem, A. Shastry, R. Baskaran and K. F. Böhringer, *Adv. Mater.*, 2012, **24**, 1545–1550.
25 J. T. Luo, N. R. Geraldi, J. H. Guan, G. McHale, G. G. Wells and Y. Q. Fu, *Phys. Rev. Appl.*, 2017, **7**, 014017.
26 T.-S. Wong, S. H. Kang, S. K. Tang, E. J. Smythe, B. D. Hatton, A. Grinthal and J. Aizenberg, *Nature*, 2011, **477**, 443–447.

27 J. D. Smith, R. Dhiman, S. Anand, E. Reza-Garduno, R. E. Cohen, G. H. McKinley and K. K. Varanasi, *Soft Matter*, 2013, **9**, 1772–1780.
28 P. Kim, T.-S. Wong, J. Alvarenga, M. J. Kreder, W. E. Adorno-Martinez and J. Aizenberg, *ACS Nano*, 2012, **6**, 6569–6577.
29 B. R. Solomon, K. S. Khalil and K. K. Varanasi, *Langmuir*, 2014, **30**, 10970–10976.
30 J. H. Guan, G. G. Wells, B. Xu, G. McHale, D. Wood, J. Martin and S. Stuart-Cole, *Langmuir*, 2015, **31**, 11781–11789.
31 X. Huang, J. D. Chrisman and N. S. Zacharia, *ACS Macro Lett.*, 2013, **2**, 826–829.
32 U. Manna and D. M. Lynn, *Adv. Mater.*, 2015, **27**, 3007–3012.
33 T. Kajiya, F. Schellenberger, P. Papadopoulos, D. Vollmer and H.-J. Butt, *Sci. Rep.*, 2016, **6**, 23687.
34 K.-C. Park, P. Kim, A. Grinthal, N. He, D. Fox, J. C. Weaver and J. Aizenberg, *Nature*, 2016, **531**, 78–82.
35 D. Vella and L. Mahadevan, *Am. J. Phys.*, 2005, **73**, 817–825.
36 L. Landau and V. Levich, *Acta Physicochim. URSS*, 1942, **17**, 42–54.
37 J. Seiwert, C. Clanet and D. Quéré, *J. Fluid Mech.*, 2011, **669**, 55–63.
38 C. Semprebon, G. McHale and H. Kusumaatmaja, *Soft Matter*, 2017, **13**, 101–110.
39 S. Biswas, Y. Pomeau and M. K. Chaudhury, *Langmuir*, 2016, **32**, 6860–6870.
40 O. D. Velev, N. D. Denkov, V. N. Paunov, P. A. Kralchevsky and K. Nagayama, *Langmuir*, 1993, **9**, 3702–3709.
41 C. Dushkin, P. Kralchevsky, H. Yoshimura and K. Nagayama, *Phys. Rev. Lett.*, 1995, **75**, 3454.
42 N. Bowden, A. Terfort, J. Carbeck and G. M. Whitesides, *Science*, 1997, **276**, 233–235.
43 R. W. Style, Y. Che, S. J. Park, B. M. Weon, J. H. Je, C. Hyland, G. K. German, M. P. Power, L. A. Wilen and J. S. Wettlaufer, *et al.*, *Proc. Natl. Acad. Sci. U. S. A.*, 2013, **110**, 12541–12544.
44 S. Karpitschka, A. Pandey, L. A. Lubbers, J. H. Weijs, L. Botto, S. Das, B. Andreotti and J. H. Snoeijer, *Proc. Natl. Acad. Sci. U. S. A.*, 2016, **113**, 7403–7407.

Energy Invariance in Capillary Systems

Élfego Ruiz-Gutiérrez, Jian H. Guan, Ben Xu, Glen McHale, Gary G. Wells, and Rodrigo Ledesma-Aguilar*
Smart Materials and Surfaces Laboratory, Faculty of Engineering and Environment, Northumbria University, Ellison Place, Newcastle upon Tyne, NE1 8ST, United Kingdom
(Received 22 February 2017; published 26 May 2017)

We demonstrate the continuous translational invariance of the energy of a capillary surface in contact with reconfigurable solid boundaries. We present a theoretical approach to find the energy-invariant equilibria of spherical capillary surfaces in contact with solid boundaries of arbitrary shape and examine the implications of dynamic frictional forces upon a reconfiguration of the boundaries. Experimentally, we realize our ideas by manipulating the position of a droplet in a wedge geometry using lubricant-impregnated solid surfaces, which eliminate the contact-angle hysteresis and provide a test bed for quantifying dissipative losses out of equilibrium. Our experiments show that dissipative energy losses for an otherwise energy-invariant reconfiguration are relatively small, provided that the actuation time scale is longer than the typical relaxation time scale of the capillary surface. We discuss the wider applicability of our ideas as a pathway for liquid manipulation at no potential energy cost in low-pinning, low-friction situations.

DOI: 10.1103/PhysRevLett.118.218003

Introduction.—Capillary surfaces, which are infinitely thin surfaces that separate two fluids, are an everyday example of how beautiful symmetrical shapes appear in nature. Because they store surface energy, capillary surfaces underpin important physical phenomena such as the extreme superhydrophobicity exhibited by many plant and animal species, the internal adhesion of granular media, and the stability of foams and emulsions [1].

The fundamental equilibrium principle of the modern theory of capillarity is the minimization of the total surface energy [2], which for a solid-liquid-gas system reads $F = \gamma_{lg}A_{lg} + \gamma_{sl}A_{sl} + \gamma_{sg}A_{sg}$, where γ_i and A_i refer to the surface energy and surface area of the liquid-gas ($i = \mathrm{lg}$), solid-liquid ($i = \mathrm{sl}$), and solid-gas ($i = \mathrm{sg}$) interfaces.

As first noted by Gauss, the minimization of F is a variational problem that yields two central equations for the shape of a capillary surface. First, the liquid-gas interface must satisfy the Young-Laplace equation,

$$\Delta p = 2\gamma_{lg}\kappa, \tag{1}$$

which relates the pressure difference between the liquid and the gas Δp to the Laplace pressure $2\gamma_{lg}\kappa$, where κ is the mean local curvature of the interface. Second, upon contact with a solid boundary, the interface profile must satisfy Young's law,

$$\cos\theta_e = \frac{\gamma_{sg} - \gamma_{sl}}{\gamma_{lg}}, \tag{2}$$

which determines the intersection angle with the solid θ_e, also known as the equilibrium contact angle.

Finding solutions of the Young-Laplace equation, subject to the boundary condition imposed by Young's law, is a paradigm in capillarity [3,4]. Once an equilibrium solution is found, its stability can be examined and the surrounding energy landscape constructed. A displacement from equilibrium can be static or dynamic, but, in most cases, will lead to a change in the surface energy. Motion can occur only if this change surpasses the static energy barrier of contact-angle hysteresis [5], and the time scale of the motion that follows is typically set by competing capillary, dissipative, and external forces [6].

The relation between symmetry and energy invariance is a central concept across physics. In general, an equilibrium state with a high degree of symmetry will have a large number of energy-degenerate configurations mapping onto that state. For capillary surfaces, this implies the existence of energy landscapes where energy-invariant equilibria are either continuously or discreetly distributed in the parameter space (a familiar example is the translational symmetry of a droplet on a flat solid surface).

It is natural to consider whether the intrinsic symmetries of a capillary surface can ensure the invariance of the surface energy upon a reconfiguration of the boundaries. If so, one can further ask if energy-invariant trajectories that achieve a net translational motion of the capillary surface can be devised. This is an interesting problem from the point of view of theory, and is experimentally challenging because of the barriers imposed by contact-angle hysteresis and dynamic frictional forces.

In this Letter we demonstrate the energy-invariant translational motion of a capillary surface upon actuation of bounding solid surfaces. We focus on spherical surfaces as a model system, which appear in numerous situations of fundamental and practical relevance. We first introduce a theoretical approach to find paths of energy-invariant equilibria, and then examine the implications of dynamic frictional forces using a Lagrangian approach. Experimentally, we exemplify our ideas by manipulating the position of a droplet in a wedge geometry using slippery liquid-infused porous surfaces (SLIPS) [7], also known as lubricant-impregnated

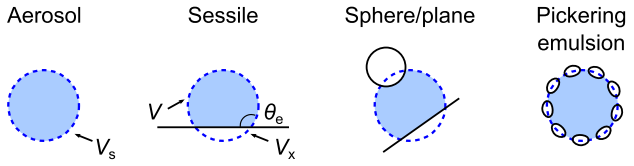

FIG. 1. Construction of energy-invariant equilibria of spherical capillary surfaces.

surfaces [8], which eliminate the contact-angle hysteresis and provide a test bed for quantifying dissipative losses out of equilibrium. We discuss the wider applicability of our results as a pathway for liquid manipulation at no surface-energy cost in low-pinning, low-friction situations.

Theory.—We start by considering the simplest solution of the Young-Laplace equation for a solid-liquid-gas system that preserves a spherical symmetry. This corresponds to an aerosol droplet of volume V_s and surface area A_s [see Fig. 1]. One can map this geometry to a sessile droplet by considering the intersection of the sphere with a solid plane of total surface area A. The required droplet shape is enforced by choosing the level of the truncation, which determines the intersection angle with the solid plane θ_e. This fixes the excluded volume of the sphere V_x and the volume of the droplet, $V = V_s - V_x$. As a result, one finds the total surface energy, $F_e = \gamma_{lg} A_s - F_x$, where $F_x = \gamma_{lg} A_s[(1+\cos\theta_e)/2 + \sin^2\theta_e \cos\theta_e/4] - \gamma_{sg} A$ is the free energy of the excluded cap, the solid-liquid footprint, and the dry portion of the solid plane.

This construction can be generalized to include an arbitrary number of nonintersecting boundaries, and of any shape. Mechanical equilibrium is guaranteed because the truncated-sphere shape satisfies the Young-Laplace equation, while the intersection with the solid boundaries now requires that Young's law is satisfied locally along each contact line. With these considerations in mind, one can immediately find the static surface energy of the capillary surface,

$$F_e = \gamma_{lg} A_s - \sum F_{xi}, \tag{3}$$

where the first term is the contribution of the full sphere and the second term is the energy arising from the portions excluded by the solid boundaries.

Here we shall focus on the situation where the solid surfaces have uniform wettability [9]. In such a case, the requirement of a constant equilibrium contact angle over a solid surface imposes the constraint that, close to the contact line, the boundaries are solids of revolution about an axis passing through the center of the sphere. It is straightforward to apply this criterion to find the force-free equilibrium states of capillary bridges between flat and curved walls [10–15], and also those of droplets in contact with suspended solid particles, such as Pickering emulsions [16] and liquid marbles [17,18].

The surface energy of such truncated-sphere solutions is invariant upon a rotation of the solid boundaries about the center of the sphere [see Fig. 1]. If one denotes X_e the equilibrium position of the center of the sphere relative to a reference frame fixed to the solid boundaries (e.g., their center of mass), then such a rotation is equivalent to a displacement of X_e relative to that reference frame. Because the surface energy does not depend on the position of the capillary surface relative to the frame of reference of the boundaries (i.e., F_e is not a function of X_e), a reconfiguration of the boundaries can result in a net translation of the capillary surface without the system incurring any work.

While this assertion is true in the quasistatic limit, more careful consideration is needed to quantify the out-of-equilibrium contribution to energy dissipation arising from the motion of the boundaries. Consider the Lagrangian of the capillary surface in the overdamped limit, $L(X,t) = -U$, where $U = F(X)$ is the potential energy and X is a coordinate describing its position relative to a set of solid boundaries. For a nonconservative system [19], the principle of minimization of action leads to the classical Euler-Lagrange equation

$$-\frac{\partial L}{\partial X} + \nu\dot{X} = 0, \tag{4}$$

where the second term on the left-hand side corresponds to the friction force and ν is the corresponding friction coefficient. Multiplying both sides of Eq. (4) by $\dot{X}$ leads to an expression for the rate of change of the total energy, $dE/dt = \partial F/\partial t - \nu(\dot{X})^2$. Close to equilibrium, $F \approx F_e + \frac{1}{2}k(X_e)(X - X_e)^2$, with a spring constant k that depends on the equilibrium configuration (here encoded through X_e). Therefore,

$$\frac{dE}{dt} = \frac{\partial F_e}{\partial t} + \frac{1}{2}\frac{\partial}{\partial t}[k(X - X_e)^2] - \nu(\dot{X})^2. \tag{5}$$

The first term in Eq. (5), $\partial F_e/\partial t = 0$, confirms the energy invariance in quasistatic situations, where $X = X_e$ and $\dot{X} = 0$. The second and third terms give the contributions to energy dissipation due to small deviations from equilibrium and frictional forces, respectively.

To quantify these contributions, we consider a slow sustained actuation of the boundaries over a time scale Δt, which results in a change in the equilibrium position ΔX_e. Within our description, this consists of prescribing an arbitrary function $X_e(t)$ in an interval $0 \le t \le \Delta t$. Expressing the second term in the right-hand side of Eq. (5) using Eq. (4), and integrating, gives the total energy consumption during the actuation,

$$\begin{aligned}\Delta E &= \int_0^{\Delta t} \frac{dE}{dt} dt \\ &= \int_0^1 \Delta X_e^2 \left\{ \frac{1}{2}\frac{\partial}{\partial T}\left[\left(\frac{\tau}{\Delta t}\right)^2 k\dot{x}^2 \right] - \left(\frac{\tau}{\Delta t}\right) k\dot{x}^2 \right\} dT,\end{aligned} \tag{6}$$

where we have defined the intrinsic relaxation time scale $\tau \equiv \nu/k$ and used the dimensionless variables $T \equiv t/\Delta t$ and $x \equiv X/\Delta X_e$. The total energy consumption will vary depending on the actuation and response signals, $X_e(t)$ and $X(t)$, subject to the initial condition $X(0)$. More importantly, both terms contributing to the energy change

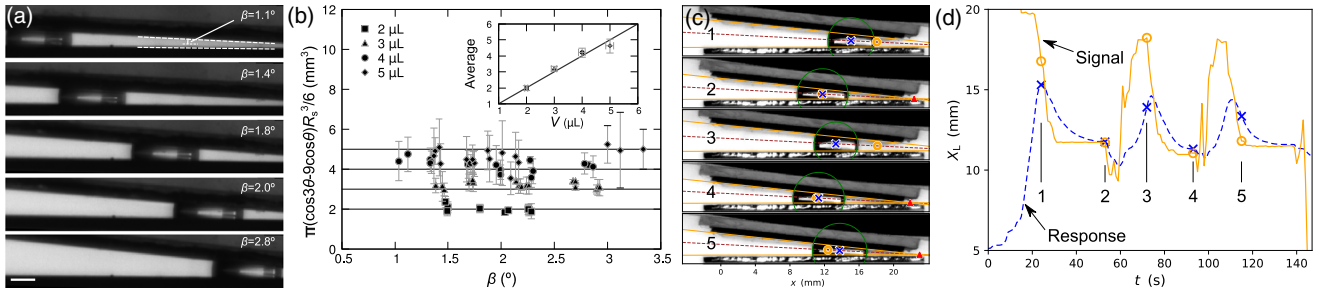

FIG. 2. Shape invariance of droplets trapped in SLIPS wedges. (a) A 4-μL water droplet equilibrates at different positions within a SLIPS wedge by adjusting the opening angle β. (b) The radius of the droplet (normalized to eliminate variations in the apparent contact angle, $\theta = 100 \pm 5°$) is invariant upon changes in the opening angle of the wedge. The inset shows the dispensed and measured droplet volumes. Error bars correspond to the standard deviation of the sample. The scale bar is 1 mm. (c) Manual actuation of a droplet by reconfiguration of the SLIPS geometry. The actuation signal shifts the position of the apex of the wedge (filled triangle). The new prescribed equilibrium position (open circle) is followed by the center of the droplet (times). (d) Equilibrium position and droplet trajectory for the sequence shown in (c). The droplet trajectory, here tracked by measuring the position of the center of the osculating sphere in the frame of reference of the lab X_L, follows the imposed signal with a lag determined by the friction force acting on the liquid.

in Eq. (6) will be negligible whenever the actuation is slow relative to the relaxation time scale, i.e., if $\tau/\Delta t \ll 1$.

Experiments.—Experimentally, a smooth transition between the energy-invariant states of a capillary surface upon boundary reconfiguration can only be achieved after eliminating contact-angle hysteresis [14]. Furthermore, to achieve the regime of negligible energy consumption during the reconfiguration [see Eq. (6)], one needs a test bed to determine the relaxation time scale of the out-of-equilibrium motion of the fluid. In our experiments, we used SLIPS [7], also known as lubricant-impregnated surfaces [8], as a means of eliminating contact-angle hysteresis. When placed on a SLIPS surface, a small water droplet adopts a spherical shape with an apparent contact angle, $\theta = 100° \pm 5°$. We also observed a wetting ridge close to the intersection between the droplet and the SLIPS surface, indicating the presence of a lubricant layer coating the droplet and preventing direct contact between the droplet and the underlying solid [8,20,21]. This was further confirmed by measurements of the effective surface tension of a water droplet coated with a thin lubricant layer, $\gamma \approx 63$ mN m^{-1}, and of extremely low sliding angles ($< 1°$) for the droplet when tilting the SLIPS surface [see Supplemental Material for more details [22]].

To illustrate the formation of truncated-sphere droplet shapes in contact with SLIPS surfaces, we created a wedge of variable opening angle β by mounting two SLIPS on an adjustable stage. For such a configuration, the free energy of a droplet in contact with the boundaries, Eq. (3), reduces to $F_e = \gamma\pi(\cos 3\theta - 9\cos\theta)R_s^2/3 + \text{const}$, with a sphere radius $R_s = \{6V/[\pi(\cos 3\theta - 9\cos\theta)]\}^{1/3}$. The natural frame of reference of the solid boundaries is the apex of the wedge, from which the equilibrium position of the center of the truncated spherical droplet along the bisector line is given by $X_e = -\cos\theta R_s/\sin\beta$. In Fig. 2(a) we present equilibrium droplet configurations where X_e is varied by adjusting the angle of the wedge in the range $1.1° \leq \beta \leq 2.8°$. Note that, because for small wedge angles $X_e \sim 1/\beta$, the droplet can be displaced several times its own width along the bisector line upon a relatively small reconfiguration of the boundaries. In Fig. 2(b) we present measurements of the cube of the droplet radius R_s as a function of the wedge angle. Because the apparent contact angle can vary from one set of SLIPS surfaces to another by a few degrees, we present our data absorbing the dependence on the contact angle, confirming the invariance of the truncated spherical shape upon changes in the orientation of the boundaries. This is equivalent to comparing the volume of the truncated sphere to the measured volume of the droplet, as shown by averaging the data over the wedge angle [see inset in Fig. 2(b)].

In Fig. 2(c) we present a sequence of droplet configurations obtained by manually imposing an arbitrary signal $X_e(t)$ [see also Video S1 in Supplemental Material [22]]. In the absence of a threshold pinning force to overcome, a sudden change in the wedge geometry results in the immediate motion of the droplet towards a new equilibrium configuration. Therefore, the droplet's trajectory follows the imposed signal [Fig. 2(d)], with a lag determined by the interplay between the actuation and relaxation time scales.

As a test bed to quantify the relaxation time of the translational motion of the droplet τ, we carried out experiments where one of the SLIPS surfaces is slowly brought into contact with a droplet. Upon contact, the droplet is allowed to relax to its equilibrium configuration [Fig. 3(a)]. In terms of our mathematical model, this corresponds to setting $X(0) = X_e + \Delta X$, where X_e and ΔX are constants. Therefore, from Eq. (4), we expect an exponential relaxation, $X(t) = X_e + \Delta X \exp(-t/\tau)$. Figure 3(a) shows a typical experimental sequence of the relaxation process, where $X(0) > X_e$. The droplet moves inwards, and follows a remarkably smooth dynamics [Fig. 3(b)]. Fixing the initial position of the droplet within the wedge to either $X(0) < X_e$ or $X(0) > X_e$, respectively, leads to outwards and inwards motions, always resulting in the same stable equilibrium state [Fig. 3(c)].

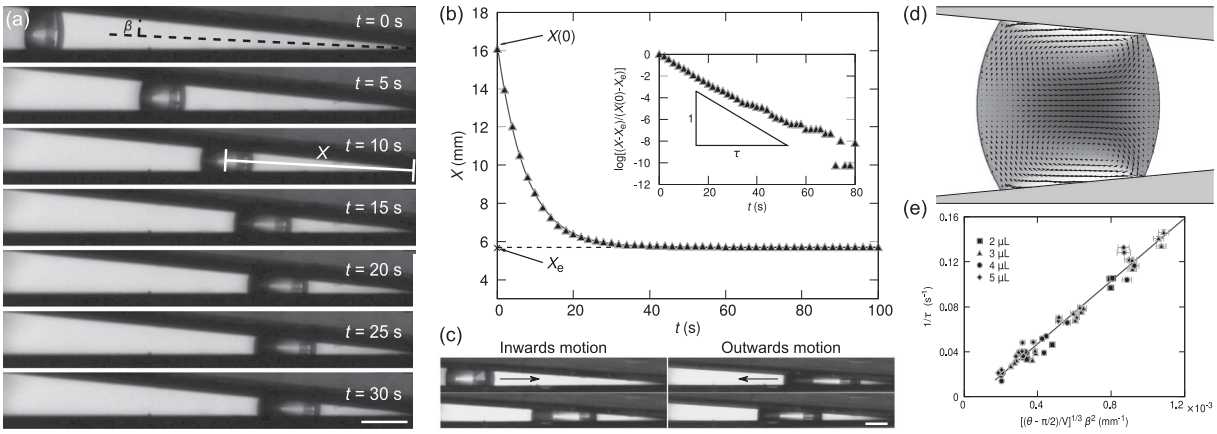

FIG. 3. Test bed for measuring the translational motion friction coefficient on SLIPS surfaces. (a) Time-lapse sequence of a 3-μL droplet moving inwards in a SLIPS wedge of opening angle $\beta = 2.8°$. (b) Time dependence of the position of the droplet, tracked by measuring the average distance of the leading and trailing menisci relative to the apex of the wedge $X(t)$. The time evolution obeys an exponential decay (continuous line) with a relaxation time scale τ (inset). (c) Inwards and outwards equilibration of droplets of the same volume ($V = 18$ μL) in wedges of the same angle, $\beta = 2.0°$. The direction of motion is indicated by the arrow. In equilibrium (bottom panels), both droplets select the same configuration. (d) Flow pattern of an inwards moving droplet (lattice Boltzmann simulation). The arrows indicate the velocity field in the frame of reference of the center of the droplet. The gray scale indicates the local speed. (e) Scaling of the relaxation time of the droplet with droplet volume, apparent contact angle, and wedge angle. The solid line is the expected scaling predicted by the theory (see text). The scale bars are 2 mm.

Because the SLIPS surfaces eliminate contact line friction [7,8], the friction force $-\nu\dot{X}$ results from the flow within the droplet, the lubricant layer, and the wetting ridge. This situation is similar to the case of a wetting capillary bridge moving within a solid wedge [23]. The contribution of the lubricant layer, relative to the bulk of the droplet, scales as $h/H \approx 10^{-2}$, where $h \approx 10$ μm is the thickness of the lubricant layer [21] and $H \approx 1$ mm is the typical thickness of the droplet, and is therefore negligible. We expect that the contribution from the ridge is also negligible, as the apparent angle is always close to its static value during the relaxation of the droplet. Therefore, we assume that the dominant contribution to the friction force comes from the flow pattern within the droplet. To gain insight into the structure of the flow, we carried out lattice Boltzmann simulations [24] of 2D droplets equilibrating in wedge geometries [see Supplemental Material for details [22]]. The simulations reveal a pressure-driven flow within the droplet, similar to a Jeffery-Hamel flow [25], truncated at the leading and trailing menisci, which move at uniform speed [Fig. 3(d)]. This effect can be captured by considering a slip length ℓ, which quantifies the lubrication imparted by the SLIPS surface on the motion of the apparent contact lines. After some manipulations, the expected friction coefficient can be expressed as $\nu \approx 12\,\mu V/(1+6\epsilon)H^2$, which is the familiar result for a Poiseuille flow with a correction that depends on the slip effect, where $\epsilon = \ell/H$ [see Supplemental Material [22]].

To compare the theoretical prediction to the measured relaxation times, we use a model for the out-of-equilibrium droplet morphology assuming a quasispherical barrel shape intersecting the solid at the apparent contact angle θ [26]. The droplet shape can then be used to construct the energy landscape $F(X)$, which in turn fixes the spring constant k. To leading order in β and $\theta - \pi/2$ (corresponding to the regime of our experiments), we obtain $k \approx 3\pi\gamma\beta^2/(\theta - \pi/2)$ [see Supplemental Material [22]]. Using the geometrical relation $H \approx (4V/\pi)^{1/3}(\theta - \pi/2)^{2/3}$, we then find a prediction for the relaxation time $\tau = \nu/k \approx [\mu/\gamma(1+6\epsilon)\beta^2][4V/\pi(\theta-\pi/2)]^{1/3}$. Figure 3(e) confirms the scaling of τ with V, θ, and β. Using the measured surface tension of the lubricant-cloaked droplets, $\gamma = 63$ mN m^{-1}, and the reported value of the viscosity of water at room temperature, $\mu = 1$ mPa s, the only unknown parameter in our prediction is the slip-length to drop-height ratio ϵ. We find a best fit to the data by choosing $\epsilon \approx 0.2$, which corresponds to a $\approx$60% drag reduction relative to the reference Jeffery-Hamel flow.

Our measurements of the relaxation time allow us to calculate the friction coefficient, and, therefore, to estimate the typical friction force experienced by the droplets upon actuation. For the actuation sequence shown in Fig. 2(d), $\nu \approx 0.013$ mN s mm^{-1}, and the droplets move with velocities ranging from -0.4 to 1.2 mm s^{-1}. Therefore, the friction force varies within -0.005–0.015 mN, and is significantly smaller than the weight of a droplet of equal size (≈ 0.04 mN). This implies that a relatively weak driving is enough to achieve translational motion, even out of equilibrium. This is evidenced in Fig. 4, where we present the corresponding reconstructed energy change, Eq. (6). After the droplet has equilibrated, the total energy E is always reduced due to the dissipation term, $-\nu\int dt\dot{X}^2$. However, the energy only changes significantly when the actuation time scale is much faster than the relaxation time scale of the drop. These "fast" events appear as intermediate

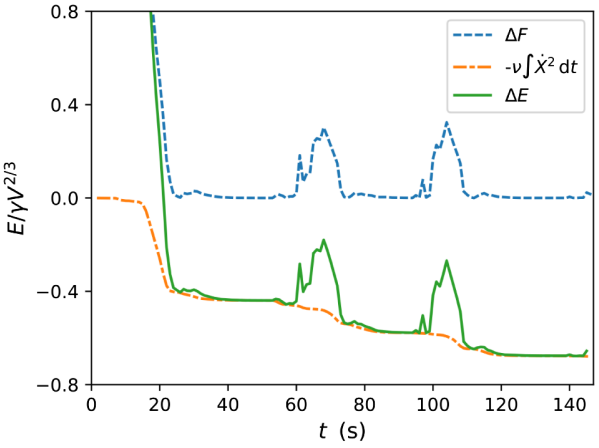

FIG. 4. Change in energy of a droplet upon manipulation within a SLIPS wedge (solid line). A fast actuation (intermediate peaks) leads to changes in the potential energy ΔF (dashed line); a slow actuation (intermediate plateaus) gives rise to small changes in the energy due to dissipation upon equilibration, $-\nu\int dt\dot{X}^2$ (dash-dotted line).

peaks in the potential energy, where the system is driven out of equilibrium, and correspond to the segments 2–3 and 4–5 in Fig. 2(d). During the rest of the actuation, where the driving is relatively slow, the change in potential energy and the energy dissipation remain negligible [plateaus in Fig. 4], confirming that it is possible to approach the limit of an energy-invariant translation of the droplet upon a slow reconfiguration of the boundaries.

Our results thus open up the possibility of developing pathways for droplet actuation at no potential energy cost and involving low energy dissipation. We highlight the relevance of these ideas in the future development of contact-free microfluidic channels that overcome both contact-line pinning and reduce viscous friction using liquid-layer mediated slip. These principles can be extended to treat multiphase systems such as encapsulated droplets, solid particles, and even cells, and can have a wider relevance in tribology [27,28] to encourage the development of technologies that remove the minimum force necessary to create motion and achieve the accurate manipulation of target objects.

Here we have focused on capillary surfaces of spherical symmetry and in contact with solids of uniform wettability as a means to illustrate energy invariance upon boundary reconfiguration. These ideas, however, can also be applied to study capillary surfaces of a different symmetry and in contact with boundaries of prescribed wettability distributions, opening the possibility of designing target energy landscapes for liquids in contact with solids as the basis for new kinds of "capillary metamaterials".

We thank F. Mugele and C. Semprebon for useful discussions. J. H. G. thanks REECE Innovation for financial support and D. Wood and J. Martin for useful discussions. J. H. G. and E. R.-G. acknowledge support from Northumbria University via Ph.D. studentships.

*rodrigo.ledesma@northumbria.ac.uk

[1] D. Bonn, J. Eggers, J. Indekeu, J. Meunier, and E. Rolley, Rev. Mod. Phys. **81**, 739 (2009).
[2] P.-G. de Gennes, F. Brochard-Wyart, and D. Quéré, *Capillarity and Wetting Phenomena: Drops, Bubbles, Pearls, Waves* (Springer Science & Business Media, New York, 2013).
[3] R. Finn, *Equilibrium Capillary Surfaces*, Grundlehren der Mathematischen Wissenschaften (Springer, New York, 2012).
[4] M. L. Anderson, A. P. Bassom, and N. Fowkes, Proc. R. Soc. A **462**, 3645 (2006).
[5] D. Quéré, Physica (Amsterdam) **313A**, 32 (2002).
[6] H. Bruus, *Theoretical Microfluidics*, Oxford Master Series in Condensed Matter Physics (Oxford University Press, Oxford, 2008).
[7] T.-S. Wong, S. H. Kang, S. K. Tang, E. J. Smythe, B. D. Hatton, A. Grinthal, and J. Aizenberg, Nature (London) **477**, 443 (2011).
[8] J. D. Smith, R. Dhiman, S. Anand, E. Reza-Garduno, R. E. Cohen, G. H. McKinley, and K. K. Varanasi, Soft Matter **9**, 1772 (2013).
[9] Although we note that the more general case of heterogenous surfaces can be of significant interest, both mathematically and physically.
[10] P. Concus, R. Finn, and J. McCuan, Indiana University mathematics Journal **50**, 411 (2001).
[11] H. Kusumaatmaja and R. Lipowsky, Langmuir **26**, 18734 (2010).
[12] M. Brinkmann and R. Blossey, Eur. Phys. J. E **14**, 79 (2004).
[13] D. Baratian, A. Cavalli, D. van den Ende, and F. Mugele, Soft Matter **11**, 7717 (2015).
[14] R. de Ruiter, C. Semprebon, M. van Gorcum, M. H. G. Duits, M. Brinkmann, and F. Mugele, Phys. Rev. Lett. **114**, 234501 (2015).
[15] T. P. Farmer and J. C. Bird, J. Colloid Interface Sci. **454**, 192 (2015).
[16] J. Guzowski, M. Tasinkevych, and S. Dietrich, Phys. Rev. E **84**, 031401 (2011).
[17] P. Aussillous and D. Quéré, Nature (London) **411**, 924 (2001).
[18] G. McHale and M. Newton, Soft Matter **11**, 2530 (2015).
[19] C. R. Galley, Phys. Rev. Lett. **110**, 174301 (2013).
[20] F. Schellenberger, J. Xie, N. Encinas, A. Hardy, M. Klapper, P. Papadopoulos, H.-J. Butt, and D. Vollmer, Soft Matter **11**, 7617 (2015).
[21] J. H. Guan, G. G. Wells, B. Xu, G. McHale, D. Wood, J. Martin, and S. Stuart-Cole, Langmuir **31**, 11781 (2015).
[22] See Supplemental Material at http://link.aps.org/supplemental/10.1103/PhysRevLett.118.218003 for further details on the experimental methods, numerical simulations and analytical calculations.
[23] E. Reyssat, J. Fluid Mech. **748**, 641 (2014).
[24] J.-C. Desplat, I. Pagonabarraga, and P. Bladon, Comput. Phys. Commun. **134**, 273 (2001).
[25] L. Rosenhead, Proc. R. Soc. A **175**, 436 (1940).
[26] E. Ruiz-Gutiérrez, C. Semprebon, G. McHale, and R. Ledesma-Aguilar, arXiv:1702.06076.
[27] M. Urbakh, J. Klafter, D. Gourdon, and J. Israelachvili, Nature (London) **430**, 525 (2004).
[28] G. He, M. H. Müser, and M. O. Robbins, Science **284**, 1650 (1999).